UNIVERSITY OF CALIFORNIA

Santa Barbara

# Mixed Lithium-Electron Conducting Polymers as Multifunctional Battery Binders

A dissertation submitted in partial satisfaction of the

requirements for the degree Doctor of Philosophy

in Chemical Engineering

by

Gordon T. Pace

Committee in charge:

Professor Rachel A. Segalman, Chair

Professor Glenn H. Fredrickson

Professor Christopher M. Bates

Professor Ram Seshadri

September 2023

The dissertation of Gordon T. Pace is approved.

---

Professor Ram Seshadri

---

Professor Christopher M. Bates

---

Professor Glenn H. Fredrickson

---

Professor Rachel A. Segalman, Committee Chair

August 7, 2023

Mixed Lithium-Electron Conducting Polymers as Multifunctional Battery Binders



by

Gordon T. Pace

ACKNOWLEDGEMENTS

First, I would like to thank my parents. I am obviously grateful for many things my parents have provided me- life, food and shelter growing up, educational and emotional support, and more. Of particular note here is how they fostered curiosity, independent thinking, and a willingness to ask questions and strive for logical answers, even from a young age. As a child, these personality traits perhaps resulted in a bit of sass- always questioning things that did not make sense to me (which is a lot when you're a kid). However, this ultimately developed critical thinking skills, a willingness to ask questions, and a desire for logical answers- all essential during my PhD. I am grateful that these characteristics were instilled in me from a young age.

I would next like to acknowledge all those with whom I have collaborated during my time at UCSB. I would like to thank my committee members (Ram Seshadri, Chris Bates, and Glenn Fredrickson) for their time and guidance during my graduate studies. I would also like to thank Michael Chabinyc. While Michael was neither a co-advisor nor a committee member, we met frequently during mixed conduction mini-meetings, and he continually provided valuable guidance and insight. If I ever had difficulty explaining an experimental result, the answer was probably contained in a paper from the 90's, and Michael could probably find said paper in a matter of seconds. Additionally, I would like to thank the entire Segalman group, who have been wonderful to work with- collaborative, supportive, smart, and hardworking.

Next, I would like to acknowledge both my advisor (Rachel Segalman) as well as Raphaële Clément, who all but formally became a co-advisor to me. I think this situation is a testament to the supportive nature of Rachel, the collaborative nature of UCSB, and the kind/helpful nature of Raphaële (in addition to her aptitude for NMR and battery research).

Through the natural progression of my research, the path that became most interesting to me relied heavily on both solid state NMR and cell testing (i.e. building actual batteries, albeit small ones). While these are outside of the Segalman group's traditional "bread and butter" techniques, Raphaële is an expert in both. I am grateful for the support Rachel continuously provides her students to pursue the paths they find most interesting. I am additionally grateful to Raphaële for providing guidance for my projects- giving substantial portions of her time to help design experiments, discuss data, and review manuscripts, ultimately contributing to every paper I published during the course of my PhD work. Rachel tells her students from day one that she provides them the seed of their project, and as they progress she is there to advise/guide, not manage. I am grateful for this methodology, as once I developed competency in polymer science fundamentals, I was able to begin asking questions of my own. Rachel embraced and guided the exploration of those questions, ultimately allowing me to pursue an interesting (in my opinion) intersection of organic electronics and battery science.

Last but not least I would like to thank Arielle. Throughout my graduate work you have provided a source of support, joy, happiness, and silliness that is much needed. I could not ask for a better partner to experience life with. You also let me use the comfy chair as I typed this dissertation, and for that my back is forever grateful.

VITA OF GORDON T. PACE

August 2023

## Education

**University of California, Santa Barbara (UCSB)** Santa Barbara, CA
Ph.D. in Chemical Engineering September 2019-September 2023

**Carnegie Mellon University (CMU)** Pittsburgh, PA
Bachelor of Science in Chemical Engineering May 2017
Additional Major in Biomedical Engineering, Minor in Business Administration
University and College Honors

## Patents

(1) **GT Pace**, ML Le, R.J. Clément, R.A. Segalman, "Systems of Polymer Binders of Lithium Ion Batteries and Methods Thereof" UC Case No. 2023-848

## Publications

(11) **GT Pace**, A Zele, P.H. Nguyen, R.J. Clément, R.A. Segalman, "Mixed Ion-Electron Conducting Polymer Complexes as High Rate Battery Binders" *Chem. Mater.* Submitted

(10) **GT Pace**, O Nordness, YJ Choi, P Nguyen, C Tran, R.J. Clément, R.A. Segalman, "Tuning Transport via Interaction Strength in Cationic Conjugated Polyelectrolytes" *Macromolecules.* (2023) DOI: https://doi.org/10.1021/acs.macromol.3c01206

(9) A Agee, **GT Pace**, V Yang, R.A. Segalman, A Furst "Biomimetic polymer enable electrochemical studies of bacterial electron transfer" *Science.* Submitted

(8) **GT Pace**, ML Le, R.J. Clément, R.A. Segalman, "A Coacervate-based Mixed Conducting Binder for High Power, High Energy Batteries" *ACS Energy Lett.* (2023) DOI: https://doi.org/10.1021/acsenergylett.3c00829

(7) A Agee, TM Gill, **GT Pace**, R.A. Segalman, A Furst "Electrochemical Characterization of Biomolecular Electron Transfer at Conductive Polymer Interfaces". *J Electrochem. Soc.* (2023) DOI: https://doi.org/10.1149/1945-7111/acb239

(6) **GT Pace**, O Nordness, K Asham, R Clément, RA Segalman, "Impact of Side Chain Chemistry on Lithium Transport in Mixed Ion-Electron Conducting Polymers". *Chem. Mater.* (2022) DOI: https://doi.org/10.1021/acs.chemmater.2c00592

(5) P Das, R Elizalde-Segovia, B Zayat, CZ Salamat, **GT Pace**, K Zhai, RC Vincent, BS Dunn, RA Segalman, SH Tolbert, SR Narayan, and BC Thompson, "Enhancing the Ionic Conductivity of Poly(3,4-propylenedioxythiophenes) with Oligoether Side Chains for

Use as Conductive Cathode Binders in Lithium-Ion Batteries". *Chem. Mater.* (2022). DOI: https://doi.org/10.1021/acs.chemmater.1c03971

(4) D Rawlings, D Lee, J Kim, IB Magdău, **GT Pace**, PM Richardson EM Thomas, S Danielsen, S Tolbert, TF Miller III, R Seshadri, RA Segalman, "Li+ and Oxidant Addition to Control Ionic and Electronic Conduction in Ionic Liquid Functionalized Conjugated Polymers". *Chem. Mater.* (2021). DOI: https://doi.org/10.1021/acs.chemmater.1c01811

(3) **GT Pace**, H. Wang, JF Whitacre, W. Wu, "Comparative study of water-processable polymeric binders in $LiMn_2O_4$ cathode for aqueous electrolyte batteries". *Nano Select.* (2020), DOI: https://doi.org/10.1002/nano.202000167

(2) P Das, B Zayat, Q Wei, CZ Salamat, IB Magdău, R Elizalde-Segovia, D Rawlings, D Lee, **GT Pace**, A Irshad, L Ye, A Schmitt, RA Segalman, TF Miller III, SH Tolbert, BS Dunn, SR Narayan, and BC Thompson, "Dihexyl-Substituted Poly(3,4-Propylenedioxythiophene) as a Dual Ionic and Electronic Conductive Cathode Binder for Lithium-Ion Batteries". *Chem Mater.* (2020), DOI: https://doi.org/10.1021/acs.chemmater.0c02601

(1) R. Garg, S.K. Rastogi, M. Lamparski, S. de la Barrera, **GT Pace**, N.T. Nuhfer, BM Hunt, V. Meunier, T. Cohen-Karni, "Nanowire-Mesh Templated Growth of Out-of-Plane Three-Dimensional Fuzzy Graphene". *ACS Nano*. (2017), DOI: 10.1021/acsnano.7b02612

**Presentations**

(7) "Overcoming Kinetic Limitations in $LiFePO_4$ Cathodes Using an Electrostatically-Stabilized Polymer Complex Binder" Materials Research Society (MRS) Spring Meeting, San Francisco, CA, 12 April 2023. Conference Presentation.

(6) "Impact of Side Chain Chemistry on Lithium Transport in Mixed Ion-Electron Conducting Polymers" Materials Research Outreach Symposium (MROP), Santa Barbara, CA, 12 May 2022. Symposium Poster Presentation.

(5) "Impact of Side Chain Chemistry on Lithium Transport in Mixed Ion-Electron Conducting Polymers" American Physical Society March Meeting, Chicago, IL, 18 March 2022. Conference Presentation.

(4) "Evaluation of Polymeric Binders in Aqueous Electrolyte Environment." 235$^{th}$ Electrochemical Society Biannual Meeting, Dallas, TX, 29 May 2019. Conference Presentation.

(3) "Analysis of the Effects of Oleic Acid on Oil-Surfactant Interfaces." Meeting of the Minds Research Symposium, Carnegie Mellon University, Pittsburgh, PA, 10 May 2017. Honors Research Presentation and Defense.

(2) "Detecting the Presence of Peanut Allergens in Food." Meeting of the Minds Research Symposium, Carnegie Mellon University, Pittsburgh, PA, 10 May 2017. Prototype Demonstration and Presentation.

(1) "E-nanomesh for Sensing and Culturing Electroactive Cells." Biomedical Engineering Research Symposium, Carnegie Mellon University, Pittsburgh, PA, 28 July 2015. Symposium Presentation.

**Awards and Honors**

| | |
|---|---|
| NSF Graduate Research Fellowship | 2020-2023 |
| UCSB Science Line, Outstanding Physical Sciences Volunteer Award | 2020, 2021 |
| Most Outstanding Senior Award, Department of Biomedical Engineering, CMU | 2017 |

**Outreach and Volunteering**

| | |
|---|---|
| UCSB MRL Zoom Outreach Leader | 2020-2023 |
| UCSB MRL Material World Volunteer | 2019-2023 |
| UCSB FUSE Volunteer | 2019-2020 |
| UCSB Science Line Contributor | 2019-2022 |

**Teaching and Mentorship**

*Teaching Assistant*:

| | |
|---|---|
| Chemical Engineering Thermodynamics | Spring 2021 |
| Introduction to Chemical Engineering Design | Fall 2021, 2023 |

*Mentored Students:*

| | |
|---|---|
| Robert Kim (Masters Student, UCSB) | Winter-Spring 2023 |
| Cassidy Tran (Undergraduate, FLAM Internship Program) | Summer 2022 |
| Kareem Asham (Masters Student, FLAM Internship Program) | Summer 2021 |

ABSTRACT

Mixed Lithium-Electron Conducting Polymers as Multifunctional Battery Binders

by

Gordon T. Pace

Polymeric battery binders are a ubiquitous component in composite lithium-ion cathodes, providing critical structural functionality. However, industry standard binders, such as polyvinylidene fluoride (PVDF) are insulating to both electrons and ions and are thus detrimental to performance. Mixed ion-electron conducting polymers are promising materials for next generation battery binders, as they can provide the adhesive properties of traditional binders, while also facilitating charge transport. However, simultaneously optimizing electronic, ionic, and lithium transport within a single system has proved a challenge, particularly given the need to maintain the mechanical function required of a binder. This work elucidates polymer design strategies for simultaneous lithium-electron conduction, while also considering the practical requirements of a battery binder (i.e. processability, electrochemical stability, and solubility). First, it is shown that side chain engineering can be used to control lithium transport in semiconducting polymers, emphasizing the importance of solvating ions without trapping them. This concept is further explored, studying $Li^+$ transport and ionic/electronic conduction in a family of polythiophenes functionalized with cationic side chains. It is found that the interaction strength between the side chain and added salt is critical for ion transport, while the structure of the side chain largely governs electron transport. These fundamental insights are then bridged into real battery binders, showing that an

electrostatically stabilized complex, comprising of a blend of a charged conjugated polymer with an oppositely charged polyelectrolyte, reduces kinetic limitations in $LiFePO_4$ cathodes. The conducting binder dramatically improves both rate capability and cycle stability, compared to the industry standard, insulating PVDF binder. Finally, the method of electrostatically stabilizing conjugated polymer complexes is shown to be an effective platform for mixed conducting binders, as several polymer chemistries afford high-performing, conductive binders.

TABLE OF CONTENTS

LIST OF FIGURES

# Chapter 1

# Introduction

Battery functionality centers around the controlled conduction of ions and electrons; yet, up to 20% by weight of most electrodes are comprised of a polymer binder that holds the battery components together, but is insulating to both species. A promising alternative to traditional non-conducting binders lies in an emerging class of organic polymers that conduct both ions and electrons, termed mixed ion-electron conductors (MIECs). MIECs can still provide the structural functions of traditional binders, but also enable ion and electron conduction. By and large, these properties have been developed in separate materials classes, making the rational integration of both properties an interesting challenge. Broadly speaking, the transport of electronic charge carriers relies on long range, delocalization of electrons along π-conjugated backbones, which occurs in ordered domains of the polymer.[1–3] Ion transport, on the other hand, is typically coupled to polymer chain dynamics, and relies on free volume and segmental motion.[4–7]

The goal of this work is to develop structure property relationships for mixed electron-lithium conduction in organic polymers, then translate these materials into real battery binders, which requires attention be paid to non-transport related properties such as solubility, electrochemical stability, and processability. As a backdrop to this study, the first chapter will review the fundamentals for both electron transport and ion transport in separate polymer systems, followed by design strategies to integrate the two properties, and finally initial applications of semiconducting polymers as battery binders. The second chapter shows how

side chain engineering can be used to control lithium transport in semiconducting polymers, emphasizing the importance of solvating ions without trapping them. Chapter three explores this concept further, studying Li+ transport and ionic/electronic conduction in a family of polythiophenes functionalized with cationic side chains. It is found that the interaction strength between the side chain and added salt is critical for ion transport, while the structure of the side chain governs electron transport. Chapter 4 bridges the fundamental insights into real battery binders, showing that an electrostatically stabilized complex reduces kinetic limitations in $LiFePO_4$ cathodes. Finally, Chapter 5 shows that complex coacervation is an effective platform for mixed conducting binders, where several polymer chemistries can form coacervates that enable highly processable slurries that lead to conductive, electrochemically stable binders.

## 1.1 Electron transport in conjugated polymers

### *Chemical design of conjugated polymers*

Compared to other polymers, conjugated polymers are unique in that they are semiconducting- intrinsically insulating (like most polymers), but upon doping can achieve electronic conductivities on par with many metals. This property stems from the structure of the conjugated backbone, which possess alternating double and single bonds. This causes overlapping p-orbitals (π- π stacking), creating a system of delocalized π-electrons..[8–10] As a result of the delocalization along the backbone, the highest occupied molecular orbital (HOMO) and the lowest unoccupied molecular orbital (LUMO) can span many repeat units. This forms valence and conduction bands similar to inorganic semiconductors.[9,10] Polyacetylene was the seminal system of Heeger, MacDiarmid, and Shirakawa,[11] however this polymer proved difficult to process and functionalize. Aromatic backbones have since addressed this issue, enabling the π- π stacking previously discussed, while also facilitating facile side chain functionalization, which can dramatically improve solvent processability as well as shift the HOMO and LUMO via electron withdrawing/donating groups.[9,12]

Figure 1.1 shows three examples of common conjugated backbones. Polyacetylene was the first reported conducting polymer, but has little modern significance. However, this system did give rise to more tunable conjugated backbones, where polythiophenes will be the focus of this work owing to their facile side chain functionalization and favorable doping potential of 3.2-3.3V vs $Li/Li^+$.

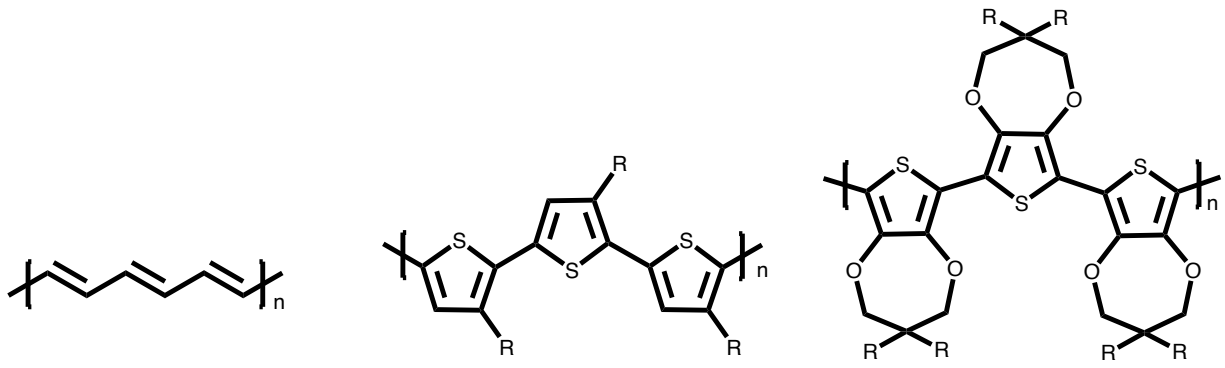


Polyacetylene Poly(3-alkylthiophenes) Poly(3,4-propylenedioxythiophenes)

**Figure 1.1: Chemical structures of common conjugated polymer backbones**

(a) Polyacetylene (PA) was the first conjugated polymer to demonstrate semiconducting properties, but lacks processability and tunability. (b) poly(3-alkylthiophenes) (P3AT) are widely studied due to facile synthesis and sidechain functionalizations, which can both improve processability and tune properties. (c) poly(3,4-propylenedioxythiophenes) (ProDOTs) are thiophenes with the 3- and 4- positions of the thiophene functionalized with an alkylenedioxy bridge. The electron donating oxygen atom attached to the thiophene ring lowers the band gap of ProDOT derivatives, exemplifying the tunability of organic semiconductors. Typical semiconducting polymers functionalize these aromatic rings with alkyl side chains to promote solubility in organic solvents (i.e. R= $C_6H_{13}$). As will be discussed later, replacing these alkyl substituents with ion solvating moieties is a common design strategy for mixed conduction.

Chemical design is only one component of the overall structure property relationships that govern charge transport in semiconducting polymers, as the long range order and semicrystallinity of the polymer also play a large role. This is due to the need for orbital overlap in the conjugated backbone, which is typically enhanced with ordered/crystalline strucutres.[9,13] Complicating the design space is that the ordered structure of a given conjugated backbone is not necessary fixed, or intrinsic to said backbone. Sidechain functionalization, as well as the introduction of dopants can both disrupt,[14,15] or drive backbone order, aggregation, and chain stiffening.[16–18] Furthermore, processing conditions, measurement methods, and substrates can substantially alter the long range order of a given system,[19,20] often making it difficult to deconvolute structure property relations intrinsic to the polymer chemistry from those induced

by the particular measurement conditions. Common measurement techniques will be discussed in Ch 1.3.

***Electronic doping of conjugated polymers***

Conjugated polymers are insulting in their un-doped, "neat" state. Imparting charge carriers requires electron density be removed from the HOMO (making the system electron deficient, p-type doping), or added to the LUMO (electron rich, n-type doping). [8,9] This is most often accomplished via a direct redox reaction, however some dopants accomplish the task via a multistep route. For example, $NOBF_4$ is a common chemical, p-type dopant. Here, $NO^+$ directly oxidizes the polymer backbone, leaving the system as NO gas and leaving $BF_4^-$ as the charge compensating counterion (these counterions are often referred to as the "dopant," as they are what remains in the system). On the other hand, HTFSI is a strong acid that protonates the backbone. When the backbone is protonated, it is currently believed that the resulting carbocation oxidizes a neighboring chain, thus forming the typical radical-hole pair.[21,22] In either case, the conjugated backbone is made electron deficient, thus accomplishing p-type doping. This work will focus on p-type semiconducting polymers, as n-type polymers are typically much less stable due to the relatively high LUMO (2-3 eV). [23,24]

Whether p-type doping is accomplished chemically (via introduction of an oxidant such as $NOBF_4$) or electrochemically (via applying a potential to the polymer on a working electrode of an electrochemical cell), the result is a positive charge on the conjugated backbone (often called a "hole") coupled with a charge compensating anion (often referred to as the "dopant"), as shown in Figure 1.2.

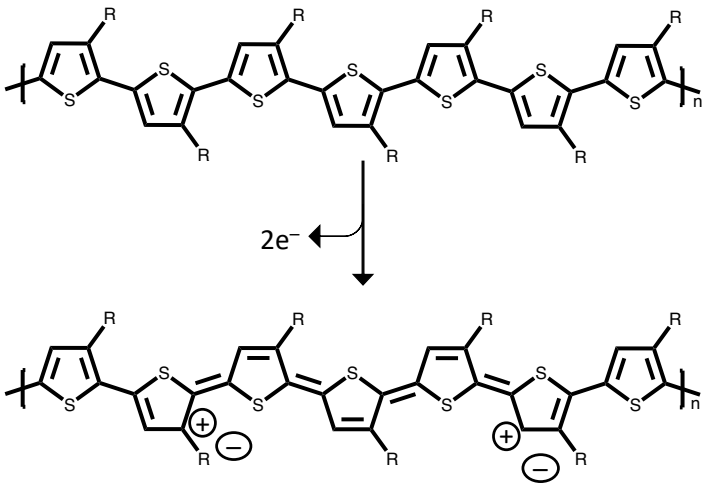


**Figure 1.2: A schematic of a p-type doping process**

A polythiophene backbone is shown as a model system. The backbone is oxidized, removing electrons and leaving positive holes with a charge compensating anion. Doping concentration can vary, but broadly speaking semi-conducting polymers are heavily doped compared to their inorganic counterparts. 1-2 dopants per 7 repeat units is typical.

Overall electronic conductivity is directly related to both the quantity of the holes (carrier density) and the rate at which the charge carriers move (carrier mobility). Carrier mobility typically increases with chain planarization and enhancements to conjugation length, [9,25] which are highly dependent on the backbone conformation. [9] As a result, it has often been viewed that electronic conductivity is coupled to the degree of crystallinity. However, it has more recently been proposed that the unifying requirement for high mobility is not degree of crystallinity, but rather interconnection between π-aggregates, even if these are small and disordered, which helps explain the good performance of many poorly ordered polymers that have been recently reported.[1] Further, complexes between conjugated polymers and polyelectrolytes have been shown to obtain high carrier mobilities due to an increase in chain planarization, but obtain little to no crystallinity.[26,27]

## 1.2 Polymeric ion transport

Similar to electronic conductivity, ionic conductivity is directly related to carrier concentration and mobility. In the case of polymeric ion transport, the charge carriers are ions- either dissociated, added salt or counterions associated to tethered ionic groups.[4,5,7,28] Thus ionic conductivity is intimately coupled to the strength of interaction between the polymer and added ions. In other words, a delicate balance between solvation and mobility is need for high conductivity. Interactions must be strong enough to solvate substantial salt (increasing carrier density), but not so strong that the ions become trapped, effectively tethering them to the polymer, reducing mobility.[29] Balancing these properties is still an active area of research, as is it is key to increasing "decoupled ion transport," which refers to transport properties not intrinsically tied to chain dynamics.

In designing polymer electrolytes, particularly for battery related applications, three key figures of merit must be consider with respect to transport- the total ionic conductivity ($\sigma$), the ion diffusion coefficients ($D_{+/-}$), and the cation transference number ($t_{Li+}$). Here, the diffusion coefficients are reflective of the mobility of dissociated ions, total conductivity reflects total charge transport (being a function of concentration and mobility of single and correlated ion motion), and the transference number reflects the fraction of current carried by the ion of interest ($Li^+$ for Li-ion batteries). As a general design rule, as polymer chain dynamics increase, so does ion transport, where chain dynamics are typically measured via the glass transition temperature ($T_g$). With this design strategy ionic conductivity comes at the direct expensive of structural properties. Much focus has been given to overcoming this limitation.

Design strategies for decoupled transport largely focus on engineering ion-ion and ion-polymer interactions, where "average-lifetime" of ion association is a critical parameter for

overall ion transport.[30,31] It has been shown that ion transport that is decoupled from chain dynamics occurs *via* formation and breaking of ion-associations with side chains, creating a need to balance polymer-ion interaction strength such that solvation occurs, but ions are not immobilized.[30,31] In this vein, charged side chains and metal ligand coordination groups have been of active interest to move beyond PEO-like design strategies. In PEO, the polar backbone drives dissolution, but the strong ether- cation interactions limit solubility, where peak conductivities are often reported at only r=0.1 or less (where r is moles of salt per mole of polymer repeat unit). Additionally, these systems are directly reliant on backbone chain dynamics for transport and practical applications typically require operation above PEO's melting temperature,[7,32] where strictly speaking the system is no longer a solid electrolyte.

Side chain functionalization with charged or ligating moieties are promising strategies to push these limitations. For instance, the imidazole group has been shown to form metal - ligand complexes with a variety of metal cations. This resulted in high conductivity and tunable mechanics, effectively decoupling the two properties.[28] Imidazolium, the cationic imidazole analogue, is a promising polymer ionic liquid (PIL) shown to have high ionic conductivity and good salt solvation ability.[15,33,34] Finally, recent design strategies have leveraged zwitterionic moieties to impart superionic charge transport, which proved advantageous for both $Li^+$ selectivity, conductivity, and electrolyte stiffness.[35]

## 1.3 Mixed ion-electron conducting polymers

While transport mechanisms and design strategies for both ion and electron conducting polymers are relatively well understood as independent materials classes, integrating each property into a single system presents an interesting challenge. As has been discussed, fast electronic and ionic conductivities require very different polymer designs. High ionic

conductivity is generally associated with both a high dielectric constant and fast segmental motion, while high electrical conductivity generally requires aromaticity combined with a high degree of order.[36–38] Hybrid designs, for example incorporating ionically conductive sidechains on an electronically conductive backbone,[14,15,37–39] generally result in a tradeoff between ionic and electronic conduction.[40] Further complicating the design space for mixed conducting battery binders, the motivation of this work, is the practical consideration that as the polymer dielectric constant increases (promoting ion transport), polar battery electrolytes dissolve the polymer.[40] Thus, the ultimate design goal is to develop structure property relationships that can predicably tune (and ideally optimize) both ionic and electronic transport in polymeric systems with sufficient stability and processability for battery applications. The following section will highlight several mixed conduction design strategies applicable to this work.

***Design strategies for incorporating ionic and electronic conduction***

Traditional electronically conducting polymers utilize a conjugated backbone, typically functionalized with alkyl side chains (Figure 1.3). These designs result in very low dielectric environments incapable of dissolving appreciable amounts of salt.[41] MIECs most overcome this by incorporating ion solvating groups, which may take the form of side chains, covalently tethered blocks, or distinct polyelectrolytes blended with the conjugated polymer. From this perspective, three categories of MIEC polymers naturally arise- single component systems utilizing side chain engineering to impart ion solvation to a conjugated backbone, block copolymer architectures with distinct ion and electron conducting blocks, and blends between electron and ion conducting polymers.

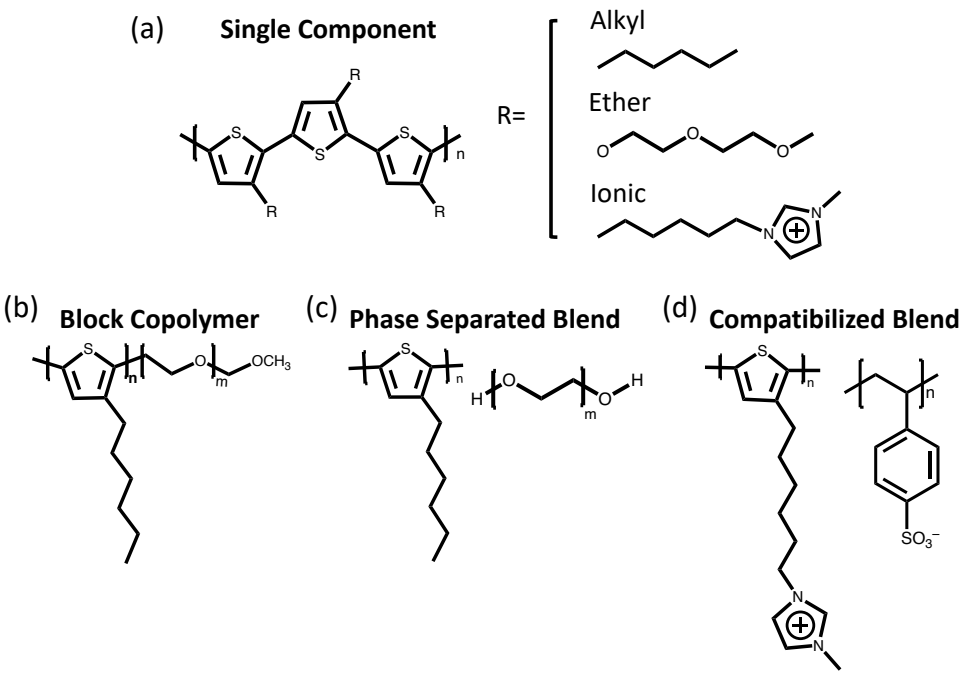


**Figure 1.3: An illustration of three common design strategies for mixed conducting polymers**

The commonly studied thiophene backbone is depicted as a model system. (a) Shows examples of sidechain engineering, where alkyl sidechains were traditionally used to impart solubility to conjugated polymers, and now polar or charged side chains are implemented for ion solvation and transport. Combining electronically conducting and ionically conducting polymers is another route to obtain a mixed conducting system, where block copolymers (b) are formed by covalently tethering the two systems, and blends (c,d) simply mix the systems. Electrostatics (d) is a common method to drive miscibility of these otherwise immiscible (c) polymer classes.

***Mixed Conducting Blends***

An intuitive method for generating a mixed conductor is to blend canonical electron and ion conducting polymers, for example P3HT and PEO. This particular blend would ultimately result in a phase separated, heterogenous system due to the disparate polarities of each polymer, along with the entropy of mixing per unit volume which scales as $1/N$, where N is the degree of polymerization of a chain.[42] However, heterogeneity is not inherently a limitation for obtaining high electronic and ionic conductivities. In fact, PEDOT:PSS is a heterogenous mixed conductor and touted as one of the most widely studied systems, reaching

electronic conductivities of 1-4,000 S/cm depending on dopants and additives.[43] However, this blend has a poorly defined microstructure and its properties heavily depend additives, and thus it is a non-ideal system for gaining fundamental structure property relationship with respect to polymeric mixed conduction.

A widely deployed strategy to provide greater thermodynamic control over mixing is to utilize electrostatic interactions, which can drive macroscopically homogenous mixed conducting blends. Specifically, conjugated polyelectrolyte complex coacervates are multicomponent systems containing oppositely charge polyelectrolytes, where at least one polymer contains a conjugated backbone.[26,27,44–49] Complex coacervates undergo an associative, liquid-liquid phase separation involving charge attractions, which usually results in a dense coacervate phase and a dilute supernatant phase.[50–52] Within the polymer rich coacervate phase, ionic crosslinks between side chains provide insolubility in many common solvents, yet retain the ability to be plasticized/swell with water and polar electrolytes.[53,54] Additionally, electrostatically stabilized complexes can drive mixing of two polymers of differing backbone chemistries, as the electrostatic interactions, along with the entropy gain of counterion release, overcomes the repulsive interactions that typically cause immiscibility in polymer blends.[42,55,56] Thus polyelectrolyte complexes enable a diverse array of backbone and side chain architectures to be implemented without macroscopic phase separation, offering immense tunability of electronic, ionic, and mechanical properties. Furthermore, complexation has been shown to have profound effects on optoelectronic and conduction properties, as structural templating of the conjugated polymer occurs during complexation, resulting in a planarized backbone with highly delocalized excited states.[26,46,49]

***Block copolymers***

Similar to blending, block copolymer mixed conductors combine two disparate backbone chemistries, with one responsible for electronic transport and the other responsible for ionic transport. Due to the covalent linking between blocks, macrophase separation will not occur, however phase separation on smaller length scales will, depending on the segment lengths and backbone chemistries.[37,57] Tuning these parameters, as well as processing conditions, affords an array of structures including cylindrical, lamellar, spherical, and gyroid phases.[57] These structures, aside from spherical, give rise to interconnected transport pathways for ionic and electronic charge carriers.[37,58] From a design perspective, this inherently imparts a trade-off for electronic and ionic conductivity, as each block is responsible for transport of one charge carrier or the other.

***Single component mixed conductors***

Single component mixed conductors leverage ion solvating moieties distributed across the entire macromolecular structure. Here, electronic conduction is typically accomplished via a uniform conjugated backbone, and ion solvation and transport is imparted via high dielectric or charged sidechains (Figure 1.3). This design strategy is most analogous to traditional conjugated polymers, where alkyl sidechains were previously employed to improve solubility in organic solvents, and now high dielectric or charged side chains are used to improve ion solvation and transport.

While conceptually analogous to traditional CPs, this design strategy is not without its limitations. For instance. The most widely deployed side chain engineering design utilizes a conjugated backbone for electronic transport, coupled with poly(ethylene oxide) (PEO)-inspired oligoether side chains to solvate ions.[15, 16, 26-29] PEO itself touts moderate to poor lithium transference (<0.2),[59–61] and this property only worsens when ether substituents are

adopted as side chains. In ether based systems, salt is solvated via interactions between the cation and electronegative oxygens. The result is stable cation complexes akin to crown ether solvation. This is indeed effective for solvating salt, but inherently limits cation mobility.[22, 32] Cation transport that does occur requires interconnectivity of these solvation sites within the polymer matrix.[30-32] When ether moieties are adopted as side chains, this interconnectivity is limited compared to the long chain PEO analogue.[33] For work such as this, motivated by battery applications, cation transport is critical. Additionally, electronic conductivities for single component mixed conductors functionalized with ion conducting side chains are notably lower than their alkyl-side chain counterparts,[14,15,39,40,62] likely owing to disruption of backbone ordering needed for high electronic carrier mobility.

***Measuring electron and ion transport in polymers***

While it is conceptually clear that the previously discussed design strategies will generate a mixed conductor, isolating and determining ionic and electronic conductivities in an accurate manner is a challenge due to the array of charge carriers moving on varying time and length scales. When electronic and ionic conductivity are modulated by adding one dopant or the other, each parameter is relatively straight forward to measure. For instance, thin films of the conjugated polymer can be spun cast onto a gold patterned substrate, enabling facile vapor phase electronic doping (Figure 1.4). This configuration is appropriate for in-plane measurement of the electronic conductivity, where in its simplest form a DC potential can be applied, the resulting current measured, and Ohms law applied to determine resistance. Specific experimental details appear in the relevant sections of this work.

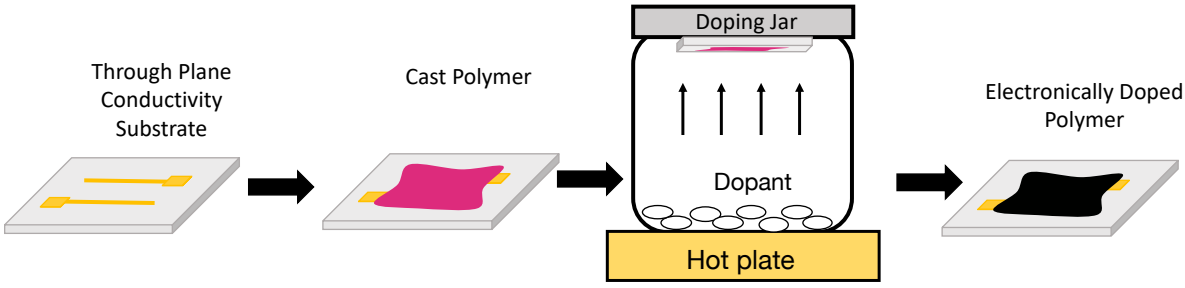


**Figure 1.4: The work flow for a standard thin film doping method**

This is a common technique for introducing dopants into conjugated polymers in a manner that enables electronic conductivity measurements. The polymer is typically spun cast onto a gold patterned substrate. This substrate has contacts which afford easy DC measurement after doping. Next, the sample is placed in a jar containing the desired dopant. Heat is applied to this jar, and dopant vapor infiltrates the polymer. Specific dopants, temperatures, and other conditions are described in the relevant sections of this work. While this is common practice for electronic doping, this format is distinct from common ionic conductivity configuration (Figure 1.5), which emphasizes the difficulty of "co-doping."

Determining bulk ionic conductivity is slightly more complex, but still relatively straight forward when only ionic charge carriers are present (i.e. salt is added, but no electronic dopants). In this situation, the polymer can be formed into a well-defined geometry and sandwiched between two ion blocking electrodes (Figure 1.5). This enables Electrochemical Impedance Spectroscopy (EIS, also referred to as AC Impedance) to be performed. In short, EIS applies a sinusoidal voltage, sweeping across frequencies at a set potential amplitude. Using well established methods, geometric features of the resulting Nyquist Plots are used to calculate the equivalent DC conductivity.[63–65] Examples of this analysis for ion conducting polymers are provided in Figure 1.6b.

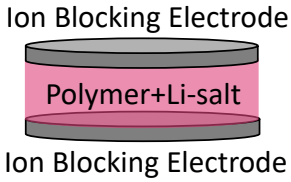


**Figure 1.5: Schematic of the setup used to determine ionic conductivity in polymers.**

A polymer mixed with the desired salt is formed into a well-defined geometry (typically a thin cylinder), and sandwiched between two ion blocking electrodes. Throughout this work, great care is given to entirely remove solvents/moisture from these samples and perform measurements in an inert environment, ensuring all ionic transport measured is from the polymer and not residual solvent. This affords easy interpretation and fitting of the Nyquist plot shown in Figure 1.6b, as there is only one material through which ions can transport, and the blocking electrodes will develop interfacial capacitance.

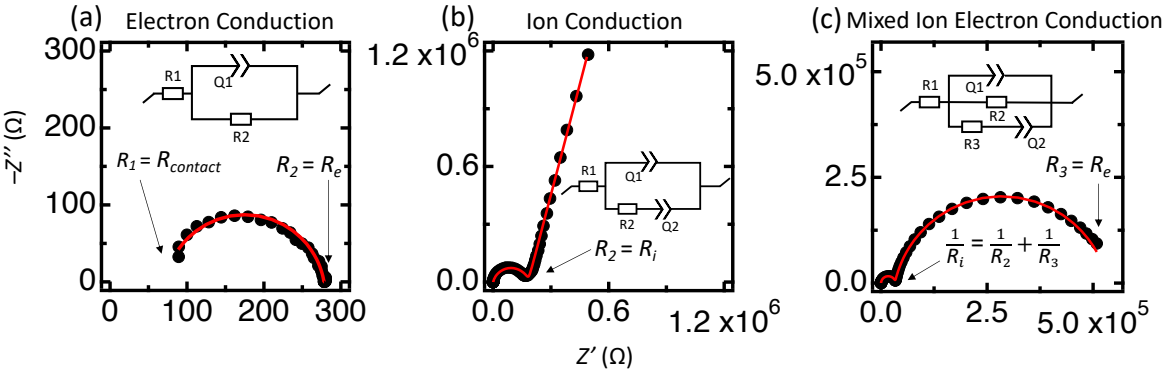


**Figure 1.6: Representative Nyquist plots for conducting polymers.**

Black circles are data, while the red lines are the fits using the respective equivalent circuits. (a) shows a single semicircle, indicative of electron conduction. (b) shows a single semicircle with a capacitive tail, representative of ion conduction. (c) shows two distinct semicircles, which is associated with mixed ion electron conduction in polymers. Equivalent circuits used to calculate resistances are shown in each respective panel. These circuits are common throughout polymer literature.[36,65]

When a mixed conducting polymer is co-doped (both salt and electronic dopants are present), the experimental execution and analysis become less straight forward. Electronic conductivity can be measured by either AC impedance or DC polarization, however the resultant current response will now vary due to contributions from both electronic and ionic charge carriers. Figures 1.6c and 1.7c show expected AC and DC responses for mixed conducting polymers between two ion blocking electrodes. In co-doped systems, ionic conductivity can be measured via AC impedance so long as ionic transport is fast relative to electronic. When this is the case, two distinct semicircles will appear in the Nyquist plot (Figure 1.6c). These features arise from electronic resistance and geometric capacitance in

parallel at low frequencies, and ionic resistance and geometric capacitance at higher frequencies. Here, interfacial capacitance is shunted by electronic current at low frequencies, meaning there is no capacitive tail, unlike the Nyquist plot for pure ion conducting polymers. If electronic transport is fast relative ionic transport, there will be no blocking of charge transport and therefore no interfacial capacitance.[65] This will result in a Nyquist plot with a single semicircle, resembling a pure electron conductor, even though the polymer may have ionic conductivity of an appreciable value. The latter case is the more common scenario, as state of the art ionic conducting polymers have room temperature conductivity on the order of $10^{-5}$-$10^{-4}$ S/cm, while electronic conduction can be well above 1 S/cm.

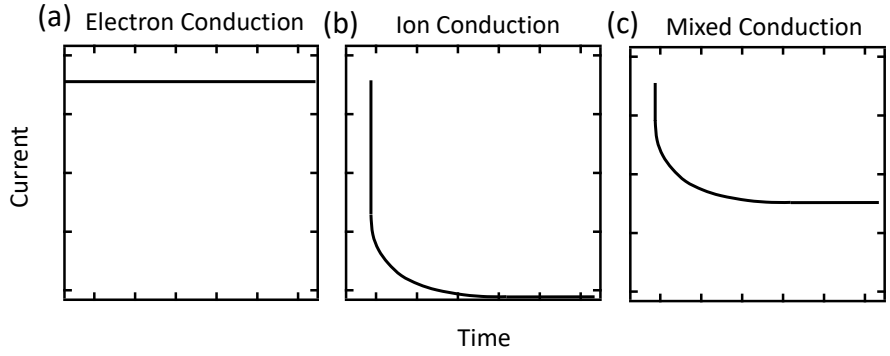


**Figure 1.7: Qualitative depictions of the current response over time when a constant DC potential is applied across a polymer between two ion blocking electrodes**

The polymer is either (a) electronically conducting, (b) ionically conducting, or (c) mixed conducting. In the case of electronically conducting polymers, there is no blocking of the predominate charge carrier, and thus a constant current is observed. For ion conducting polymers, the only charge carrier are ions, which are blocked at the electrodes. Thus initially current is observed due to interfacial capacitance, but this quickly declines. A similar result is observed in mixed conducting polymers, however, as capacitive current from ionic transport decays, a non-zero steady state current will be achieved due to electronic current. It is worth emphasizing that this figure is illustrative only, presented to show how DC responses can be altered when multiple charge carriers are present. In a practical sense, DC polarization with ion blocking electrodes is rarely (or never) used to quantitatively determine ionic conductivity, as the transient nature of the current response creates issue with how quickly the instrument can initially collect data. Ionic conduction is best determined via AC impedance. If DC measurements are attempted, and a response similar to (b) or (c) is observed, this is a good indication that AC Impedance should be performed.

Given the signal from electrical current typically dominates the response in AC impedance, co-doping is often not performed, and other techniques, such as Pulsed Field Gradient (PFG) NMR can be employed to determine ion mobility. However these measurements typically require elevated temperatures, and thus thermal dedoping becomes an issue for electronically doped systems. One group has recently reported an electrochemical technique for deconvoluting each transport property, however this has not been widely adopted due to the specialization required.[66] As it stands, accurately measuring ionic conductivity in a co-doped systems is an active area of research for the field. Here, transport of each charge carrier is typically studied independently.

Even when electronic dopants are absent, obtaining a complete view of ionic transport is a non-trivial task. While bulk ionic conductivity is straight forward to determine via EIS, more information is needed to make impactful insights with respect to polymer design for battery applications. Bulk ionic conductivity describes transport of all charged species- dissociated anions and cations as well as aggregated charged clusters (Figure 1.8).

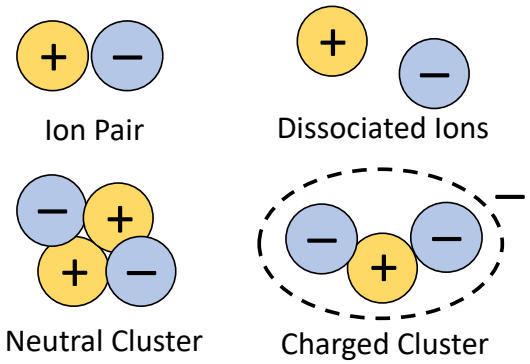


**Figure 1.8: A schematic of various scenarios salt can undergo when in a solvation medium**

In dilute, ideal electrolytes, full dissociation is assumed. However, realistically a complex equilibrium between all species typically exists.

Battery applications must optimize transport of the metal cation of interest ($Li^+$ for Li-ion batteries), as the anion is not involved in the electrochemical reaction. To determine Li conductivity, the overall conductivity is typically measured, and then combined with a lithium transference number ($t_{Li+}$), which can be conceptualized as the fraction of the total current carried by $Li^+$. Rigorously, the transference number refers to the fraction of total electrical current carried by a particular species when a potential difference is applied between adjacent electrodes,[65] and determining this requires the combination of three independent electrochemical techniques.[67] However, given the motivation is Li-ion battery binders, attention need not be given to lithium contained in an anionic charge cluster, as from the perspective of the battery, this is effectively an anion (Figure 1.8). Optimizing the current carried by freely diffusing $Li^+$ with respect to all other ionic charge carriers is the design goal (i.e. $Li^+$ conductivity). This parameter is easily measured with a technique developed by Bruce and Vincent,[68] where the polymer sample is place between two lithium metal electrodes, which conduct electrons and Li+, but are blocking to other charge carriers. Relating the initial current (which results from all charge species) to the steady state current (which ideally only stems from Li+), provides $t_{Li+}$.

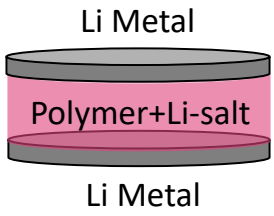


**Figure 1.9: The sample configuration for a lithium transference measurement**

This is very similar to that of an ionic conductivity measurement (Figure 1.5). However, here lithium metal electrodes are used, rather than ion blocking electrodes. Lithium metal is blocking to all ionic charge carriers other than $Li^+$, enabling the determination of the steady state lithium ion current.

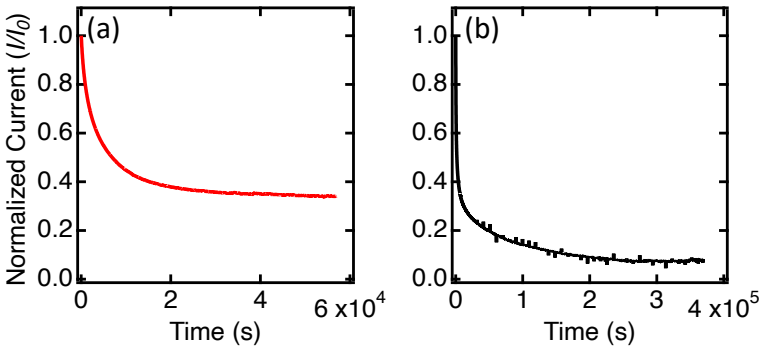


**Figure 1.10. Exemplary current profiles for DC polarization $t_{Li+}$ measurements**

Initially, all ions contribute to the current response ($Li^+$, anions, and charged clusters). Over time, capacitive layers will build for the blocked species (all ions other than $Li^+$), and the only current will be due to migration of lithium ions.

Given the lithium metal electrodes are blocking to all ionic species other than $Li^+$, the transference number can be qualitatively viewed as the as the steady state normalized current, which is around 0.38 and 0.1 in Figure 1.10a and b respectively. However, realistically surface layers and charge transfer kinetics result in interfacial resistances, and to account for these a modified equation relating the initial current to the steady state current is used.

$$t_{Li+} = \frac{I_{ss}(\Delta V - I_\Omega R_0)}{I_\Omega(\Delta V - I_{ss}R_{ss})}$$

Here, ΔV is the applied potential, $R_0$ and $R_{ss}$ are the initial and steady-state interfacial resistances, respectively, $I_{ss}$ is the steady- state current, and $I_\Omega$ is the initial current determined from Ohm's law:

$$I_\Omega = \frac{\Delta V}{R_\Omega}$$

where $R_\Omega$ is the initial cell resistance (bulk and interfacial) measured by EIS. As discussed previously, speed of data acquisition by the instrument is a limitation for DC ionic conductivity measurements, which is why the resistance as determined from AC impedance is typically used

to calculate the initial current. Failing to do this would lead to over estimation of the transference number due to an erroneously low initial current

Finally, solid state NMR techniques are a powerful tool to corroborate insights form the Bruce Vincent Method and EIS. Pulsed Field Gradient NMR (PFG NMR) directly probes the self-diffusion coefficient of the nucleus of interest.[69–71] Luckily for battery research, both $^{7}$Li (a common cation) and $^{19}$F (present in many anions) are NMR active. The self-diffusion coefficient itself is of interest, as it implies how mobile an ion is in a given medium. Additionally, this parameter enables the calculation of ionic conductivity and transference number, shown in the equations below.

$$\sigma = \frac{F^2}{RT}(c_+ D_+ + c_- D_-)$$

$$t_+ = \frac{\sigma_+}{\sigma_+ + \sigma_-}$$

Each calculation has the underlying assumption of full ion dissociation.[69] While these assumptions are typically not valid in polymer systems, the results still provide a valuable comparison to transference numbers and ionic conductivity determined via the Bruce Vincent Method and EIS, respectively. In instances were diffusion coefficients cannot be determined via PFG NMR (slowly diffusing ions, or $T_1/T_2$ limited systems), relaxometry can be a helpful alternative to gain ion specific insights with respect to dynamics. $T_1$, $T_2$, and $T_{1\rho}$ relaxometry will be discussed in detail later, but in short, these techniques can provide insight as to local ion interactions, activation energies, and mobilities for both mobile and immobile species, unlike PFG NMR which only probes diffusing species.

## 1.4 Semiconducting polymers in batteries

Lithium ion batteries are by far the most widely used system and will thus be the model for this work. As the name implies, the transport of lithium ions is central to battery operation. Cells are composed of an anode and cathode with a separator/electrolyte in between (Figure 1.11). Ions can flow through this medium, but electrons must flow through an external circuit, thus powering a device. The polymer binder provides a critical mechanical function- providing adhesion both between electrode particles and with the current collector. However, current industrially used binders are insulating to both ions and electrons, which can impede the core charge transport requirements of the cell.

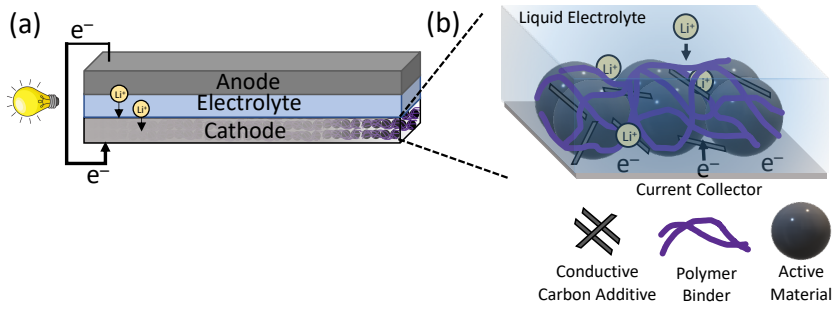


**Figure 1.11: Material composition and interactions in typical lithium-ion batteries.**

(a) Shows a schematic of overall functionality of the battery, where on discharge lithium ions migrate from the anode to the cathode via the electrolyte. Electrons flow through the external circuit to power the device. Zooming in on the cathode (b) shows how the composite consists of may materials working in tandem to enable overall functionality. The active material (black spheres) is responsible for redox activity. Conductive additive (black lines) is responsible for electron transport. Holding the system together is a binder (purple lines). Current technologies use resistive plastics, like PVDF. During the charge/discharge process, ion transport occurs between the electrolyte and active material, and electrons flow between the conductive additive and current collector. Resistive binders inhibit each functionality by creating barriers to the transport of these charge species.

Adding conductivity to the binder should improve on this limitation, however the binder must ideally still serve the "normal" functions- namely stability and processability. The most common way to fabricate electrodes is through a slurry process. Powders are homogenized, then mixed with a binder/solvent combination, in which the powders become

suspend to form a homogenous slurry. This slurry is then blade coated onto the current collector and dried to afford the final electrode. Central to this process is the polymers ability to be dissolved in an appropriate solvent in reasonably high solids loadings to form a viscous slurry- not a property for which conjugated polymers are traditionally touted. Additionally, the polymer must be electrochemically stable in the potential window of the given Li-ion chemistry, which can be up to 3.8-4.6 V vs $Li/Li^+$ depending on the active material. Finally, conventional Li-ion batteries use organic, carbonate based electrolytes, and it is critical the binder withstand dissolution. As will be discussed, this latter point is a particular challenge for ion conducting systems.

While there is still much to be learned about fundamental design strategies to optimize mixed conduction in semiconducting polymers, many studies have already applied these systems as battery binders. Polythiophene derivatives have been the most widely studied family in this regard, owing to their stability and favorable doping potential around 3.2-3.4V vs Li/Li+, meaning they will be conductive for the duration of the charge/discharge process of most Li-ion cathodes.[16,40,72] Polythiophenes also enable facile functionalization, affording highly tunable properties. Perhaps the most widely studied conducting binder is the thiophene based PEDOT:PSS (poly[3,4-ethylenedioxythiophene]:poly[styrenesulfonate]). This has been shown as a promising PDVF alternative, however is suffers from poor processability, as PEDOT:PSS is used as a low concentration colloidal suspension in water, resulting in non-homogeneous mixing with cathode materials. In fact, when applied in cathodes, PEDOT:PSS is often used in conjugation with another polymer binder, such as carboxymethyl cellulose,[73,74] styrene-butadiene rubber,[73] and polyacrylic acid.[75]

Beyond PEDOT:PSS, other thiophene derivatives have shown adding electronic conductivity to the binder improves rate capability in composite cathodes, when compared to analogous cells prepared with a PVDF binder.[16,40,72] Further, mixed ion-electron conducting block copolymers have shown some utility as binders for LFP cathodes, with success at low (dis)charge rates.[64,76,77] While these polymers improve overall performance, most are far better electronic conductors than ionic conductors. Other hybrid designs, such as incorporating ionically conductive sidechains on an electronically conductive backbone,[14,15,37–39] have also shown a similar tradeoff between ionic and electronic conduction.[40] Additionally, current mixed conducting polymers face practical hurdles when applied as binders, as increasing the density of ionically conductive side chains drives dissolution in the polar battery electrolyte.[40]

***Knowledge gap in mixed conducting polymers as Li-ion battery binders***

Developing the next generation of battery binders must focus on both fundamental polymer transport, as well as practical considerations such processability, stability, and compatibility with other battery components. Simultaneously optimizing both electronic and ionic transport is still a design challenge facing the field, and for battery applications the need to optimize for $Li^+$ specific transport further complicates the matter. Initial strategies have often been faced with practical limitations when the polymers are applied as binders- poor processing, dissolution in electrolytes when ionic conductivity is added to the polymer, the need for support polymers for binding functionality, and/or low lithium mobility. The goal of this work is to explore new design strategies, first elucidating fundamental structure property relationships for simultaneous electron-$Li^+$ transport in polymers, then considering practical application as cathode binders.

## Permissions

Parts of this dissertation were reproduced in part with permissions from:

(1) GT Pace, O Nordness, K Asham, R Clément, RA Segalman, "Impact of Side Chain Chemistry on Lithium Transport in Mixed Ion-Electron Conducting Polymers". *Chem. Mater.* (2022) DOI: https://doi.org/10.1021/acs.chemmater.2c00592

(2) GT Pace, ML Le, R.J. Clément, R.A. Segalman, "A Coacervate-based Mixed Conducting Binder for High Power, High Energy Batteries" *ACS Energy Lett.* (2023) DOI: https://doi.org/10.1021/acsenergylett.3c00829

(3) GT Pace, O Nordness, YJ Choi, P Nguyen, C Tran, R.J. Clément, R.A. Segalman, "Tuning Transport via Interaction Strength in Cationic Conjugated Polyelectrolytes" *Macromolecules.* (2023) DOI: https://doi.org/10.1021/acs.macromol.3c01206

# Chapter 2

# Impact of side chain chemistry on lithium transport in mixed ion-electron conducting polymers

## 2.1 Abstract

Typical design strategies for mixed ion-electron conduction in polymers have focused on overall ionic conductivity, without specificity for anion vs. cation conduction. Here, we demonstrate that side chain chemistry can be used to control $Li^+$ conductivity in semiconducting polymers. This design principle is significant for applications which require $Li^+$ specific transport, such as Li-ion batteries. We show that a polythiophene functionalized with an ionic liquid side chain demonstrates higher conductivity and lithium transference than a more commonly studied ether-functionalized P3AT derivative. Poly(3-(6'-(N-methylimidazolium) hexyl)thiophene $TFSI^-$) (P3HT-$Im^+TFSI^-$) can solvate and conduct ions up to salt concentrations of r=1.0 (where r = [moles of salt]/[moles of monomer]) while achieving ionic conductivity of $\approx 10^{-3}$ S/cm at 80°C, and a lithium transference number of 0.36. On the other hand, poly(3-(methoxyethoxyethoxymethyl) thiophene) (P3MEEMT) shows a peak conductivity of $\approx 10^{-5}$ S/cm at r=0.05 and 80°C, with near zero lithium transport. This work shows that multiple high dielectric moieties can be used to drive ion conduction in semiconducting polymers, but diffuse, cationic side chains such as imidazolium are preferred for Li-ion conduction.

## 2.2 Introduction

Simultaneous ion and electron conduction is essential for electrochemical applications spanning fuel cells, batteries, supercapacitors, transistors, and bioelectronics.[37,78–82] Conjugated polymers have emerged as an attractive materials class for these applications due to their flexibility, solution processability, and the availability of facile synthetic design strategies.[36,77,83–86] While traditional conjugated polymer research has focused on semiconductor doping to optimize electronic transport,[37,80,87,88] more recent studies have focused on derivates functionalized with ion conducting moieties for electrochemical applications,[15,39,45,89] thus giving rise to the field of organic mixed ion electron conductors (MIECs).

Rational design of mixed conducting organic materials is challenging because ion and electron conduction follow different design rules spanning different length scales.[37] Broadly speaking, the transport of electronic charge carriers relies on long-range delocalization of electrons along π-conjugated backbones, which occurs in ordered domains of the polymer.[2,3,90] Ion transport, on the other hand, is typically coupled to polymer chain dynamics, and relies on free volume and segmental motion which are higher in amorphous domains of the polymer.[4,5,7,60] While optimizing both phenomena in a single system is seemingly at odds, the combination of these properties is required for many electrochemical applications.

The most widely deployed design strategy for adding ionic conductivity to semiconducting polymers has been to utilize conjugated backbones to conduct electronic charge carriers,

coupled with poly(ethylene oxide) (PEO)-inspired oligoether side chains to solvate ions.[17,39,89,91–93] Ion transport in PEO occurs *via* solvation sites that resemble crown ethers, where ions hop from site to site within the polymer matrix.[59,94,95] This crown-ether-like solvation enhances salt solubility by creating stable cation complexes, but these complexes in turn severely limit cation mobility.[4,59] This limitation is particularly apparent when this structural motif is adopted in the form of ether side chains attached to a non-polar backbone. Here, cation transport suffers compared to PEO due to a lack of interconnectivity of the solvation sites.[96] Limited cation mobility is not necessarily problematic for many mixed conduction studies that already adopt the ether functionalized conjugated backbone design strategy, as they serve as ideal model systems for fundamental research focused on p-type semiconductor doping, which relies on anion transport.[89,91,93] More recently, however, mixed conducting polymers have garnered attention as materials for electrochemical applications requiring cation transport. Present mixed conducting polymer design principles cannot sufficiently predict the relative motion of the anion vs. cation based on chemical structure. Thus, it is paramount to develop structure-property relationships for controlling the selectivity of ion transport in MIECs, enabling rational design of systems tailormade for a variety of electrochemical applications.

Of specific interest in recent literature is using MIECs as protective coatings and binders for Li-ion battery electrodes.[16,40,72] PVDF, the most widely used polymer binder, suffers from low electronic and Li-ion conductivities. This increases electrode impedance by interfering with charge transport during battery operation.[97–99] It stands to reason that utilizing a polymeric MIEC would lower this impedance and improve battery performance. While there are many

studies describing the design of mixed ion-electron polymer-based conductors,[37,87,91,100] most focus on "bulk-ionic conductivity", i.e. total anion and cation transport. For Li-ion battery applications, however, emphasis must be placed on optimizing Li-ion transport, as the counterion does not participate in the electrode reactions. While a handful of studies have reported the use of semiconducting polymer binders to improve Li-ion battery performance over standard electrode film formulations based on a PVDF binder,[40,72] none specifically elucidated the extent to which the polymer binder itself facilitates lithium transference.

Here, we use the well-studied P3AT polymer family to demonstrate the impact of side chain chemistry on Li-ion transport. The most widely studied P3AT derivative, poly(3-hexylthiophene) (P3HT) is known for its relatively narrow band gap, good processability, and high hole mobility.[100,101] A drawback of P3HT is that its hexyl side chain lacks ion conducting functionality. Thus, thiophene backbones with the 3-position functionalized with high polarity side chains have been chosen for this study. The polymer electrolyte literature has established that tethering an imidazolium ($Im^+$) to a polymer backbone enables cation conduction.[4,28,102,103] Additionally, we have previously demonstrated the mixed conducting ability of the conjugated polymer ionic liquid P3HT-$Im^+BF_4^-$.[15] Building upon these findings, we focus here on the P3HT-$Im^+TFSI^-$ system containing a bulky, polarizable cationic side chain and charge compensating anion that serve to weaken ion binding, thus increasing ion dynamics in the absence of a liquid phase solvent.[26,104] We compare the performance of the P3HT-$Im^+TFSI^-$ system to a non-ionic thiophene derivative with ether side chains (poly(3-(methoxyethoxyethoxymethyl) thiophene) or P3MEEMT) that was previously demonstrated to exhibit appreciable ionic conductivity upon addition of LiTFSI in the work of Dong *et al.*[39]

The latter system was selected due to its high ionic conductivity compared to other ether functionalized thiophenes, such as poly(3-(methoxyethoxyethoxy)thiophene) (P3MEET),[39] which allows us to monitor ion conduction and transference via pulsed field gradient (PFG) NMR. The structures for each polymer are shown in Figure 2.1(a). For consistency, LiTFSI was selected as the salt of interest for both systems.

## 2.3 Experimental Methods

### *2.3.1 Synthetic Methods*

Poly[3-(6'-bromohexyl)thiophene] (P3BrHT) was synthesized according to previous literature.[26] An oven-dried Schlenk flask containing 2,5 dibromo-3-(6-bromohexyl)thiophene was placed under vacuum for 2 hours. Dry, degassed THF was added via syringe and the mixture was sparged with Nitrogen. Isopropylmagnesium chloride was added dropwise and the mixture was stirred for 1 hr at ambient temperature under Nitrogen. The desired amount of $Ni(dppp)Cl_2$ was added via syringe. The polymerization was stirred for 1 h at 60°C and quenched by rapid addition of 1M HCl, and precipitated into methanol. The polymer was purified by washing in a Soxhlet apparatus with methanol and acetone before extraction with THF. The product was concentrated under vacuum.

The P3BrHT polymer was post-functionalized through an amine quaternization reaction. The polymer was first dissolved in THF. 1 methylimidazole (10 eq.) was added to the solution in ambient conditions. The solution was then stirred for 24 h under reflux. After 12 h, some polymer precipitate was observed in the flask. A small amount of methanol was added to fully dissolve the resulting polymer and the solution was stirred for an additional 24 hours to help achieve quantitative conversion. The polymers were then dialyzed using 10 kDa cutoff dialysis

membranes against a mixture of methanol and THF, with the dialysate replaced every 12 h. The resulting polymer was then mixed with 10 molar equivalents of LiTFSI and stirred at 50°C in methanol and acetonitrile followed by dialysis for 48h in a 50:50 mixture of methanol and acetonitrile. Complete anion exchange was confirmed via XPS.

2,5-dibromo-3-methoxyethoxyethoxymethylthiophene synthesis was adapted from previous literature.[39] 2,5-dibromo-3(bromomethyl)thiophene was purchased form Polymer Source. To a round bottom flask anhydrous THF (100 mL) and diethylene glycol monomethyl ether (1.5 eq), and NaH (2 eq) were added. The NaH was allowed to react for 1 hour, ensuring $H_2$ gas evolution had ceased. 2,5-dibromo-3(bromomethyl)thiophene (1 eq.) was dissolved in THF, then added to the reaction. It was then added dropwise over 15 min, after which the reaction was allowed to stir overnight. The reaction was quenched by pouring in to 10% $Na_2SO_4$ in water, then extracted with diethyl ether. The organic phase was successively washed with water, dried over MgSO4, and solvent removed using rotary evaporation. The crude product was purified using a silica gel column with 3:2 hexanes:ethyl acetate.

Poly(3-methoxyethoxyethoxymethylthiophene) was polymerized through a GRIM polymerization. An oven-dried Schlenk flask containing 2,5 dibromo-3-methoxyethoxyethoxymethylthiophene (1 eq) was placed under vacuum for 2 hours. Dry, degassed THF was added via syringe and the mixture was sparged with Nitrogen. Isopropylmagnesium chloride (1.1 eq) was added dropwise and the mixture was stirred for 5 hr at ambient temperature under Nitrogen. The desired amount of Ni(dppp)$Cl_2$ (0.01 eq) was added via syringe. The polymerization was stirred for 1 h at 60°C and quenched by rapid

addition of 1M HCl, and precipitated into hexanes. The polymer was purified in a Soxhlet apparatus with hexanes, then washed with methanol and water and dialyzed in 10 kDa tubing in acetonitrile.

### *2.3.2 Electrochemical Impedance Spectroscopy (EIS)*

Polymer samples were solution doped by dissolving the appropriate amount of polymer in acetonitrile and mixed with the appropriate amount of LiTFSI/acetonitrile solution to achieve the desired doping level. The polymer/salt solution was then drop cast onto clean circular indium tin oxide (ITO) substrates top-coated with a 150 μm Kapton spacer in which a well of known diameter was punched. Compared to thin films often used to probe conductivity in semiconducting polymers, this thick format geometry for ionic conductivity minimizes any substrate induced texturing effects, enabling a better comparison to PFG NMR, which requires large cylindrical samples. The samples were sealed with clean ITO substrates and dried under high vacuum ($2 \times 10^{-8}$ torr) at 90°C for 12 hours. Characterization was done with a Biologic SP-200 potentiostat inside a nitrogen filled glovebox. Transparent ITO/ glass electrodes were used to ensure the absence of bubbles and proper interfacial contact. A sinusoidal voltage with amplitude 100 mV was applied in the frequency range of 0.1 Hz−3 MHz. To distinguish the ionic and electronic contributions to the signal, equivalent circuits were fit to the Nyquist plots, which account for the ionic resistance, the electronic resistance, and the contact resistance, as appropriate. Exemplary Nyquist plots and equivalent circuits are shown in Figure 2.19.

Electronic doping was achieved via vapor phase infiltration, which relies on thin films being exposed to dopant vapor. Thus, for the electronic conductivity measurements, interdigitated

gold electrodes sourced from Metrohm Dropsense were used, as opposed to the ITO symmetric cells used to measure “thick film” ionic conductivity. Films were drop cast to achieve thickness c.a. 200 nm.

Vapor doping with HTFSI and $NOBF_4$ was performed in a sealed vessel on a hot plate inside a nitrogen filled glove box. Pristine films were attached to the lid of a jar containing crystals of the desired dopant using double sided Kapton tape. The jar was closed and placed on the hot plate to be heated at the desired temperature and time. HTFSI doping was performed at 50°C for 30 min and $NOBF_4$ doping was performed at 70°C for 10 and 30 min. Further details of electrode geometry and equivalent circuit fitting can be found in Figure 2.19.

### *2.3.3 DC Polarization*

DC polarization was performed on symmetric lithium−polymer−lithium cells. Samples were assembled in an argon glovebox utilizing a Controlled Environment Sample Holder (CESH) from Biologic LLC and tested using their Intermediate Temperature System (ITS) in conjunction with their VSP-300 potentiostat to 81°C for consistency with the PFG NMR measurements. Samples were equilibrated until the interfacial resistance, monitored via EIS, stabilized. This indicated the complete formation of a solid−electrolyte interphase (SEI) layer. Next, a 100 mV potential bias was applied and the resulting current measured over time. EIS measurements with a 20 mV amplitude were performed at 20 minute intervals to monitor changes in the interfacial resistance. Lithium transference numbers were calculated following the method of Bruce and Vincent:[28,68]

$$t_{Li+} = \frac{I_{ss}(\Delta V - I_{\Omega}R_0)}{I_{\Omega}(\Delta V - I_{ss}R_{\mathrm{ss}})}$$

Here, ΔV is the applied potential (100 mV), $R_0$ and $R_{ss}$ are the initial and steady-state interfacial resistances, respectively, $I_{ss}$ is the steady- state current, and $I_\Omega$ is the initial current determined from Ohm's law:

$$I_{\Omega} = \frac{\Delta V}{R_{\Omega}}$$

where $R_\Omega$ is the initial cell resistance (bulk and interfacial) measured by EIS. Using $I_\Omega$ instead of the initial current measured by the potentiostat eliminates errors related to the speed at which the instrument can record the current. Current decay curves are shown in Figure 2.27.

### *2.3.4 NMR Techniques*

PFG NMR samples were prepared in the same manner as described for the AC Impendence samples. Here, drop casting was performed into a quartz trough that facilitated approximately 100 mg of material to be loaded into the center of the NMR tube. All sample preparation was done in a nitrogen glovebox, and the NMR tubes were sealed before removal from the glovebox to maintain an oxygen and water free environment during measurement.

Measurements were performed on a Bruker Avance III super-wide-bore spectrometer with a Bruker DIFF50 diffusion probe with replaceable radio-frequency (RF) inserts for $^{7}$Li and $^{19}$F. Due to signal noise and slow diffusion times at room temperature, measurements were performed at 72 and 81°C on both $^{19}$F and $^{7}$Li nuclei. A stimulated echo pulse sequence was used, and the attenuation of the intensity (*I*) was fit to the following equation.[105]

$$I(G) = I(0)\exp\left[-G^2 D\,\gamma^2\delta^2\left(\Delta - \frac{\delta}{3}\right)\right]$$

Where $G$ is gradient field strength, $I(0)$ is the intensity of the magnetization when $G$=0, $\gamma$ is the gyromagnetic ratio, $\delta$ is the gradient pulse length, $\Delta$ is the interval between gradient pulses, and D is the diffusion coefficient.

$T_1$ and $T_2$ relaxation experiments were performed on the same samples, at the same time as PFG NMR. Here $T_1$ is used to refer to the longitudinal relaxation time, while $T_2$ is used to refer to the transverse relaxation time. The $T_1$ experiment utilized a saturation recovery pulse program,[106] while the $T_2$ utilized the Carr-Purcell-Meiboom-Gill (CPMG) sequence.[107,108] Exemplary $T_1$ data is shown in Figure 2.29. $T_2$ fitting data is shown in Figure 2.30. Figure 2.31 shows the resulting $T_2$ values along with the phase distribution vs temperature.

$$I(t) = I(0)[1 - \exp\left(\frac{-t}{T1}\right)]$$

$$I(t) = I(0)\exp\left(\frac{-t}{T2}\right)$$

### *2.3.5 Grazing Incidence Wide Angle X-ray Scattering (GIWAXS)*

Grazing Incident Wide Angle X-ray Scattering (GIWAXS) was performed on beamline 11-BM at the Brookhaven National Laboratory (NSLS-II). Calibration to determine the beam center and sample to detector distance was done using silver behenate. An incidence angle of 0.1° with a 10 second exposure time was used. Experiments were performed on drop-cast films on quartz substrates, as this results in relatively thick samples (≈50 μm), and thus no substrate induced texturing was observed. This was chosen, as opposed to thin films, to be consistent with diffusion NMR experiments, which require large pucks of material (c.a. 100 mg). The drop cast samples were prepared in the same manner describe for EIS.

### *2.3.6 UV-Vis Adsorption Spectroscopy*

UV-Vis adsorption was performed on an Agilent Cary 60 UV–vis Spectrophotometer. Spectra were taken on 0.5 mm-thick quartz substrates.

## 2.4 Results and Discussion

The goal of this work is to understand the role of side chain chemistry in controlling Li-ion transport in mixed ion/electron conducting polymers. Herein, we use two thiophene derivatives functionalized with either ionic liquid-inspired or ether-based side chains (poly(3-(6'-(N-methylimidazolium) hexyl)thiophene $TFSI^-$) or P3HT-$Im^+TFSI^-$, and poly(3-(methoxyethoxyethoxymethyl) thiophene) or P3MEEMT, respectively) in the entirely dry (water-, solvent-, and electrolyte-free) state. Following the addition of electronic dopants and LiTFSI, both systems demonstrate appreciable electronic and ionic conduction, thus establishing each polymer's ability to perform as a mixed conductor. The primary goal of this work is to move beyond these two traditionally studied phenomena in order to understand how chemical design can be used to control the relative motion of the lithium ion with respect to its counterion. In this vein, we next report a thorough analysis of ionic conductivity and ion specific transport properties, demonstrating the superior performance of P3HT-$Im^+TFSI^-$ as a lithium ion conductor over P3MEEMT. P3MEEMT strongly interacts with Li-ions, impeding cation transport relative to anion transport. Further, P3HT-$Im^+TFSI^-$ has a superior ability to solvate salt leading to a monotonic increase in conductivity up to salt loadings of r=1.0, whereas P3MEEMT's conductivity declines appreciably beyond a molar salt ratio of r=0.05. These results suggest the need for application-specific chemical design criteria for mixed

conducting polymers, where anion-selective conduction may be favored for facile p-type semiconductor doping, while Li-ion conduction and high salt solvation capability are necessary for battery applications.

### *2.4.1 System Design*

As discussed above, P3MEEMT and P3HT-$Im^+TFSI^-$ were selected for this study, with the former mimicking the well-known polyelectrolyte, PEO, and the latter bearing an ionic liquid-like sidechain.[15,39] Both polymers are fairly disordered and exhibit two characteristic scattering peaks when examined by GIWAXS (Figure 2.1b), in agreement with previous literature.[39,109] Additionally, the raw scattering patterns (Figure 2.18) show the diffraction rings are fairly isotropic. Due to the lack of texture in these thick, drop cast samples, the 2D GIWAXS patterns are readily integrated without information loss to 1D profiles. In both systems, peaks observed at ≈0.3-0.4 $Å^{-1}$ and ≈1.5-1.6 $Å^{-1}$ have been previously attributed to side chain spacing and π-stacking, respectively.[15,39,109] The peak that appears just below 1 $Å^{-1}$ in P3HT-$Im^+TFSI^-$ has been previously reported in an analogous system with both a picrate and $[B(Ph)_4]^-$ anion.[109] Due the broad features observed here, no attempt was made to deconvolute the exact location of the π-stack peak from the amorphous signal.

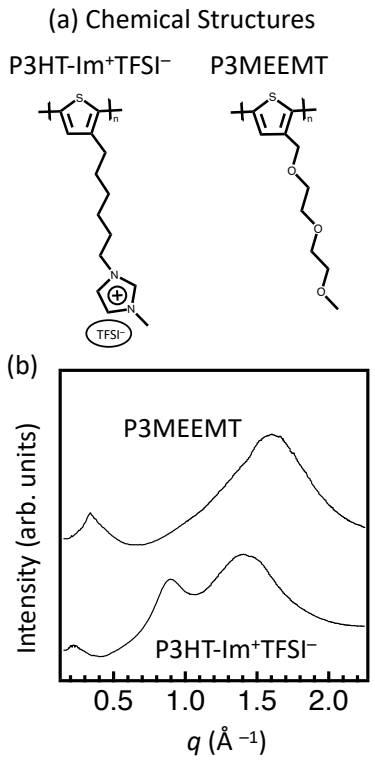


**Figure 2.1: Chemical structures and GIWAXS profiles**

(a) Chemical structures for Poly(3-(6'-(N-methylimidazolium) hexyl) thiophene) (P3HT-$Im^+TFSI^-$) and Poly(3-(methoxyethoxyethoxymethyl) thiophene) (P3MEEMT). (b) GIWAXS profiles obtained via full, radial integration for P3HT-$Im^+TFSI^-$ and P3MEEMT.

### *2.4.2 P3HT-$Im^+TFSI^-$ and P3MEEMT as mixed ion/electron conductors*

Both P3HT-$Im^+TFSI^-$ and P3MEEMT can function as ionic conductors, electronic conductors, or mixed ion/electron conductors, depending on the dopant used. The UV-Vis spectra presented in Figure 2.2 probe characteristic electronic transitions upon addition of salt (LiTFSI) or electronic dopants ($NOBF_4$, HTFSI) to the two polymer systems of interest. While LiTFSI only serves to add ionic charge carriers, doing little to change the electronic structure of the systems, HTFSI and $NOBF_4$ react with the polymer backbone, making it electron deficient (p-type doping), but do so *via* different mechanisms. $NOBF_4$ directly oxidizes the polymer, where $NO^+$ undergoes electron exchange, leaving the system as NO gas with $BF_4^-$

remaining as the counterion to the oxidized backbone. HTFSI is a strong acid which protonates the backbone. When the backbone is protonated, it is believed that the resulting carbocation oxidizes a neighboring chain, thus forming the typical radical-hole pair.[21,22]

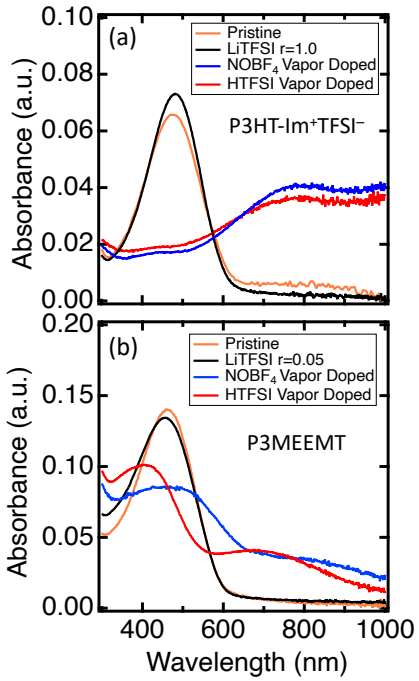


**Figure 2.2: UV-Vis absorption spectra**

The spectra show the optical transitions upon doping (a) P3HT-Im$^+$TFSI$^-$ and (b) P3MEEMT with HTFSI, $NOBF_4$, and LiTFSI.

Upon doping with $NOBF_4$ and HTFSI, P3HT-Im$^+$TFSI$^-$ demonstrates a decrease of the neutral polymer signal centered around 475 nm and a broad polaronic peak beginning around 750 nm appears, indicating the presence of electronic charge carriers.[15,80,88] P3MEEMT shows a less pronounced optical transition upon electronic doping with both HTFSI and $NOBF_4$, indicating that P3HT-Im$^+$TFSI$^-$ is more readily doped under the given conditions, in line with its higher electronic conductivity discussed below.

Figure 2.3 shows representative Nyquist plots obtained from AC Impedance experiments, where distinct features (associated with the equivalent circuits shown in the right column) are indicative of ionic conduction, electronic conduction, and mixed ion/electron conduction.[36,65,77] Further discussion of these measurements can be found in Appendix 2.6. P3HT-$Im^+TFSI^-$ is readily doped with both HTFSI and $NOBF_4$ and achieves an electronic conductivity of 1.65 mS $cm^{-1}$ (Figure 2.3b). Interestingly, when P3MEEMT is doped with HTFSI, there is sufficient delocalization to observe an optical transition, but the electronic conductivity is below the detection limit of our AC impedance method. In fact, the Nyquist plot is indicative of predominately ionic charge carriers (Figure 2.20). Only when doped with $NOBF_4$ is there sufficient carrier mobility to impart measurable electronic conductivity on the order of 0.161 mS $cm^{-1}$(Figure 2.3e). While the exact mechanism for this behavior is not apparent, GIWAXS studies of the doped polymers (Figure 2.17) indicate it is likely related to differing degrees of dopant induced ordering. In semiconducting polymers, carrier mobility is dependent on several structural factors, but in general delocalization along ordered conjugated backbones is necessary.[90,110–112] As shown in Figure 2.1(b), undoped P3HT-$Im^+TFSI^-$ and P3MEEMT are both fairly disordered polymers. Consequently, their ability to conduct electrons is associated with chain rearrangement upon doping, which has been reported in polythiophenes.[16,18] Here, $NOBF_4$ facilitates this rearrangement, as evidenced by the narrow peak centered around 1.6 $Å^{-1}$ in Figure 2.17, as compared to the broad feature that results from HTFSI doping.

Finally, a range of LiTFSI loadings were studied to determine the doping concentration that maximizes ionic conductivity. We find that P3HT-$Im^+TFSI^-$ and P3MEEMT achieve their

maximum ionic conductivities at LiTFSI loadings of r=1.0 and r=0.05, respectively (Figure 2.4), with representative Nyquist plots for these salt loadings are shown in panels (a) and (d) of Figure 2.3 (80°C), as well as the room temperature data in Figures 2.22 and 2.23. Both systems demonstrate the typical response of ion conducting polymers at all LiTFSI concentrations and temperatures studied in this work.

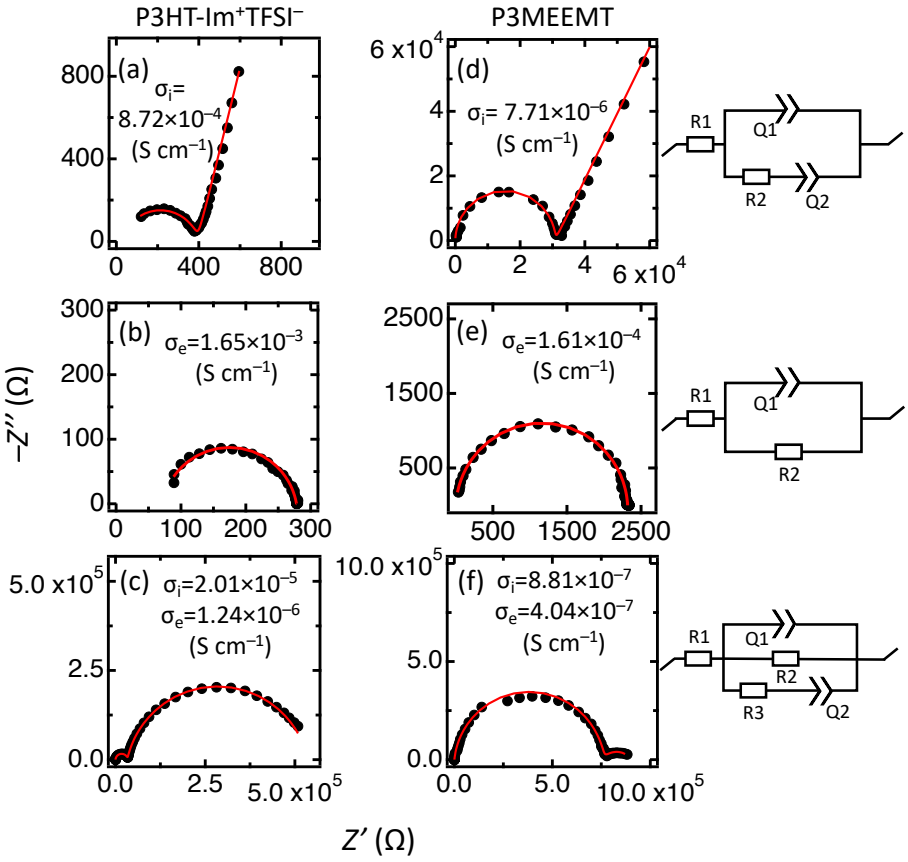


**Figure 2.3: Representative Nyquist plots, conductivity values, and equivalent circuits**

(a) P3HT-Im$^+$TFSI$^-$ with r=1.0 LiTFSI, (b) P3HT-Im$^+$TFSI$^-$ vapor doped with HTFSI, (c) P3HT-Im$^+$TFSI$^-$ co-doped with r=0.8 for both HTFSI and LiTFSI, (d) P3MEEMT with r=0.05 LiTFSI, (e) P3MEEMT vapor doped with $NOBF_4$ for 30 minutes, (f) P3MEEMT vapor doped with $NOBF_4$ for 10 minutes. The right column shows the equivalent circuit associated with each row, indicating that different dopants lead to either pure ionic, pure electronic, or mixed conduction in P3HT-Im$^+$TFSI$^-$ and P3MEEMT. Black circles are data, while the red lines are the fits using the respective equivalent circuits. For all systems, r is defined as [moles of salt]/[moles of monomer], $\sigma_i$ refers to ionic conductivity and $\sigma_e$ refers to electronic conductivity. Panels (a) and (d) were collected at 80°C for consistency with NMR experiments.

Room temperature data can be found in Figure 2.22. Electronic conductivity data is presented at room temperature to avoid potential thermal de-doping.

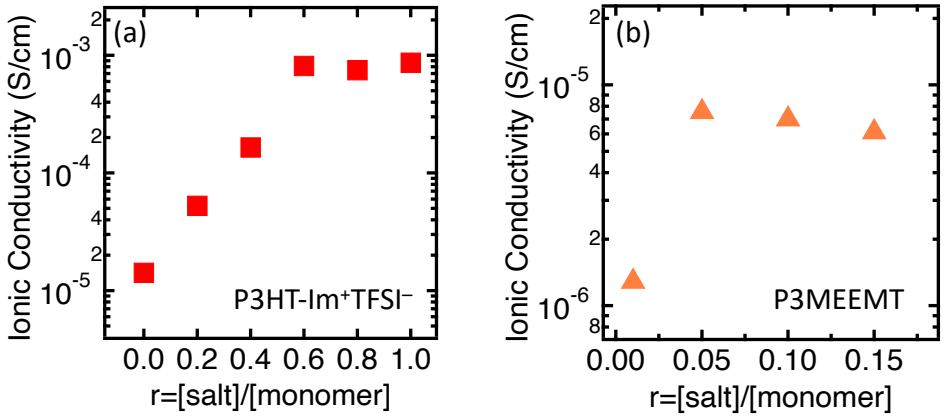


**Figure 2.4: Ionic conductivity as a function of LiTFSI salt concentration**

(a) P3HT-Im$^+$TFSI$^-$ and (b) P3MEEMT. The results indicate the ability of P3HT-Im$^+$TFSI$^-$ to solvate higher quantities of salt and achieve two orders of magnitude higher conductivity than P3MEEMT. r is defined as [mole LiTFSI]/[mole monomer]. The data was collected at 80°C to be able to compare with diffusion NMR measurements carried out at similar elevated temperatures.

When doped with LiTFSI salt, P3HT-Im$^+$TFSI$^-$ achieves an ionic conductivity two orders of magnitude higher than that of P3MEEMT at 80°C (Figure 2.4). Given the diffuse, cationic nature of the ionic liquid sidechain, P3HT-Im$^+$TFSI$^-$ does not experience as strong of interactions with $Li^+$, and thus can be loaded with salt up to a 1:1 molar ratio, which equates to 35% by mass of salt, with a monotonic increase in conductivity up to r=0.6, at which point the conductivity plateaus at a value $\approx 10^{-3}$ S cm$^{-1}$. On the other hand, P3MEEMT has a peak ionic conductivity at r=0.05, consistent with previously-reported values.[39] The behavior of P3MEEMT is similar to that of typical ion conducting polymers, which show a maximum conductivity between r=0.1 and r=0.2.[39,102] In these systems, the salt either precipitates or acts as a transient crosslinker at higher concentrations, resulting in an observed decrease in conductivity.[39] While previous literature only reports P3MEEMT's conductivity up to an

LiTFSI concentration of r=0.15, we also tested r=1.0 (Figure 2.21) for consistency with the P3HT-$Im^+TFSI^-$ system. As expected, at these much higher salt loadings (r=1.0 and 80°C), there was a marked decrease in ionic conductivity to $3.75\times10^{-8}$ S $cm^{-1}$.

### *2.4.3 Lithium Transference*

While the decrease in conductivity at relatively low salt loadings is an indicator of limited $Li^+$ mobility in P3MEEMT, EIS measurements alone cannot quantify the individual contributions of the $Li^+$ or $TFSI^-$ ions to the total conductivity of the system. Thus, we employed pulsed-field-gradient (PFG) NMR and DC polarization measurements to determine the relative fraction of current carried by $Li^+$ ($t_{Li+}$), with results shown in Table 2.1 at the respective peak conductivity salt concentrations (r=0.05 and r=1.0 for P3MEEMT and P3HT-$Im^+TFSI^-$, respectively).

$Li^+$ is effectively immobile in P3MEEMT ($t_{Li+}\approx0$ and no measurable signal in the $^7$Li PFG NMR experiments) but P3HT-$Im^+TFSI^-$ achieves a $t_{Li+}$ between 0.32 and 0.36 (Table 2.1). The NMR conductivity ($\sigma_{NMR}$) and $Li^+$ transference number ($t_{Li+}$) were computed from PFG-NMR self-diffusion coefficients obtained for $^{19}$F nuclei in P3MEEMT and for $^7$Li and $^{19}$F in P3HT-$Im^+TFSI^-$ using the following equations:

$$\sigma_{NMR} = \frac{F^2}{RT}(c_{Li+}D_{Li+} + c_{TFSI-}D_{TFSI-}),$$

$$t_{Li+} = \frac{\sigma_{Li+}}{\sigma_{Li+} + \sigma_{TFSI-}},$$

where $\sigma_{Li+}$ and $\sigma_{TFSI-}$ are the conductivities of $Li^+$ and $TFSI^-$, $F$ is Faraday's constant, $R$ is the ideal gas constant, $T$ is temperature, $c_{Li+/TFSI-}$ is the concentration, and $D_{Li+/TFSI-}$ the self-diffusion coefficient of the respective ion in the system.

To provide confidence in the accuracy of the diffusion NMR experiments, $t_{Li+}$ was also measured *via* the DC polarization technique developed by Bruce and Vincent.[68] The very low $t_{Li+}$ value of 0.04 for P3MEEMT measured *via* DC polarization lies below the detection limit of PFG NMR and confirms the relative immobility of $Li^+$ in P3MEEMT (Table 2.1). Since PFG NMR measurements characterize the average self-diffusion of all mobile ions in the system, this technique includes contributions both from fully solvated (charged) ions as well as ion pairs and larger aggregates. While there is considerable debate about the presence of ionic aggregates and pairs in polyelectrolytes and related materials, the primary focus here is on transport of the lithium ion itself ($Li^+$). The steady state current of the Bruce-Vincent method is inherently derived from singly charge lithium ions and is thus a measure of the fraction of the ionic current carried by $Li^+$ with respect to all other ionic charge carriers. The agreement between the transference number derived from this technique and PFG NMR indicates the majority of the mobile lithium ions reside as singly charge ions, at least within the diffusional time scales being probed. Additionally, the good agreement between the EIS conductivity values and those calculated from the NMR self-diffusion coefficients (Table 2.1) indicates that the conductivity is well explained by the NMR data, lending further credence to the reported transference values and indicating relatively few ion pairs are formed.

**Table 2.1** $Li^+$ and $TFSI^-$ self-diffusion coefficients ($D_{Li+}$ and $D_{TFSI-}$), calculated conductivity for each respective ion ($\sigma_{Li+}$ and $\sigma_{TFSI-}$), total conductivity calculated from PFG NMR ($\sigma_{NMR}$), conductivity measured *via* EIS ($\sigma_{EIS}$), $Li^+$ transference number calculated *via* PFG NMR ($t_{NMR}$) and via the Bruce Vincent method ($t_{BV}$). Data is shown for both P3HT-$Im^+TFSI^-$ and P3MEEMT with LiTFSI added at r=1.0 and 0.05 respectively.

| | Self-Diffusion Coefficient ($m^2\ s^{-1}$) | | Ionic Conductivity ($S\ cm^{-1}$) | | | | | |
|---|---|---|---|---|---|---|---|---|
| **T(°C)** | $D_{TFSI-}$ | $D_{Li+}$ | $\sigma_{TFSI-}$ | $\sigma_{Li+}$ | $\sigma_{NMR}$ | $\sigma_{EIS}$ | $t_{NMR}$ | $t_{BV}$ |
| P3MEEMT | | | | | | | | |
| 81 | $3.96 \times 10^{-13}$ | – | $6.19 \times 10^{-6}$ | – | $6.19 \times 10^{-6}$ | $7.75 \times 10^{-6}$ | 0 | 0.04 |
| 72 | $2.22 \times 10^{-13}$ | – | $3.56 \times 10^{-6}$ | – | $3.56 \times 10^{-6}$ | $3.64 \times 10^{-6}$ | 0 | 0.04 |
| P3HT-$Im^+TFSI^-$ | | | | | | | | |
| 81 | $4.72 \times 10^{-13}$ | $4.31 \times 10^{-13}$ | $2.47 \times 10^{-4}$ | $1.35 \times 10^{-4}$ | $3.82 \times 10^{-4}$ | $8.25 \times 10^{-4}$ | 0.36 | 0.32 |
| 72 | $2.54 \times 10^{-13}$ | $2.28 \times 10^{-13}$ | $1.34 \times 10^{-4}$ | $7.48 \times 10^{-5}$ | $2.09 \times 10^{-4}$ | $4.24 \times 10^{-4}$ | 0.36 | 0.32 |

### *2.4.4 NMR relaxometry*

NMR relaxometry indicates that the low $Li^+$ mobility in P3MEEMT is due to strong interactions between $Li^+$ and its local environment, whereas $Li^+$ diffuses more readily in P3HT-$Im^+TFSI^-$ as the diffuse, cationic imidazolium experiences no such interaction with $Li^+$. Here spin-lattice ($T_1$) and spin-spin ($T_2$) relaxation measurements were conducted to quantify the dynamics of $Li^+$ and $TFSI^-$ ions and determine the number of distinct $^7Li/^{19}F$ local environments, respectively. Unlike PFG NMR, NMR relaxometry is sensitive to mobile and immobile nuclei, offering insight into ions that are effectively "trapped" within the system. Together, these techniques indicate that $TFSI^-$ ions are well solvated and highly mobile in both polymers. In P3MEEMT, $Li^+$ exhibits a high activation energy for diffusion and is effectively immobilized by its local solvation environment, likely through caging in the ether side chain. Relative to P3MEEMT, $Li^+$ experiences shorter-lived local correlations in P3HT-$Im^+TFSI^-$, in line with the higher mobility probed via PFG NMR and DC polarization. Qualitative and quantitative agreement was found between the local, ion specific $T_1$ relaxometry data and techniques that probe longer time/length scales (EIS and PFG NMR). This indicates that, in

these polymers, long range ion transport is predominately governed by local interactions within the ions' solvation environments.

***T1 Relaxometry***

Spin-lattice relaxation ($T_1$) measurements describe the dissipation of energy from the spinning nucleus to the surrounding lattice. $T_1$ relaxation times measured on polymeric systems are typically representative of an average over all nuclear environments for the species under study, rather than a site-specific property.[113]

The temperature dependence of $T_1$ provides important insight into local ion dynamics.[114,115] $T_1$ is sensitive to ion reorientation rates on the order of $10^{-9}$ $s^{-1}$, and therefore probes the dynamics of the local solvation environment.[115] The minimum $T_1$ relaxation time of a nucleus occurs when its tumbling rate (i.e. its correlation time ($\tau_c$)) is equal to the inverse of its resonant frequency $\omega_0$ ($\omega_0\tau_c = 1$). As the correlation time $\tau_c$ increases (or decreases) away from this value, relaxation becomes less efficient and $T_1$ increases. The Arrhenius-like temperature dependence of $\tau_c$ leads to two behavioral regimes for $T_1$: a short correlation time (high temperature) regime where $T_1$ increases with increasing temperature, and a long correlation time (low temperature) regime where $T_1$ decreases with increasing temperature.[116] In the systems investigated in this work, $^{7}$Li relaxation takes place in the low temperature regime, indicating lower $Li^+$ ion mobility, whereas the $^{19}$F relaxation follows high temperature behavior, indicative of greater $TFSI^-$ ion mobility.

In the more freely diffusing environment of $TFSI^-$, faster anion motion results in more rapid changes to its local environment and shorter relaxation (faster energy exchange). This is

consistent with the data shown in Figure 2.5(a), where P3HT-Im$^+$TFSI$^-$ shows shorter $^{19}$F $T_1$ relaxation values, in line with the higher mobility and concentration of TFSI$^-$ in this system. In the long correlation time regime of $^7$Li, the spin-lattice relaxation behavior is determined by how tightly bound Li$^+$ ions are. In P3MEEMT, Li$^+$ is likely caged by the ether side chain and exhibits a shorter $T_1$. Li$^+$ is more mobile in P3HT-Im$^+$TFSI$^-$ and has less interaction with the lattice, exhibiting a longer $T_1$, as shown in Figure 2.5 (b).

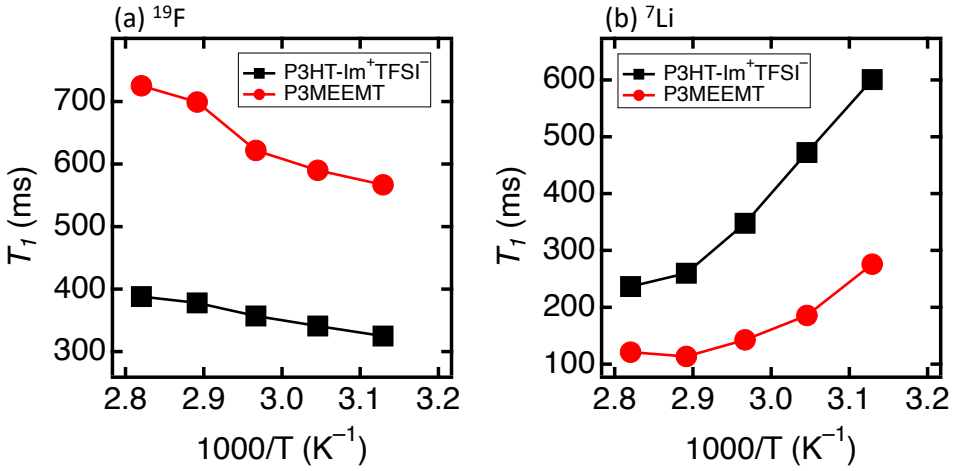


**Figure 2.5: $T_1$ relaxation times**

(a) $^{19}$F $T_1$ relaxation vs. inverse temperature. (b) $^7$Li $T_1$ relaxation vs. inverse temperature.

These qualitative observations can be quantified using ion-specific activation energy barriers obtained from fits of the variable temperature $T_1$ data (Figure 2.6). It should be noted that $T_1$ does not inherently describe long-range translational motion, but if the diffusional process depends on ion binding/unbinding, then $T_1$ dynamics are related to longer-range ion hopping.[115,117,118] To enable a quantitative comparison between nuclei, the Bloembergen, Purcell and Pound (BPP) equation[119] for homonuclear dipole-dipole interactions was used to fit the temperature-dependent correlation time ($\tau_c$) and determine the activation energy barrier ($E_a$):

$$\frac{1}{T_1} = k\left(\frac{\tau_c}{1+\omega_0^2\tau_c^2} + \frac{4\tau_c}{1+4\omega_0^2\tau_c^2}\right),$$

$$\tau_c = \tau_0 \exp\left(\frac{E_a}{RT}\right).$$

Here, $\omega_0$ is the Larmor Frequency of the nucleus under study (Hz), $k$ is constant from fitting the data, $\tau_0$ is the correlation time at infinite temperature, and $R$ is the gas constant.

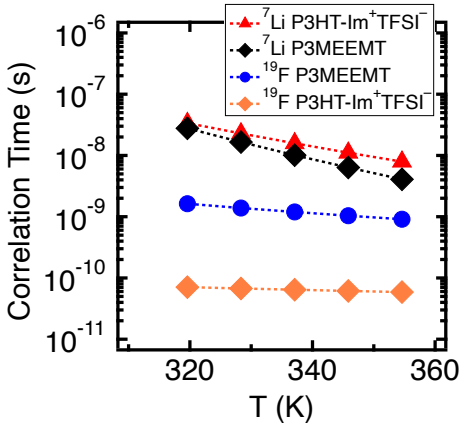


**Figure 2.6: Correlation time vs. temperature for $^{19}$F and $^7$Li in P3HT-Im$^+$TFSI$^-$ and P3MEEMT**

Dotted lines represent the respective exponential fits from which activation energies were obtained.

The fits indicate that $^7$Li has a relatively high energy barrier in P3MEEMT, 51.6 kJ/mol compared to 39.1 kJ/mol in P3HT-Im$^+$TFSI$^-$ (Table 2.2). Qualitatively, these results are consistent with the conductivity data, as P3HT-Im$^+$TFSI$^-$ has the lowest activation energy for both $^7$Li and $^{19}$F, and in turn has a higher ionic conductivity and Li$^+$ transport. Additionally, the high $E_a$ of $^7$Li in P3MEEMT indicates a large thermodynamic barrier to local motion, in line with the near zero Li$^+$ transference observed with PFG NMR and DC polarization.

**Table 2.2** Activation energies ($E_a$) and correlation time at infinite temperature ($\tau_0$) for $^{19}$F and $^7$Li in P3HT-Im$^+$TFSI$^-$ and P3MEEMT. P3HT-Im$^+$TFSI$^-$ displays lower activation energies for both $^7$Li and $^{19}$F nuclei.

| Sample | $\tau_0$ (s) | $E_a$ (kJ/mol) |
|---|---|---|
| P3HT-Im$^+$TFSI$^-$ $^{19}$F | $1.10 \times 10^{-11}$ | 4.9 |
| P3MEEMT $^{19}$F | $4.63 \times 10^{-12}$ | 15.6 |
| P3HT-Im$^+$TFSI$^-$ $^7$Li | $1.39 \times 10^{-14}$ | 39.1 |
| P3MEEMT $^7$Li | $1.02 \times 10^{-16}$ | 51.6 |

To quantify the relation between local ion hopping and long-range transport, we can compare the above ($T_1$-derived) activation energies with those derived from EIS conductivity measurements, which probe ion transport on a longer time/length scale (on the order of kHz). Here, variable temperature EIS data is analyzed using the (Vogel–Fulcher–Tamman) (VFT) formalism to account for the segmental dynamics of the polymers above $T_g$:[120]

$$\sigma = A \exp\left(-\frac{E_a}{R(T-T_0)}\right),$$

where $\sigma$ is the ionic conductivity, $A$ is the prefactor, $E_a$ the activation energy, and $T_0$ is the Vogel temperature, which is equal to the glass transition temperature in ideal glasses, but typically assumed to be 50° C below $T_g$.[120,121] Figure 2.7 shows data plotted in an Arrhenius and VFT fashion, along with the calculated activation energies.

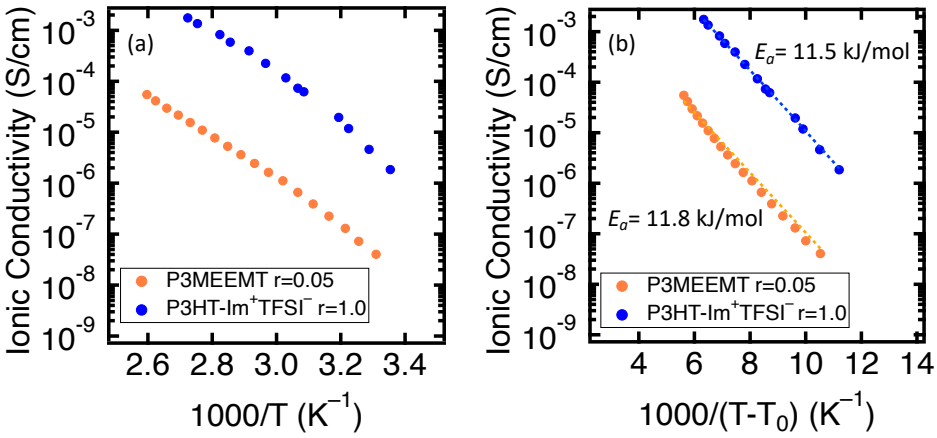


**Figure 2.7: Variable temperature ionic conductivity**

(a) Variable temperature EIS data for P3MEEMT and P3HT-Im$^+$TFSI$^-$. (b) The same data linearized by normalizing to $T_0$. Dotted lines represent the VFT fits from which activation energies were calculated.

EIS inherently probes average properties of all mobile ions, whereas the activation energies presented in Table 2.2 are ion specific. Hence, a quantitative comparison between local and long-range energy barriers requires calculation of a weighted average of the overall activation energy. To do this, local activation energies obtained for individual nuclei (Table 2.2) are weighted by the ion's contribution to conductivity (determined from the transference numbers in Table 2.1):

$$E_{a,NMR} = (t_{Li+})\left(E_{a,7Li}\right) + (1 - t_{Li+})\left(E_{a,19F}\right).$$

For P3MEEMT:

$$E_{a,NMR} = (0.04)(51.6) + (0.96)(15.6) = 17.0\ kJ/mol$$

For P3HT-$Im^+TFSI^-$:

$$E_{a,NMR} = (0.32)(39.1) + (0.68)(4.9) = 15.8\ kJ/mol$$

The reasonable agreement between these two methods, which probe very different length scales, indicates that the long-rang ionic transport is strongly influenced by short-range ionic mobility. It should again be emphasized that $T_1$ derived activation energies need not agree with those of EIS as a general rule, as $T_1$ probes local dynamics. However, the similarity in this instance indicates long-range motion is associated with fast (shorter-range) fluctuations.[115,117,118] In particular, the lack of $Li^+$ diffusion can be largely attributed the high local energy barrier for $Li^+$ hopping in P3MEEMT.

***T2 Relaxometry***

Finally, $T_2$ relaxometry is an effective technique to quantify the distribution of ion local environments[70,107,108] and indicates that, in P3HT-$Im^+TFSI^-$, the imidazolium and $Li^+$

counterions form a single, uniform anionic network. In both systems, the $^{19}F$ $T_2$ relaxation curves are well fit by a single exponent across all temperatures of interest (see Figure 2.22 and further details in the Appendix 2.6), indicating a single anion environment. This indicates that in both polymers, the $TFSI^-$ anion is fully solvated and does not exist in charged clusters, as free and clustered $TFSI^-$ would display unique $T_2$ values. This is particularly interesting for P3HT-$Im^+TFSI^-$, as this conjugated polymer ionic liquid has a covalently bound, cationic imidazolium pendant with ionically associated $TFSI^-$ (Figure 2.1(a)). When LiTFSI is added, one could imagine that interactions between imidazolium and $TFSI^-$ are distinct from those of $Li^+$ and $TFSI^-$. However, this would lead to two distinct $T_2$ values. The presence of a single $T_2$ value for $^{19}F$ in P3HT-$Im^+TFSI^-$ indicates that the added $TFSI^-$ and the $TFSI^-$ originally paired to the imidazolium become indistinguishable, forming an anionic network through which $Li^+$ can move. This phenomenon has been previously reported by MD simulation in the similar P3HT-$Im^+BF_4^-$ system.[15]

On the other hand, $^7Li$ is present in two distinct environments in both polymers (see Figure 2.22), as demonstrated by the need for a two-component exponential fit of the respective relaxation curves. The exact nature of these environments cannot be determined by NMR relaxation alone, but a reasonable hypothesis is that $Li^+$ is continuously binding and unbinding on a fast time scale, and the $^7Li$ environment associated with a shorter $T_2$ is representative of $Li^+$ ions experiencing stronger interactions at a given moment. PFG NMR probes longer time scales, which explains why a single average $^7Li$ diffusion coefficient is measured for P3HT-$Im^+TFSI^-$, as has been reported for other polymer electrolytes.[122]

## 2.5 Conclusions

This work demonstrates that two thiophene derivatives with distinct side chain chemistries, P3HT-Im$^+$TFSI$^-$ and P3MEEMT, are promising as mixed ion-electron conductors. However, only P3HT-Im$^+$TFSI$^-$ facilitates $Li^+$ transport. The cationic side chain coordinates with the TFSI$^-$ anion, sufficiently weakening the Li—TFSI interaction such that $Li^+$ moves through the polymer-salt network at very high salt loadings (1:1 molar ratio). $Li^+$ displays very short relaxation times in P3MEEMT, indicative of a highly restricted, "bound" environment, likely caged in the ether side chain. This results in the overall bulk conductivity arising solely from TFSI$^-$ anion motion. Additionally, this results in a relatively poor ability to solvate salt, as high amounts of $Li^+$ act as transient crosslinkers, serving to reduce chain dynamics. Peak conductivity is observed at r=0.05, consistent with previous studies, whereas P3HT-Im$^+$TFSI$^-$ exhibits a monotonic increase in conductivity up to a concentration of r=1.0. These results provide insight into the impact of side chain chemistry on the relative motion of cations and anions in mixed conducting polymers, enabling application-specific designs for advanced organic electronics.

**Acknowledgments**

We gratefully acknowledge the Center for Synthetic Control Across Length-Scales for Advancing Rechargeables (SCALAR), an Energy Frontier Research Center funded by the U.S. Department of Energy, Office of Science, Basic Energy Sciences under Award #DE-SC0019381, for support of device fabrication and materials characterization. G.T.P. and R.A.S. gratefully acknowledge support from the Department of Energy Office of Basic Energy Sciences (DE-SC0016390) for polymer synthesis. The research reported here made use of

shared facilities of the National Science Foundation Materials Research Science and Engineering Center (MRSEC) at UC Santa Barbara (NSF DMR 1720256), which is a member of the Materials Research Facilities Network (www.mrfn.org). This research used X-ray scattering resources (NSLS-II, beamline 11-BM, Brookhaven National Laboratory) of the National Synchrotron Light Source II, a U.S. Department of Energy (DOE) Office of Science User Facility operated for the DOE Office of Science by Brookhaven National Laboratory under Contract No. DE-SC0012704. O.N. gratefully acknowledges support from the National Science Foundation (NSF) through the Materials Research Science and Engineering Center at UC Santa Barbara, DMR-1720256 (IRG-2). G.T.P. gratefully acknowledges support from the National Science Foundation Graduate Research Fellowship Program under Grant No. 1650114. Any opinions, findings, and conclusions or recommendations expressed in this material are those of the authors and do not necessarily reflect the views of the National Science Foundation.

## 2.6 Appendix

### Synthesis

#### *P3HT-Im$^+$TFSI$^-$ Synthesis*

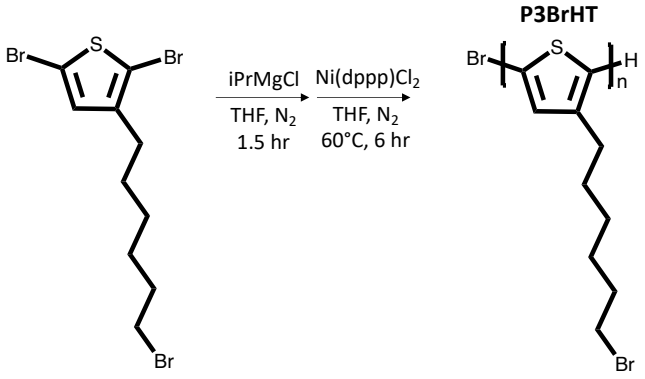


**Figure 2.8: Synthesis of P3BrHT**

**Poly(3-(6'-bromohexyl)thiophene) (P3BrHT)**

Dibromo-3-(6-bromohexyl)thiophene was synthesized according to previous literature.[26] An oven-dried Schlenk flask containing 2,5 dibromo-3-(6-bromohexyl)thiophene was placed under vacuum for 2 hours. Dry, degassed THF was added via syringe and the mixture was sparged with Nitrogen. Isopropylmagnesium chloride was added dropwise and the mixture was stirred for 1 hr at ambient temperature under Nitrogen. The desired amount of Ni(dppp)$Cl_2$ was added via syringe. The polymerization was stirred for 1 h at 60°C and quenched by rapid addition of 1M HCl, and precipitated into methanol. The polymer was purified by washing in a Soxhlet apparatus with methanol and acetone before extraction with THF. The product was concentrated under vacuum.

1H NMR (600 MHz, CDCl3) δ 7.18 − 6.92 (s, 1H), 3.53 − 3.37 (m, 2H), 2.93 − 2.55 (m, 2H), 2.04 − 1.81 (m, 2H), 1.80 − 1.58 (m, 2H), 1.57 − 1.30 (m, 4H)

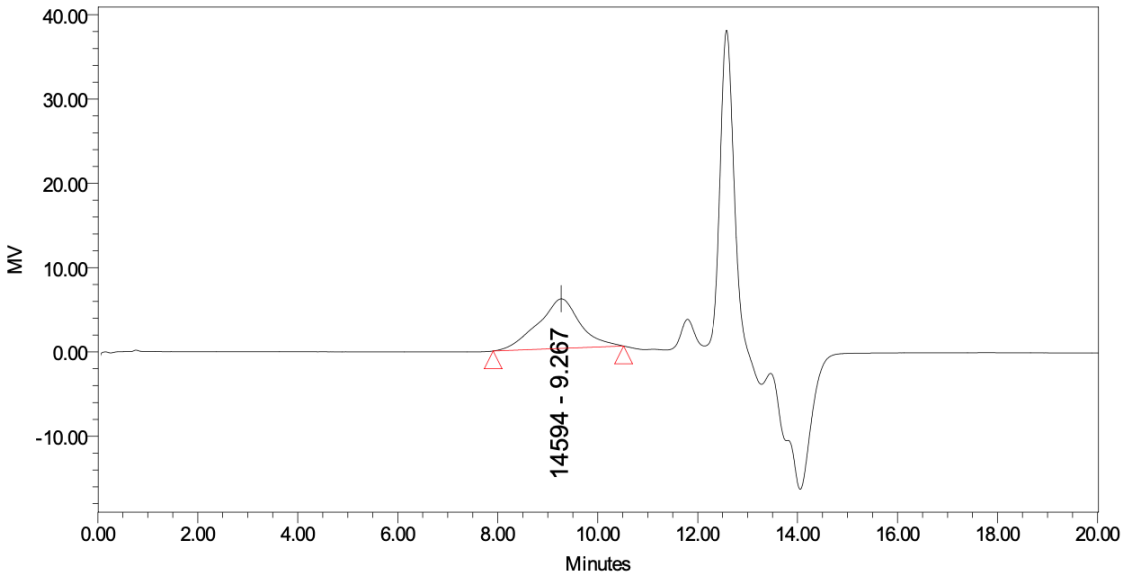


**Figure 2.9: Gel permeation chromatography (GPC) trace**

GPC was performed on a Waters e2695 equipped with THF as the mobile phase. Results are quantified using a polystyrene standard calibrant. $M_n$=13.0 kDa, $M_w$=19.2 kDa, PDI = 1.47.

***Post Polymerization Functionalization***

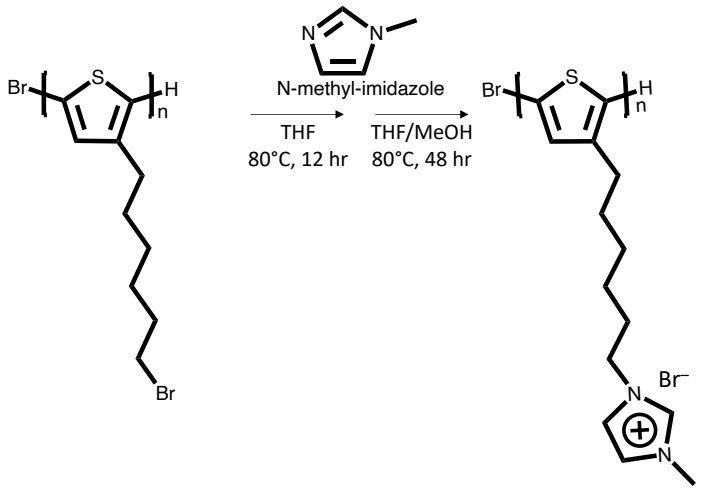


**Figure 2.10: Post-polymerization functionalization to form P3HT-Im$^+$Br$^-$**

**Poly(3-(6'-(N-methylimidazolium)hexyl)thiophene)**

The P3BrHT polymer was post-functionalized through an amine quaternization reaction. The polymer was first dissolved in THF. 1 methylimidazole (10 eq.) was added to the solution in ambient conditions. The solution was then stirred for 24 h under reflux. After 12 h, some polymer precipitate was observed in the flask. A small amount of methanol was added to fully dissolve the resulting polymer and the solution was stirred for an additional 24 hours to help achieve quantitative conversion. The polymers were then dialyzed using 10 kDa cutoff dialysis membranes against a mixture of methanol and THF, with the dialysate replaced every 12 h. The resulting polymer was then mixed with 10 molar equivalents of LiTFSI and stirred at 50°C in methanol and acetonitrile followed by dialysis for 48h in a 50:50 mixture of methanol and acetonitrile. Complete anion exchange was confirmed via XPS.

1H NMR (600 MHz, CD3CN) δ 8.50 (s, 1H), 7.39-7.34 (m, 2H), 4.14 (m, 2H), 3.83 (s, 3H), 2.85 (m, 2H), 1.87 (m, 2H), 1.71 (m, 2H), 1.48 (m, 2H), 1.39 (m, 2H)

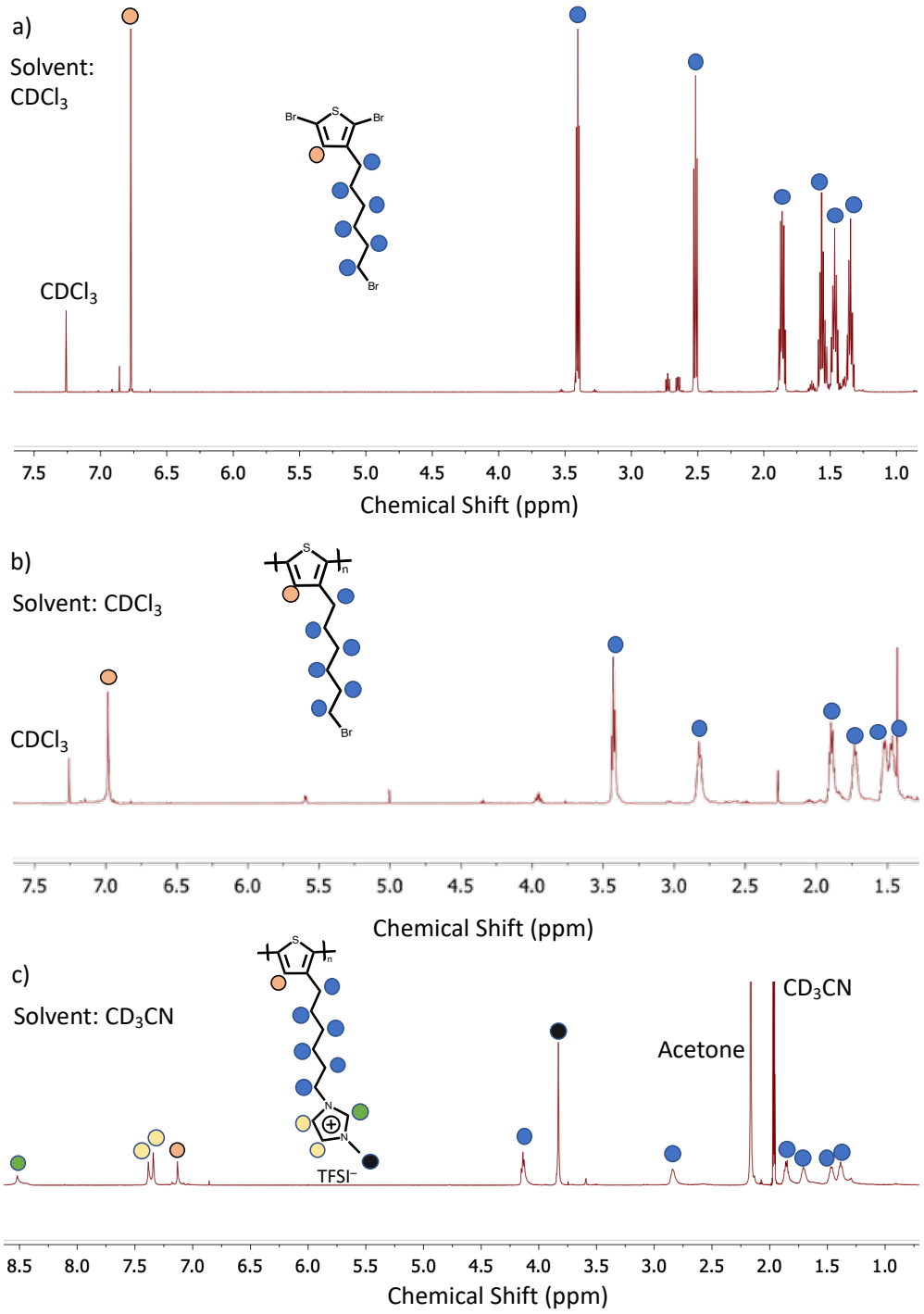


**Figure 2.11: Solution state proton NMR spectra**

a) Brominated 3BrHT, b) P3BrHT, and c) P3HT-Im$^{+}$TFSI$^{-}$.

***P3MEEMT Synthesis***

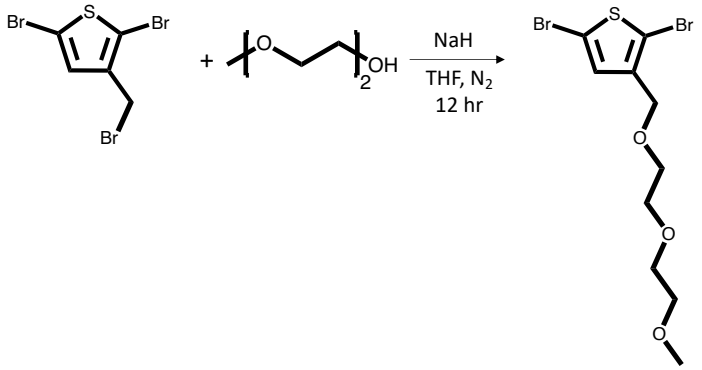


**Figure 2.12: Synthesis of 2,5-dibromo-3-methoxyethoxyethoxymethylthiophene**

**2,5-dibromo-3-methoxyethoxyethoxymethylthiophene**

2,5-dibromo-3(bromomethyl)thiophene was purchased form Polymer Source. To a round bottom flask anhydrous THF (100 mL) and diethylene glycol monomethyl ether (1.5 eq), and NaH (2 eq) were added. The NaH was allowed to react for 1 hour, ensuring $H_2$ gas evolution had ceased. 2,5-dibromo-3(bromomethyl)thiophene (1 eq.) was dissolved in THF, then added to the reaction. It was then added dropwise over 15 min, after which the reaction was allowed to stir overnight. The reaction was quenched by pouring in to 10% Na2SO4 in water, then extracted with diethyl ether. The organic phase was successively washed with water, dried over MgSO4, and solvent removed using rotary evaporation. The crude product was purified using a silica gel column with 3:2 hexanes:ethyl acetate.

1H NMR (600 MHz, CDCl3)δ 7.0 (s, 1H), 4.43 (s, 2H), 3.65 (m, 6H), 3.57 (m, 2H), 3.39 (s, 3H).

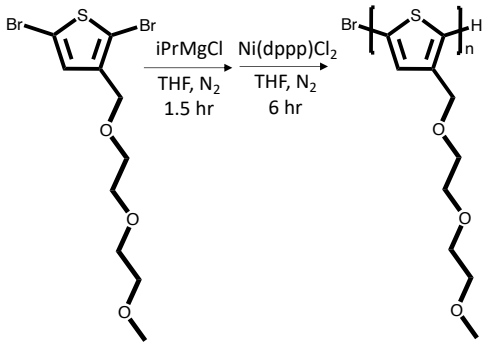


**Figure 2.13: Synthesis of Poly(3-methoxyethoxyethoxymethylthiophene)**

**Poly(3-methoxyethoxyethoxymethylthiophene)**

An oven-dried Schlenk flask containing 2,5 dibromo-3-methoxyethoxyethoxymethylthiophene (1 eq) was placed under vacuum for 2 hours. Dry, degassed THF was added via syringe and the mixture was sparged with Nitrogen. Isopropylmagnesium chloride (1.1 eq) was added dropwise and the mixture was stirred for 5 hr at ambient temperature under Nitrogen. The desired amount of $Ni(dppp)Cl_2$ (0.01 eq) was added via syringe. The polymerization was stirred for 1 h at 60°C and quenched by rapid addition of 1M HCl, and precipitated into hexanes. The polymer was purified in a Soxhlet apparatus with hexanes, then washed with methanol and water and dialyzed in 10 kDa tubing in acetonitrile.

1H NMR (600 MHz, CDCl3) 7.0 (s, 1H), 4.67 (s, 2H), 3.75 (s, 4H), 3.67 (m, 2H), 3.57 (m, 2H), 3.37 (s, 3H).

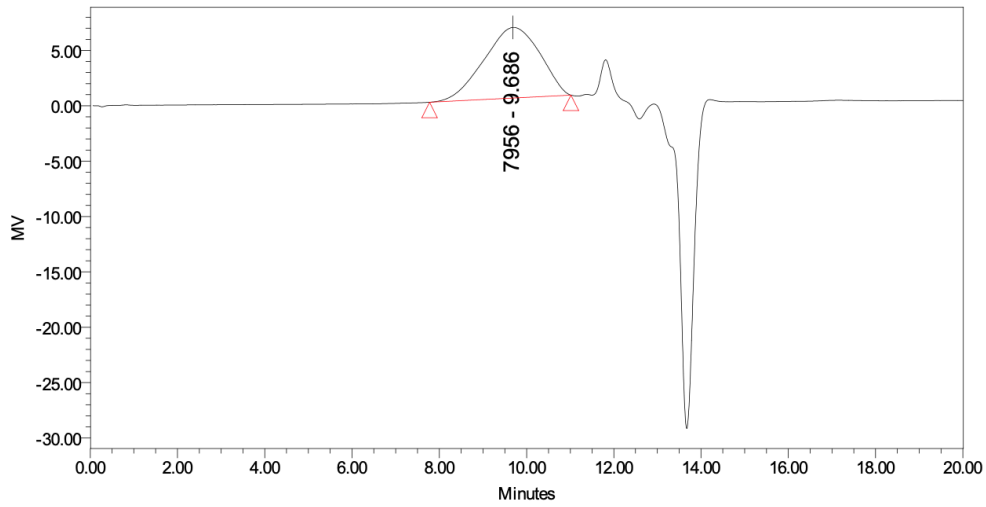


**Figure 2.14: Gel permeation chromatography (GPC) trace**

GPC was performed on a Waters e2695 equipped with THF as the mobile phase. Results are quantified using a polystyrene standard calibrant. $M_n$=6.4 kDa, $M_w$=11.8 kDa, PDI = 1.84.

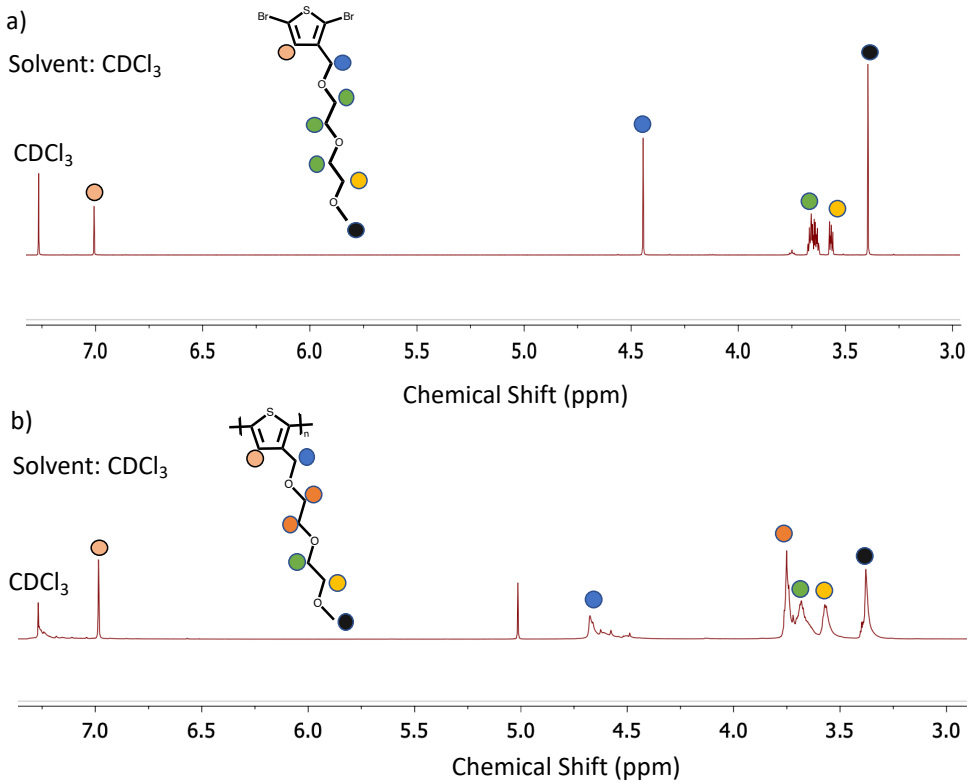


**Figure 2.15: Solution state proton NMR spectra**

a) Brominated 3MEEMT b) P3MEEMT.

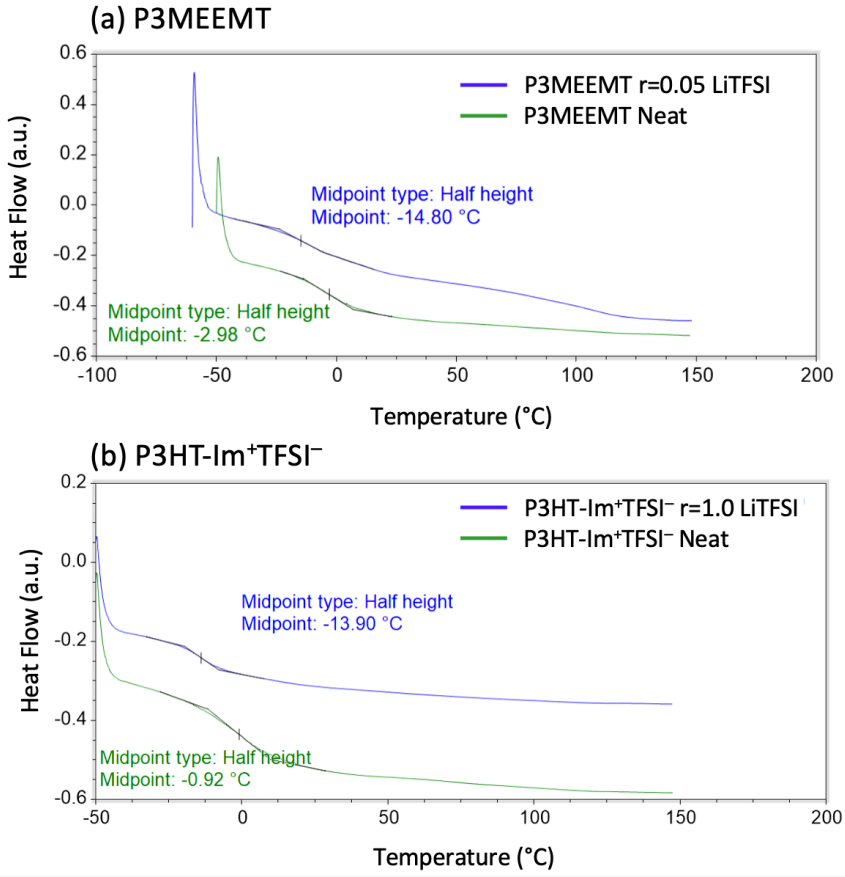


**Figure 2.16: Glass transition temperature ($T_g$) measurements *via* dynamic scanning calorimetry (DSC)**

a) P3MEEMT and b) P3HT-Im$^+$TFSI$^-$ Polymer samples were drop cast into hermetic aluminum pans. The samples were sealed and characterized with a TA DSC 2500 to measure $T_g$. Samples were initially heated to 150 °C, held for 5 min, then rapidly quenched in order to enhance the $T_g$ signal. Reported curves are on second heating at 20 °C min$^{-1}$.

**GIWAXS**

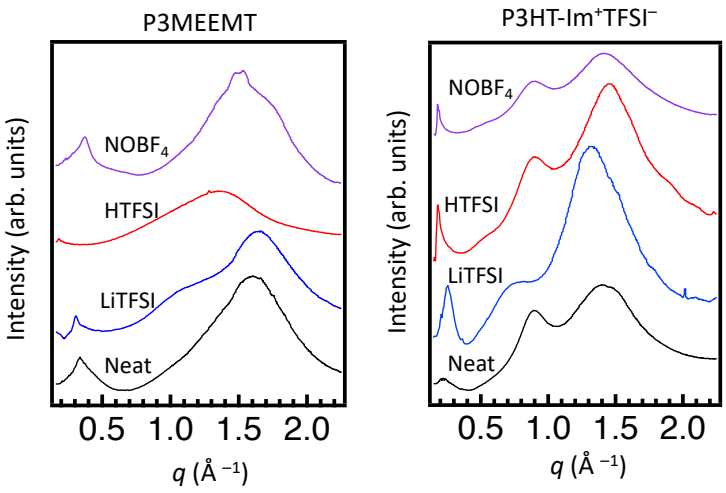


**Figure 2.17: Circular averaged GIWAXS profiles**

Profiles are for (a) P3MEEMT and (b) P3HT-Im$^{+}$TFSI$^{-}$ upon the addition of the indicated dopants.

In both polymers, addition of LiTFSI shows a broad feature around 1.0 Å$^{-1}$, which is often referred to as an LiTFSI aggregation peak. Adding HTFSI to P3MEEMT results in a broad signature around 1.5 Å$^{-1}$, whereas $NOBF_4$ doping causes a narrower peak near 1.6 Å$^{-1}$, indicative of doping induced ordering, in line with the electronic conductivity data discussed in the main text.

Additionally, electronic doping of P3HT-Im$^{+}$TFSI$^{-}$ demonstrates a π-shift to higher $q$ (lower d- spacing) accompanied by a lamellar shift to lower $q$ (higher d-spacing), which is indicative of reorientation of the π-stacking direction to incorporate dopant counterions in the lamellar side-chain region, which is often reported in polythiophenes,[40] which could explain the enhanced polaronic signal compared to P3MEEMT (Figure 2.3).

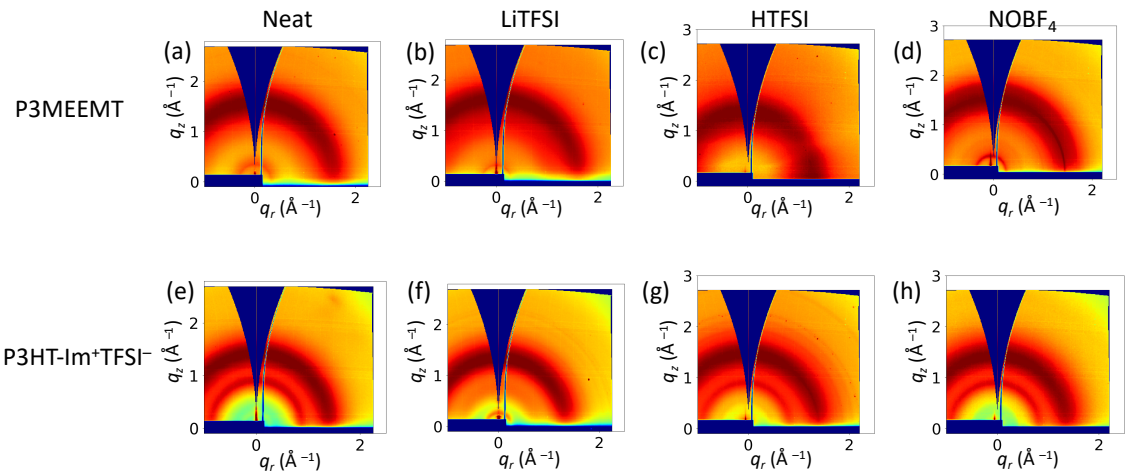


**Figure 2.18: GIWAXS patterns**

a) P3MEEMT neat, (b) P3MEEMT r=0.05 LiTFSI, (c) P3MEEMT vapor doped with HTFSI, (d) P3MEEMT vapor doped with $NOBF_4$, (e) P3HT-$Im^+TFSI^-$ neat, (f) P3HT-$Im^+TFSI^-$ r=1.0 LiTFSI, (g) P3HT-$Im^+TFSI^-$ vapor doped with HTFSI, (h) P3HT-$Im^+TFSI^-$ vapor doped with $NOBF_4$. GIWAXS experiments were performed on drop-cast films, as this results in relatively thick samples (≈50 µm), and thus no substrate induced texturing was observed. This was chosen, as opposed to thin films, to be consistent with diffusion NMR experiments, which require large pucks of material (c.a. 100 mg).

## Electrochemical Techniques

### *AC Impedance sample preparation and equivalent circuits*

Polymer samples were solution doped by dissolving the appropriate amount of polymer in acetonitrile and mixed with the appropriate amount of LiTFSI/acetonitrile solution to achieve the desired doping level. The polymer/salt solution was then drop cast onto clean circular indium tin oxide (ITO) substrates top-coated with a 150 µm Kapton spacer in which a well of known diameter was punched. The samples were sealed with clean ITO substrates and dried under high vacuum ($2 \times 10^{-8}$ torr) at 90°C for 12 hours. Characterization was done with a Biologic SP-200 potentiostat inside a nitrogen filled glovebox. Transparent ITO/ glass electrodes were used to ensure the absence of bubbles and proper interfacial contact. A sinusoidal voltage with amplitude 100 mV was applied in the frequency range of 0.1 Hz−3

MHz. To distinguish the ionic and electronic contributions to the signal, equivalent circuits were fit to the Nyquist plots, which account for the ionic resistance, the electronic resistance, and the contact resistance, as appropriate. Exemplary Nyquist plots and equivalent circuits are shown below in Figure 2.19. For the curious reader, panel (a) is data from P3HT-Im$^{+}$TFSI$^{-}$ vapor doped with HTFSI. Panel (b) is data from P3HT-Im$^{+}$TFSI$^{-}$ with LiTFSI added at a molar ratio of r=1.0. Panel (c) is data from P3HT-Im$^{+}$TFSI$^{-}$ with both LiTFSI and HTFSI added at a molar ratio of r=0.8.

From these equivalent DC resistances, conductivity was calculated according to the following.

$$\sigma = \frac{1}{R}\frac{t}{A}$$

Where $t$ is the thickness of the polymer film and $A$ is the area, both of which are defined by the Kapton spacer.

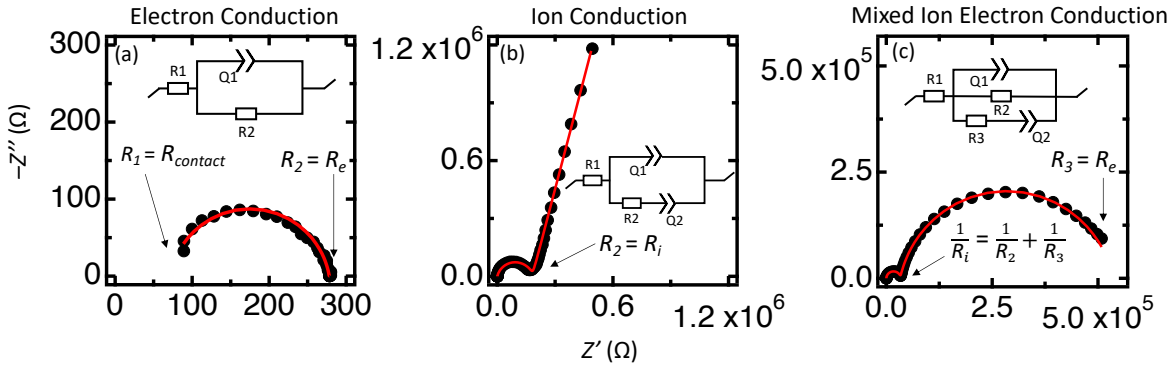


**Figure 2.19: Representative Nyquist plots for conducting polymers**

Black circles are data, while the red lines are the fits using the respective equivalent circuits. (a) shows a single semicircle, indicative of electron conduction. (b) shows a single semicircle with a capacitive tail, representative of ion conduction. (c) shows two distinct semicircles, which is associated with mixed ion electron conduction in polymers. Equivalent circuits used to calculate resistances are shown in each respective panel. These circuits are common throughout polymer literature.[36,65]

***Electronic Doping***

Vapor doping of semiconducting polymers relies on thin films being exposed to dopant vapor. Thus, for the electronic conductivity measurements, interdigitated gold electrodes sourced from Metrohm Dropsense were used, as opposed to the ITO symmetric cells used to measure "thick film" ionic conductivity. Films were drop cast to achieve thickness c.a. 200 nm.

Vapor doping with HTFSI and $NOBF_4$ was performed in a sealed vessel on a hot plate inside a nitrogen filled glove box. Pristine films were attached to the lid of a jar containing crystals of the desired dopant using double sided Kapton tape. The jar was sealed and placed on the hot plate to be heated for the desired temperature and duration. HTFSI doping was performed at 50°C for 30 min and $NOBF_4$ doping was performed at 70°C for 10 and 30 min.

Conductivity measurements were performed as previously describe, now using the following equation related to the IDE geometry

$$\sigma = \frac{1}{R}\frac{d}{(N-1)lh}$$

Here $\sigma$ is the conductivity, $R$ is the resistance determined from EIS, $d$ is the distance between the gold electrodes, $N$ is the number of digits, $l$ is the length of each digit, and $h$ is the polymer film thickness. Here, $d$=10 $\mu m$, $l$=6760 $\mu m$, and $N$=250. As mentioned in the main text, P3MEEMT displayed predominately ionic conductivity when vapor doped with HTFSI, despite undergoing the expected electronic structural transition, as shown below in Figure 2.20.

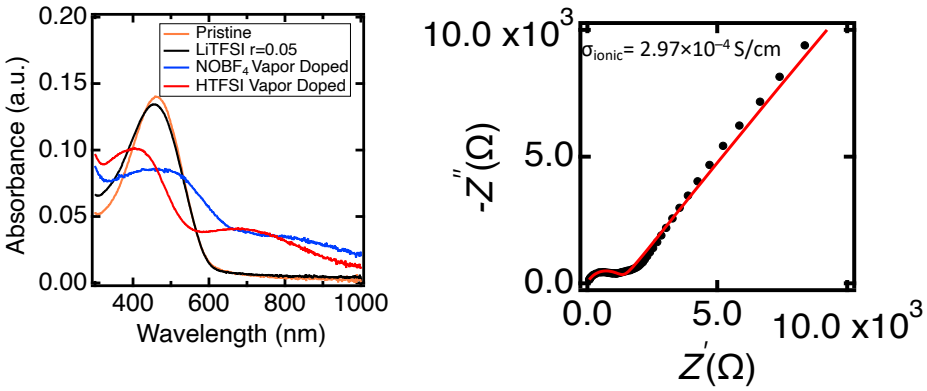


**Figure 2.20: UV-Vis spectra and Nyquist plot of HTFSI doped P3MEEMT**

UV-Vis indicates that HTFSI doping induces a change in the electronic structure of P3MEEMT (left), yet the Nyquist plot is indicative of a system with predominately ionic conductivity (right).

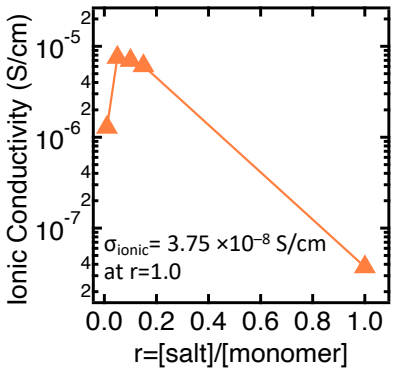


**Figure 2.21: P3MEEMT vs salt, showing r=1 for reference. Collected at 80°C**

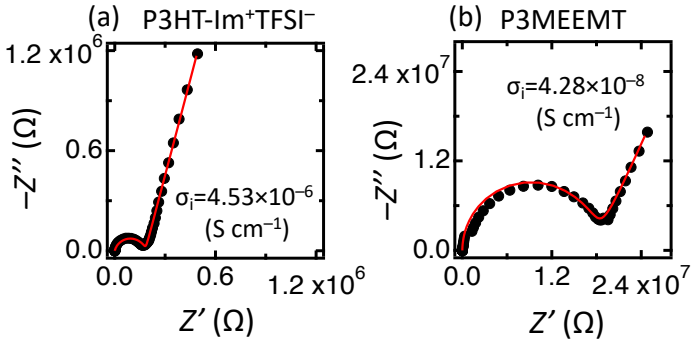


**Figure 2.22: Representative Nyquist plots collected at 30 °C**

(a) P3HT-Im$^+$TFSI$^-$ with r=1.0 LiTFSI and (b) P3MEEMT with r=0.05 LiTFSI.

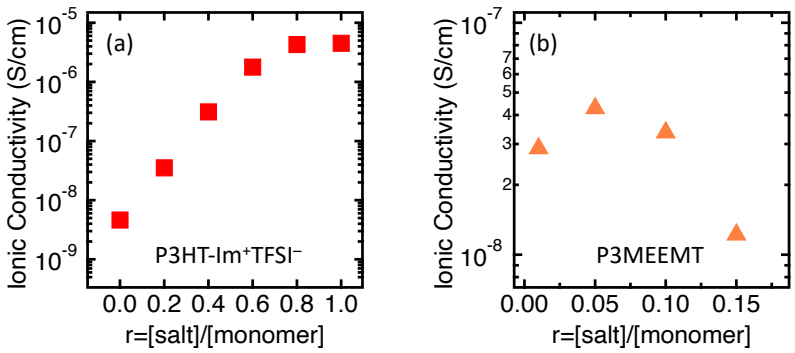


**Figure 2.23: Ionic conductivity as a function of LiTFSI salt concentration at 30 °C**

(a) shows data for P3HT-Im$^{+}$TFSI$^{-}$ and (b) shows that of P3MEEMT.

***DC Polarization***

DC polarization was performed on symmetric lithium−polymer−lithium cells. Samples were assembled in an argon glovebox utilizing a Controlled Environment Sample Holder (CESH) from Biologic LLC and tested using their Intermediate Temperature System (ITS) in conjunction with their VSP-300 potentiostat to 81°C for consistency with the PFG NMR measurements. Samples were equilibrated until the interfacial resistance, monitored via EIS, stabilized. This indicated the complete formation of a solid−electrolyte interphase (SEI) layer. Next, a 100 mV potential bias was applied and the resulting current measured over time. EIS measurements with a 20 mV amplitude were performed at 20 minute intervals to monitor changes in the interfacial resistance. Lithium transference numbers were calculated following the method of Bruce and Vincent:[28,68]

$$t_{Li+} = \frac{I_{ss}(\Delta V - I_{\Omega}R_0)}{I_{\Omega}(\Delta V - I_{ss}R_{\mathrm{ss}})}$$

Here, ΔV is the applied potential (100 mV), $R_0$ and $R_{ss}$ are the initial and steady-state interfacial resistances, respectively, $I_{ss}$ is the steady- state current, and $I_{\Omega}$ is the initial current determined from Ohm's law:

$$I_\Omega = \frac{\Delta V}{R_\Omega}$$

where $R_\Omega$ is the initial cell resistance (bulk and interfacial) measured by EIS. Using $I_\Omega$ instead of the initial current measured by the potentiostat eliminates errors related to the speed at which the instrument can record the current. Figures 2.24 and 2.25 show the initial Nyquist plots which indicate formation of the SEI as well as the final Nyquist plot used to calculate $R_{ss}$ after polarization. Figure 2.26 shows the equivalent circuit used to fit $R_0$ and $R_{ss}$, while Table 2.3 shows the resulting values. Current decay curves are shown in Figure 2.27.

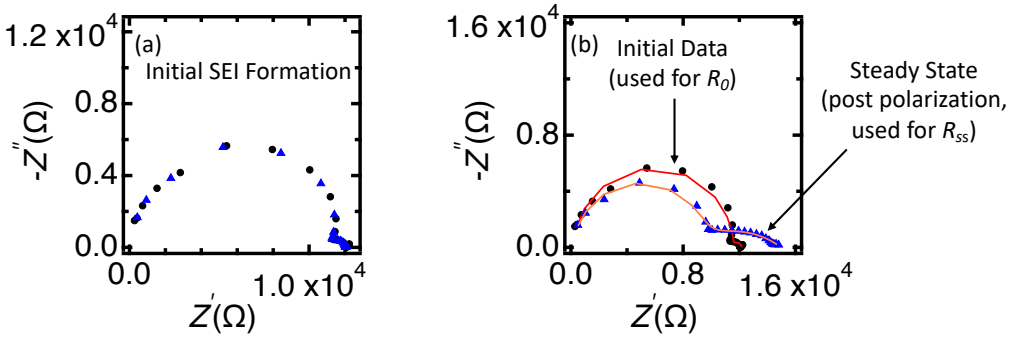


**Figure 2.24: Nyquist spectra from the DC polarization experiment**

Data is for P3HT-Im$^+$TFSI$^-$ r=1.0 LiTFSI (a) Overlapping Nyquist spectra for the final two measurements (separated by 1 hour) during the initial equilibration period indicates complete formation of the SEI layer prior to beginning polarization. (b) Initial and steady state Nyquist spectra used for calculating $R_0$ and $R_{ss}$. Points represent data and lines represent the fit to the equivalent circuit shown in Figure 2.26.

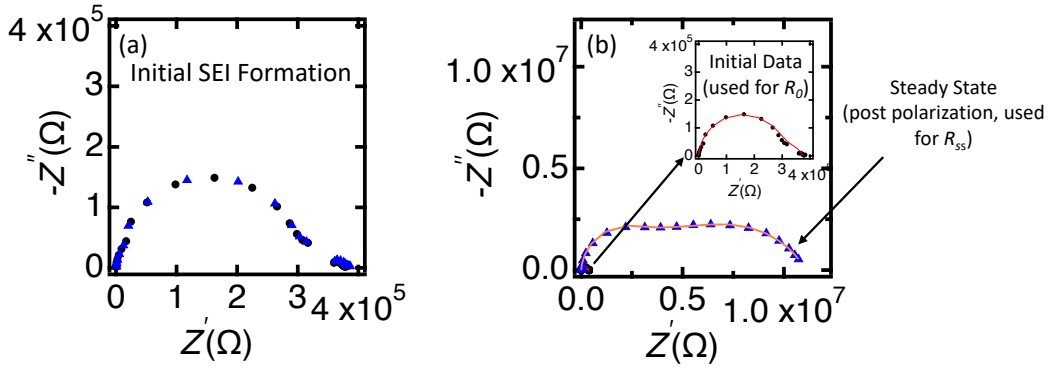


**Figure 2.25: Nyquist spectra from the DC polarization experiment**

Data is for P3MEEMT r=0.05 LiTFSI (a) Overlapping Nyquist spectra for the final two measurements (separated by 1 hour) during the initial equilibration period indicates complete formation of the SEI layer prior to beginning polarization. (b) Initial and steady state Nyquist spectra used for calculating $R_0$ and $R_{ss}$. Points represent data and lines represent the fit to the equivalent circuit shown in Figure 2.26. The inset shows a zoomed in view of the initial spectra. Due to the low $Li^+$ conductivity of P3MEEMT and the rapid decline in conductivity at high $Li^+$ content (Figure 2.21), impedance grew significantly over the course of the polarization experiment.

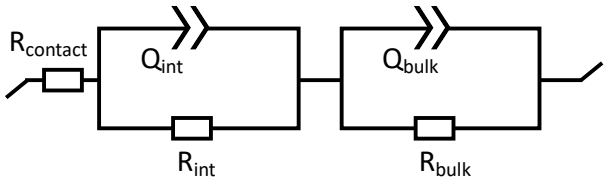


**Figure 2.26: The Equivalent circuit used to fit EIS data from the Bruce-Vincent experiments**

**Table 2.3** Bulk ($R_B$) and interfacial ($R_I$) resistance values calculated from the above Nyquist plots.

| | $R_{B,0}$ (Ω) | $R_{I,0}$ (Ω) | $R_{B,SS}$ (Ω) | $R_{I,SS}$ (Ω) |
|---|---|---|---|---|
| P3HT-$Im^+TFSI^-$ | 11247 | 573 | 8586 | 6362 |
| P3MEEMT | 294039 | 87313 | $3.61\times10^6$ | $6.76\times10^6$ |

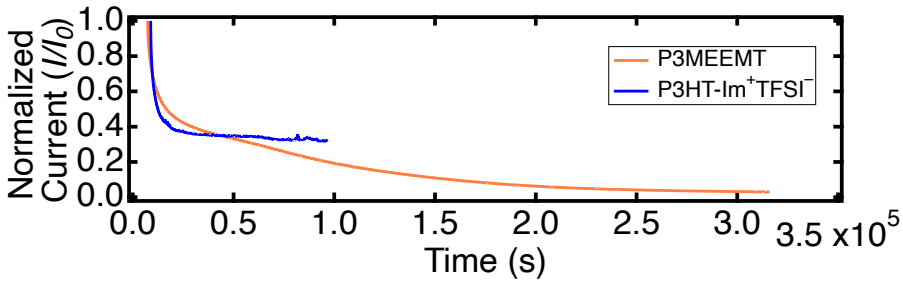


**Figure 2.27: Current decay for DC polarization study**

Data is for P3HT-$Im^+TFSI^-$ and P3MEEMT. Data was collected for less time for P3HT-$Im^+TFSI^-$ as the current reached a steady state quicker.

**NMR Techniques**

***PFG NMR***

Pulsed Field Gradient (PFG) NMR measures the self-diffusion coefficients of any NMR active nuclei. $^{7}$Li and $^{19}$F are both NMR active, and correlate to the cation and anion in our systems, respectively. Operating under the assumptions of Dilute Solution Theory, conductivity and lithium transference number ($t_{Li+}$) can be calculated, as shown below.

$$\sigma = \frac{F^2}{RT}(c_{Li+}D_{Li+} + c_{TFSI-}D_{TFSI-})$$

$$t_{Li+} = \frac{\sigma_{Li+}}{\sigma_{Li+} + \sigma_{TFSI-}}$$

Here, $\sigma$ is conductivity, $F$ is Faraday's constant, $R$ is the ideal gas constant, $T$ is temperature, $c_{+/-}$ is the concertation on the respective ion in the system, and $D_{+/-}$ is the self-diffusion coefficient for the respective ion.

The PFG NMR samples were prepared in the same manner as described for the AC Impendence samples. Here, drop casting was performed into a quartz trough that facilitated approximately 100 mg of material to be loaded into the center of the NMR tube. All sample preparation was done in a nitrogen glovebox, and the NMR tubes were sealed before removal from the glovebox to maintain an oxygen and water free environment during measurement.

Measurements were performed on a Bruker Avance III super-wide-bore spectrometer with a Bruker DIFF50 diffusion probe with replaceable radio- frequency (RF) inserts for $^{7}$Li and $^{19}$F. Due to signal noise and slow diffusion times at room temperature, measurements were

performed at 72°C and 82°C for both $^{19}F$ and $^{7}Li$ nuclei. A stimulated echo pulse sequence was used, and the attenuation of the intensity ($I$) was fit to the following equation.[105]

$$I(G) = I(0)\exp\left[-G^2 D\,\gamma^2\delta^2\left(\Delta - \frac{\delta}{3}\right)\right]$$

Where $G$ is gradient field strength, $I(0)$ is the intensity of the magnetization when $G$=0, $\gamma$ is the gyromagnetic ratio, $\delta$ is the gradient pulse length, $\Delta$ is the interval between gradient pulses, and D is the diffusion coefficient.

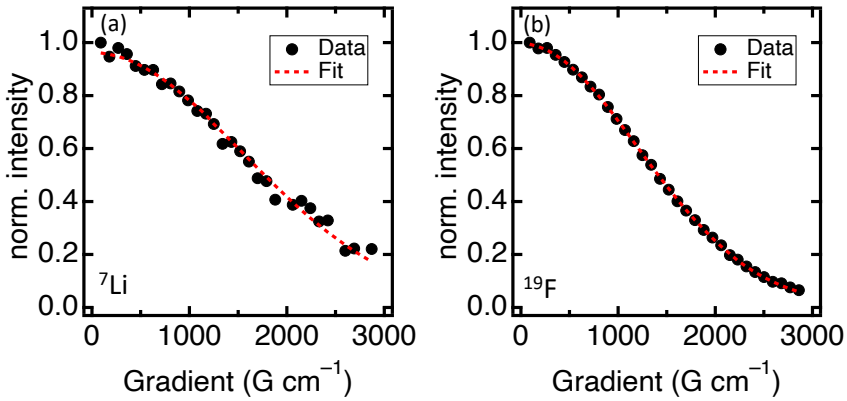


**Figure 2.28: Diffusion exponential decay curves and their respective mono-exponential fits**

Data is for (a) $^{7}Li$ in P3HT-Im$^{+}$TFSI$^{-}$ at 81°C and (b) $^{19}F$ in P3HT-Im$^{+}$TFSI$^{-}$ at 81°C.

It should be noted that signal to noise is expected to be worse when measuring $^{7}Li$ when compared to $^{19}F$ due to the quadrupolar moment of $^{7}Li$ and the fact that for every $^{7}Li$ nuclei added to the system, 6 $^{19}F$ nuclei are added due to the chemical composition of TFSI$^{-}$ ($[(CF_3SO_2)_2N]^-$).

### *$T_1$ and $T_2$ Relaxation*

Here $T_1$ is used to refer to the longitudinal relaxation time, while $T_2$ is used to refer to the transverse relaxation time. $T_1$ and $T_2$ relaxation experiments were performed on the same

samples, at the same time as PFG NMR. The $T_1$ experiment utilized a saturation recovery pulse program,[106] while the $T_2$ utilized the Carr-Purcell-Meiboom-Gill (CPMG) sequence.[107,108] Exemplary $T_1$ data is shown below in Figure 2.29. $T_2$ fitting data is shown in Figure 2.30. Figure 2.31 shows the resulting $T_2$ values along with the phase distribution vs temperature.

$$I(t) = I(0)[1 - \exp\left(\frac{-t}{T1}\right)]$$

$$I(t) = I(0)\exp\left(\frac{-t}{T2}\right)$$

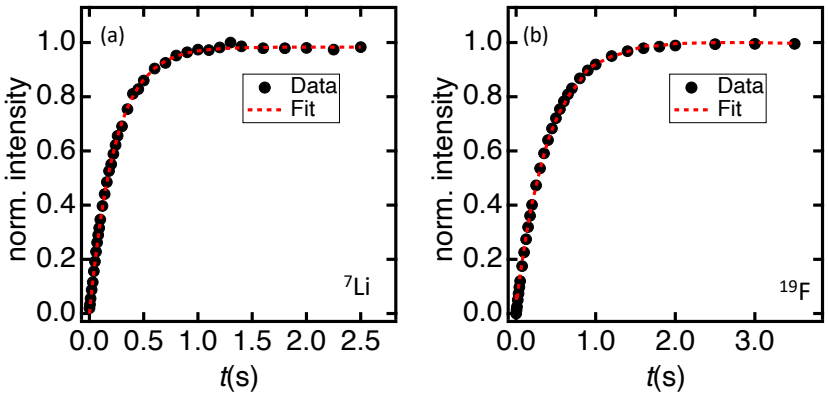


**Figure 2.29: Exemplary Saturation Recovery curves and their respective mono-exponential fits**

Data is for (a) $^{7}$Li in P3HT-Im$^{+}$TFSI$^{-}$ at 81°C and (b) $^{19}$F in P3HT-Im$^{+}$TFSI$^{-}$ at 81°C.

Figure 2.30 shows representative $T_2$ decay curves for $^{7}$Li and $^{19}$F in P3HT-Im$^{+}$TFSI$^{-}$ at 81°C. In Figure 2.30(a), the $^{19}$F data is fit to both a single and bi-exponential decay, however fitting to a bi-exponential shows little improvement to the fit. The resulting phase distribution is 95%-5%, where the $T_2$ value for 95% of the nuclei matches that of the single phase (8.63 ms for single phase and 8.71 ms for the 95% phase resulting from bi-exponential). Effectively, the bi-exponential fit recreates that of the single exponential, providing confidence that a single phase is sufficient to describe the data. This is not the case for the $^{7}$Li data, shown in Figure 2.30(b).

The bi-exponential fit describes the data far better than the single exponential fit, indicating Li+ resides in two environments. A similar trend is observed for P3MEEMT.

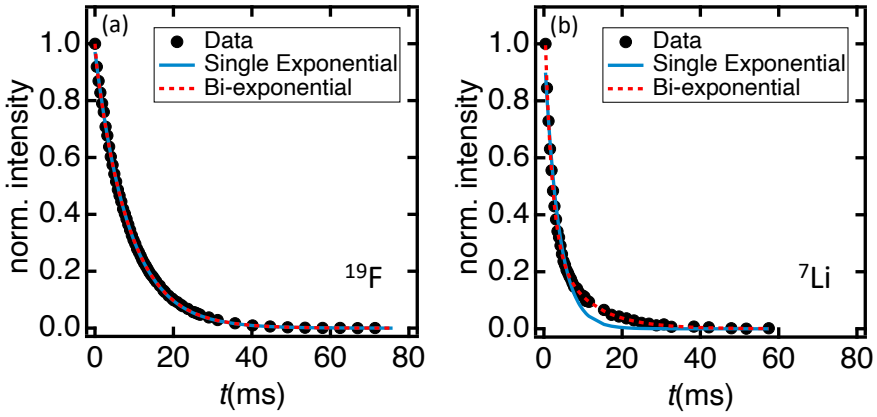


**Figure 2.30: Representative $T_2$ exponential decay curves**

Data is for (a) $^{19}F$ and (b) $^{7}Li$. Data is shown from P3HT-Im$^{+}$TFSI$^{-}$ at 81°C. P3MEEMT showed the same trend. Black points represent data, the solid blue line represents a single exponential fit, and the dotted red line represents a bi-exponential fit.

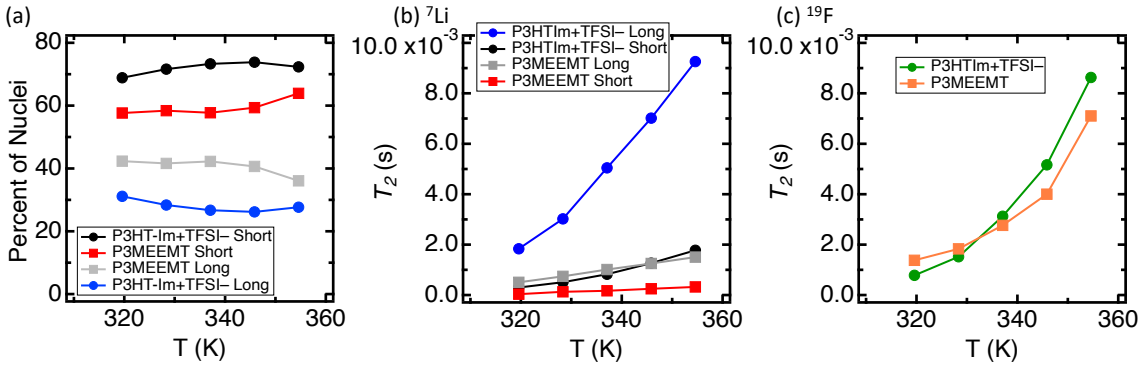


**Figure 2.31: $T_2$ relaxation data**

(a) Distribution of the two $^{7}Li$ phases vs. temperature for each polymer. (b) $T_2$ values vs. temperature for both $^{7}Li$ phases, and (c) $T_2$ values vs temperature for $^{19}F$.

# Chapter 3

# Tuning transport via interaction strength in cationic conjugated polyelectrolytes

## 3.1 Abstract

Tuning polymer-ion interaction strength is critical for balancing ion solvation and transport in solid polymer electrolytes for battery applications. In mixed Li+/electron conducting systems for improved battery binders, the design space is further complicated by seemingly opposing design rules for electron and ion conducting polymers. Conjugated polymers functionalized with cationic side chains have demonstrated high ionic conductivity, lithium transport, and electronic conductivity by combining long range polymer ordering with diffuse ion interactions. Herein, we demonstrate a family of mixed conducting polythiophenes functionalized with a range of cationic side chains, namely imidazolium, trimethylammonium, and ammonium groups. The strength of ionic interactions and structure of the side chains govern lithium-selective transport resulting in high Li+ conductivity (~$10^{-4}$ S/cm at 80°C), and electronic conductivity. The more diffuse imidazolium ion affords labile ionic interactions, resulting in higher lithium transference than the other cations studied. Electronic conductivity is also higher in the imidazolium system, stemming from the ability of the planar side chains to stack while also accommodating the bulky $TFSI^-$ counterions. These results demonstrate the importance of interaction strength in ion transport, while also indicating that the physical structure of the side chain has an impact on electronic conduction. The imidazolium group strikes a balance, achieving superior properties across all metrics.

## 3.2 Introduction

Mixed conducting polymers offer solution processability, mechanical flexibility, and synthetic versatility, while simultaneously facilitating ionic and electronic charge transport. While this powerful combination of properties has garnered much attention, their development faces significant challenges due to the disparate polymer design rules required to afford both electronic and ionic conduction. For instance, high electronic conductivity is typically associated with ordered, semicrystalline structures, while high ionic conductivity relies on a high dielectric constant and fast segmental motion.[36–38] Nonetheless, many design strategies have proved successful in creating mixed conducting architectures, including nanostructured block copolymers,[36,64,77,123] polymer blends,[26,44,45] and single component polymer systems.[14,15,39,40,89,124] Now much focus is on the optimization of each property. However, given the broad range of electrochemical applications in which mixed conducting polymers can be applied, the focus must turn to charge transport criteria more specific than high overall ionic and electronic conduction. For example, fuel cells require $H^+$ conduction, while batteries rely on metal cation conduction. Anion transport can also be of interest, where semiconducting applications typically focus on mixed conduction in the context of dopant counterion diffusion.[125] For the next generation of mixed conducting polymers, structure-property relationships must be developed to enable predictable tunability of a range of transport properties for these highly-tailored applications.

Of particular interest here are design strategies for mixed conducting polymers applied as battery binders. When used as binders in battery electrode composites, mixed conducting polymers have been shown to significantly decrease resistance and improve rate

performance.[16,40,72,126] For battery applications, the polymer must not only be electronically and ionically conductive, but also selective in terms of ionic transport of the metal cation of interest (eg. $Li^+$ in Li-ion batteries). Existing design principles for achieving "bulk-ionic conductivity" (i.e., total anion and cation transport) in polyelectrolytes, including conjugated polyelectrolytes (CPEs), focus on ion solvation and do not provide for selectivity. In fact, most high conductivity polyelectrolytes have a transference number ($t_+$) of <0.2, where $t_+$ is defined as the fraction of current carried by the ion of interest.[61] Indeed, the quintessential polymeric ion conductor, poly(ethylene oxide) or PEO, is particularly effective at dissolving lithium salts, but the overall ionic conductivity is dominated by counterion diffusion. Strategies to increase $t_{Li+}$ often come at the expense of overall transport. For instance, single-ion-conductors have transference numbers approaching 1 but low conductivity.[32,102] Modern PEO derivatives can achieve high ionic conductivity approaching 10 mS, but transference numbers below 0.1.[7,32] This tradeoff between conductivity and transference has been captured by a Robeson-type plot compiled by Balsara and coworkers, where there is a clear "upper bound" to the optimization.[61]

Ion conduction can be seen as a two-step process: salt dissolution, which controls the number of metal cations able to conduct, followed by ion transport. The incorporation of certain functional groups (ether oxygens or coordinating groups pendant to the backbone) promotes salt dissolution. Metal cation mobility is then strongly tied to segmental dynamics, resulting in increased conductivity in systems that are well above their glass transition temperatures ($T_g$). With this design strategy, efforts to increase ionic conductivity strive to find polyelectrolytes with lower $T_g$.[7] However, in many instances both rapid ion transport and control over polymer mechanics is desired, generating a need for design strategies that decouple ion transport from

segmental motion of the polymer. Critical parameters here are ion-polymer interactions to promote salt dissolution as well as the "average-lifetime" of ion association.[30,31] Indeed, it has been demonstrated that a careful balance must be achieved to obtain optimal salt dissolution with weak interactions such that the metal cation can hop freely between sites.[29] Imidazolium functional groups have emerged as a promising chemistry that both balances these requirements and can also be included with sufficient density to control the spacing of "hopping sites."[127] Finally, it has also been emphasized that side chain length, linker chemistry, polymer molecular weight, and backbone rigidity can influence overall conductivity.[29,30,128,129]

These findings emphasize the importance of tuning not only the dielectric environment, but the strength of ion-specific interactions in order to balance salt solvation and cation-selective transport in CPEs. Insufficient interactions will not solvate the added salt, but strong interactions can effectively immobilize cations through solvation.[29] Most designs for mixed Li+ conducting CPEs focus on adding PEO-inspired ether substituents, either as side chains[39,40,62,130] or additional blocks[36,77,131], on a conjugated polymer backbone. Indeed, incorporation of ether substituents has proved an effective strategy for a breadth of mixed conduction applications, enabling control over the mode of operation and ion uptake in transistors,[92,132] as well as tunability of ionic conductivity, crystallinity, thermal stability, and swelling in mixed conductors.[39,62,89] Additionally, block copolymer architectures between P3HT and PEO have been shown to form bicontinuous electron/ion conductive phases.[36] However, these design strategies are limited with respect to $Li^+$ selective transport, as the ether substituents promote dissolution via strong interactions with $Li^+$, but do not promote substantial $Li^+$ mobility compared to its counterion. We previously demonstrated that

imidazolium-functionalized polythiophenes have enhanced salt solubility, bulk-ionic conductivity, and $Li^+$ transport compared to an analogous ether functionalized polythiophene due to the ability of the cationic imidazolium side chain to facilitate salt dissociation without impeding transport to the same degree as the ether substituents.[14] Unlike design rules for traditional polymer electrolytes, however, the rational design of mixed conducting polymers also requires the maintenance of electronic transport pathways via pi-pi stacking of the conjugated backbones.

Here, we demonstrate a series of cationic functionalized polythiophenes, where the cation group size and charge localization plays a strong role in electronic and ionic conductivity as well as lithium selective transport. The more diffusely charged substituent most effectively balances these requirements, resulting in the best overall performance. We synthesize three cationic conjugated polyelectrolytes consisting of poly(3-(6'-(N-methylimidazolium)hexyl)thiophene $TFSI^-$) (P3HT-$Im^+TFSI^-$), poly(3-(6'-trimethylammonium)hexyl)thiophene $TFSI^-$) (P3HT-$TMA^+TFSI^-$), and poly(3-(6'-ammonium)hexyl)thiophene $TFSI^-$) (P3HT-$NH_3^+TFSI^-$) based on a poly(3-(6'-bromohexyl)thiophene) synthetic platform designed to enable consistent molecular weights and high regioregularity *via* Grignard metathesis (GRIM) polymerization.[133] Post polymerization functionalization of the uniform poly(3-(6'-bromohexyl)thiophene allows us to isolate the effects of the cationic side chains on CPE performance (Figure 3.1). Thorough characterization reveals high ionic conductivity and salt solubility in all three systems compared to the widely investigated alkyl and ether substituted polythiophenes. The

imidazolium system achieves the highest ionic, electronic, and lithium conductivity, suggesting that diffuse charges on planar side chains are advantageous.

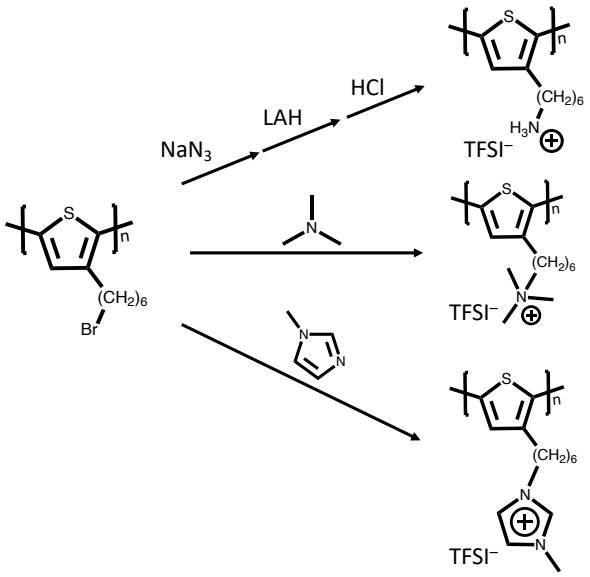


**Figure 3.1: Overview of the synthetic strategy for generating a family of cationic conjugated polyelectrolytes.**

By first performing a GRIM polymerization to form poly(3-(6'-bromohexyl)thiophene), regioregular CPEs of uniform molecular weight can be prepared via post-polymerization functionalizations.

## 3.3 Experimental Methods

### Polymer Synthesis

Synthesis of P3HT-Im$^+$TFSI$^-$, P3HT-TMA$^+$TFSI$^-$, and P3HT-NH$_3^+$TFSI$^-$ were performed using modified literature procedures.[14,133,134] Poly(3-(6'-bromohexyl)thiophene) (P3BrHT) was first polymerized, and then post-polymerization functionalizations were performed to obtain the desired cationic thiophene derivatives. All reagents were sourced from Sigma-Aldrich unless otherwise stated. ACS grade solvents were sourced from Fisher Scientific. Isopropylmagnesium chloride was purchased as a 1.3M soliton in THF. 2,5-dibromo-3-(6-

bromohexyl)thiophene was purchased from eNovation Chemicals. Detailed description of reaction conditions and material characterization can be found in Appendix 3.6.

**Ionic Conductivity**

Ionic conductivity samples were prepared by first dissolving the appropriate amount of polymer in 50/50 methanol/acetonitrile for P3HT-$Im^+TFSI^-$ and P3HT-$TMA^+TFSI^-$. It was found that 80/20 methanol/water was ideal for P3HT-$NH_3^+TFSI^-$. LiTFSI/methanol solution was added to achieve the desired salt concentrations and solutions were thoroughly mixed. The polymer/salt solution was then drop cast onto clean circular indium tin oxide (ITO) substrates top-coated with a 150 μm Kapton spacer in which a well of known diameter was punched. The samples were sealed with clean ITO substrates and dried under high vacuum ($2 \times 10^{-8}$ torr) at 115°C for 12 hours. Samples were then loaded into an argon glovebox and loaded into a Controlled Environment Sample Holder (CESH) from Biologic LLC, which maintains an inert atmosphere during measurement. Variable temperature conductivity measurements were performed using Biologic's Intermediate Temperature System (ITS) in conjunction with their VSP-300 potentiostat. A sinusoidal voltage with amplitude 100 mV was applied in the frequency range of 0.1 Hz-3 MHz. Data was then fit to the equivalent circuit shown in Figure 3.13 to extract the resistance. From these equivalent DC resistances, conductivity was calculated according to the following.

$$\sigma = \frac{1}{R}\frac{t}{A}$$

Where $t$ is the thickness of the polymer film and $A$ is the area, both of which are defined by the Kapton spacer.

**NMR Relaxometry**

$T_{1,\rho}$ Relaxometry measurements were performed on a 300 MHz Bruker Avance III super-wide-bore spectrometer with replaceable radio-frequency inserts for $^{7}$Li and $^{19}$F. A spin-locking frequency of 10 kHz was used in order to probe ion dynamics on a similar timescale (0.1 ms) as ionic conductivity measurements, and to quantify the distribution of ions amongst the different local environments present in the polymer electrolytes of interest. Polymer/LiTFSI mixtures were prepared in the same manner described for ionic conductivity measurements. Here, an LiTFSI concentration of r=1 was used, where r is the molar ratio of LiTFSI to cationic side chain. This corresponds to the highest LiTFSI concentration analyzed via AC Impedance, and was selected as high concentrations are needed for the $T_{1,\rho}$ measurement for sufficient signal to noise. Once the polymer/LiTFSI solutions were prepared, samples were drop cast into a custom made quartz trough to facilitate thorough drying ($2 \times 10^{-8}$ torr at 115°C for 12 hours) prior to loading the sample into the NMR tube, which was hermetically sealed inside an Argon filled glovebox. Further detail on fitting and experimental conditions can be found in Appendix 3.6.

**DC Polarization**

Polymer/LiTFSI mixtures were prepared as previously described. An LiTFSI loading of r=1 was used, consistent with the $T_{1,\rho}$ Relaxometry experiments. Symmetric lithium−polymer−lithium cells were assembled in an argon glovebox utilizing a Controlled Environment Sample Holder (CESH) from Biologic LLC and tested using their Intermediate Temperature System (ITS) in conjunction with their VSP-300 potentiostat at a temperature of 80°C. After assembly, samples were allowed to rest overnight, then heated to 80°C and

equilibrated until the interfacial resistance, monitored via EIS, stabilized. Next, a 100 mV potential bias was applied and the resulting current measured over time. Lithium transference numbers were calculated following the method of Bruce and Vincent:[68]

$$t_{Li+} = \frac{I_{ss}(\Delta V - I_{\Omega}R_0)}{I_{\Omega}(\Delta V - I_{ss}R_{\mathrm{ss}})}$$

Here, $\Delta V$ is the applied potential (100 mV), $R_0$ and $R_{ss}$ are the initial and steady-state interfacial resistances, respectively, $I_{ss}$ is the steady- state current, and $I_{\Omega}$ is the initial current determined from Ohm's law:

$$I_{\Omega} = \frac{\Delta V}{R_{\Omega}}$$

$R_{\Omega}$ is the initial cell resistance (bulk and interfacial) measured by EIS. Using $I_{\Omega}$, rather than the initial current measured by the instrument, improves accuracy by reducing errors associated with the speed at which the instrument can record the current.

**Electronic Conductivity**

Electronic conductivity was measured using custom made gold digits on a thermal oxide silicon substrate. Samples were spun cast from methanol/acetonitrile or methanol/water solutions as previously described. Samples were cast from 10 mg/mL polymer solutions at 750 rpm, then dried/annealed under high vacuum ($2 \times 10^{-8}$ torr) at 115°C for 12 hours. Film thickness was c.a. 200 nm, as determined by ellipsometry. Vapor doping with HTFSI was performed in a sealed vessel on a hot plate inside a nitrogen filled glovebox. Pristine films were attached to the lid of a jar containing HTFSI crystals using double sided Kapton tape. The jar was sealed and placed on the hot plate to be heated for the desired temperature and duration. Doping was performed at 50°C for 15 min, 45 min, 75 min, and 17 hours. DC

conductivity measurements were performed by applying DC potentials between -500 mV and 500 mV at 50 mV intervals. Figure 3.17 shows exemplary Current vs Voltage profiles for each polymer, from which resistance was determined. Once resistance was determined, conductivity was found using the following equation.

$$\sigma = \frac{1}{R}\frac{d}{lh}$$

Here $\sigma$ is the conductivity, $R$ is the resistance, $d$ is the distance between the gold digits, $l$ is the length of each digit, and $h$ is the polymer film thickness. Here, $l$=2.7 mm and $d$ was 100 μm, 150 μm, and 200 μm, as the substrate utilized several groups of digits at these 3 spacings, of which the average results are reported.

**UV-Vis Absorbance Spectroscopy**

Samples were spun cast on to 0.5 mm thick quartz substrates in the same manner described for electronic conductivity. UV−Vis absorbance spectroscopy was performed on an Agilent Cary 60 UV−Vis Spectrophotometer.

## 3.4 Results and Discussion

The goal of this study is to understand the role of side chain architecture and interaction strength on ionic conductivity, lithium transference, and electronic conductivity in mixed conducting polymers. Cationic polyelectrolytes can promote lithium mobility through preferential interaction with the anion. However, these interactions can also drive clustering or limit overall mobility depending on charge strength and localization. Additionally, the size and architecture of the side chain functional group will have a strong influence on polymer ordering and electronic transport. We synthesize and characterize a family of polythiophene derivates

functionalized with varying cationic groups, namely imidazolium (-$Im^+$), trimethylammonium (-$TMA^+$), and ammonium (-$NH_3^+$). Utilizing a post-polymerization functionalization provides structural consistency, removing any influence of linker chemistry, side chain length, molecular weight, or backbone rigidity. Through this model system, we show that all CPEs display appreciable bulk ionic conductivity, but stronger cationic charges limit lithium specific mobility. Ion specific NMR relaxometry shows that both the anion and $Li^+$ have strong local confinement in the -$NH_3^+$ and –$TMA^+$ systems. This result, in conjunction with the bulk ionic conductivity data, suggests that in the CPEs with less diffuse charges, a substantial portion of the ions exist in charged clusters, reducing the amount of freely mobile lithium. The diffuse charge of imidazolium promotes a more labile ionic environment, with appreciable $Li^+$ mobility. Furthermore, it is that found the aromatic structure of the imidazolium group is favorable for electronic transport. All polymers undergo similar optical transitions upon electronic doping, but P3HT-$Im^+TFSI^-$ displays an electronic conductivity over an order of magnitude higher than the -$TMA^+$ and -$NH_3^+$ derivatives, suggesting enhanced mobility in the imidazolium system. These results demonstrate the complexity that exists when developing structure-property relationships for mixed lithium-electron conduction, and ultimately concludes that diffuse, aromatic cationic side chains are advantageous for optimizing both properties.

All three polymer systems achieve promising bulk ionic conduction (Figure 3.2), demonstrating the ability of cationic side chains to solvate and transport added salt, while simultaneously highlighting the importance of side chain chemistry in facilitating ion transport. Looking at the neat (r=0) ionic conductivity indicates the relative interaction strength between

each cationic side chain and the $TFSI^-$ counterion. P3HT-$Im^+TFSI^-$ has the highest neat conductivity, indicating weaker interactions and a more diffuse charge compared to P3HT-$TMA^+TFSI^-$ and P3HT-$NH_3^+TFSI^-$. This trend holds for the $T_g$ normalized data, which accounts for contributions due to chain dynamics (Figure 3.14). Ultimately, the same relative trend holds for the maximum conductivity values achieved upon salt addition (Figure 3.2a), suggesting that strong polymer-anion interactions inhibit ion transport in the P3HT-$TMA^+TFSI^-$ and P3HT-$NH_3^+TFSI^-$ systems. Further, by studying ionic conductivity across a broad range of LiTFSI salt loadings, we find the diffuse imidazolium side chains have superior solvation capability compared to trimethylammonium side chains, as P3HT-$TMA^+TFSI^-$ experiences a sharp decline in conductivity beyond r=0.6. A peak and subsequent decline in conductivity at high salt concentrations stems from competing effects between increased charge carriers and decreased ion mobility via ion-ion and ion-polymer interactions.[29]

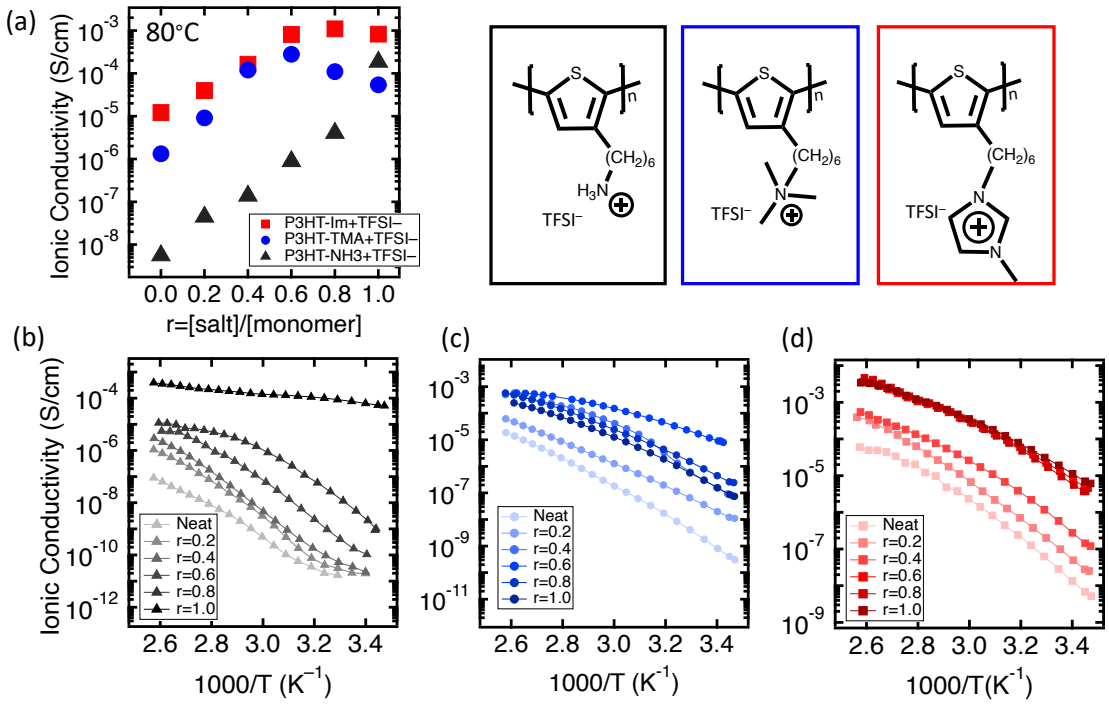


**Figure 3.2: Ionic conductivity as a function of LiTFSI concentration and temperature**

Data for P3HT-$NH_3^+$TFSI$^-$ (b, black), P3HT-$TMA^+$TFSI$^-$ (c, blue), and P3HT-$Im^+$TFSI$^-$ (d, red). (a) Shows conductivity values for all polymers as a function of added salt at 80°C. The diffuse imidazolium affords higher ionic conductivities in the neat polymer system and upon addition of LiTFSI at all salt loadings ranging from r=0.2 to r=1.0, where r is defined as the molar ratio of LiTFSI to cationic side chain.

Interestingly, P3HT-$NH_3^+$TFSI$^-$ does not experience a similar decline in ionic conductivity beyond r=0.6. This is likely due to the protic nature of the -$NH_3^+$ functional group, enabling contributions of $H^+$ to the total ionic conductivity. Unlike the $Li^+$ and TFSI$^-$ ions, proton conduction can occur via both vehicular transport and proton-hopping, which is not inherently coupled to chain dynamics or charge localization, but rather to the density of the hydrogen bonding network.[135] Thus, as the ionic environment becomes more dense at high salt loadings, $Li^+$ mobility may decline due to clustering and proton hopping may contribute more substantially to the overall conductivity.

$^{7}$Li and $^{19}$F nuclear magnetic resonance (NMR) relaxation measurements (Figure 3.3) reveal greater local confinement of both the $Li^+$ and $TFSI^-$ ions in P3HT-$TMA^+TFSI^-$ and P3HT-$NH_3^+TFSI^-$ compared to P3HT-$Im^+TFSI^-$, confirming the importance of the diffuse nature of the pendant cation in governing ion dynamics. NMR spin-lattice relaxation time measurements in the rotating frame of reference ($T_{1\rho}$) measure the decay of magnetization along the radio frequency field ($B_1$) as dictated by the spin-lock frequency ($\omega_1$), rather than along the main magnetic field ($B_0$), enabling ion dynamics to be probed across longer timescales. Here, we use a spin-lock frequency of 10 kHz with measurements taken on the timescale of $10^{-4}$ $s^{-1}$ (compared to $10^{-9}$ $s^{-1}$ for traditional $T_1$ measurements), allowing us to probe ion dynamics on the same approximate time and length scales as EIS measurements. The temperature dependence of $T_{1\rho}$ provides important insight into ion-specific dynamics (i.e. $^{7}$Li for $Li^+$ and $^{19}$F for $TFSI^-$), as the tumbling rate of the nucleus under consideration (i.e. its correlation time ($\tau_c$)) depends on both temperature (T) and mobility within its surrounding environment. The minimum in the $T_{1\rho}$ vs. T curve of a given nucleus occurs when its tumbling rate is equal to the inverse of the spin-lock frequency $\omega_1$ ($\omega_1\tau_c \sim 1$). As the correlation time $\tau_c$ increases (or decreases) away from this value, relaxation becomes less efficient and $T_{1\rho}$ increases. The temperature dependence of $\tau_c$ leads to two behavioral regimes for $T_{1\rho}$: a short correlation time (high temperature or fast diffusion) regime where $T_{1\rho}$ increases with increasing temperature, and a long correlation time (low temperature or slow diffusion) regime where $T_{1\rho}$ decreases with increasing temperature.

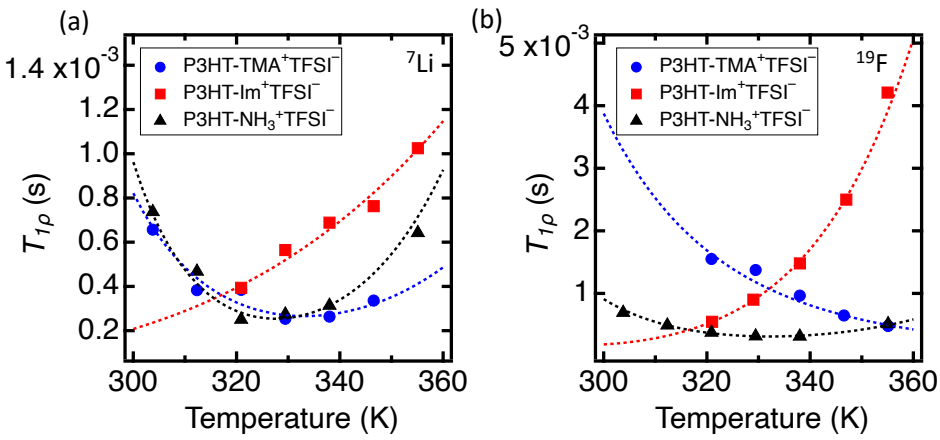


**Figure 3.3: $T_{1\rho}$ relaxation times**

Relaxation times are shown for all three polymers for $^{7}$Li (a) and $^{19}$F (b) species. Dotted lines represent fits of the experimental measurements to the Bloembergen, Purcell, and Pound (BPP) equation.[136]Both $^{7}$Li and $^{19}$F results for P3HT-Im$^{+}$TFSI$^{-}$ exhibit a temperature dependence indicative of the fast diffusion regime, whereas P3HT-TMA$^{+}$TFSI$^{-}$ and P3HT-NH$_3^{+}$TFSI$^{-}$ show both a slow and a fast regime or only a slow diffusion regime for Li$^{+}$ and TFSI$^{-}$ over the temperature range probed here.

For the P3HT-Im$^{+}$TFSI$^{-}$ electrolyte, both $^{19}$F and $^{7}$Li $T_{1\rho}$ values fall in the short correlation time regime, indicative of greater ion mobility. For P3HT-NH$_3^{+}$TFSI$^{-}$ and P3HT-TMA$^{+}$TFSI$^{-}$ both ions exist near their minimum or in the long correlation time regime, indicating more slowly diffusing Li$^{+}$ and TFSI$^{-}$ ions. Those results agree well with the EIS measurements indicating reduced ion mobility in these systems compared to P3HT-Im$^{+}$TFSI$^{-}$. Additionally, at temperatures above 340 K the longer $T_{1\rho}$ relaxation times for $^{7}$Li in P3HT-Im$^{+}$TFSI$^{-}$ compared to the other polymer systems suggests greater ion mobility, as faster ion tumbling leads to decreased energy transfer rates between the nucleus and its surrounding environment. In summary, the short correlation time behavior of both $^{19}$F and $^{7}$Li in P3HT-Im$^{+}$TFSI$^{-}$, coupled with the relatively long $T_{1\rho}$ relaxation times, reveal that both nuclei experience shorter interaction times with their local environment, implying less ionic confinement compared to P3HT-NH$_3^{+}$TFSI$^{-}$ and P3HT-TMA$^{+}$TFSI$^{-}$.

Lithium transference, $t_{Li+}$, measurements using the Bruce Vincent DC polarization method corroborate the qualitative insights gained from NMR relaxometry. These measurements show significantly enhanced lithium transport in P3HT-Im$^+$TFSI$^-$ ($t_{Li+}$ = 0.32) compared to P3HT-TMA$^+$TFSI$^-$ ($t_{Li+}$ = 0.05) and P3HT-NH$_3^+$TFSI$^-$ ($t_{Li+}$ = 0.04). Importantly, this technique measures the ionic current carried by free Li$^+$ ions, and does not account for the current carried by all other ionic charge carriers (e.g. counterions and ion clusters). The near-zero values for P3HT-NH$_3^+$TFSI$^-$ and P3HT-TMA$^+$TFSI$^-$ indicates very little Li$^+$ is able to freely migrate or diffuse, rather it is likely immobilized or exists in charged clusters, either of which would result in the long correlation, solid-like $T_{1\rho}$ measurements discussed in the previous paragraph. P3HT-Im$^+$TFSI$^-$ has a $t_{Li+}$ of 0.32, indicating that a reasonable fraction of the ionic current is carried by free Li$^+$, in line with the more labile ionic interactions afforded by the diffuse imidazolium ion. Notably, the transference number of 0.32 and ionic conductivity near 1 mS/cm of P3HT-Im$^+$TFSI$^-$ are state-of-the-art values with respect to all polymeric ion conductors, not just conjugated polymers, as these values sit on the upper-bound for the trade-off between cation selectivity and overall conductivity previously discussed.[35,61]

**Table 3.1:** Lithium transference data obtained from DC-polarization Bruce-Vincent measurements in a lithium symmetric cell at 80°C.

| | P3HT-Im$^+$TFSI$^-$ | P3HT-TMA$^+$TFSI$^-$ | P3HT-NH$_3^+$TFSI$^-$ |
|---|---|---|---|
| $t_{Li+}$ | 0.32 | 0.05 | 0.04 |

Interestingly, P3HT-Im$^+$TFSI$^-$ also achieves the highest electronic conductivity of the three polymer systems (Figure 3.4). This result is of considerable significance as mixed conducting polymer design rules typically suggest that ionic and electronic conductivity are inversely correlated, with ionic conduction increasing with chain dynamics, and electronic conduction

relying on an ordered conjugated polymer framework.[2–5,7,37] Here, the aromatic, planar structure of imidazolium can facilitate both dopant counterion inclusion and chain aggregation, which likely explains the superior electronic conductivity.

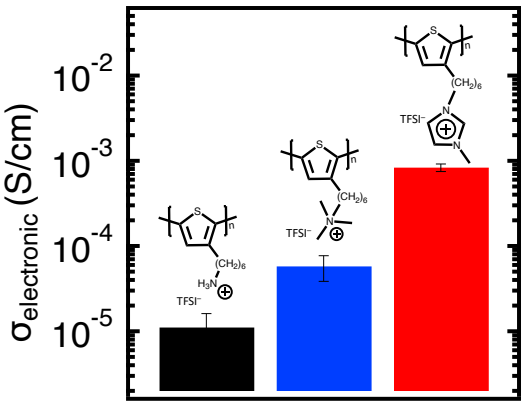


**Figure 3.4: Electronic conductivity**

Data obtained from thin films vapor doped with HTFSI. Various doping conditions were tested, and the maximum conductivity values for each system are reported here. Further details can be found in Figure 3.16.

In their neat state, all polymers are predominately disordered with no substantial crystallinity (Figure 3.18) or aggregation (Figure 3.5). Additionally, each system is similarly doped upon introduction of HTFSI, as evidenced by their consistent optical transitions (Figure 3.5). Here, all neat polymers display a single, featureless peak centered around 470 nm, indicating no appreciable inter- or intra-chain aggregates.[137] To induce electronic charge carriers, conjugated polymers must be doped. In the case of polythiophenes, electron density is removed from the highest occupied molecular orbital (HOMO), referred to as p-type doping.[138] Here, this is performed with the molecular dopant HTFSI. The change in electronic structure during doping has an expected optical transition, where a decrease in the neutral peak centered around 470 nm is accompanied by the appearance of a broad feature near 790 nm associated with polaronic

charge carriers.[80,88] Importantly, all three polymers undergo nearly identical transitions, indicating the backbones are similarly doped. This suggests the variation in electronic conductivity stems from structure and mobility rather than substantial differences in dopant concentration.

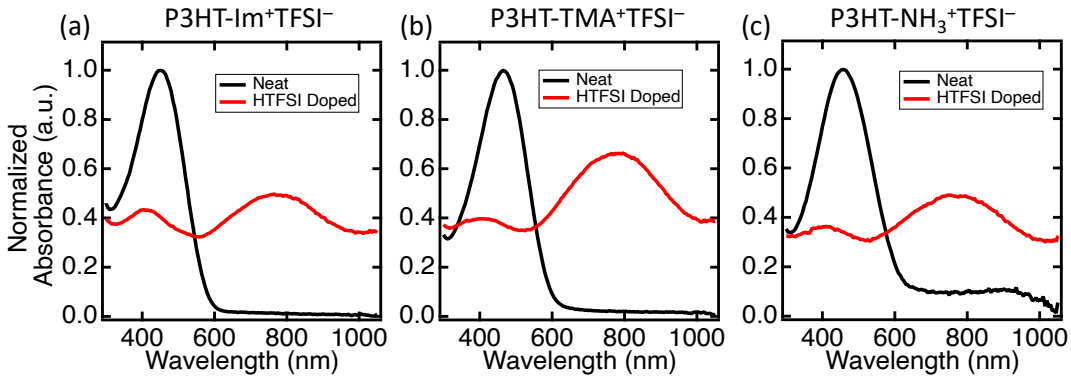


**Figure 3.5: UV-Vis spectra**

Data for P3HT-Im$^+$TFSI$^-$ (a), P3HT-TMA$^+$TFSI$^-$ (b), and P3HT-NH$_3^+$TFSI$^-$ (c). Black curves represent neat polymers, and red curves are HTFSI doped polymers.

While WAXS data for all systems is insufficient to indicate long-range order (Figure 3.18); aggregates can form from as few as two adjacent chains,[27] which could result in substantial mobility differences but would not be apparent from WAXS. From this, in conjunction with the similar observed doping levels and higher conductivity of P3HT-Im$^+$TFSI$^-$, we can infer that the aromaticity of the imidazolium group aids in aggregation or chain planarization, either of which promotes higher mobility and conductivity. This is in line with other reports of polythiophenes, including P3HT-Im$^+$TFSI$^-$, which are known to undergo major reorganization upon doping to incorporate counterions into the side chain region.[14,40,139,140] Additionally, in polymer systems where the electronic properties are consistent (i.e. identical thiophene backbones), large variations in conductivity have been attributed to the influence of side chain

structure on carrier mobility, specifically variations in steric repulsion altering the pi-stacking distance.[112] While -$NH_3^+$ and -$TMA^+$ are physically smaller pendants, the aromaticity of the imidazolium group provides the ability to $\pi^+$-$\pi^+$ stack. [141–143] In fact, this property plays an important role in stabilizing the structure of imidazolium-based ionic liquids,[141–143] and here likely facilitates a balance of order and counterion accommodation during doping.

## 3.5 Conclusions

In conclusion, we investigate a series of cation functionalized polythiophenes demonstrating the general applicability of cationic side chains for achieving high ion conduction in mixed conducting polymers. While all three polymers display appreciable ionic conductivity (~$10^{-4}$ S/cm at 80°C), the more diffuse imidazolium affords labile ionic interactions, resulting in higher lithium transference. $T_{1\rho}$ NMR relaxometry provides valuable insights into ion-specific dynamics on the same timescale as bulk ionic conductivity measurements *via* electrochemical impedance spectroscopy. These measurements show that both the $Li^+$ and $TFSI^-$ ions exist in a more mobile environment within P3HT-$Im^+TFSI^-$ when compared to P3HT-$NH_3^+TFSI^-$ and P3HT-$TMA^+TFSI^-$, further emphasizing the influence polymer-ion and ion-ion correlations can have on bulk transport properties. Furthermore, the superior electronic conductivity observed in P3HT-$Im^+TFSI^-$ aligns with the ability of this aromatic functional group to facilitate aggregation without impeding the inclusion of counterions. Importantly, this exemplifies a mixed ion-electron conduction design that simultaneously improves each property. These results not only support the utility of imidazolium as a functional group, but also provide a broader perspective for the rational design of mixed ion electron conducting polymers, showing that both structure of the side chain and strength of ionic interactions have large impacts on lithium transference and electronic conductivity.

**Acknowledgments**

We gratefully acknowledge support from U.S. Department of Energy, Office of Science, Basic Energy Sciences under Award DE-SC0016390. The research reported here made use of shared facilities of the UC Santa Barbara Materials Research Science and Engineering Center (MRSEC, NSF DMR 1720256), a member of the Materials Research Facilities Network (https://www.mrfn.org). A portion of this work was performed in the UC Santa Barbara Nanofabrication Facility, an open access laboratory. In addition, G.T.P. and P.H.N. gratefully acknowledges support from the National Science Foundation Graduate Research Fellowship Program under Grant No. 1650114 and Grant No. 2139319, respectively.

## 3.6 Appendix

**Synthesis**

***Polymerization***

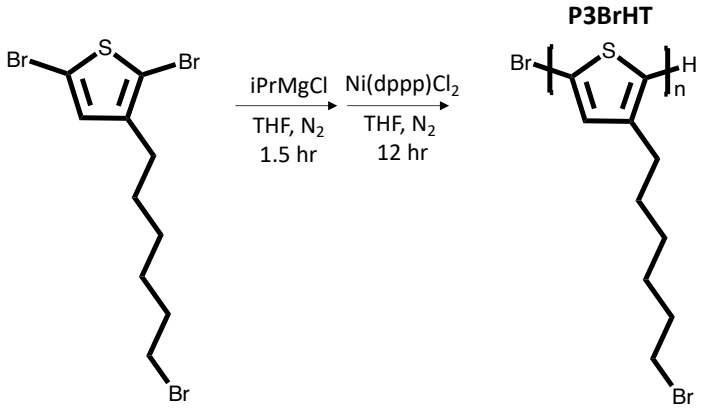


**Figure 3.6 Synthesis of P3BrHT**

**Poly(3-(6'-bromohexyl)thiophene) (P3BrHT)**

1 eq of 2,5 dibromo-3-(6-bromohexyl)thiophene was added to an oven-dried Schlenk flask, which was placed under vacuum for 2 hours. Dry, degassed THF was added via syringe and

the mixture was sparged with Nitrogen. Isopropylmagnesium chloride (1.01 eq) was added dropwise and the mixture was stirred for 1.5 hr at ambient temperature under Nitrogen. 0.01 eq. of Ni(dppp)$Cl_2$ was added via syringe. The polymerization was stirred for 12 hr then quenched by rapid addition of 1M HCl and precipitated into methanol. The polymer was purified by washing in a Soxhlet apparatus with methanol and acetone before extraction with THF. The product was concentrated under vacuum.

$^1$H NMR (600 MHz, CDCl3) δ 7.18 − 6.92 (s, 1H), 3.53 − 3.37 (m, 2H), 2.93 − 2.55 (m, 2H), 2.04 − 1.81 (m, 2H), 1.80 − 1.58 (m, 2H), 1.57 − 1.30 (m, 4H)

Gel permeation chromatography was performed on a Waters e2695 equipped with THF as the mobile phase. Results are quantified using a polystyrene standard calibrant.*:* ***P3BrHT*–:** Mn = 16 kDa , Mw= 20 kDa, Đ = 1.3

***Post Polymerization Functionalizations***

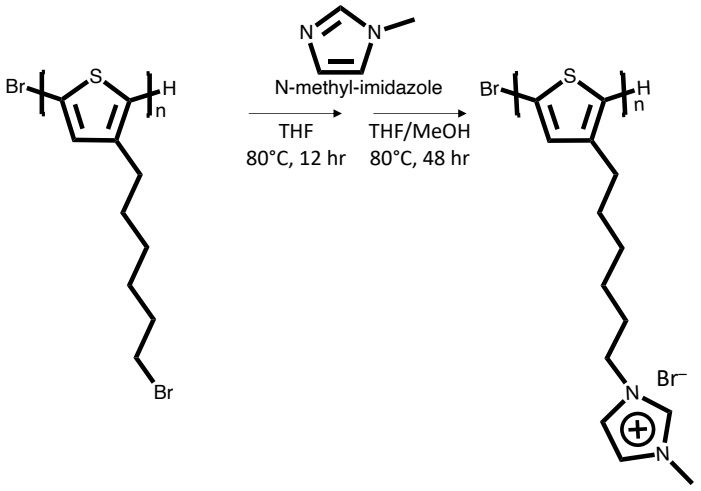


**Figure 3.7: Post-polymerization functionalization to form P3HT-Im$^+$Br$^-$**

**Poly(3-(6'-(N-methylimidazolium)hexyl)thiophene)**

The P3BrHT polymer was post-functionalized through an amine quaternization reaction. The polymer was first dissolved in THF. 1-methylimidazole (10 eq.) was added to the solution in ambient conditions. The solution was then stirred for 12 h under reflux. After 12 h, some polymer precipitate was observed in the flask. A small amount of methanol was added to fully dissolve the resulting polymer and the solution was stirred for an additional 24 hours to achieve quantitative conversion. The polymer was then dialyzed using a 10 kDa cutoff dialysis membrane against a mixture of methanol and THF, with the dialysate replaced every 12 h. The resulting polymer was then mixed with 10 molar equivalents of LiTFSI and stirred at 50°C in methanol and acetonitrile followed by dialysis in a 50:50 mixture of methanol and acetonitrile, with the dialysate replaced every 12 h.

$^1$H NMR (600 MHz, CD3CN) δ 8.50 (s, 1H), 7.39-7.34 (m, 2H), 7.18 (s, 1H), 4.14 (m, 2H), 3.83 (s, 3H), 2.85 (m, 2H), 1.87 (m, 2H), 1.71 (m, 2H), 1.48 (m, 2H), 1.39 (m, 2H)

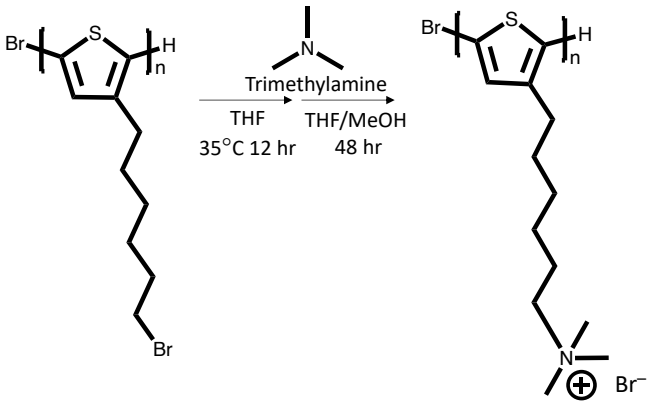


**Figure 3.8: Post-polymerization functionalization to form P3HT-TMA$^+$Br$^-$**

**Poly(3-(6'-trimethylammonium)hexyl)thiophene)**

The P3BrHT polymer was post-functionalized through an amine quaternization reaction. The polymer was first dissolved in THF. Trimethylamine (10 eq.) was added to the solution in

ambient conditions. The solution was then stirred for 12 h at 35°C. After 12 h, some polymer precipitate was observed in the flask. Methanol was added to fully dissolve the resulting polymer, and an additional 2 eq of trimethylamine was added. The solution was stirred for an additional 24 hours, then the temperature was increase to 80°C and the system was refluxed for an additional 24 hours. The polymer was then dialyzed using a 10 kDa cutoff dialysis membrane against a mixture of methanol and THF, with the dialysate replaced every 12 h. The resulting polymer was then mixed with 10 molar equivalents of LiTFSI and stirred at 50°C in methanol and acetonitrile followed by dialysis in a 50:50 mixture of methanol and acetonitrile, with the dialysate replaced every 12 h.

$^1$H NMR (600 MHz, $CD_3OD$) δ 7.18 (s, 1H), 3.35 (m, 2H), 3.12 (s, 9H), 2.85 (m, 2H), 1.87 (m, 2H), 1.71 (m, 2H), 1.48 (m, 2H), 1.39 (m, 2H)

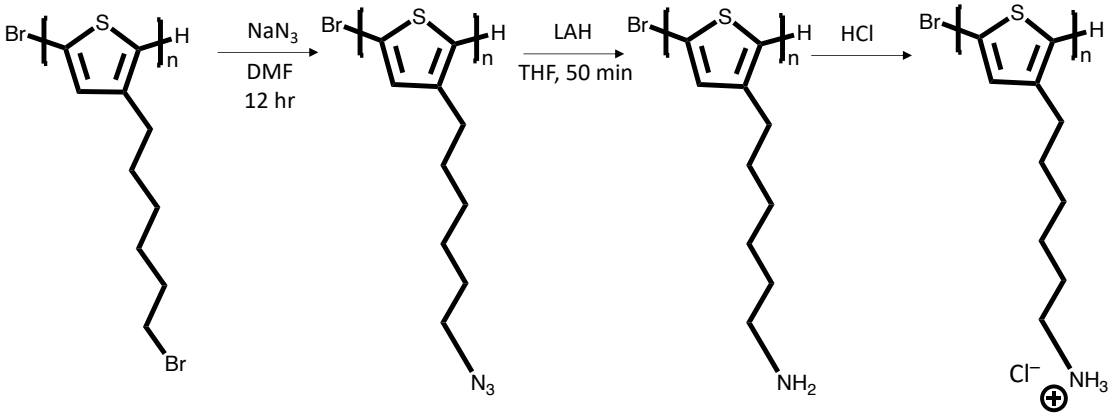


**Figure 3.9: Post-polymerization functionalization to form P3HT-$NH_3^+Cl^-$**

**Poly(3-(6'-azido)hexyl)thiophene)**

A solution of P3BrHT and 10 eq. of sodium azide in DMF was refluxed overnight. After the reaction, the solution was slowly quenched in methanol, precipitating the polymer. The solid

polymer was collected via filtration and washed with methanol using a Soxhlet extractor. FT IR spectrum indicates that bromine was completely substituted with the azide functional group (Figure 3.10).

$^1$H NMR (600 MHz, $CDCl_3$) δ 7.18 − 6.92 (s, 1H), 3.4 (m, 2H), 2.93 − 2.55 (m, 2H), 2.04 − 1.81 (m, 2H), 1.80 − 1.58 (m, 2H), 1.57 − 1.30 (m, 4H)

**Poly(3-(6'-ammonium)hexyl)thiophene)**

Poly(3-(6'-azido)hexyl)thiophene) in dried THF was stirred at 0 °C under nitrogen. Lithium aluminum hydride in THF solution (2 ml, 5 eq) was slowly injected into the solution via a syringe. After the solution was stirred for 50 min, the solution was quenched in a 1M HCl aqueous solution. The precipitate was filtered and dried under vacuum. The primary amine peak at 3348 $cm^{-1}$ in FT IR was observed to confirm substitution of the azide group. The amine-functionalized polymers were then dialyzed using 10 kDa cutoff dialysis membranes against a methanol and 2 ml 1M HCl (aq), with the dialysate replaced every 12 h. To perform ion exchange, the resulting polymer was then mixed with 10 molar equivalents of LiTFSI and dialyzed in 50% methanol and 50% deionized water with the dialysate replaced every 12 h.

$^1$H NMR (600 MHz, $CD_3OD$) δ 7.2 (s, 1H), 3.0 − 2.25 (m, 4H), 1.75 − 1.6 (m, 4H), 1.48 − 1.29 (m, 4H).

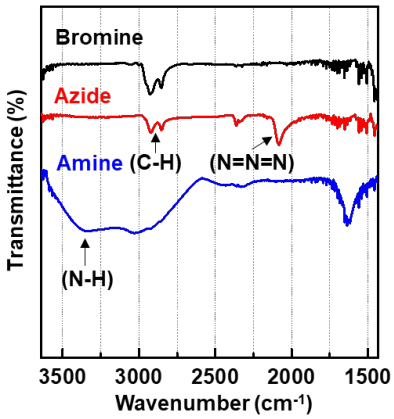


**Figure 3.10: FT IR spectra**

Spectra of poly(3-(6-bromohexyl) thiophene) and poly(3-(6-azidohexyl) thiophene), and poly(3-(6-aminohexyl) thiophene) to confirm the complete conversion to the $NH_3^+$ functional group.

## Conductivity

Electrochemical Impedance Spectroscopy (EIS, also referred to as AC Impedance) is a common technique to measure polymeric ionic conductivity. In short, EIS applies a sinusoidal voltage, sweeping across frequencies at a set potential amplitude. Using well-established methods, geometric features of the resulting Nyquist Plots are fit to equivalent circuits to calculate the equivalent DC conductivity. EIS can also be used to measure electronic conductivity, but in practice DC techniques are more common. As described in the main text, the most common methods for introducing ionic and electronic charge carriers are quite different. Ionic charge carriers are added by homogenously mixing the polymer with the desired salt in a known ratio, then casting the polymer in a predefined well of known geometry such that the cell constant can be determined (Figure 3.12). Electronic dopants are often introduced via vapor phase infiltration of molecular dopants (HTFSI in this work), which requires thin polymer films. Here, substrates with predefined gold digits of known length and

spacing are used to determine the geometric constant, and neat polymer films are spun cast onto these substrates (Figure 3.11).

Additionally, ionic and electronic transport typically occur on very different timescales. Some works report measuring "co-doped" samples via EIS,[14,15] however this relies on an appropriate relative mobility of electronic and ionic charge carriers. In co-doped systems, ionic conductivity can be measured via AC impedance so long as ionic transport is fast relative to electronic transport. When this is the case, two distinct semicircles will appear in the Nyquist plot.[14,65] These features arise from electronic resistance and geometric capacitance in parallel at low frequencies, and ionic resistance and geometric capacitance at higher frequencies. Here, interfacial capacitance is shunted by electronic current at low frequencies, meaning there is no capacitive tail, unlike the Nyquist plot for pure ion conducting polymers (Figure 3.13).[65] If electronic transport is fast relative ionic transport, there will be no blocking of charge transport and therefore no interfacial capacitance.[65] This will result in a Nyquist plot with a single semicircle, resembling a pure electron conductor, even though the polymer may have ionic conductivity of an appreciable value. In other words, ionic conductivity cannot be determined due to the dominant signal from electronic transport. The latter case is the more common scenario, as even state-of-the-art ion conducting polymers have room temperature conductivity on the order of $10^{-5}$-$10^{-4}$ S/cm, much lower than even poor electron conductors. Finally, ionic conductivity is typically measured across elevated temperatures, where electronic dopants often thermally de-dope. In sum, ionic and electronic transport are measured independently due to a variety of reasons — distinct sample geometries required for dopant addition, dramatically different time scales of charge transport, and thermal de-doping constraints.

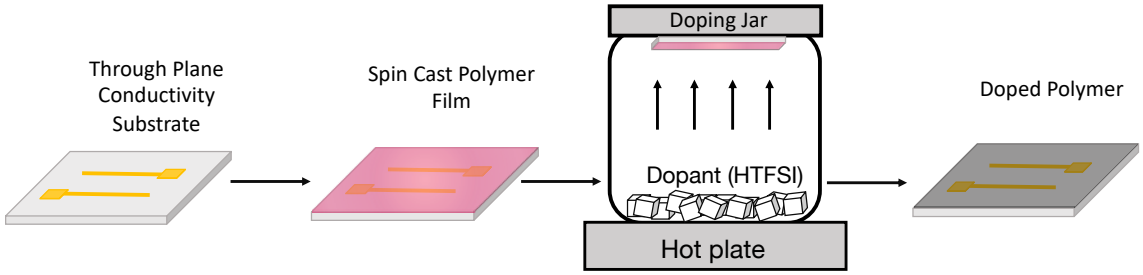


**Figure 3.11: A schematic of the process to prepare electronic conductivity samples**

Polymers are spun cast onto custom made substrates with gold digits, dried and annealed under vacuum, then doped via vapor phase infiltration of HTFSI. The resistance of doped polymer films is then measured using a probe station to make contact with the gold digits in order to apply a series of DC potentials across the through plane geometry, as described in the methods section of the main text.

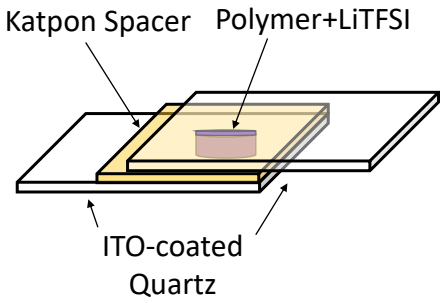


**Figure 3.12: A schematic of the sample geometry used for AC Impedance to determine ionic conductivity**

ITO-coated quartz slides are used as ion blocking electrodes. A Kapton well is used to hold the polymer sample in a well-defined geometry.

### *Ionic conductivity*

Using the form factor described in Figure 3.12, AC impedance is performed on polymers with LiTFSI concentrations between r=0 and 1, as outlined in the main text. A representative Nyquist plot indicative of predominately ionic transport through the polymer is shown in Figure 3.13. This is then fit to the equivalent circuit shown in Figure 3.13, which provides the ionic resistance.

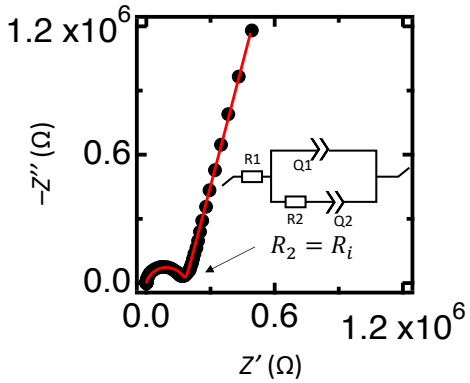


**Figure 3.13: Representative Nyquist plot for ion conducting polymers between two symmetric blocking electrodes**

Data is from P3HT-Im+TFSI– with r=1.0 LiTFSI

These measurements were performed across a series of temperatures ranging from 10°C to 110°C to inform the contribution of chain dynamics above $T_g$ to overall conductivity. This is particularly useful for the neat samples, where the only ionic charge carrier is the side chain's charge compensating anion, as this indicates the polymer-anion interaction strength. Figure 3.14 presents the $T_g$ normalized data for the neat polymers, using the Vogel-Fulcher-Tamman (VFT) formalism where $T_0$ is taken to be 50°C below $T_g$.[120,121]

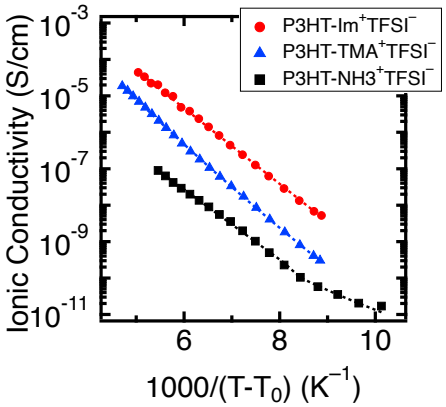


**Figure 3.14: Neat, $T_g$ correct ionic conductivity**

Conductivity at temperatures above $T_g$ were fit to the VFT equation, where $T_0$ is the Vogel temperature and taken to be 50°C below $T_g$.

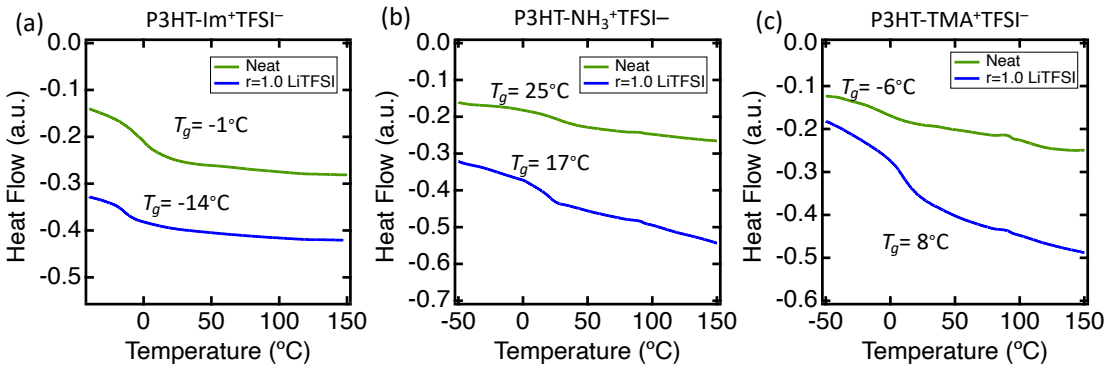


**Figure 3.15: Glass transition temperature ($T_g$) measurements *via* dynamic scanning calorimetry (DSC)**

Data for (a) P3HT-Im$^+$TFSI$^-$, (b) P3HT-NH$_3^+$TFSI$^-$, and (c) P3HT-TMA$^+$TFSI$^-$. Polymer samples were drop cast into hermetic aluminum pans, sealed, and characterized with a TA DSC 2500 to measure $T_g$. Samples were initially heated to 150 °C, held for 5 min, then rapidly quenched in order to enhance the $T_g$ signal. Reported curves are on second heating at 20 °C min$^{-1}$. Curves have been shifted vertically for clarity. Small features that appear around 100°C are associated with a baseline issue with the instrument.

***Electronic conductivity***

The electronic conductivity of semiconducting polymers can vary dramatically with doping time. A wide range of doping durations were tested (Figure 3.16), with the maximum achieved electronic conductivity values for each polymer reported in the main text.

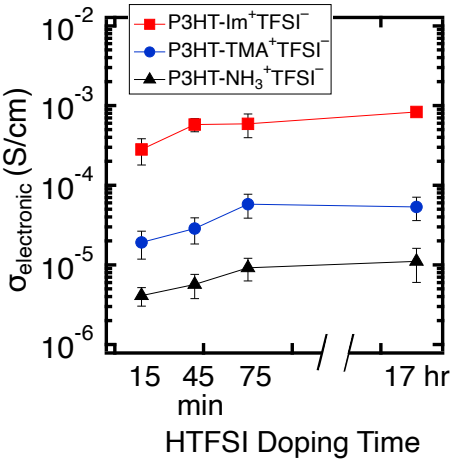


**Figure 3.16: Electronic conductivity vs HTFSI doping time**

Data for P3HT-Im$^+$TFSI$^-$ is shown with red squares, P3HT-TMA$^+$TFSI$^-$ with blue circles, and P3HT-NH$_3^+$TFSI$^-$ with black triangles.

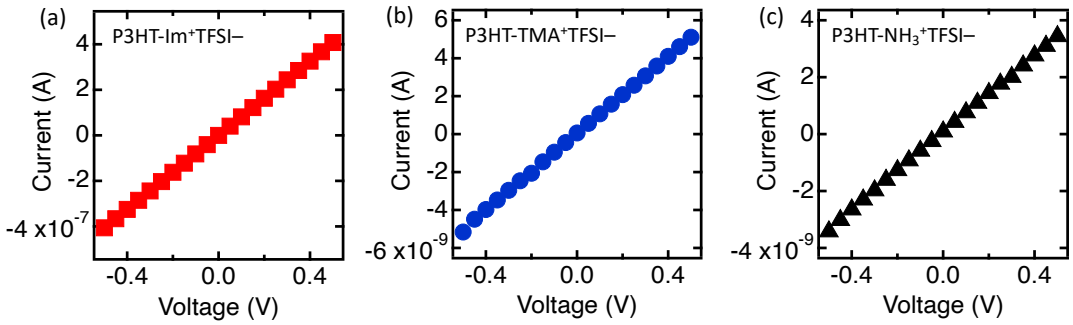


**Figure 3.17: Exemplary current vs voltage for DC electronic conductivity measurements**

Data for (a) P3HT-Im$^{+}$TFSI$^{-}$, (b) P3HT-TMA$^{+}$TFSI$^{-}$, and (c) P3HT-NH$_3^{+}$TFSI$^{-}$. All polymers display the expected linear trend.

### Wide Angle X-ray Scattering (WAXS*)*

Transmission mode WAXS was performed on a custom-designed X-ray scattering diffractometer equipped with a XENOCS Genix 50 W X-ray source (1.54 Å wavelength, 50 µm focus size) and a Dectris EIGER 1M detector. Wells were created using steel washers with a Kapton backing, into which samples were dropcast. Samples were then dried/annealed under high vacuum ($2 \times 10^{-8}$ torr) at 115°C for 12 hours. Samples were then loaded into an Argon filled glovebox. Pristine samples were sealed with another layer of Kapton and measured. Doped samples were loaded in to jars for vapor infiltration of HTFSI, overnight at 50°C. After doping, samples were sealed with Kapton and measured. All exposures were taken at a sample-to-detector distance of c.a. 157 mm with 20-minute exposure time. Calibration of sample-to-detector distance and beam center were done using a silver behenate calibrant. All scattering data reduction were performed using Nika, an Igor package.[144]

While P3HT-Im$^{+}$TFSI$^{-}$ does experience the most pronounced structural change after doping, the high $q$ peak is still too broad (indicative of a primarily disordered structure), to quantitatively fit peaks attributed to pi-stacking.

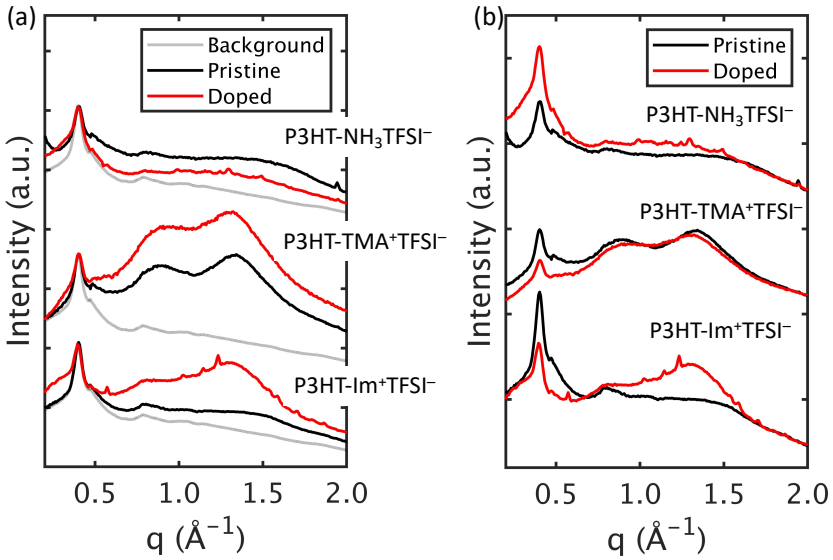


**Figure 3.18: WAXS profile for the neat and doped CPEs**

(a) Shows the data normalized to the Kapton peak, while (b) shows data normalized to the high $q$ region to more clearly emphasize any differences between pristine and doped samples.

### DC Polarization ($t_{Li+}$ measurement)

Lithium transference was measured at 80°C and at a LiTFSI concentration of r=1 in order to provide sufficient lithium current for reasonable signal to noise, as is common for this technique. The technique follows that of Bruce and Vincent,[68] as discussed in the main text and previously reported.[14,28,35]

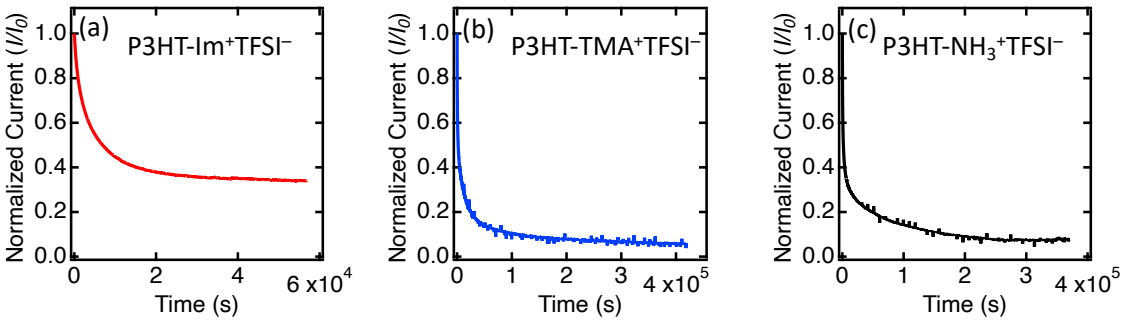


**Figure 3.19: Current decay for DC polarization**

Data for (a) P3HT-Im$^+$TFSI$^-$, (b) P3HT-TMA$^+$TFSI$^-$, (c) P3HT-NH$_3^+$TFSI$^-$.

### $T_{1,\rho}$ Relaxation Measurements

As mentioned in the main text, $T_{1,\rho}$ measurements enable the spin-locking frequency to be chosen such that specific time scales can be probed. Here, a spin-locking frequency of 10 kHz allowed ion dynamics to be analyzed on a similar timescale (0.1 ms) as ion conductivity measurements.

In the P3HT-Im$^+$TFSI$^-$ and P3HT-TMA$^+$TFSI$^-$ systems, the $^{19}$F $T_{1,\rho}$ relaxation curves are best fit using a single exponential (eq. S1) and a single stretched exponential (eq. S2), respectively, indicating a single TFSI$^-$ environment within the polymer electrolyte. On the other hand, the $T_{1,\rho}$ relaxation measurements for the P3HT-NH$_3^+$TFSI$^-$ systems are best fit using a bi-exponential (eq. S3), indicating two distinct environments for the TFSI$^-$ anion.

$$I(t) = I_0 \exp\left(\frac{-t}{T_{1\rho}}\right)$$

$$I(t) = I_0 \exp\left\{-\left(\frac{t}{T_{1\rho}}\right)^{\beta}\right\}$$

$$I(t) = I_{0,1} \exp\left\{-\frac{t}{T_{1\rho,1}}\right\} + I_{0,2} \exp\left\{\frac{t}{T_{1\rho,2}}\right\}$$

$^{7}$Li $T_{1,\rho}$ relaxation measurements for all three polymer systems are best fit using a bi-exponential curve, revealing two distinct $Li^{+}$ environments in all three polymer systems. Interestingly, the distribution of lithium between these two environments shows little dependency on polymer chemistry. In all three polymer systems the lithium is distributed with approximately ~95% of $Li^{+}$ existing in a faster relaxing regime (typically suggesting a confined ion environment with restricted mobility) and the remaining lithium existing in a significantly slower relaxing (i.e. longer $T_{1\rho}$ times) regime typical of more mobile ion species.

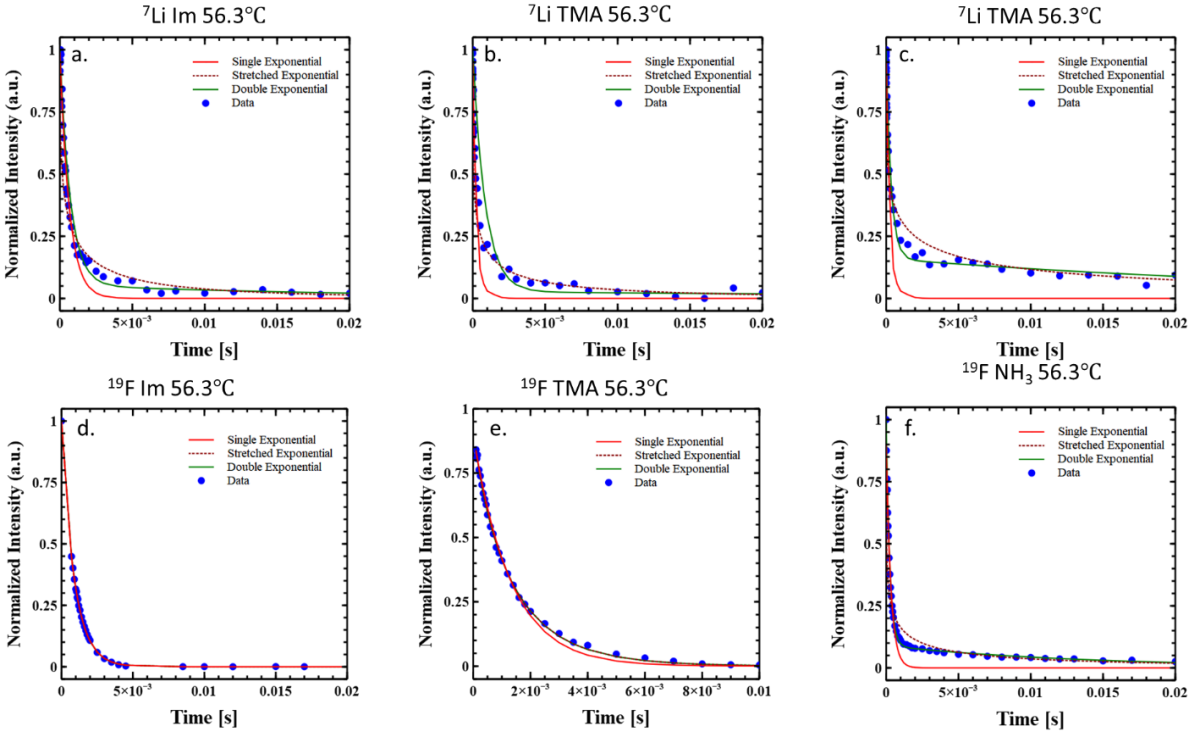


**Figure 3.20: Representative $T_{1\rho}$ exponential decay curves**

(a-c.) Shows data for $^{7}$Li and (d-f.) $^{19}$F nuclei in P3HT-Im$^{+}$TFSI$^{-}$ (a, d), P3HT-TMA$^{+}$TFSI$^{-}$ (b,e) and P3HT-$NH_3^{+}$TFSI$^{-}$ (c,f) at 56.3°C. Blue points represent the experimental data, solid red lines represent single exponential fits, dashed red lines represent stretch exponential fits, and solid blue lines represent bi-exponential fits.

$T_{1,\rho}$ vs. temperature data can be fit based on the resonant frequency of the nuclei and the spin-locking frequency using a modified version of the Bloomberg Parcel Pound equation[136] shown below.

$$\frac{1}{T_{1,\rho}} = R_{1,\rho} = k\left(\frac{3\tau_c}{1+4\omega_1^2\tau_c^2} + \frac{5\tau_c}{1+\omega_0^2\tau_c^2} + \frac{2\tau_c}{1+4\omega_0^2\tau_c^2}\right)$$

Here, $\omega_0$ is the Larmor Frequency (Hz) of the nucleus under study, $\omega_1$ is the spin-locking frequency, $k$ the fitting constant, and $\tau_c$ is the correlation time. The correlation time, $\tau_c$ can be expressed in the form of an Arrhenius-type expression, where $\tau_0$ is the correlation time at infinite temperature, $R$ is the gas constant, and $E_a$ is the activation energy.

$$\tau_c = \tau_0 \exp\left(-\frac{E_a}{RT}\right)$$

# Chapter 4

# A coacervate-based mixed-conducting binder for high power, high energy batteries

## 4.1 Abstract

Polymer binders add crucial structural integrity to lithium ion battery composite cathodes, but industry standard binders, such as polyvinylidene fluoride (PVDF), are insulating to ions and electrons, detrimentally adding resistance to the overall system. In this work, we use electrostatics to stabilize a blend of a charged conjugated polymer with an oppositely charged polyelectrolyte, providing a processable, stable binder with high ionic and electronic conduction. Using $LiFePO_4$ cathodes as a model system, we show significant improvement in rate capability and stability, with the conducting binder enabling a 39% utilization at 6C compared to 1.6% when PVDF is the binder. Additionally, the conducting binder affords a 63% capacity retention over 400 C/2 cycles, compared to only a 6% retention over 400 cycles when PVDF is the binder. These results show that electrostatically stabilized complexation is a promising strategy to integrate both electronic and ionic conductivity into a binder, while simultaneously maintaining stability and processability.

## 4.2 Introduction

Lithium ion battery demand is expected to continue to skyrocket as electric vehicles and large scale stationary storage become more widespread. In parallel, significant scientific barriers towards further enhancements in storage capacity and long-term stability must be addressed by improving the design of battery components (the anode, cathode, and electrolyte) and of the interfaces between them. Regardless of specific chemistry, the electrodes are generally a composite of the active material in polycrystalline powder form (80-90% of the total mass), carbon additives to enhance electronic conductivity, and a polymer binder (usually poly(vinylidene fluoride), PVDF) that is generally insulating and serves only to hold the electrode composite together. While the active materials govern the theoretical capacity and indeed largely influence overall cell performance, the resistive nature of most polymer binders has been shown to significantly limit performance, particularly at high rates.[16,40,72,126] Herein we demonstrate a new binder that conducts both ions and electrons, decreasing the resistance in the electrode while simultaneously maintaining electrochemical stability and compatibility with other cell components, resulting in improved rate capability and good cycle stability.

Often, improvements to power, energy and other figures of merit focus on engineering the active material, where crystal structure, intrinsic ionic and electronic conductivity, particle size, carbon coating, and other properties play large roles in the resulting cell performance. Furthermore, the cathode active material (CAM) is the primary cost driver in Li-ion batteries,[145,146] and thus much attention has been focused on engineering low cost CAMs that do not sacrifice performance. For example, two chemical classes currently dominate the Li-ion cathode market: layered transition metal oxides ($LiMO_2$, with M= Ni, Mn, Al, and/or Co,

typically abbreviated NMC and NCA) and phospho-olivines (LFP being the most widely used).[147–149] NMC and NCA cathodes promise high energy due to their high specific capacity and average voltage (>200 mAh/g and >3.6V vs Li/Li+).[147,150] However, they are burdened with substantial financial and ethical costs due to their reliance on cobalt and nickel.[146] LFP is an attractive alternative due to its inexpensive material composition and reasonable theoretical capacity of 170 mAh/g and redox potential (~3.5V vs Li/Li+).[147,151] While already in use, LFP suffers from low electronic conductivity and relatively poor Li-ion transport,[150] limiting its rate capability and practical power output. Many methods have been explored to address these limitations. A few examples include reducing LFP particle size to shorten the Li diffusion length[152–154] and carbon coatings to improve electronic conductivity.[151,155–158] However, smaller particles increase total surface area, which then requires more carbon additive and binder to maintain electronic conductivity and hold the smaller particles together, respectively.[159] This increased binder in turn limits performance due to the binder's resistive nature.

A key to enabling high rate capability in cobalt-free cathodes may not lie solely in active material engineering, but rather in modification of the previously-inactive polymer binder. An emerging class of organic polymers that conduct both ions and electrons, termed mixed ion-electron conductors (MIECs), significantly decrease the overall resistance of the electrode composite while still providing the structural integrity of traditional binders. Perhaps the most widely studied conducting binder is PEDOT:PSS (poly[3,4-ethylenedioxythiophene]:poly[styrenesulfonate]). This has been shown as a promising PDVF alternative in LFP cathodes, however is suffers from poor processability, as PEDOT:PSS is

used as a low concentration colloidal suspension in water, resulting in non-homogeneous mixing with cathode materials. In fact, when applied in cathodes, PEDOT:PSS is often used in conjugation with another polymer binder, such as carboxymethyl cellulose,[73,74] styrene-butadiene rubber,[73] and polyacrylic acid.[75]

Beyond PEDOT:PSS, multiple single component thiophene derivatives have shown adding electronic conductivity to the binder improves rate capability in composite cathodes, when compared to analogous cells prepared with a PVDF binder.[16,40,72] Mixed ion-electron conducting block copolymers have also shown some utility as binders for LFP cathodes, with success at low (dis)charge rates.[64,76,77] While these polymers improve overall performance, most are far better electronic conductors than ionic conductors. This observation is consistent with the fact that fast electronic and ionic conductivities require very different polymer designs. High ionic conductivity is generally associated with both a high dielectric constant and fast segmental motion, while high electrical conductivity generally requires aromaticity combined with a high degree of order.[36–38] Hybrid designs, for example incorporating ionically conductive sidechains on an electronically conductive backbone,[14,15,37–39] generally result in a tradeoff between ionic and electronic conduction.[40] In a practical sense, these hybrid materials face hurdles when applied as binders, as increasing the density of ionically conductive side chains drives dissolution in the polar battery electrolyte.[40]

Herein, we demonstrate a new polymer design strategy for mixed-conducting binders. The binder under consideration allows for dramatic improvements in the performance of composite cathodes, with the more challenging LFP chemistry used as an example. The binder is obtained

through electrostatic stabilization of a conjugated polymer (a polyelectrolyte) with an oppositely charged polyelectrolyte, compatibilizing the two polymers into a viscous gel the affords facile processing (Figure 4.7b). Electrostatic interactions between the positively and negatively charged polyelectrolytes serve as ionic crosslinks that impart mechanical strength and prevent dissolution of the complex in common battery electrolytes (Figure 4.8). Interestingly, complexation templates the conformation of the conjugated polymer, leading to a 3-order-of-magnitude improvement in the electronic conductivity of the system from 0.001 S/cm to 1 S/cm.[27] The resulting binder exhibits a unique combination of high ionic and electronic conductivity, compatibility with a standard electrolyte (1M $LiPF_6$ in 1:1 EC:DMC), and electrochemical stability, enabling a drop in system that improves the overall rate capability and energy density of the cathode.

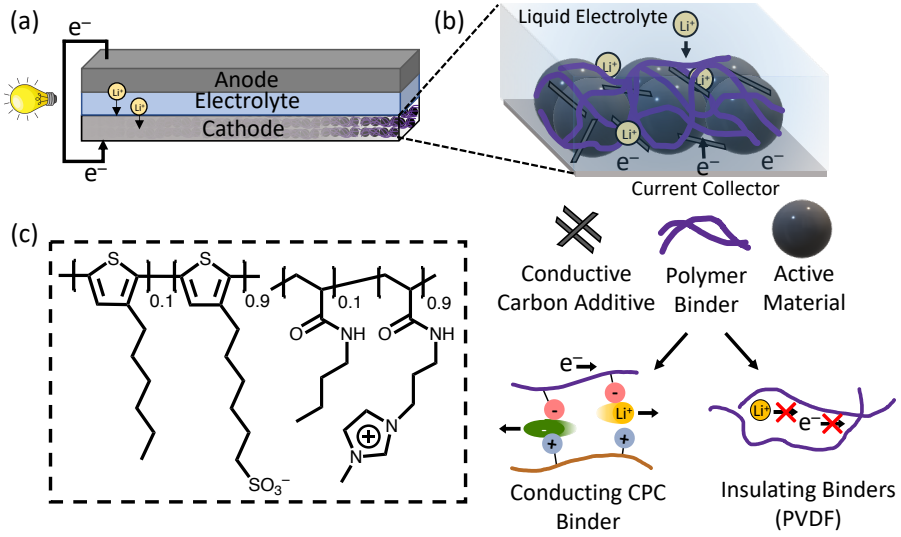


**Figure 4.1: A schematic of cathode composition and the application of the conducting binder**

(a) Conventional lithium ion batteries are composed of a composite anode, a composite cathode, and a separator soaked with a liquid electrolyte that allows the flow of ions while preventing the passage of electronic current. (b) Cathode composite composition and interactions: the crystalline active material (black spheres) is responsible for redox activity.

Conductive additives (black) improve electron transport, while a binder (purple) holds the active material + conductive additive system together. Current technologies use resistive plastics for the latter, such as PVDF. During the charge/discharge process, ion transport occurs between the electrodes via the electrolyte, requiring good ionic diffusion at the electrolyte/ active material interface, and electrons flow between the electrodes via the external circuit, requiring fast electron transport from the conductive additive to the current collector and vice versa. Resistive binders create barriers to the transport of both of these charged species, reducing overall performance. (c) Our polymer complex serves as a multifunctional binder, enabling ion and electron transport, as well as binding.

## 4.3 Experimental Methods

### *Polymer complexation*

Polymers were synthesized according to previously reported literature,[104,124,160,161] with details reported in the below in Appendix 4.6. The polymer complex was prepared according to our prior work.[26,161] Polymer concentrations of 1M in 40/60 THF/water were selected to ensure formation of a viscous coacervate (rather than precipitate).[26] Equimolar ratios of each polymer were add to a centrifuge tube, vortexed, then centrifuged for 10 min at 7,000 rpm. The resulting mixture consisted of a viscous coacervate, and a dilute supernatant phase- containing released counterions and dilute polymer. The supernatant was decanted, and the coacervate was thoroughly rinsed with the THF/water mixture. The mass that was removed was weighed in order to inform the remaining mass of polymer complex, which would later be used as the binder.

### *Ionic Conductivity*

Ionic conductivity was measured on bulk samples in a through plane configuration. First, isolated coacervates were thoroughly washed to remove all polymer counterions, as confirmed by the negligible ionic conductivity of the resulting system (Figure 4.11). Concentrated solutions of LiTFSI in water were then used to introduce a controlled amount of LiTFSI to the

system, which was vortexed and allowed to equilibrate for 2 days, after which the complexes appeared as a homogenous gel. The complex was then cast onto an aluminum current collector with a well-defined thickness provided by the use of a Kapton spacer. The sample was then dried at 110°C at $10^{-8}$ torr for 12 hours to remove any trace solvent. Samples were then loaded into an argon glovebox and a second aluminum current collector was pressed on top of the sample to afford through plane EIS conductivity measurements.

For electrolyte swollen conductivity measurements, the complex was prepared, cast, and dried as describe above. PVDF was solvent cast using NMP, then dried at 110°C at $10^{-8}$ torr for 12 hours in the same manner as the complex. After drying, the samples were loaded into a glovebox and excess electrolyte (1M $LiPF_6$ in 1:1 EC:DMC) was pipetted onto the top surface of the samples. Samples were allowed to passively swell and equilibrate for 24 hours. After 24 hours, excess electrolyte was removed via wicking with a Kimwipe. The samples were then sealed with the top aluminum current collector and measured.

For measurement, samples were placed into a Controlled Environment Sample Holder (CESH) from Biologic LLC, which maintains an inert atmosphere during measurement. Variable temperature conductivity measurements were performed using Biologic's Intermediate Temperature System (ITS) in conjunction with their VSP-300 potentiostat. A sinusoidal voltage with amplitude 100 mV was applied in the frequency range of 0.1 Hz−3 MHz. Data was then fit to the equivalent circuit shown in Figure 4.12 to extract the resistance. From these equivalent DC resistances, conductivity was calculated according to the following.

$$\sigma = \frac{1}{R}\frac{t}{A}$$

Where *t* is the thickness of the polymer film and *A* is the area, both of which are defined by the Kapton spacer.

***DC Polarization***

DC polarization was performed on symmetric lithium−polymer−lithium cells. Samples were assembled in an argon glovebox utilizing a Controlled Environment Sample Holder (CESH) from Biologic LLC and tested using their Intermediate Temperature System (ITS) in conjunction with their VSP-300 potentiostat to 80°C. It is common to perform this test at elevated temperature in order to improve signal to noise (due to higher ionic current at elevated temperature). Samples were allowed to rest for 12 hours after construction and were then equilibrated at 80°C and monitored via EIS until the system stabilized. Next, a 100 mV potential bias was applied and the resulting current measured over time. EIS measurements with a 20 mV amplitude were performed at 40-minute intervals to monitor changes in the interfacial resistance. Lithium transference numbers were calculated following the method of Bruce and Vincent:[68]

$$t_{Li+} = \frac{I_{ss}(\Delta V - I_{\Omega}R_0)}{I_{\Omega}(\Delta V - I_{ss}R_{\mathrm{ss}})}$$

Here, ΔV is the applied potential (100 mV), $R_0$ and $R_{ss}$ are the initial and steady-state interfacial resistances, respectively, $I_{ss}$ is the steady- state current, and $I_{\Omega}$ is the initial current determined from Ohm's law:

$$I_{\Omega} = \frac{\Delta V}{R_{\Omega}}$$

where $R_\Omega$ is the initial cell resistance (bulk and interfacial) measured by EIS. Using $I_\Omega$ instead of the initial current measured by the potentiostat eliminates errors related to the speed at which the instrument can record the current.

***Cell construction***

Cathode films were prepared via slurry processing. A composition of 85:6:9 by mass (LFP:Carbon:Polymer) was used for the carbon-containing cells, while a composition of 85:15 (LFP:Polymer) was used for the carbon-free cells, which are within the ranges typically reported for LFP cathodes.[43,74,162,163] LFP (MTI) and carbon black (Timcal super C65) were first mixed in the appropriate ratio using a mortar and pestle. To ensure consistency between cells, the same batch of homogenized LFP/Carbon (85:6) was used for both PVDF and CPC cells, ensuring the only variable was the polymer binder. The appropriate amount of this powder was then added to polymer solutions- PVDF (Solef, Solvay) in *N*-methyl-2-pyrrolidone (NMP) and our complex in THF/water. The slurries were thoroughly mixed then cast onto aluminum foil (MTI) using a doctor blade. The electrodes were slowly heated to 80°C until they were visually dry. They were then transferred into a vacuum chamber for 1 hr. After initial drying, the films were then punched into disks to obtain the electrodes, which then underwent a final drying stage for 12 hours at 110°C and $2\times10^{-8}$ torr. The average electrode mass loadings were around 2 mg $cm^{-2}$ for the carbon containing cells and 7 mg $cm^{-2}$ for the carbon free cells.

It should be noted that the LFP powder sourced from MTI (Lib-LFPOS21) was a 1.45 wt.% carbon composite. Given the low electronic conductivity of LFP, it is standard for commercial

materials to use a carbon composite. 1.45 wt.% is a very low mass percent compared to other reported composite formulations that reach 15 wt.% carbon.[151]

After drying, the cathodes were transferred into an Argon filled glovebox (<0.5 ppm oxygen, <0.5 ppm water) for cell assembly. CR2032 coin cells (Hohsen) were fabricated with lithium metal as the anode/counter electrode and Celgard 2325 (PP/PE/PP) separators. The electrolyte was either 1M LiTFSI or 1M $LiPF_6$ in 1:1 ethylene carbonate and dimethyl carbonate (1/1 v/v EC:DMC) as indicated in each data set. Cells were crimped using a pressure-controlled crimper (MTI) set to 0.9 MT.

***Testing***

Both variable rate and cycle stability tests were performed using galvanostatic cycling, where the C rate is defined using the theoretical capacity of 170 mAh/g for LFP. After construction, cells were allowed to rest for 12 hours while the OCV was monitored. After this, five C/10 cycles were performed to ensure complete SEI formation before subsequent testing. Electrochemical impedance spectroscopy (EIS) was performed at the top of charge and bottom of discharge of the $4^{th}$ cycle. The cells were allowed to rest for 1 hour prior to each EIS test. After the C/10 formation cycles, Galvanostatic intermittent titration technique (GITT) was performed. Here, constant current (C/10 rate) was held for 1 hour, then cells were allowed to relax for 2 hours while the OCV was monitored. The sequence was repeated until 1 charge/discharge cycle was complete. After GITT, the variable rate CV test was performed. Next, variable rate cycling was performed, where cells underwent 5 cycles at each rate of C/5, C/2, 1C, 2C, 4C, 6C, and C/5. Immediately following the variable rate test, the C/2 cycle

stability test was performed. All test were performed at room temperature using a Biologic VSP-potentiostat.

## 4.4 Results and Discussion

### Complexation

Complexing two polyelectrolytes with oppositely charged sidechains (Figure 4.1c) provides synergistic effects for the key properties necessary for a mixed ion-electron conducting battery binder, namely stability, (in)solubility, conductivity, and processability. Here, we demonstrate this using an anionic conjugated polyelectrolyte (CPE) complexed with a cationic polymeric ionic liquid (PIL) to form a CPE-PIL Complex (CPC). Various CPCs have been reported in literature, with focus on electronic conductivity,[27] optoelectronic properties,[26] and nanostructure.[161] Here we study poly[6-(thiophen-3-yl)hexane-1-sulfonate-co-3-(hexylthiophene)] (PTHS:P3HT) (90:10) as the CPE and poly[(3-methyl-1-propylimidazolylacrylamide)-co-3-methyl-1-(propyl acrylamide)] (90:10) as the PIL due to our previous work reporting the relatively high electronic conductivity of 1 S/cm, three orders of magnitude higher than that of the CPE itself.[27] Additionally, the thiophene backbone utilized in this CPC is semiconducting or, more specifically, insulating until oxidization occurs around 3.2V vs Li/$Li^+$. This electronic behavior is suitable for LFP cathodes, as the flat (dis)charge voltage profile characteristic of LFP's two-phase reaction occurs above this potential (around 3.4-3.2V). Hence, our binder is conductive over the entire potential range of the charge and discharge processes, but transitions to an insulator below 3.2V, which has been suggested to offer protection against overdischarge.[72] The PIL was chosen to be an acrylate functionalized with an imidazolium side chain, as this group is known to have a wide electrochemical stability window,[44,164] as well as favorable lithium transport properties owing to its diffuse charge.[14,15]

These properties indeed translate to the complex, which is found to have intrinsic ionic conductivity of $6\times10^{-8}$ S/cm at room temperature and lithium transference of 0.25, which is noteworthy given the high electronic conductivity of 1 S/cm, as shown in Figures 4.12-4.14. Additionally, Figure 4.16 shows the system is electrochemically stable up to 4.5V vs Li/Li+, more than sufficient for the 2-4V operating window of LFP.

Notably, complexation also provides advantageous physical properties, namely preventing dissolution in the battery electrolyte while also maintaining processability during slurry casting. Each polyelectrolyte taken by itself is soluble in the battery electrolyte (Figure 4.8), but after complexation and drying, the CPC proves insoluble due to the ionic crosslinks. This solves a major hurdle faced by many multifunctional polymer binders, where improvements in ionic conductivity also lead to greater solubility in battery electrolytes because the highly polar or charged groups capable of transporting ions dissolve in the highly polar electrolyte solution. Prior to drying, this CPC chemistry affords the formation of a coacervate phase,[161] which is critical for applying CPCs as binders. While solution, precipitate, and coacervate phases have been reported for CPCs,[26,44] only the coacervate phase is processable in a manner appropriate for battery applications. For example, the precipitate phase contains polymer dense, irregular solids with very low solvent content,[26] preventing a uniform coating of the cathode powders. A single phase solution may enable uniform coating and slurry casting, however, each polyelectrolyte would still contain its respective counterion (tetramethylammonium and $Cl^-$ in this system), which could interfere with battery operation by competing with Li+ transport. Coacervation involves a counterion release into the supernatant phase (the entropic gains of which are a driving force for the coacervate phase formation), and subsequent rinsing can

remove residual ions.[161] Finally, the isolated coacervate phase remains processable, maintaining the ability to flow and form uniform coatings. Further details can be found in Figure 4.6.

**Cell Design**

All data presented below were obtained from 2032 coin cells using lithium metal as the anode/reference electrode and commercially-available $LiFePO_4$ (LFP, sourced from MTI) as the cathode active material. As mentioned earlier, standard cathode film fabrication utilizes the active material in conjunction with a carbon additive and a polymer binder. Here, composite cathodes were prepared using 85% LFP, 6% carbon black, and 9% binder (all mass pecents). This composition is within the range commonly reported for LFP studies, where active loadings are often lower than those of NMC and NCA cathodes as the low intrinsic conductivity of LFP requires more additives.[43,74,162,163,165] The binder was either our CPC or PVDF. Additionally, carbon black-free cells were constructed by replacing the carbon additive with additional binder (85:15 LFP:Binder) to better evaluate the impact of the electronic conductivity of the binder on performance. Data for carbon free cells is found in Figures 4.17-4.20.

**Rate performance**

Composite cathodes containing the CPC binder exhibit greater capacity at all rates tested, from C/10 to 6C, compared to those based on PVDF. To determine this, five symmetric galvanostatic charge/discharge cycles were performed at each rate of interest (Figure 4.2a). At cycling rates up to 2C, the performance of the two types of composite cathodes is rather similar,

both achieving about 75% of their initial C/10 capacity. At high cycling rates (4C and 6C), a dramatic difference in performance is observed between the CPC- and PVDF-containing cathodes. Cathodes containing the CPC binder exhibit a much higher discharge capacity, achieving 102 mAh/g at 4C (61% of the C/10 capacity) and 65 mAh/g at 6C (39% of the C/10 capacity), compared to 44 mAh/g and 2 mAh/g (30% and 1.6 % of the C/10 capacity, respectively) for the PVDF-containing cathodes. Both binders are stable during rate performance testing, and the initial slow rate capacity is fully recovered during the final C/5 cycles.

The higher rate capability of the CPC-cell is consistent with its reduced polarization (Figures 4.2c,d), indicating that the CPC binder improves charge transport kinetics within the composite electrode. Cell polarization is a form of electrochemical hysteresis (sometimes called dissipative hysteresis) that results from sluggish kinetic processes as opposed to other, thermodynamic mechanisms of hysteresis, including first-order phase transitions, displacement and conversion reactions, reaction path hysteresis, etc.[166] Polarization leads to an overpotential, i.e., a deviation of the potential from the true equilibrium potential of the redox reaction at play - here, Li extraction from LFP on charge, Li reinsertion into LFP on discharge -, and therefore to a voltage hysteresis between the charge and discharge processes. From the galvanostatic charge/discharge voltage profiles shown in Figures 4.2c,d, it is clear that, at slow rates (C/10 and C/5), the polarization is rather similar for the CPC and PVDF cells, indicating that charge transfer through the binder is not rate limiting. However, at higher rates, smaller overpotentials during both charge and discharge are observed for cells containing the CPC binder compared to those containing PVDF. For example, at 2C the PVDF cell's average

charge potential is of around 3.77 V, and its discharge potential of about 2.97 V, while those of the CPC cells are 3.61V on charge and 3.16 V on discharge. Since the binder is the only variable between the two types of cells, those results indicate that at high rates the resistivity of PVDF is a limiter to charge transfer through the cathode composite. Figure 4.21 provides a different graphical representation of the data highlighting the differences in polarization/overpotential of the two types of cells at each rate.

The reduced polarization and enhanced capacity at high discharge rates is of great practical importance. By reducing resistive barriers, the CPC binder enables the passage of higher current densities and the delivery of higher potentials on discharge, thus increasing the cell's power output and energy density, as shown by the mathematical relations between power, energy, current ($I$), potential ($V$), and time ($t$) below:

$$Power = I \times V$$

$$Energy = Power \times t$$

The greater utilization of the cathode containing the CPC binder at high current densities is evident from the power/energy curves shown in Figure 4.2b.

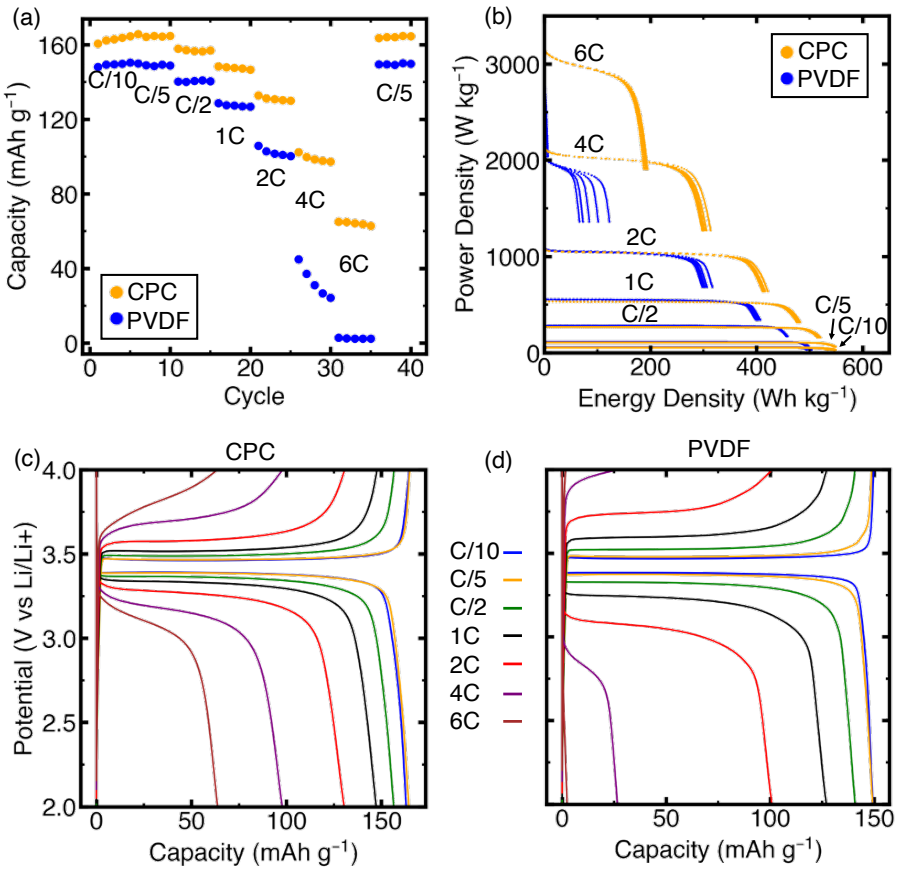


**Figure 4.2: Rate capability**

Data for LFP:Carbon:Binder (85:6:9 wt.%) composite cathodes during symmetric galvanostatic charge/discharge. (a) Discharge capacity and (b) resulting power/energy curves at various cycling rates, where normalization is based on mass of LFP. Potential profiles recorded for the 4$^{th}$ charge-discharge cycle at various rates for cathode composites containing (c) the CPC binder, and (d) a standard PVDF binder. Results shown here are for single cells, with replicates reported in Figure 4.20.

### Kinetics and lithium diffusion

To better understand the impact each binder has on charge transport kinetics, Galvanostatic Intermittent Titration Technique (GITT) and Cyclic voltammetry (CV) were employed. GITT results indicate that the CPC binder reduces the kinetic barriers to charge transport during charge and discharge. GITT is a powerful technique to separate kinetic and thermodynamic overpotentials.[167–169] As mentioned earlier, kinetic overpotentials or polarization result in a

dissipative form of voltage hysteresis that can be minimized by systematically reducing the rate with which the battery is charged and discharged.[166] In a GITT experiment, the kinetic overpotential is the difference between the potential during the constant current pulse and the equilibrium potential after a sufficiently long rest period when no current is flowing through the circuit (see Figure 4.3a inset). The thermodynamic overpotential depends on the nature of the electrochemical reaction taking place and, in a GITT experiment, is evaluated from the hysteresis between the discharge and charge equilibrium potentials (Figure 4.3a inset). Given that all composite cathodes tested here utilize the same LFP active cathode material, the thermodynamic overpotential is expected to be similar for cathode films comprising the CPC binder and for those containing PVDF, which is indeed the case. However, a reduced kinetic overpotential is observed for the composite cathodes containing the CPC binder over the potential plateau (at 3.4-3.5 V), signifying faster charge transfer kinetics. Once again, the greater capacity recorded for cathodes containing the CPC binder indicate a greater utilization of the LFP cathode: all of the Li can be reversibly extracted from and reinserted into LFP on charge and discharge. To better understand the impacts of the binder itself, GITT was performed on carbon-free analogues (Figure 4.18), which show a similar but more pronounced reduction in kinetic overpotential.

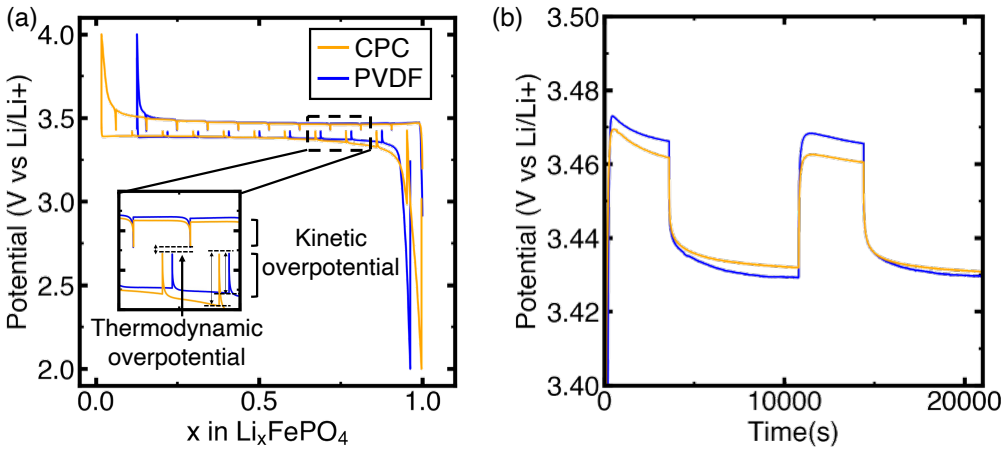


**Figure 4.3: GITT for composite cathodes containing CPC and PVDF binders**

(a) Plots curves vs. Li content (x in $Li_xFePO_4$), while (b) show the potential response to the first two charge current pulses, plotted vs. time, to better visualize the differences in overpotential during initial Li extraction from the two types of LFP composite cathodes. The inset in (a) highlights the features associated with kinetic and thermodynamic overpotentials.

CV experiments indicate that the CPC binder increases the apparent lithium diffusion coefficient within the cathode film ($D_{Li+}$). CV scans of composite cathodes containing either the CPC binder or PVDF are shown in Figures 4.4a,b, where kinetic limitations manifest themselves as a shift of the anodic and cathodic peaks to lower and higher potentials, respectively, upon increasing the potential scan rate. The smaller shifts observed for the composite cathode utilizing the CPC binder are in line with the smaller overpotentials observed via galvanostatic cycling and GITT.[167] The kinetic differences between the two types of composite cathodes can be quantified via the apparent diffusion coefficient using the Randles-Sevcik equation,

$$I_p = 0.4463 n^{\frac{3}{2}} F^{\frac{3}{2}} C S R^{\frac{-1}{2}} T^{\frac{-1}{2}} D_{Li+}^{\frac{1}{2}} v^{\frac{1}{2}}$$

where $I_p$ is the peak current (A), $n$ is the charge transfer number, $F$ is the Faraday's constant (96486C $mol^{-1}$), $C$ is the concentration, $S$ is the electrode surface area ($cm^2$), $R$ is the gas constant (8.314 J $mol^{-1}$ $K^{-1}$ ), $T$ is temperature (K), $D_{Li+}$ is the apparent diffusion coefficient ($cm^2$ $s^{-1}$), and ν is the scan rate (V $s^{-1}$).

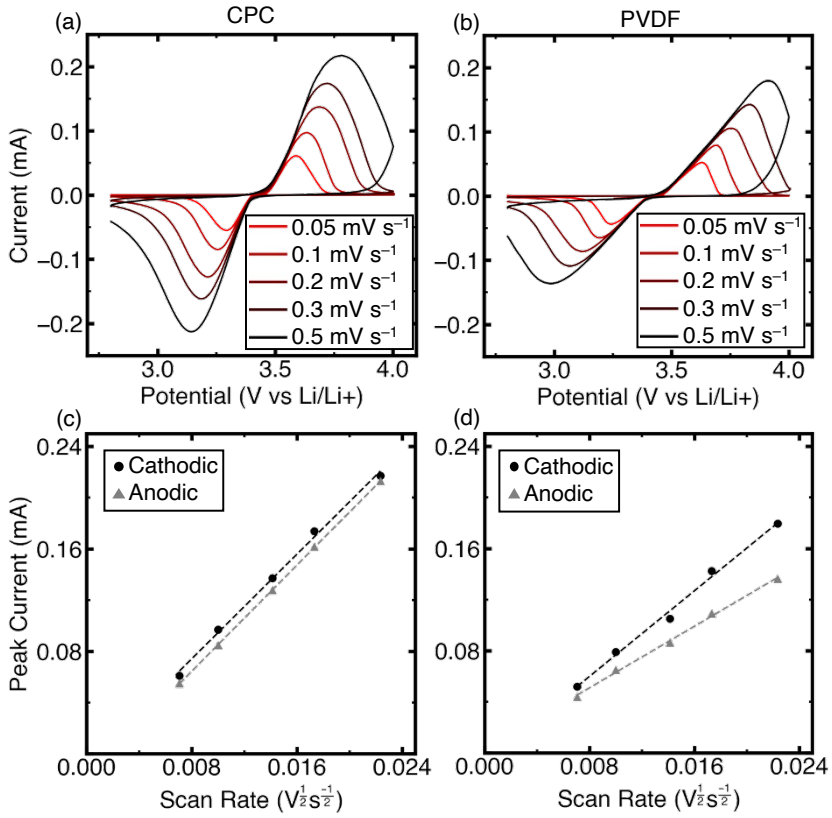


**Figure 4.4: Randles–Sevcik cyclic voltammetry data**

Cyclic voltammetry results obtained at various scan rates for LFP:Carbon:Binder (85:6:9 wt.%) composite cathodes, where the binder is (a),(c) our CPC and (b),(d) PVDF. The cyclic voltammograms are shown in (a) and (b), and peak currents as a function of the square root of the scan rate in (c) and (d).

$I_p$ is plotted as a function of the square root of $v^{\frac{1}{2}}$ to determine $D_{Li+}$ in Figures 4.4c,d. Here, $D_{Li+}$ is the apparent lithium diffusion coefficient, representative of the average kinetics of all $Li^+$ diffusional processes occurring in the cathode film.[159,170] Given that the only difference between the composite cathodes is the binder, any variation in $D_{Li+}$ stems from the binder's

impact on overall kinetics. As expected, the composite cathode containing the CPC binder has higher anodic (charge) and cathodic (discharge) diffusion coefficients ($D_{Li+}$ = $7.4\times10^{-15}$ and $7.1\times10^{-15}$ $m^2s^{-1}$, respectively) compared to PVDF ($D_{Li+}$ = $2.4\times10^{-15}$ and $4.8\times10^{-15}$ $m^2s^{-1}$, respectively). Interestingly, the CPC cathode has nearly overlapping curves for the anodic and cathodic sweeps (Figure 4.4c), indicating similar kinetics for lithium extraction from and reinsertion into the LFP composite cathode. The PVDF cell has differing kinetics, where the lithiation process (discharge) is more sluggish, consistent with previous reports.[159,167,170] Overall the results from CV, GITT, and rate capability paint a consistent picture, where the electronic conductivity, ionic conductivity, and lithium transference (detailed in Figures 4.9-4.15) afforded by the CPC binder results in superior Li+ mobility, enhanced charge transport kinetics, and ultimately superior rate capability for the composite cathodes.

**Cycling stability**

In addition to improving kinetics, the CPC binder leads to stable electrochemical performance over many cycles, and in fact the CPC cell shows improved retention beyond 100 cycles, compared to its PVDF counterpart (Figures 4.5 a,b). The normalized capacity vs. cycle number (Figure 4.5b) probes the reversibility of the redox reactions over many charge-discharge cycles, irrespective of the initial cathode utilization (greater for the CPC cell than the PVDF cell). Over the first 100 cycles, the reactions taking place within the CPC and PVDF cells appear to be similarly stable, leading to 93% and 92% capacity retention, respectively. Beyond cycle 100, the capacity retention of the CPC cell is significantly better than that of the PVDF cell, as it maintains 72% of its initial capacity at cycle 300 and 63% at cycle 400 (compared to 61% and 6% for the PVDF cell).

The origin of the capacity fade is likely not binder degradation, as PVDF is known to be electrochemically stable, but rather parasitic side reactions aggravated by the use of a resistive binder. Hereafter, differential capacity (dQ/dV) analysis is used to identify even subtle changes in electrochemical behavior and side reactions that occur during cycling. Figures 4.5c,d show the dQ/dV curves corresponding to the 1$^{st}$, 100$^{th}$, 200$^{th}$, 300$^{th}$, and 400$^{th}$ C/2 cycles during the stability test, as well as the initial formation cycle at C/10 for comparison. The plateaus in the potential profiles result in well-defined peaks in the dQ/dV curves, making the evolution of redox reactions and increase in overpotential easier to identify in the differential data. The dQ/dV curves of the CPC cell exhibit a single, well-defined redox peak as expected for the two-phase reaction between the $LiFePO_4$ and $FePO_4$ end-members on charge and discharge.[171] Upon cycling the CPC cell at C/2, only very minor changes to the dQ/dV peaks occur over 400 cycles, indicating minimal structural degradation of the LFP cathode particles and negligible side reactions. Additionally, the overpotential recorded at C/2 is only slightly higher than that recorded at C/10 and does not increase substantially over 400 cycles. On the other hand, new dQ/dV peaks appear for the PVDF cell upon cycling, and are clearly apparent at cycles 200, 300, and 400, indicating structural degradation of the LFP particles and/or side reactions upon extended cycling. Additionally, a large increase in overpotential is noted from C/10 to C/2 cycling, and again during the progression of the C/2 stability test. The increasing overpotential on charge likely triggers further side reactions as cycling goes on, exacerbating electrochemical instabilities.[172] In particular, these side reactions likely involve the $LiPF_6$ electrolyte salt, as cells utilizing an LiTFSI salt instead (Figures 4.22, 4.23) show no sign of side reactions or overpotential growth in either the CPC or PVDF cells. Carbonate $LiPF_6$ electrolytes are well known to undergo many decomposition reactions, producing LiF, $POF_3$, $POF_2(OH)$, and

$POF(OH)_2$, which can form ionically insulating surface layers, as well as HF that causes Fe dissolution from LFP.[150,173,174] While LiTFSI is known to be a more stable salt,[175] $LiPF_6$ is still widely used due to its lower cost. Thus improving the long term stability of cells utilizing $LiPF_6$ has substantial relevance for real world applications. Overall, by improving the reversibility of the redox reactions, the CPC binder mitigates structural degradation of the cathode particles, overpotential growth, and side reactions, resulting in exceptional cycling stability for the LFP cathode.

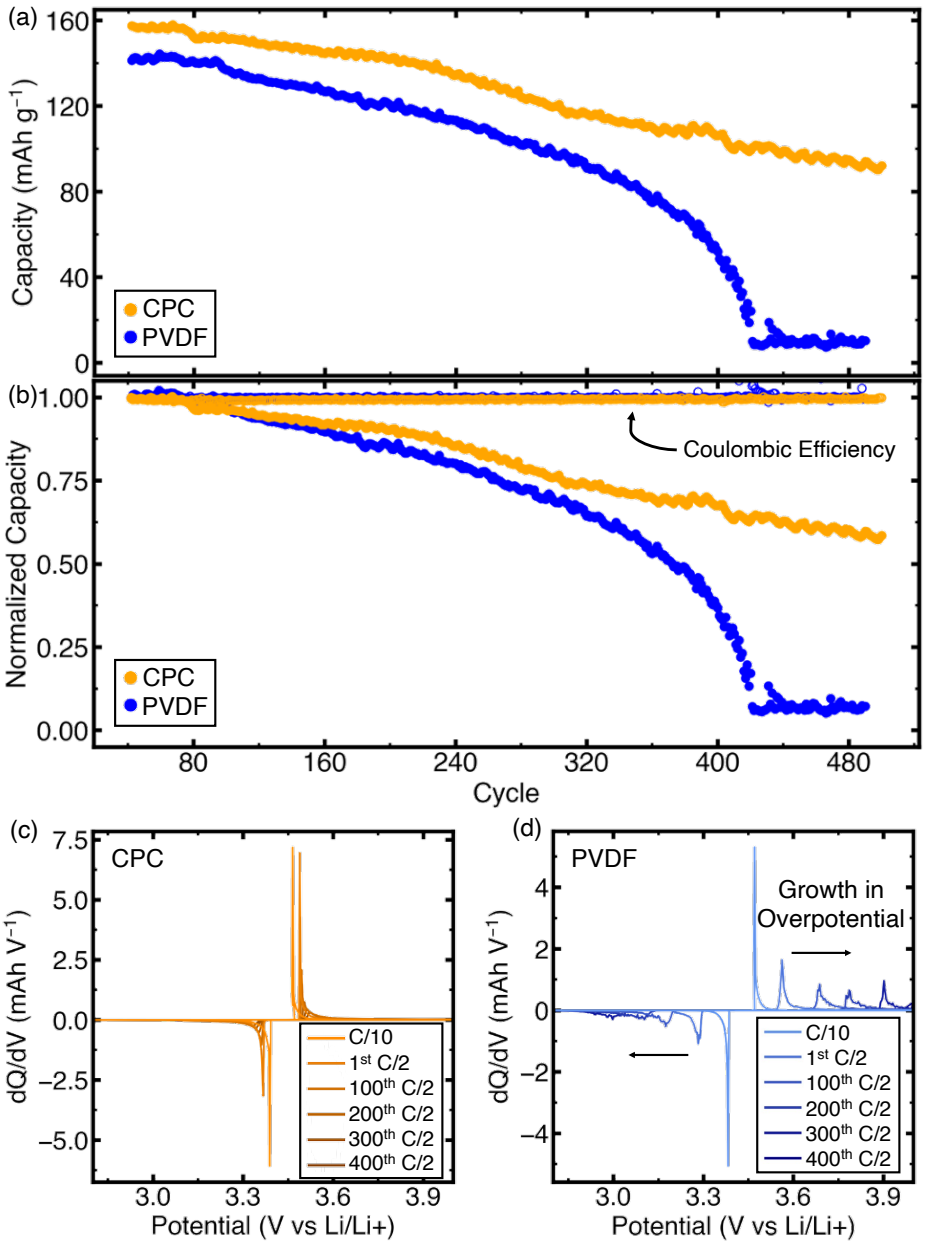


**Figure 4.5: Cycling stability for LFP:Carbon:Binder (85:6:9 wt.%) composite cathodes using the CPC binder or PVDF**

Capacity retention of composite cathodes (a) shown as specific capacity vs. cycle number and (b) shown as capacity retention, where each cycle's discharge capacity is normalized to that of the first cycle. (c) and (d) show differential capacity curves for the initial formation cycle at C/10, and for the 1$^{st}$, 100$^{th}$, 200$^{th}$, 300$^{th}$, and 400$^{th}$ C/2 cycles of the stability test.

## 4.5 Conclusions

In conclusion, we have shown that implementing a mixed conducting polymer complex as the binder in $LiFePO_4$ (LFP) composite cathodes is an effective method to improve charge transport within the electrode film. By reducing the kinetic overpotential (polarization) and increasing the apparent lithium diffusion coefficient, the novel binder enables superior rate performance for LFP composites, achieving 65 mAh/g at 6C, while composites containing a standard PVDF binder only achieve 2 mAh/g at the same rate. Further, the CPC binder is sufficiently electronically conductive to enable carbon-free LFP composite cathodes with a reasonable discharge capacity of 126 mAh/g at C/2, whereas the PVDF-containing composite is unable to cycle at this rate in the absence of conductive additive. Finally, the electrostatically stabilized complex affords a unique combination of conductivity and stability, as the ionic crosslinks prevent dissolution of the binder, proving stable over 400 cycles. LFP composite cathodes based on the CPC binder show exceptional cycling stability, with a 93% and 63% capacity retention after 100 and 400 cycles at C/2, respectively, compared to a 92% and 6% retention at cycles 100 and 400 when using a PVDF binder. This can be attributed to the negligible structural degradation of the LFP particles, increase in overpotential, and side reactions in the presence of a the newly-developed conducting binder. The results presented here suggest that replacing PVDF with a mixed conducting polymer complex could be a “pick and place” method to quickly achieve large performance improvements in LFP batteries targeted at high power applications, such as electric vehicles.

**Acknowledgments**

We gratefully acknowledge support from U.S. Department of Energy, Office of Science, Basic Energy Sciences under Award DE-SC0016390. The research reported here made use of shared facilities of the UC Santa Barbara Materials Research Science and Engineering Center (MRSEC, NSF DMR 1720256), a member of the Materials Research Facilities Network (https://www.mrfn.org). In addition G.T.P. gratefully acknowledges support from the National Science Foundation Graduate Research Fellowship Program under Grant No. 1650114.

## 4.6 Appendix

### Polymer Synthesis

***Synthesis of Poly(3-(6'-bromohexyl)thiophene-co-3-hexylthiophene) (P3BrHT:P3HT) (90:10)***

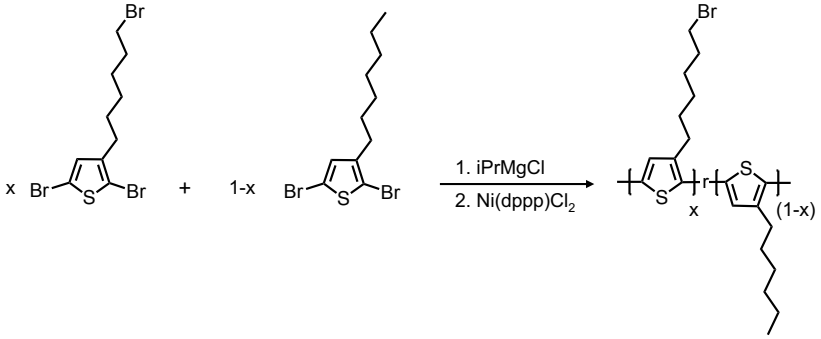


P3BrHT:P3HT random copolymers was synthesized based on a previously reported protocol.[104] In an oven-dried round bottom flask equipped with a magnetic stir bar, 2,5-dibromo-3-(6-bromohexyl)thiophene and 2,5-dibromo-3-hexylthiophene were mixed in 9:1 molar ratio. The reaction flask was then sealed with rubber septa and was dried overnight under active vacuum. Anhydrous THF was added to the flask to dissolve the dry monomer mixture, and the flask was purged with dry nitrogen for 20 minutes. Isopropylmagnesium chloride was

added dropwise to the reaction flask, and the mixture was stirred at ambient temperature under nitrogen. Care was taken to prevent contact of isopropylmagnesium with air during the transferring process. After 2 hours, Ni(dppp)Cl2 suspended in dry THF was added to the reaction. Immediate color change from pale yellow to vibrant red was observed, indicating the polymerization taking place. After 12 hours, the polymerization was quenched by rapid addition of 1M HCl solution, and was precipitated into cold methanol. The obtained polymer was purified by washing in a Soxhlet apparatus with methanol, acetone, and ethyl acetate respectively before extraction with THF. The product was concentrated under vacuum, yielding a red-purple solid. The isolated product was then dried overnight under vacuum to remove any remaining solvent.

$H^1$ NMR (600 MHz) in CDCl3: δ 7.0 (1H, s), δ 3.4 (1.74H, t), δ 2.8 (1.41H, t), δ 1.5 – 1.8 (8.1H, m), δ 0.9 (0.32H, t).

GPC in THF (PS standard): Mn = 13.6 kDa, Mw = 20.6 kDa, $Đ$ = 1.52

***Synthesis of Poly[6-(thiophen-3-yl)hexane-1-sulfonate-co-3-(hexylthiophene)] (PTHS:P3HT) (90:10)***

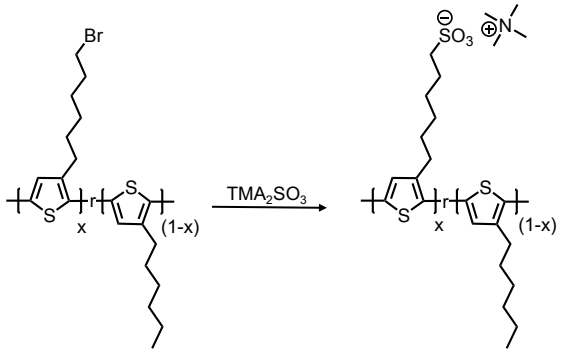

In a round bottom flask equipped with a magnetic stir bar, P3BrHT-P3HT was dissolved with THF. The flask was sealed with a rubber septa, and the solution was purged with dry nitrogen gas for 30 minutes. 1M bis(tetramethylammonium)sulfite (TMA2SO3) salt solution in methanol was prepared following a previously reported protocol.[124] 10-fold excess of TMA2SO3 was added to the reaction flask, and the mixture was heated to 70°C and refluxed for 1 hour. After that, more methanol was added to the reaction mixture to help dissolve the ionic-functionalized polymer and drive the reaction to completion. The reaction mixture was left to react overnight. The polymer was purified by dialyzing using 10 kDa cutoff dialysis membranes against deionized water for 3 days, with the dialysate replaced every 12 h. The isolated product was dried with lyophilizer, yielding the CPE as a red-purple solid.

$H^1$ NMR (600 MHz) in Methanol: δ 7.1 (1H, s), δ 2.8 (3.9H, t), δ 1.8 – 1.5 (7.78H, m), δ 0.93 (0.305H, t).

***Synthesis of Poly(N-hydroxysuccinimidyl acrylate) (PNHSA)***

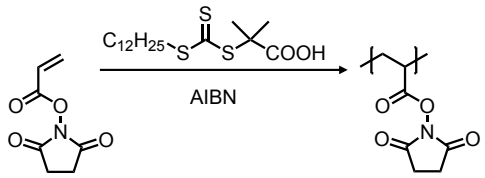


Synthesis of PNHSA was carried out following a previously reported protocol.[160] In a Schlenk flask equipped with a magnetic stir bar, N-acryloxysuccinimide, DDMAT, and AIBN were dissolved in anhydrous DMF. The solution was degassed using five freeze-pump-thaw cycles. After the fifth cycle, the flask was filled with dry nitrogen and heated to 70˚C in an oil bath. The reaction was kept at that temperature for 24 h, and during the process the mixture was stirred vigorously. After cooling to 25˚C, the polymer was precipitated from methanol, filtered and dried in ambient, dissolved in DMF and reprecipitated from methanol, twice. The polymer

was filtered and dried under a vacuum at 60˚C for 24 h to yield a pale yellow powder. NMR end-group analysis indicate an average DP of 82 for the PIL.

$H^1$ NMR (600 MHz) in DMSO: δ 3.13 (27H, br), δ 2.80 (125H, br), δ 2.05 (55.6H, br), δ 1.27 (6.3H, s), δ 0.8 (1H, t)

***Synthesis of Poly[(1-propylimidazolacrylamide)-co-3-methyl-1-(propyl acrylamide)]***

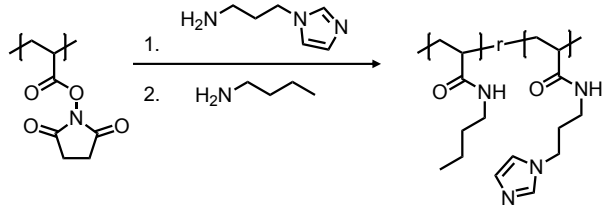


PNHSA repeat units were randomly functionalized with imidazole-amine and butylamine following a previously reported protocol.4 The polymer was first dissolved in anhydrous DMF in a round bottom flask. The flask was sealed with rubber septa and degassed with dry nitrogen for 30 minutes. After that, 0.9 molar equivalent of 1-(3- aminopropyl)imidazole solution in anhydrous DMF was added dropwise to the vigorously stirring polymer solution. The reaction was left running for 12 hours at 25˚C using a water bath. The resulting polymer was precipitated from ethyl acetate, dissolved in methanol, and re-precipitated from diethyl ether twice. The polymer was collected by centrifugation and dried under a vacuum at 60˚C for 12 h to obtain a pale yellow brittle solid. It was then dissolved in anhydrous DMF and the NHSA groups were reacted with 5-fold excess of butylamine for 12 h at 25˚C f to yield the neutral random copolymers. Integrations of the Imidazolium proton peaks δ 7.6 (17H, s), δ 7.1 (17H, s), δ 6.9 (17H, s) suggests an average 75 repeat units per chain were functionalized, corresponding to a charge fraction of 91%

***Synthesis of Poly[(3-methyl-1-propylimidazolylacrylamide)-co-3-methyl-1-(propyl acrylamide)]***

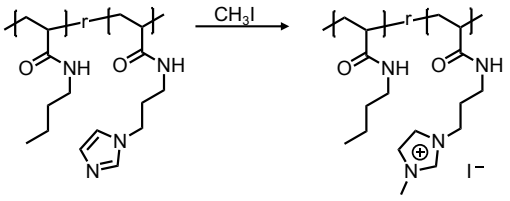


In a round bottom flask, the neutral copolymer was dissolved in anhydrous DMF. The flask was sealed with a rubber septa, and the solution mixture was purged for 30 minutes using dry nitrogen. 3-fold excess of iodomethane (with respect the imidazole) was added to the flask, and the reaction mixture was heated slightly and kept at 40$^{o}$C for 12 hours. The polymer was then precipitated from diethyl ether and dried under vacuum overnight. The iodine anion was exchanged to chloride by co-dissolving the polymer in methanol with 10-fold excess of NaCl. This mixture was stirred vigorously at 45$^{o}$C overnight. After that, the solution mixture was dialyzed using a 10 kDa cutoff dialysis membranes against methanol for 4 days, with the dialysate replaced every 12 h. The isolated product was dried under vacuum at 90˚C for 24 h, yielding an off-white solid.

## Additional Data

### *Conjugated Polymer Complex Properties*

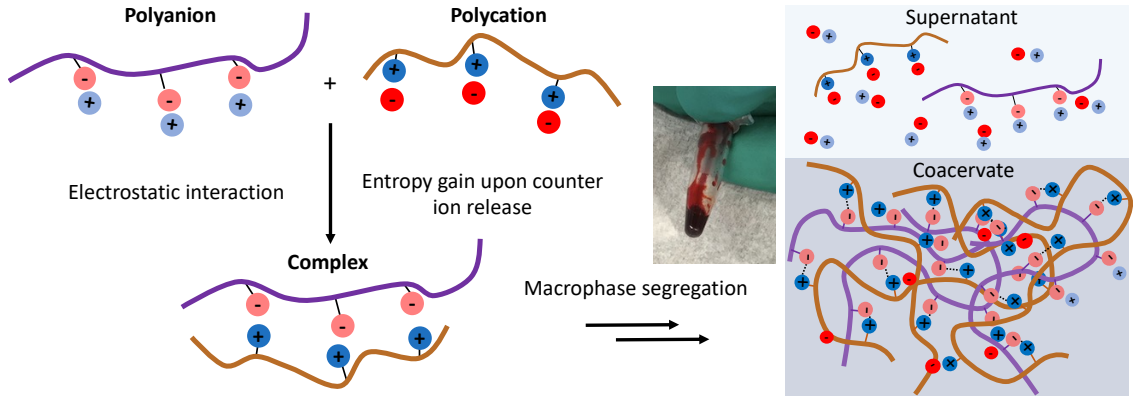


**Figure 4.6: A schematic of the complex coacervation process**

When a polyanion and polycation are mixed, the electrostatic interactions and entropy gains of counterion release drive complexation. This typically results in macrophase separation, and when solvent quality is properly tuned (i.e. 40/60 THF/water v/v), a polymer rich coacervate phase is in equilibrium with a polymer dilute, counterion rich supernatant phase. The coacervate phase can be isolate via centrifuge, and further studied.

Throughout this work, analysis was performed on the isolated, dried coacervate phase. Strictly speaking, once isolated/dried, this phase is no longer a coacervate, but rather an electrostatically stabilized complex. Hence the binder is ultimately referred to as a conjugated polyelectrolyte (CPE)-polymeric ionic liquid (PIL) complex (CPC). The desire to form and isolate a coacervate stems from practical processing considerations. The final CPC affords ionic conduction via the charged side chains and enhances electronic conductivity due to planarization of the conjugated backbone, as discussed in the main text. Additionally, the final CPC is an ionically crosslinked solid, which will not redissolve in the solvent or battery electrolyte (Figure 4.8). While withstanding electrolyte dissolution is crucial for battery applications, an intermediate phase for processing is required to form an electrode slurry. By

tuning polymer concentration and solvent quality, we are able to initially form a coacervate (Figure 4.6), which is a polymer rich phase that maintains the ability to flow, swell with solvent, and form coatings prior to drying. Through this liquid-liquid phase separation, the bulk of the polymer is concentrated in the coacervate phase, while the bulk on the counterions and dilute polymer are in the supernatant phase.[26,50] Thus coacervation is an effective strategy to drive miscibility to two distinct polymers to ultimately generate a system with enhanced stability and conductivity, while maintaining intermediate processability.


**Figure 4.7: Optical images of the isolated coacervate phase**

The isolated coacervate was used as a binder in this work. (a) shows the coacervate and supernatant in a centrifuge tube, (b) shows the isolated coacervate phase, and (c) is an optical microscope image of the isolated coacervate, sandwiched between two glass slides. The homogenous red color indicates a lack of precipitate, which would appear as dark, irregular solids. The scale bar represents 100 μm.

Each individual polyelectrolyte is soluble in the battery electrolyte, but the ionic crosslinks afforded by complexation prevents dissolution (Figure 4.8). Importantly, this occurs after drying to remove all processing solvent. Prior to drying, the complex forms a viscous, coacervate phase that enables facile coating, as shown in Figure 4.7b

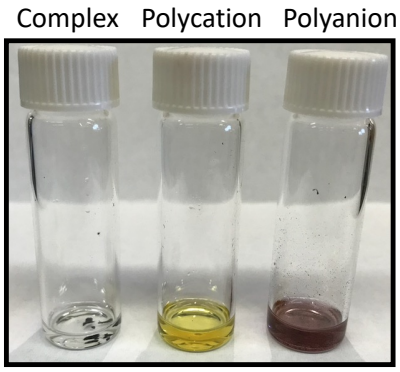


**Figure 4.8: A demonstration of the solubility change upon complexation**

When immersed in 1M LiTFSI in 1:1v EC:DMC, the complex (left) is insoluble, but the individual polycation (middle) and polyanion (right) are soluble.

***Electronic conductivity, ionic conductivity, and lithium transference***

Here, further detail about the intrinsic electronic conductivity, ionic conductivity, and lithium transference of the polymer complex are discussed. Measuring the intrinsic transport properties, in addition to battery performance, is valuable in order to establish fundamental mixed conduction structure-property relationships.

Figures 4.9 and 4.10 show schematics of sample setups for bulk ionic conductivity (Figure 4.9a), lithium transference (Figure 4.9b), and electronic conductivity (Figure 4.10). For all measurements, washing the complex with a 40/60 (v/v) THF/water mixture ensured the bulk of the sidechain counterions were removed. This is evidenced by the lack of ionic conductivity of the complex, shown in Figure 4.11. For ionic conductivity and transference measurements, controlled amounts of LiTFSI were introduced after washing but prior to drying, as described in the methods section. LiTFSI was selected (rather than $LiPF_6$), as variable temperature measurements are typically performed in ion conducting polymers, and $LiPF_6$ degrades at

relatively low temperatures. Ionic conductivity samples were cast, dried, and sandwich between two ion blocking electrodes to enable AC impedance in a typical fashion for ion conducting polymers.[14,65] Transference measurements took a similar geometry, but utilized lithium metal electrode to enable the DC polarization technique developed by Bruce and Vincent.[68] Electronic conductivity was performed on vapor doped thin films in our prior work and is described here for clarity.[27]

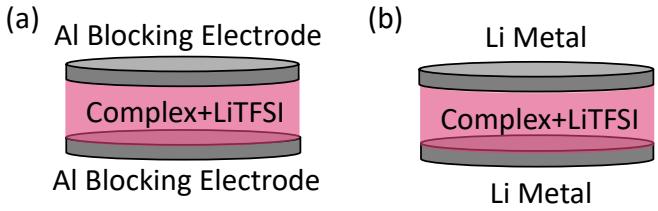


**Figure 4.9: Schematic of the setup used to determine intrinsic ionic transport properties of the complex**

Broadly, the setup is the same for ionic conductivity (a) and lithium transference (b), with the difference being the former uses blocking electrodes. In each, the polymer is sandwiched between two metal electrodes. For ionic conductivity, these electrodes were selected to be aluminum, which are blocking to all ionic charge carriers. For $t_{Li+}$ measurements, lithium metal was used, as this is blocking to all ionic charge carriers other than $Li^+$, enabling the determination of the steady state lithium ion current.

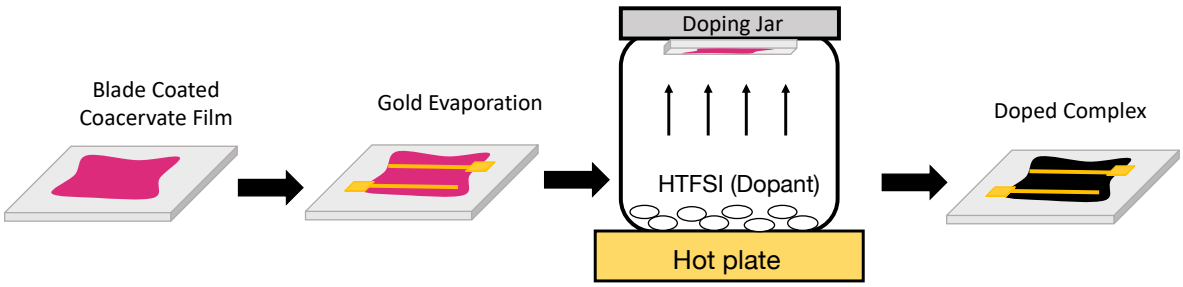


**Figure 4.10: Schematic of the setup used to determine intrinsic electronic transport properties of the complex**

Complex were first blade coated onto quartz substrates and then dried. Next, Gold electrical contacts (≈ 60 nm thick) were deposited at 1 Å s−1 rate onto the casted polymer film on quartz via controlled thermal evaporation through a shadow mask. Transmission line measurements were carried out to determine in-plane electronic conductivity of the polymer film using a Keithley 6485 picoammeter. Measurements were carried out inside a nitrogen glovebox at

room temperature. After various doping conditions were tired, a conductivity of 1 S/cm was achieved.[27]

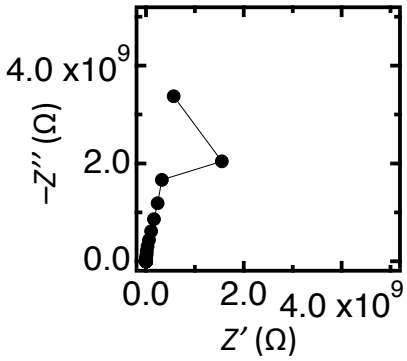


**Figure 4.11: Ionic conductivity of the neat complex**

This indicates the complexation/washing process sufficiently removes charge compensating counterions. The Nyquist plot is indicative of an open circuit, in line with a lack of ionic charge carriers. The line between points is provided as a guide for the eye.

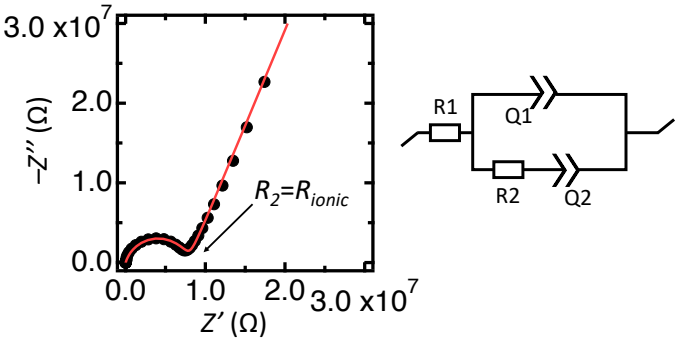


**Figure 4.12: Representative Nyquist plot for the ion conducting complex between two, symmetric blocking electrodes.**

Data is from the r=1.0 sample at room temperature (r= LiTFSI/$SO_3^-$ group). Black dots represent data and the red line represents the fit obtained using the equivalent circuit shown on the right.

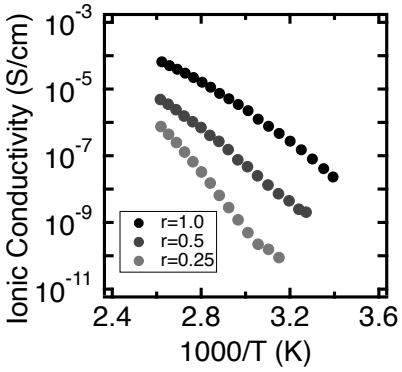


**Figure 4.13: Variable temperature, intrinsic ionic conductivity**

Data is for the dry complex upon addition of controlled amount of LiTFSI, where r=[moles LiTFSI]/[moles -$SO_3^-$ group].

Despite the stabilizing ionic cross links, the conjugated polymer complex experiences a monotonic increase in conductivity from r=0.25 to r=1.0 LiTFSI, indicating the complex intrinsically has a good ability to solvate and transport ions. A maximum room temperature conductivity of $6.05 \times 10^{-8}$ S/cm is achieved at r=1.0 LiTFSI. Measurements of the electrolyte swollen system are presented and discussed below in Figure 4.15. As Figure 4.14 indicates, there is also reasonable lithium transference, indicating good mobility of $Li^+$ through the complex.

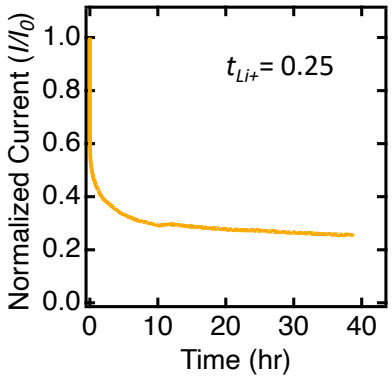


**Figure 4.14: Current decay for the DC polarization study**

The complex with r=1.0 LiTFSI is sandwiched between lithium metal electrodes and a DC potential is applied as described in the methods section of the main text.

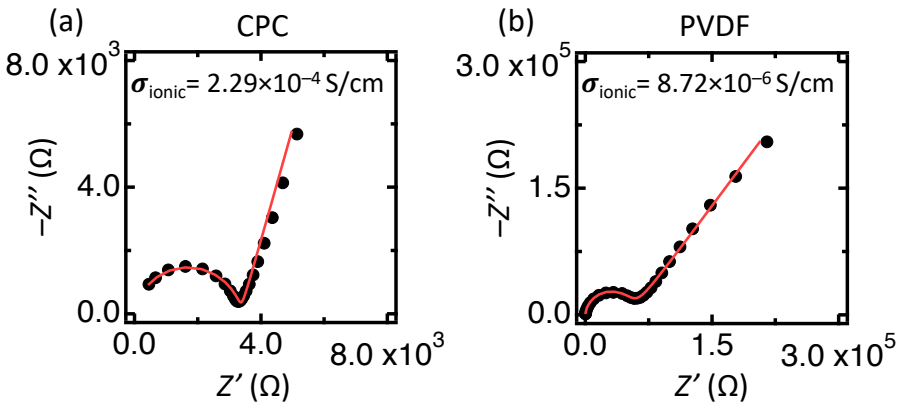


**Figure 4.15: Ionic conductivity data for the electrolyte swollen polymers**

(a) Shows the Nyquist plot and resulting ionic conductivity for the swollen CPC system and (b) shows that of swollen PVDF. For each, the polymers were cast and dried as previously described, then allowed to passively swell with electrolyte as outlined in the methods section. AC impedance was then performed on the swollen polymer systems. Black points represent data and red lines represent the fit to the equivalent circuit presented in Figure 4.12, from which ionic resistance was determined. Data was collected at room temperature.

The intrinsic ionic conductivity of PVDF is too low to be measured in the same manner as that of the CPC binder, as PVDF cannot solvate salt in its dry state. However, during actual battery operation, the polymer binder is swollen by liquid electrolyte and in this swollen state exhibits appreciable ion transport.[40,176,177] Hence, to better mimic polymer binders in a normal battery environment, measurements of the ionic conductivity of the polymers were performed on electrolyte-swollen systems.

The swollen CPC achieves an ionic conductivity of $2.29\times10^{-4}$ S/cm, nearly two orders of magnitude higher than that of swollen PVDF (Figure 4.15). To determine these values, the polymers were cast, dried, and then exposed to excess electrolyte for 24 hours. The excess electrolyte was then removed, and the ionic conductivity was measured on the passively swollen polymers. The resulting ionic conductivity is thus a function of the polymer's affinity to swell with electrolyte. The results presented here are consistent with the higher intrinsic

ionic conductivity of the CPC, as the charged sidechains that facilitate ion transport should also provide enhanced electrolyte swelling compared to PVDF.

***Cyclic Voltammetry***

To assess the electrochemical stability and reversibility of the complex, cyclic voltammetry (CV) was performed. It should again be emphasized that this complex contains a conjugated polymer, and thus it is expect to have reversible redox peaks between 3.2 and 4V vs $Li/Li^+$. Here, the complex was blade coated directly onto aluminum foil, dried at 110°C and $2\times10^{-8}$ torr, and then loaded into coin cells as previously described, where the complex serves as the working electrode and lithium metal serves as the counter/reference electrode.

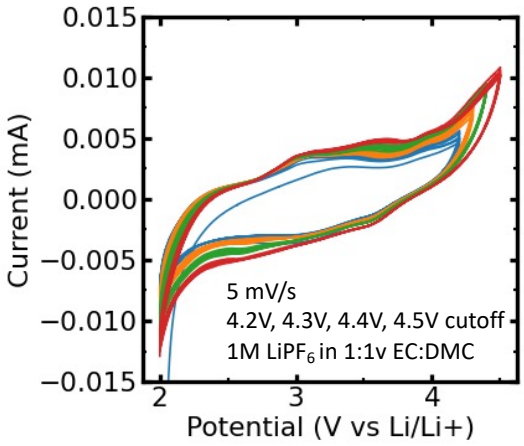


**Figure 4.16: Cyclic voltammograms of the complex**

CV was performed at scan rate of 5 mV/s to various cutoff potentials, with 5 cycles at each cutoff.

The good overlap of the CV curves obtained for each cycle indicates the stability of the CPC up to 4.5V. It should be noted that conjugated polymers are expected to undergo a form of

"break in" during their first cycle, which here is associated with the blue (4.2V upper potential limit) curve shifted to lower currents.

***Carbon Free Cells***

The performance of cathode films containing no carbon additive further emphasizes the ability of our CPC binder to facilitate long-range electron transport within the composite cathode (Figure 4.17). We note that carbon is typically introduced in two forms in electrode composites: first, the active material in powder form is coated with a thin layer of carbon prior to composite fabrication to enhance the electronic conductivity of individual particles, and second, carbon black and/or carbon nanotubes are added to the slurry during electrode film fabrication to create long-range electron transport pathways. The commercial LFP active material used here has already been coated with carbon (1.4% by mass), and for all of the electrochemical results presented thus far carbon black was added to the electrode slurry to provide long-range electron transport pathways. To test whether the CPC binder provides sufficient electronic conductivity to enable reasonable cathode utilization in the absence of carbon additive, composite cathodes were prepared whereby carbon black was replaced with additional binder (85:15 wt.% LFP:binder, as opposed to 85:6:9 wt.% LFP:CB:Binder). As shown in Figure 4.17, the carbon-free cathode composite containing the CPC binder performs remarkably better than the PVDF-based cathode composite. Specifically, the PVDF-based cathode is unable to provide any discharge capacity at rates above C/5, whereas the CPC cell achieves 126 mAh/g at C/2 and 47 mAh/g at 1C. A dramatic decrease in cell polarization is also observed for the CPC cells (Figures 4.17b,c,), again emphasizing the improvements in long-range electronic conduction provided by the CPC binder. This ability to facilitate long-

range electron transport results in a lower overall resistance within the composite cathode, and thus the electronic conductivity of the CPC is an important contributor to the enhanced rate performance reported in the main text.

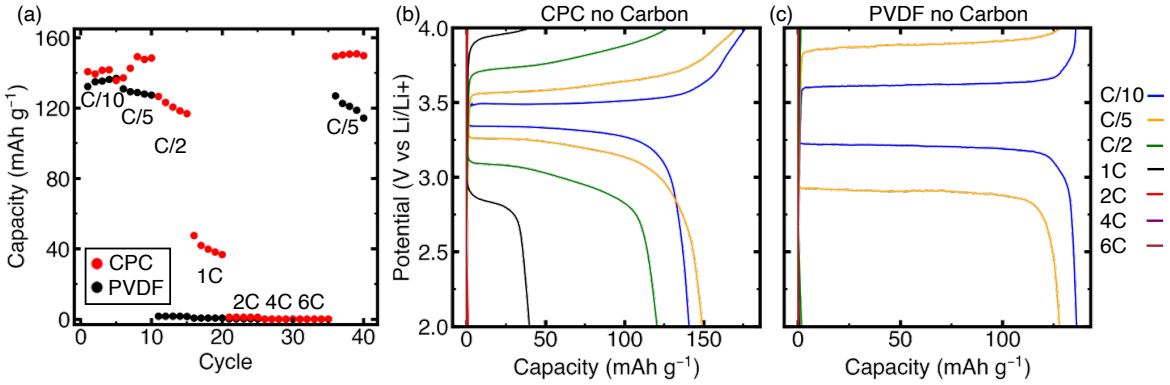


**Figure 4.17: Rate capability data obtained for cells containing carbon-free cathode composites**

The composition was 85:15 wt.% LFP:Binder and symmetric galvanostatic charge/discharge cycling was performed. (a) Discharge capacity at various cycling rates. Potential profiles recorded for the 4$^{th}$ charge-discharge cycle at various rates for cathode composites containing (b) the CPC binder, and (c) a standard PVDF binder.

GITT results for carbon free cells (Figure 4.17) provide similar insight to those reported in the main text. However, here the difference in overpotential is more pronounced, as the conducting binder is the only electronic transport pathway between active material particles. While the rate capability of these carbon free cells may not support practical application for carbon free cells, these GITT result provide useful insight as to the "*in situ* charge transport" ability of the CPC binder. Previously discussed electronic and ionic conductivity results show the CPC has appreciable, intrinsic conductivity. However, the battery environment is very different than that of the controlled measurements on bulk samples. During battery operation, the polymer is in contact which electrolyte, excess salt, active material particle, etc. The dramatic reduction in kinetic overpotential shown in the carbon-free GITT results indicate the CPC binder does indeed have superior conductivity than PVDF, even during battery operation. Importantly, this

indicates the fundamental structure property relationships for mixed-conduction in the CPC are consistent with *in situ* performance.

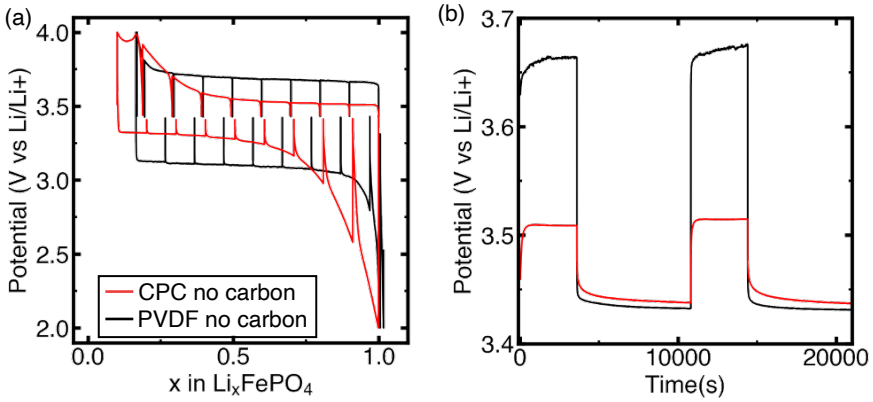


**Figure 4.18: GITT results for carbon free cells (85:15 LFP:Binder)**

The data presented here show similar, but more pronounced results to those reported for carbon containing cells in the main text. (a) displays potential vs. Li content (x in $Li_xFePO_4$), while (b) shows the potential response to the first two charge current pulses, plotted vs. time

The improved kinetics afforded by the CPC binder are also supported by AC impedance of both carbon containing and carbon free cells (Figure 4.19), which show smaller change transfer resistances when the CPC is the binder compared to PVDF. Here, the high frequency semicircle is typically associated with charge transfer processes.[73] Compared to PVDF, cells utilizing the CPC binder show significantly smaller charge transfer resistance at both top of charge and bottom of discharge in 85:6:9 (a,c) and 85:15 (b,c) cells.

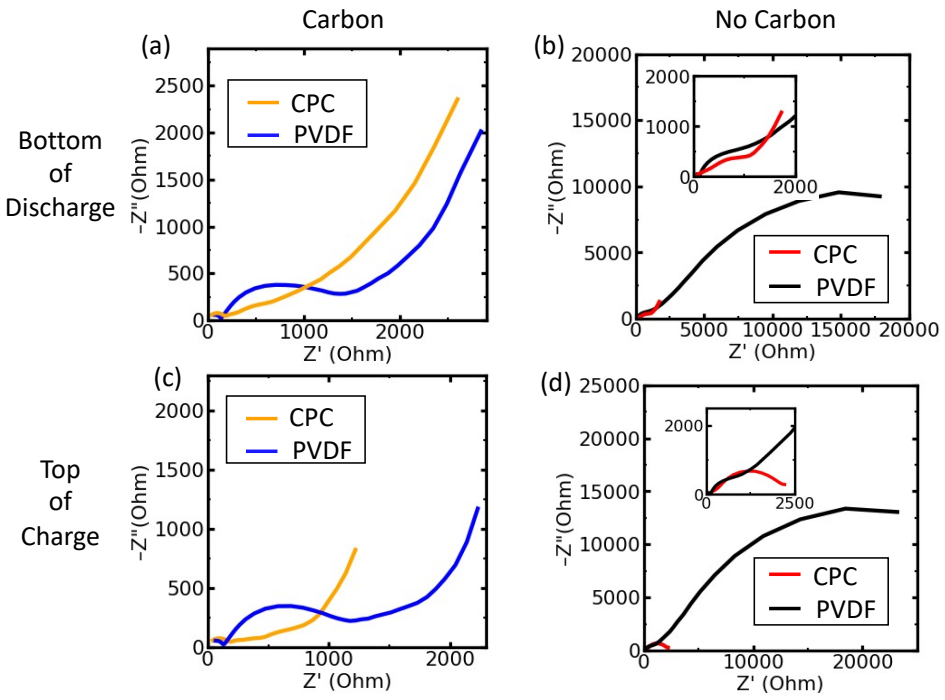


**Figure 4.19: Nyquist plots of cells**

These results show the reduction in impedance provided by the complex binder at both the top of charge (ToC) and bottom of discharge (BoD) of the 4$^{th}$ C/10 cycle.

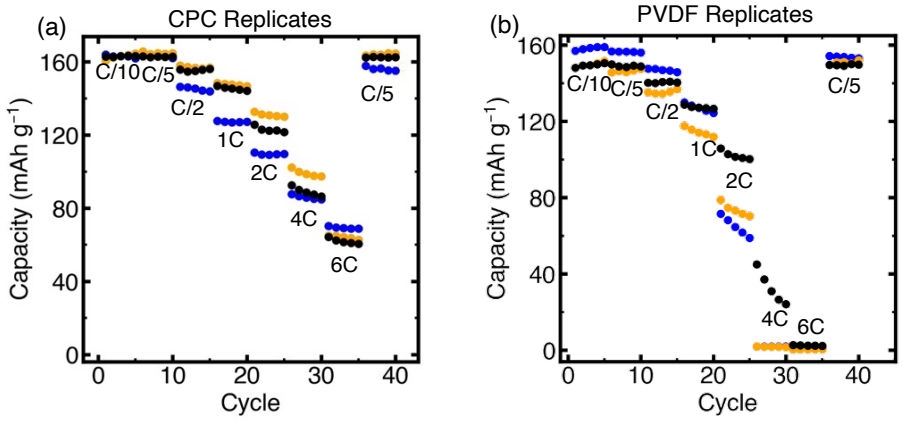


**Figure 4.20: Rate capability data showing good consistency between replicate cells**

Cells contain LFP:Carbon:Binder (85:6:9 wt.%) composite cathodes for (a) the CPC binder and (b) PVDF. Color coding is arbitrary and simply used to distinguish data points between replicates.

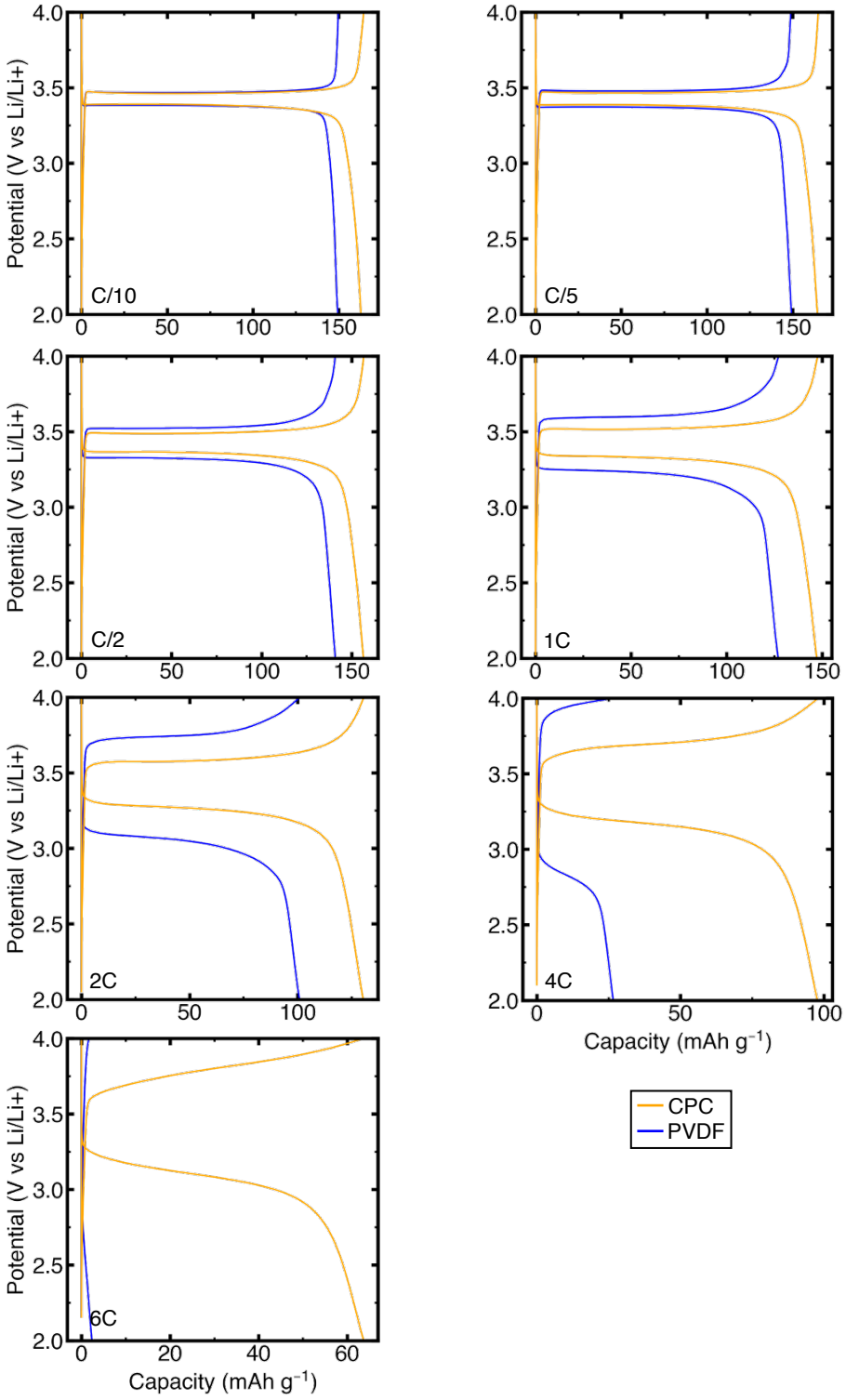


**Figure 4.21: Potential vs. capacity curves**

Expanded representation of the data shown in Figures 4.2c,d in the main text. Here, the galvanostatic Potential vs. Capacity curves obtained for the PVDF cell and CPC cell at a given cycling rate are overlaid, enabling easier comparison of the different overpotentials for the two types of cells.

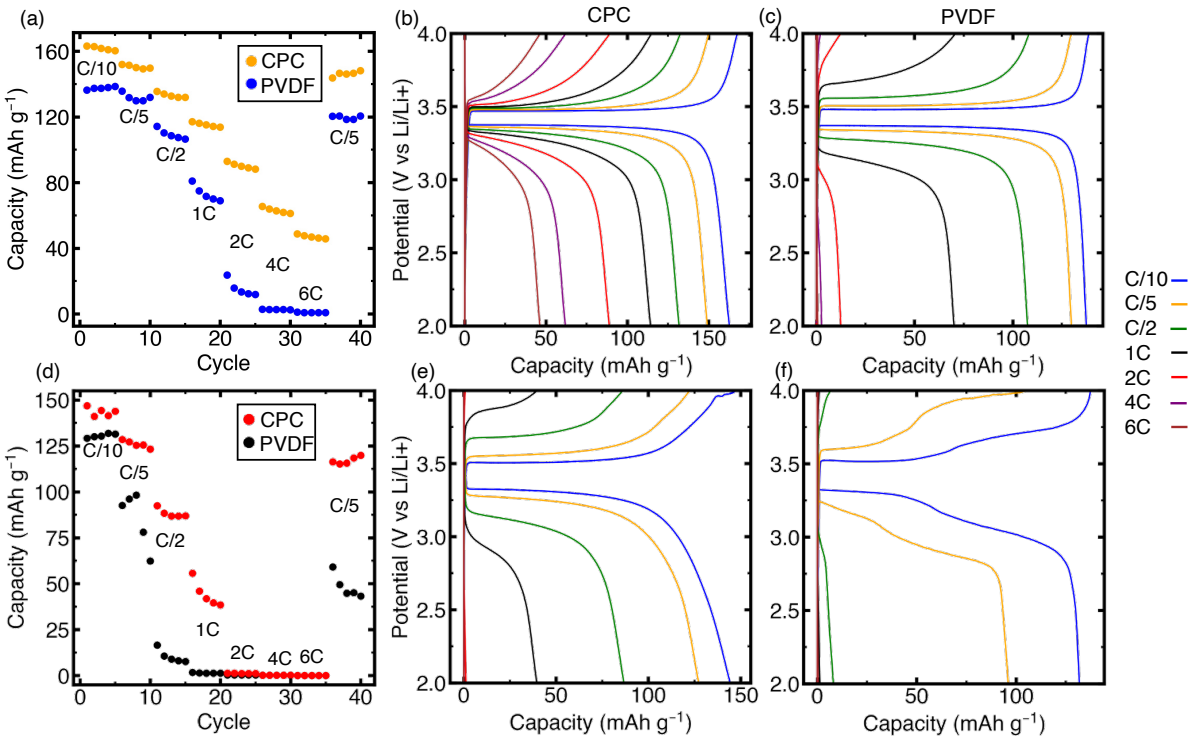


**Figure 4.22: Variable rate data for cells utilizing a 1M LiTFSI in 1:1 v EC:DMC electrolyte**

Data is presented for 85:6:9 LFP:Carbon:Binder cells (a,b,c) and 85:15 LFP:Binder cells (d,e,f) utilizing a 1M LiTFSI in 1:1v EC:DMC electrolyte solution. A different electrolyte was tested to probe the charge screening/solubility impacts on the complex. It is evident that the complex performs dramatically better than PVDF in both LiTFSI and $LiPF_6$ electrolytes.

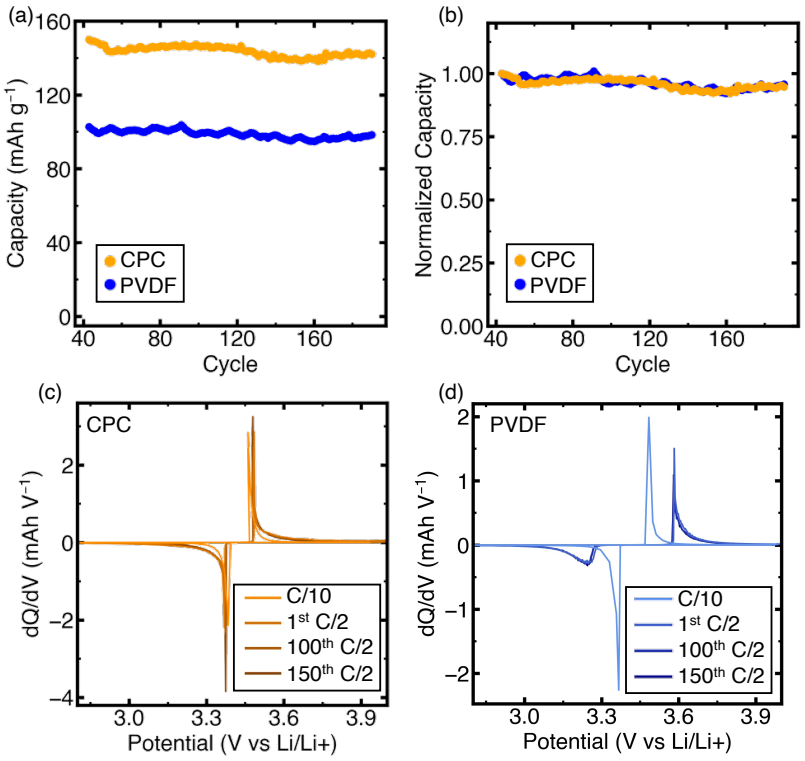


**Figure 4.23: Cycle stability data cells utilizing a 1M LiTFSI in 1:1v EC:DMC electrolyte**

Capacity retention of (85:6:9 wt.%) composite cathodes (a) shown as specific capacity vs. cycle number and (b) shown as capacity retention, where each cycle's discharge capacity is normalized to that of the first cycle. (c) and (d) show differential capacity curves for the initial formation cycle at C/10 and for the first, 100$^{th}$, and 150$^{th}$ C/2 cycle of the stability test.

Cycle stability results for the LiTFSI cells (Figure 4.23) show similar stability between the CPC and PVDF binders, confirming the conclusion from the main text that the ionic crosslinks in the CPC binder remain stable over many cycles. Here, both binders maintain 94% of their initial C/2 capacity over 150 cycles. As discussed, this improved stability with respect to the $LiPF_6$ electrolyte is not surprising given the numerous parasitic reactions $LiPF_6$ is known to undergo.[173–175] The lack of such side reactions here is evident by looking at Figures 4.23 c,d, which shown dQ/dV analysis for cells containing the CPC and PVDF binders utilizing a 1M LiTFSI in1:1 EC:DMC electrolyte. Neither cell shows significant growth in overpotential or appearance of additional peaks, indicating little to no side reactions are occurring.

# Chapter 5

# Mixed ion-electron conducting polymer complexes as high rate battery binders

## 5.1 Abstract

Next generation battery binders must have both the adhesive properties of traditional binders (i.e. polyvinylidene fluoride (PVDF)) as well as high electronic and lithium ion conductivity to facilitate good rate performance. Here, we demonstrate a broadly applicable strategy of using electrostatic compatibilization between a conjugated and non-conjugated polyelectrolyte, which provides intrinsic ionic and electronic conduction while also maintaining stability with conventional battery materials, resulting in high rate capability in $LiFePO_4$ (LFP) based cathodes. Three polythiophene based polyelectrolyte complexes demonstrate electronic conductivities as high as 0.8 S/cm and room temperature ionic conductivities above $10^{-4}$ S/cm when swollen with electrolyte ($\approx 1\times10^{-7}$ S/cm dry, without the presence of small molecule electrolyte). Each complex proves to be an excellent binder when applied in LFP composite cathodes, enabling dramatic reductions in overpotential and improved performance at high cycling rates compared to cells utilizing a PVDF binder. The improved charge transport afforded by the conducting binders enables up to 70% of the cathode's capacity to be utilized at 6C, compared to only 1.4% when PVDF is the binder. These results demonstrate that complexation of conjugated polyelectrolytes is not only an effective design strategy for intrinsic mixed ion-electron conduction, but also provides the stability and

processability necessary for Li-ion battery binder applications, making them promising "pick and place" materials to achieve large performance improvements in LFP cathodes.

## 5.2 Introduction

Polymer binders serve a crucial, adhesive role in lithium (Li)-ion battery cathode films, holding together the active material and conductive additive, and binding each to the current collector. Polyvinylidene fluoride (PVDF) is the most widely used polymer for this task due to its chemical stability, yet it is insulating to both ions and electrons and therefore constitutes a resistive bottleneck to charge transport limiting performance, particularly at high rates.[97,98,126,178] Electronically conductive conjugated polymers have been shown to address this limitation, reducing resistance and improving rate capability when applied as binders and protective coatings.[16,40,72,178–183] Polythiophene derivatives have been the most widely studied family in this regard, owing to their stability and favorable doping potential around 3.2-3.4V vs $Li/Li^+$, meaning that they conduct for the duration of the charge/discharge process of most Li-ion cathodes.[16,40,72] Polythiophenes also enable facile functionalization, affording highly tunable properties. For example, functionalizing both the 3- and 4- position with an alkylenedioxy bridge affords poly(3,4-propylenedioxythiophenes) (PProDOTs), which possess an expanded electrochemical stability window and lower onset for oxidation due to the electron donating oxygens atoms covalently bound to the thiophene ring.[184,185] These systems have been demonstrated as promising binders in both NCA and LFP cathodes.[16,40,186] Other design strategies have explored poly(3-hexylthiophene) (P3HT) and its analogues, where side chain engineering of the 3-position with charged moieties affords high ionic conductivity and good lithium transference,[14,15] critical properties for battery functionality.

However, the charged side chains also drive dissolution of the polymer in polar solvents, including conventional battery electrolytes, drastically limiting their applicability.

Balancing ionic conductivity, electronic conductivity, lithium transference, and dissolution has proved a challenge from a polymer design perspective. In single component systems, the addition of ion conducting side chains to a conjugated polymer backbone improves ion transport within the polymer,[15,39,40,124] but as the polymer becomes increasingly polar, it dissolves in the battery electrolyte.[40] Specifically, ether functionalized ProDOTs have mixed ion-electron conducting properties,[17,40] but to prevent dissolution the ether substituted monomers had to be copolymerized with the less polar, dihexyl substituted ProDOT. In fact, the ether side chain density was limited to 25% to avoid dissolution,[40] placing an intrinsic limit on the ability to impart ionic conductivity to the polymer binders. Conjugated polymer-PEO block copolymers have also shown promise as mixed conducting binders.[64,77,179,182] However, the self-assembled block copolymer architecture leads to an intrinsic tradeoff between ionic and electronic transport, as each block is responsible for transport of one charge carrier or the other. Furthermore, recent work on lithium-specific transport in mixed conducting polymers has shown that while ether substituents impart good overall ionic conductivity, they immobilize the lithium ion leading to low transference numbers.[14] With respect to lithium transport, charged side chains appear to be advantageous.[14,15,35] Thus, new binder design strategies may be necessary to both enhance lithium conduction, retain electronic conduction, and prevent dissolution in the battery electrolyte.

We have recently suggested complex coacervates as high conductivity, dissolution-resistant battery binders.[187] Associative, liquid-liquid phase separation driven by electrostatic attraction is routinely used in the formulation of industrial products and is also thought to be the mechanism by which high solids loading biological fluids and membraneless organelles are formed.[50,188,189] Coacervation is driven by the combination of electrostatic attraction of oppositely charged polymers and entropy gained via the expulsion of the remaining counterions. This driving force is so large that it overcomes the repulsive interactions of the otherwise immiscible polymer backbones and results in a dense coacervate phase and a dilute supernatant phase.[42,50–52,55,56] While in the fluid state, the polymer-rich coacervate phase has very high solids loading (on the order of 50 wt.%) and low viscosity, when this phase is dried, ionic crosslinks between side chains provide insolubility in many common solvents.[53,54] As a result, polyelectrolyte complexes enable a diverse array of backbone and side chain architectures to be implemented in homogenous systems, offering immense tunability of electronic, ionic, and mechanical properties.

In conjugated polymer coacervates,[26,27,44–49] complexation affords the solubility, miscibility, and processing advantages already mentioned, but has also been shown to have profound effects on optoelectronic and conduction properties, as structural templating of the conjugated polymer occurs during complexation, resulting in a planarized backbone with highly delocalized excited states.[26,46,49] For instance, complexing a conjugated polyelectrolyte (CPE) with electronically insulating polyelectrolytes has been shown to increase the conjugation length and carrier mobility of the CPE, resulting in higher overall electronic conductivity, despite the system being composed of 50 mol.% of an electronic insulator.[27] Additionally,

conjugated polymer complexes can form high solids loading, viscous coacervate phases, substantially improving processability compared to single component conjugated polymers.[44] Thus, conjugated polymer complexes combine the tunability and processability of polymer complexes with the electronic conductivity of conjugated polymers, making them promising materials for electrochemical applications. In fact, we recently demonstrated an electrostatically-stabilized conjugated polymer complex that can serve as a high performing battery binder in $LiFePO_4$ composite cathodes. This is due to the high conductivity of the complex, which reduces the overpotential and improves charge transport kinetics. Additionally, the ionic crosslinks provide stability in conventional electrolytes, enabling a drop-in mixed ion-electron conducting battery binder.

Here, the broad applicability of electrostatic compatibilization as a binder formulation strategy is demonstrated. We find that improved conductivity and stability are universal across a diverse array of conjugated polyelectrolyte complexes. Specifically, a variety of charged, ionic groups are demonstrated to enable polyelectrolyte complexation, which affords both facile processing during electrode fabrication and good stability during cycling. This is a particularly important observation as it allows for the incorporation of relatively inexpensive, commodity polyelectrolytes as a major component of the binder. Electrostatic interactions compatibilize the two polymers, initially forming a coacervate phase which maintains the ability to flow and form coatings. Upon drying of the electrode slurry, the ionic interactions between the two polyelectrolytes form strong cross-links, leading to good stability during cycling. The intrinsic electronic conductivity, ionic conductivity, lithium transference, and electrochemical stability of all complexes display similar advantageous properties- a broad electrochemical stability

window, high conductivity, and lack of dissolution in a standard battery electrolyte (1M $LiPF_6$ 1:1v EC:DMC). It follows that each complex dramatically improves the rate capability when applied as a binder in $LiFePO_4$ cathodes. This work provides the critical insight that electrostatically-stabilized complexes enhance electronic conductivity, provide high ionic transport, and are stable in a Li-ion battery environment, making them an ideal platform for conductive binders.

## 5.3 Experimental Methods

### *2.1 Complexation*

Conjugated polymers were synthesized according to previously published procedures,[14,133,134] which are described in detail in Appendix 5.6 (Figures 5.9-5.11). Poly(sodium 4-styrenesulfonate) ($Na^+PSS^-$) was purchased from Sigma-Aldrich (70 kDa), further purified by dialysis in ultrapure Milli-Q deionized water using 10kDa cutoff membranes, and finally collected as a fluffy white powder via lyophilization. The polymer complexes were prepared according to previously published procedures:[26,27] Polymer concentrations of 1M in 40/60 THF/water were selected to ensure formation of a viscous coacervate (rather than precipitate).[26] Charge balanced ratios of each polymer were added to a centrifuge tube, vortexed, then centrifuged for 10 min at 7,000 rpm to isolate the coacervate phase. The polymer dilute, counterion-rich supernatant phase was then decanted, followed by thorough washing of the coacervate with the THF/water mixture. The removed mass was weighed to inform the remaining mass of polymer complex.

### *2.2 Optical Microscopy*

A small volume of each of the conjugated polymer complexes was sandwiched between two quartz slides. Images were taken on an Olympus BX51 microscope in bright-field mode, calibrated in StreamView (Olympus).

### *2.3 Conductivity*

*Electronic Conductivity*

Custom made silicon substrates with gold digits were used for electronic conductivity measurements. CPE samples were spun cast from 10 mg/mL polymer solutions at 1000 rpm for 60 seconds. Complex samples were prepared as previously described and blade coated onto the substrates. Samples were dried/annealed under high vacuum ($2 \times 10^{-8}$ torr) at 130°C for 12 hours. Film thickness were determined by ellipsometry.

HTFSI was used as the dopant and introduced via vapor phase infiltration. Inside a nitrogen filled glovebox, pristine films were attached to the lid of a jar containing HTFSI crystals using double sided Kapton tape. The sealed jar was placed on the hot plate set at 50°C for 1, 3, and 12 hours. DC conductivity measurements were performed by applying DC potentials between -1V and 1V at 100 mV intervals. Once resistance was determined, conductivity was found using the following equation.

$$\sigma = \frac{1}{R}\frac{d}{lh}$$

where $\sigma$ is the conductivity, $R$ is the resistance, $d$ is the distance between the gold digits, $l$ is the length of each digit, and $h$ is the polymer film thickness. Here, $l$=2.7 mm and $d$=100 μm,

150 μm, and 200 μm, as the substrate utilized several groups of digits at these 3 spacings, of which the average results are reported.

*Ionic Conductivity*

A through plane configuration utilizing ion blocking electrodes was used to determine ionic conductivity via AC impedance. First, isolated coacervates were thoroughly washed to remove all polymer counterions, as confirmed by the negligible ionic conductivity of the resulting system (Figure 5.16). Concentrated solutions of LiTFSI in water were then used to introduce a controlled amount of LiTFSI to the system, which was vortexed and allowed to equilibrate for 2 days, after which the complexes appeared as a homogenous gel. The complex was then cast onto an aluminum current collector with a well-defined thickness provided by the use of a Kapton spacer. The same was then dried at 150°C at $10^{-8}$ torr for 12 hours to remove any trace solvent. Samples were then loaded into an argon glovebox and a second aluminum current collector was pressed on top of the sample to afford through plane EIS conductivity measurements.

Electrolyte swollen samples were initially prepared in the same manner described above- the complex was prepared, cast, and dried. PVDF was solvent cast using NMP, then dried at 150°C at $10^{-8}$ torr for 12 hours in the same manner as the complex. After drying, the samples were placed in a glovebox and excess electrolyte (1M $LiPF_6$ in 1:1 v EC:DMC) was pipetted onto the top surface. Polymers were allowed to passively swell for 24 hours, after which excess electrolyte was removed via wicking with a Kimwipe. Samples were sealed with the top aluminum current collector and measured.

Samples were placed into a Controlled Environment Sample Holder (CESH) from Biologic LLC, which maintains an inert atmosphere during measurement. Variable temperature conductivity measurements were performed using Biologic's Intermediate Temperature System (ITS) in conjunction with their VSP-300 potentiostat. A sinusoidal voltage with amplitude 100 mV was applied in the frequency range of 0.1 Hz−3 MHz. Data was then fit to the equivalent circuit shown in Figure 5.15 to extract the resistance. From these equivalent DC resistances, conductivity was calculated according to the following.

$$\sigma = \frac{1}{R}\frac{t}{A}$$

Where $t$ is the thickness of the polymer film and $A$ is the area, both of which are defined by the Kapton spacer.

### *2.4 DC Polarization*

DC polarization was performed following the widely reported technique developed by Bruce and Vincent.[14,35,68] Symmetric lithium−polymer−lithium cells were assembled in an argon glovebox and loaded into a Controlled Environment Sample Holder (CESH) from Biologic LLC. Test were performed on Biologic's Intermediate Temperature System (ITS) in conjunction with their VSP-300 potentiostat to 80°C, which is common practice as elevated temperature improves signal to noise. Samples were allowed to rest for 12 hours after construction and were then equilibrated at 80°C and monitored via EIS until the system stabilized. A 100 mV potential bias was applied and the resulting current measured over time. EIS measurements with a 20 mV amplitude were performed at 40-minute intervals to monitor changes in the interfacial resistance. Lithium transference numbers were calculated following the method of Bruce and Vincent:[68]

$$t_{Li+} = \frac{I_{ss}(\Delta V - I_\Omega R_0)}{I_\Omega(\Delta V - I_{ss}R_{ss})}$$

Here, ΔV is the applied potential (100 mV), $R_0$ and $R_{ss}$ are the initial and steady-state interfacial resistances, respectively, $I_{ss}$ is the steady- state current, and $I_\Omega$ is the initial current determined from Ohm's law:

$$I_\Omega = \frac{\Delta V}{R_\Omega}$$

where $R_\Omega$ is the initial cell resistance (bulk and interfacial) measured by EIS. Using $I_\Omega$ instead of the initial current measured by the potentiostat eliminates errors related to the speed at which the instrument can record the current.

### *2.5 UV-Vis Absorption Spectroscopy*

UV−Vis absorption was performed on an Agilent Cary 60 UV−Vis Spectrophotometer. Spectra were taken on 0.5 mm thick quartz substrates. CPE samples were spun cast, while coacervates were both blade coated and sandwiched between two slides and sheared to form sufficiently thin films for measurement, both methods provided the same absorption spectra.

### *2.6 Cell Construction and Testing*

Cathodes were prepared via slurry processing using a composition of 85:6:9 by mass (LFP:Carbon:Polymer). LFP (MTI) and carbon black (Timcal super C65) were first mixed in the appropriate ratio using a mortar and pestle. The appropriate amount of this powder was then added to polymer solutions- PVDF (Solef, Solvay) in *N*-methyl-2-pyrrolidone (NMP) and the polyelectrolyte complexes in THF/water. The slurries were then thoroughly mixed and cast onto aluminum foil using a doctor blade. The electrodes were allowed to slowly air dry, then

heated to 80°C until they were visually dry and placed under vacuum for 10 minutes. The films were then punched into disks to obtain the electrodes, which then underwent a final drying stage for 12 hours at 150°C and $2\times10^{-8}$ torr. The average mass loadings were around 2 mg/cm$^2$.

After thorough drying, the cathodes were transferred into an Argon filled glovebox (<0.5 ppm oxygen, <0.5 ppm water). CR2032 coin cells sourced from Hoshen were fabricated using lithium metal anode/counter electrodes and Celgard 2325 (PP/PE/PP) separators. The electrolyte was 1M $LiPF_6$ in 1:1 ethylene carbonate and dimethyl carbonate (1/1 v/v EC:DMC). Cells were crimped using a pressure-controlled crimper (MTI) set to 0.9 MT.

Rate capability tests were performed using galvanostatic cycling, where the C rate is defined using the theoretical capacity of 170 mAh/g for LFP. For clarity: 1C indicates a current such that the entire (theoretical) capacity of the cell would be utilized in 1 hour. C/2, is half that rate, meaning the capacity is utilized in 2 hours. Initially, cells were allowed to rest for 12 hours while the OCV was monitored. After this, 5 C/10 cycles were performed to ensure complete SEI formation before subsequent testing. EIS was performed at the top of charge and bottom of discharge of the 4$^{th}$ cycle. The cells were allowed to rest for 1 hour prior to each EIS test. After the C/10 formation cycles, the variable rate cycling was performed, where cells underwent 5 cycles at each rate of C/5, C/2, 1C, 2C, 4C, 6C, and C/5.

## 5.4 Results and Discussion

The goal of this work is to show the versatility of electrostatically-stabilized, conjugated polyelectrolyte complexes (CPCs) as conductive battery binders, particularly focusing on

intrinsic transport properties that translate to improved rate capability of the battery. Our previous work demonstrated a sulfonate functionalized polythiophene complexed with an imidazolium functionalized acrylate as a high performing binder in $LiFePO_4$ (LFP) cathodes.[187] Here, we show the diverse applicability of mixed conducting CPCs as binders, studying a series of model polythiophenes functionalized with cationic side chains, namely poly(3-(6'-(N-methylimidazolium)hexyl)thiophene $Br^-$) (P3HT-$Im^+Br^-$), poly(3-(hexylthiophene)-co-3-(6'-(N-methylimidazolium)hexyl)thiophene $Br^-$) 50:50 (P3HT-co-P3HT-$Im^+Br^-$), and poly(3-(6'-trimethylammonium)hexyl)thiophene $Br^-$) (P3HT-$TMA^+Br^-$), each complexed with the sulfonate containing poly(sodium 4-styrenesulfonate) ($Na^+PSS^-$), as shown in Figure 5.1b. This series demonstrates the universality of this approach across a wide variety of ionic chemistries. Notably, $Na^+PSS^-$ is a low cost and commercially available polyelectrolyte, increasing the relevance of these systems to real battery applications. In each system, high mixed electron-lithium conductivities were observed: electronic conductivities of up to 0.8 S/cm accompanied by ionic conductivities of $\approx 10^{-7}$ S/cm when dry and $10^{-4}$ S/cm when swollen with electrolyte, with lithium transference numbers ($t_{Li+}$) of up to 0.26. Additionally, each complex is stable in a standard, liquid battery electrolyte (1M $LiPF_6$ in 1:1 EC:DMC), which often dissolves ionically-conducting binders.[40] Here, the ionic crosslinks prevent dissolution, making the CPCs ideal candidates for Li-ion cathode binders, where they indeed provide a dramatic improvement in rate capability compared to cells with a PVDF binder, utilizing 70% of the cathode's capacity at 6C compared to only 1.4% for PVDF-containing cells. Thus, by improving processability, solubility, and conductivity, it is shown that electrostatically-stabilized complexes serve as an ideal platform for conductive battery binders. Furthermore, the universality of this approach across a wide variety of chemistries

suggests an ability to independently tune the binder chemistry without altering the stability and processibility afforded by the polyelectrolyte complex.

### *3.1 System Design*

Complexing two polyelectrolytes with oppositely charged sidechains (Figure 5.1) imparts stability, (in)solubility, conductivity. Ionic interactions initially compatibilize the two polyelectrolytes into a processable coacervate phase, which upon drying/solvent removal forms hard ionic-crosslinks, preventing dissolution in the polar battery electrolyte (1M $LiPF_6$ in 1:1 v EC:DMC). Specifically, three catatonically-functionalized polythiophenes are complexed with the anionic polyelectrolyte $Na^+PSS^-$. Thiophene derivatives are advantageous for cathode applications, as they are semiconducting with low conductivities (in the insulating regime) at low potentials until oxidization occurs around 3.2V vs $Li/Li^+$. This is suitable for LFP cathodes, as the flat (dis)charge voltage profile characteristic of LFP's two phase reaction occurs above this potential (around 3.4-3.5V). As a result, the binder is conductive over the entire charge/discharge cycle. Additionally, the system is electrochemically stable up to 4.6V vs $Li/Li^+$. $Na^+PSS^-$ is an ideal model anionic polyelectrolyte, as it has been previously shown to complex with both imidazolium and trimethylammonium functionalized conjugated polymers.[26,190] Additionally, its low cost and commercial availability increases the impact these developments could have on real battery systems.

While each individual conjugated polyelectrolyte is soluble in the battery electrolyte (Figure 5.12), upon complexation, electrostatic interactions, along with entropy gains upon the release of the counterions, drive and stabilize the complex. This solves a major hurdle faced by many

conducting polymer binders, in that high ionic conductivity is typically at odds with stability against dissolution in the electrolyte (highly polar or charged groups capable of transporting ions will also dissolve in the highly polar battery electrolyte). Finally, the complexes form a viscous coacervate phase, enabling removal of counterions and slurry coating of electrodes.

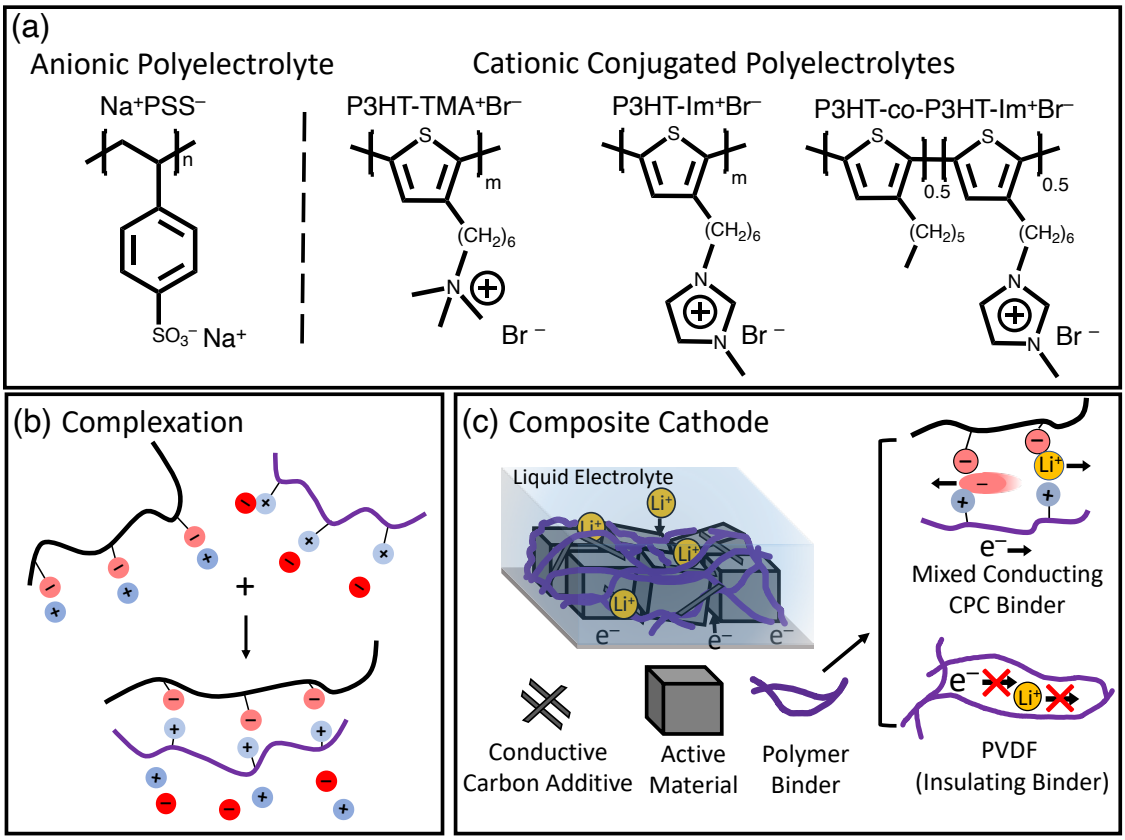


**Figure 5.1: Overview of polymer chemistry, complexation strategy, and electrode format studied here**

(a) The polymers used in this work. Conjugated polyelectrolytes bearing cationic side chains (right) were complexed with the anionic polyelectrolyte $Na^+PSS^-$ (left). A schematic of the general complexation scheme is shown in (b), where the electrostatic interactions, as well as the entropy gain upon release of the counterions, makes complexation thermodynamically favorable. (c) Typical construction of a composite cathode, where the active material (grey cubes) supports lithium ion (de)intercalation, carbon additives are added for electronic conduction, and liquid electrolyte is used for ion transport. The polymer binder (purple lines) is typically PVDF, which is insulating to charge transport. Conducting polymers (right) remove this resistive barrier, facilitating charge transport between the active material particles, electrolyte, and current collector.

### *3.2 Complex coacervation*

Conjugated polyelectrolyte complexes can form solutions, precipitates, and coacervate phases,[26,44] however the coacervate phase is needed to achieve processability in a manner appropriate for battery applications.[187] During complex coacervation, counterions ($Na^+$ and $Br^-$ in the present case) are predominately released into the supernatant phase,[191–193] resulting in entropic gains which, along with electrostatic interactions, make complexation thermodynamically favorable.[55,194–196] Subsequent rinsing effectively removes residual ions, such that there is no appreciable ionic conduction in the neat complexes (Figure 5.16).[161] Importantly, coacervates maintain the ability to flow with relatively low viscosity, allowing formation of uniform coatings and slurry processing. Each complex studied here shows a similar ability to coacervate. Optical microscopy (Figure 5.2) shows homogenous, red images, indicative of the isolated coacervate phase. A solid precipitate would appear as a dark (opaque) solid features (Figure 5.14).[26]

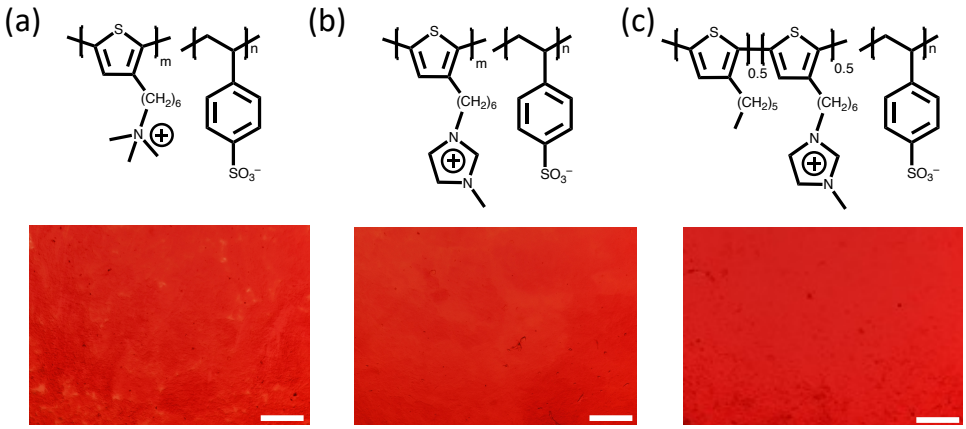


**Figure 5.2: Optical microscope images of isolated coacervates**

Structures of the complexes (top) corresponding to each optical microscope image depicting the isolated, polymer-rich coacervate phase (bottom). The homogeneous red color indicates a lack of precipitate, which would appear as irregular, dark solids. Scale bars represent 200 μm.

### *3.3 Electronic and ionic transport*

Complexation of conjugated polyelectrolytes with an insulating polyelectrolyte appears to both drive chain planarization and improve the arrangements between chains resulting in substantially increased charge mobility and much higher electronic conductivity than each analogous neat conjugated polymer substituent, despite the complexes containing 50 mol% of an electronic insulator. This effect is particularly pronounced in the complexes consisting of conjugated homopolymers, which demonstrate a roughly 2 order of magnitude increase in conductivity upon complexation. This increase in conduction has generally been accompanied by planarization and conjugation length extension upon coacervation, as evidenced by a red-shift in the optical absorbance,[26,39] which is consistent with the observation here for P3HT-$Im^+PSS^-$ and P3HT-$TMA^+PSS^-$ (Figure 5.4). UV-Vis absorbance shows that the neat CPE homopolymers have absorbance peaks centered around $\lambda \approx 465$ nm, and an absorption edge around $\lambda \approx 600$ nm, consistent with predominately disordered polymers. Upon complexation, a peak shift is observed to $\lambda \approx 500$ and 515 nm, and the absorption edge shifts to around $\lambda \approx$ 627 and 634 nm (for P3HT-$Im^+PSS^-$ and P3HT-$TMA^+PSS^-$, respectively), consistent with an extension of the $\pi$-conjugation length. Interestingly, the copolymer does not experience a red shift upon complexation. However, unlike the homopolymers, P3HT-co-P3HT-$Im^+Br^-$ does display some level of order prior to complexation, with the absorbance peak centered around $\lambda \approx 512$ nm and an absorption edge around $\lambda \approx 650$, as well as the presence of a small shoulder around $\lambda \approx 590$ nm often associated with aggregates.[137] This explains the higher conductivity of P3HT-co-P3HT-$Im^+Br^-$ relative to the homopolymer counterparts. Additionally, similar absorbance spectra and conductivity trends have been reported for other partially charged CPCs.[27]

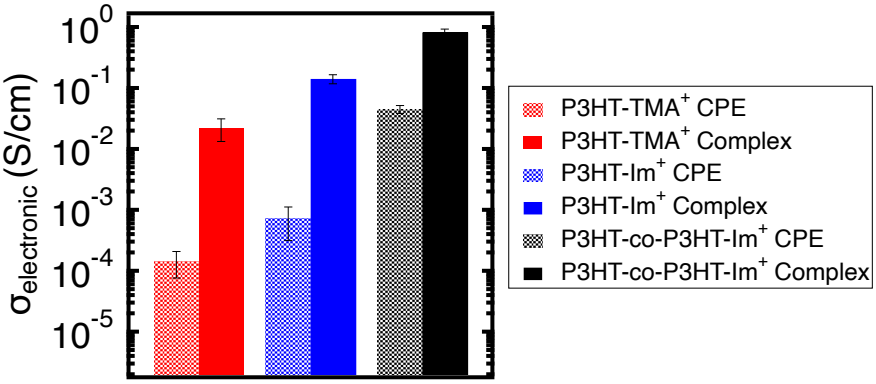


**Figure 5.3: Electronic conductivity of HTFSI doped samples**

Shaded bars represent data from the neat CPEs, while solid bars represent data from their respective complexes with $PSS^{-}$. All systems display an increase in conductivity upon complexation. Vapor phase HTFSI doping was performed under several conditions, with the highest obtained values reported here.

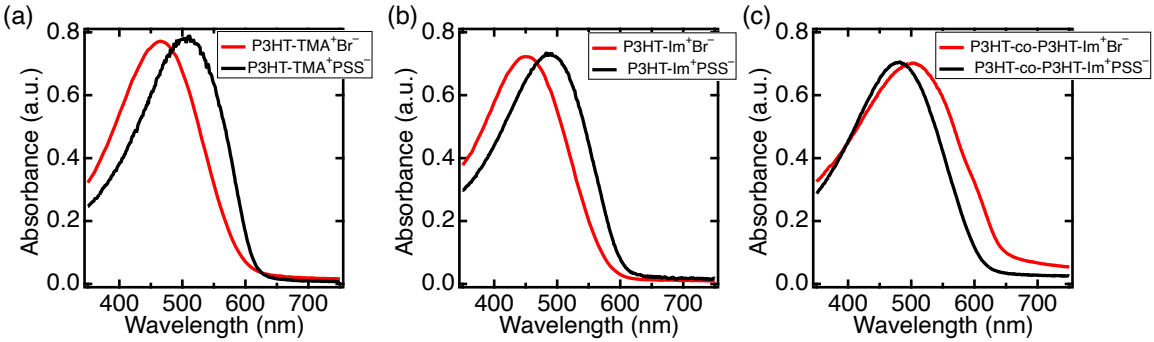


**Figure 5.4: UV-Vis absorbance spectra**

Spectra for the neat CPEs (red) and for their respective complexes with $PSS^{-}$ (black): (a) P3HT-$TMA^{+}$, (b) P3HT-$Im^{+}$, and (c) P3HT-co-P3HT-$Im^{+}$.

*Ionic Transport*

Each complex demonstrates appreciable intrinsic ionic conductivity upon addition of LiTFSI, achieving conductivities between $10^{-5}$ and $10^{-7}$ S/cm at 80°C (Figure 5.5). By studying several LiTFSI concentrations, differences in solvation capability become apparent, where the imidazolium containing CPCs display a monotonic increase in conductivity as LiTFSI is

added, and the trimethylammonium CPC shows a substantial decline from r=0.5 to r=1.0. This trend results from competing effects between the higher charge carrier concentrations and reduced ion mobility resulting from ion-ion and ion-polymer interactions.[29] Additionally, the trimethylammonium group has a more localized cationic charge, increasing ion-polymer interaction strength and reducing its ability to solvate large quantities of salt.[29,197] This general trend is consistent with reports of analogous CPE and PIL systems bearing imidazolium and trimethylammonium pendants,[198,199] as well as zwitterionic polyelectrolytes containing $Im^+/SO_3^-$ groups and $TMA^+/SO_3^-$ groups, where the imidazolium containing system displays far superior ionic conductivity.[35] It is worth noting that while higher ionic conductivities have been reported for the individual CPEs,[198] the complexes display far superior electronic conduction, establishing complexation as a valuable design strategy to balance both properties in mixed conductors. Additionally, an appreciable fraction of the ionic conductivity for each complex comes specifically from the $Li^+$ ion, displaying transference numbers between 0.17 and 0.26, as measured by the DC polarization method developed by Bruce and Vincent (Figure 5.17).[68]

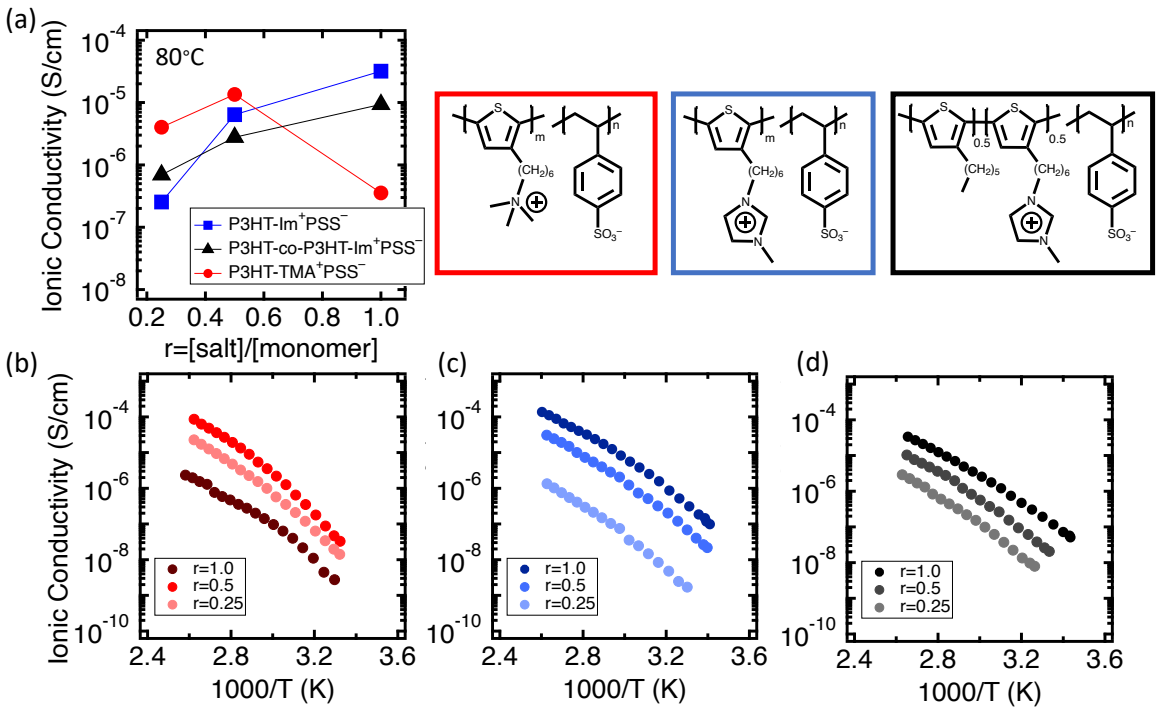


**Figure 5.5: Ionic conductivity as a function of (a) LiTFSI concentration and (b-d) temperature**

P3HT-TMA$^+$PSS$^-$ (b, red), P3HT-Im$^+$PSS$^-$ (c, blue), and P3HT-co-P3HT-Im$^+$PSS$^-$ (d, black). The diffuse imidazolium affords higher ionic conductivity both in the homopolymer and copolymer system, compared to the trimethylammonium counterpart.

Of note for typical battery applications where liquid electrolyte is present, each conjugated polymer complex displays higher ionic conductivity than PVDF when passively swollen with electrolyte (1M $LiPF_6$ in 1:1 v EC:DMC). This is unsurprising as PVDF has no ion solvating moieties, and thus no appreciable intrinsic conductivity. However, in typical Li-ion batteries, liquid electrolytes are used which will passively swell the polymer binder, affording ion transport even to otherwise insulating polymers.[40,176,177] As shown in Figure 5.6, all swollen complexes show ionic conductivities over an order of magnitude higher than that of swollen PVDF. Here, the ionic conductivity is a direct function of the polymers affinity to passively take up electrolyte. In the complexes, the charged side chains facilitate this electrolyte uptake to a greater extent compared to PVDF.

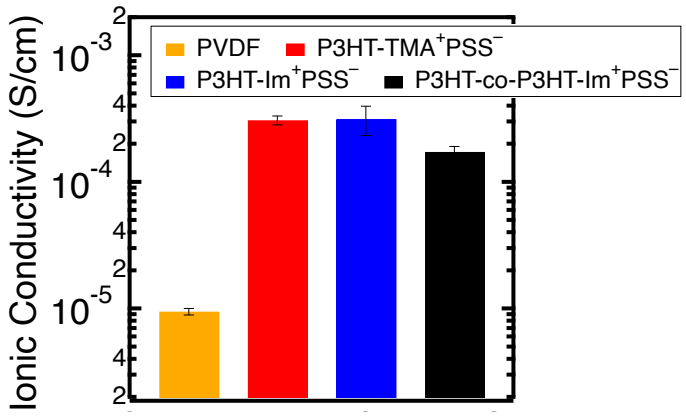


**Figure 5.6: Ionic conductivity values for polymers passively swollen with 1M $LiPF_6$ in 1:1 v EC:DMC**

From left to right, the polymers and their respective ionic conductivities are PVDF ($9.5\times10^{-6}$ S/cm), P3HT-$TMA^+PSS^-$ ($3.1\times10^{-4}$ S/cm), P3HT-$Im^+PSS^-$ ($3.1\times10^{-4}$ S/cm), and P3HT-co-P3HT-$Im^+PSS^-$ ($1.7\times10^{-4}$ S/cm).

### *3.4 Performance as a cathode binder*

In addition to favorable ion and electron transport properties, the CPCs also demonstrate electrochemical stabilities that are more than sufficient for applicability as cathode binders. Here, three key factors were evaluated: the redox potential, lack of dissolution upon repeated cycling, and electrochemical stability over the practical potential window for an LFP half-cell. Polythiophenes (and their complexes) are neutral until doped, which occurs upon oxidation of the polythiophene backbone. Figure 5.7 shows that this oxidation occurs near 3.2V vs. $Li/Li^+$, in line with the expectation for polythiophene derivatives. This means that the complex will be electronically conductive above 3.2V, which is an ideal range for LFP cathodes operating near 3.4-3.5 V vs $Li/Li^+$.

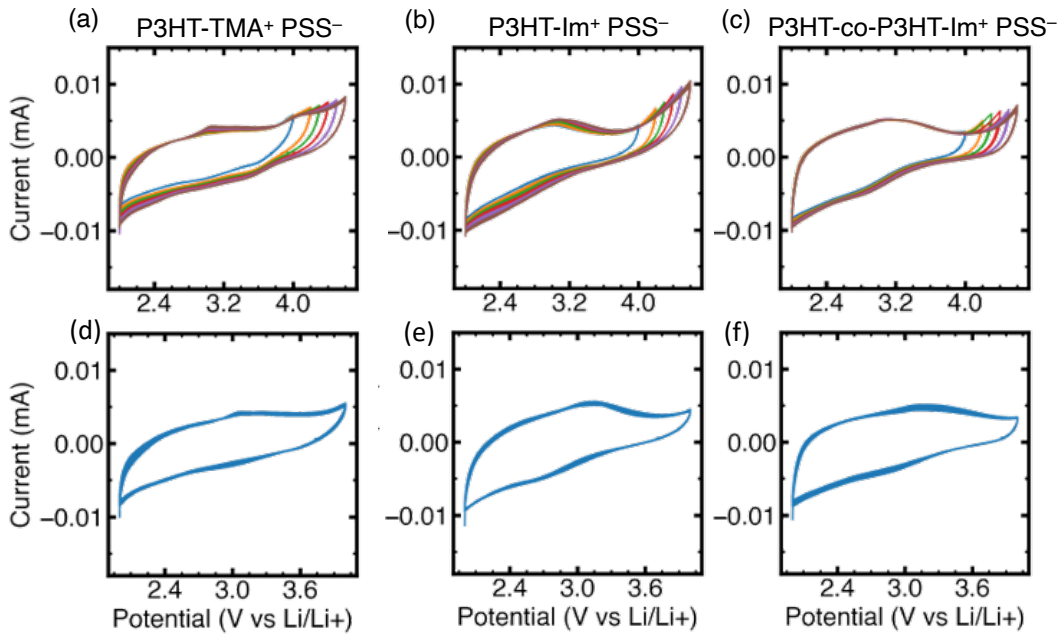


**Figure 5.7: Cyclic voltammograms of the CPCs**

CVs obtained using a lithium metal counter/reference electrode, 1M $LiPF_6$ in a 1:1 EC:DMC electrolyte, and the respective complex cast onto aluminum foil as the working electrode. (a-c) Stability tests upon increasing the upper potential limit, where 5 cycles at 10 mV/s were performed between a lower voltage cutoff of 2.0 V vs $Li/Li^+$ and a upper cutoff of 4.0, 4.2, 4.3, 4.4, 4.5, and 4.6 V vs $Li/Li^+$. (d-f) Stability tests involving 50 cycles at 10 mV/s between 2.0 and 4.0 V vs $Li/Li^+$.

To evaluate electrochemical stability of the CPCs over various potential ranges, 5 scans were performed over an increasingly larger potential window, from a lower bound of 2.0 V vs $Li/Li^+$ to an upper bound of 4.0, 4.2, 4.3, 4.4, 4.5, and 4.6 V vs. $Li/Li^+$. The lack of evolution of the cyclic voltammograms in Figures 5.7a-c, combined with the consistent redox peak shape obtained, indicate that the polymer complexes are stable up to 4.6 V vs. $Li/Li^+$. Dissolution or degradation would result in either a current increase due to degradation reactions, or a decrease due to dissolution of the polymer from the working electrode. A second stability test was carried out, this time involving 50 cycles between 2.0 and 4.0 V vs. $Li/Li^+$ to ensure no dissolution occurred over time. This is particularly important as the liquid electrolyte used (1M

$LiPF_6$ in 1:1 v EC:DMC) may induce charge screening within the complex. In theory, this could drive dissolution, as each individual CPE is soluble in this electrolyte (Figure 5.12). However, the ionic crosslinks of the complexes prove sufficiently robust to avoid appreciable charge screening, rendering the CPCs insoluble as indicated by the highly reproducible CV curves in Figures 5.7d-f.

Finally, the complexes were used as binders in LFP cathode films, and all showed a substantial decrease in overpotential and improvement in high rate performance compared to a standard PVDF binder. To assess this, five symmetric galvanostatic charge/discharge cycles were performed at each rate of interest between C/10 and 6C (Figure 5.8a). Surprisingly, while the P3HT-co-P3HT-$Im^+PSS^-$ complex exhibits only marginally better electronic conductivity than the other CPCs, and comparable total ionic and lithium conductivity to P3HT-$Im^+PSS^-$, it has far superior rate performance. Nonetheless, all CPC containing cathodes outperformed the PVDF-containing cell at high rates (4 and 6C). At slow rates, all composite cathodes perform similarly, regardless of the binder, with cells achieving capacities of 158-163 mAh/g at C/10, and utilizing similar levels of their initial capacity (between 83% and 91%) up to 1C. At rates higher than 1C, appreciable performance differences begin to emerge. For instance, the P3HT-co-P3HT-$Im^+PSS^-$ binder utilizes 76% of its initial capacity at 4C, while the P3HT-$Im^+PSS^-$, P3HT-$TMA^+PSS^-$, and PVDF containing cells utilize 49%, 43%, and 3% respectively. This trend continues at 6C, where the composite cathode containing P3HT-co-P3HT-$Im^+PSS^-$ again performs the best, delivering 114 mAh/g (70% of the C/10 capacity). When P3HT-$Im^+PSS^-$ and P3HT-$TMA^+PSS^-$ are used as binders, a capacity of 45 mAh/g (28% of the C/10 capacity) and 39 mAh/g (25% of the C/10 capacity) is instead achieved. In contrast, the PVDF-

containing cell delivers negligible capacity (2.2 mAh/g or 1.4% of the C/10 capacity). Importantly, all cells fully recover their initial slow rate capacity during the final C/5 cycles, which indicates that all cathodes are stable during high rate cycling, and performance differences stem from kinetic limitations related to PVDF's insulating properties, rather than degradation, dissolution, or other irreversible processes.

The kinetic differences observed via capacity utilization at high rates are consistent with the reduced polarization afforded by the complex binders (Figure 5.8b-d). Cell polarization, which is derived from kinetic limitations rather than thermodynamic constraints, leads to an overpotential.[166] This kinetic overpotential results in an observable voltage gap between the charge and discharge processes that can be eliminated upon very slow cycling. Additionally, path hysteresis between the Li extraction and reinsertion processes can lead to a second, thermodynamic voltage hysteresis between charge and discharge. Hence, the observed voltage gap between the charge and discharge curves obtained during galvanostatic cycling is a convolution of kinetic and thermodynamic effects. Given that all half-cells tested in the present work are prepared with a commercially-sourced LFP cathode active material, the path hysteresis is expected to be the same, and differences in the charge-discharge voltage gap between cells can provide insight as to differences in kinetic limitations associated with the different binder chemistries. For instance, the galvanostatic charge/discharge voltage profiles in Figures 5.8b-d show that at the slow, C/10 rate, the polarization is rather similar for the CPC and PVDF cells, indicating that charge transfer through the binder is not rate limiting. However, at higher rates, smaller overpotentials during both charge and discharge are observed for cells containing the CPC binders compared to those containing PVDF. Specifically, at

C/10, all cells exhibit average charge/discharge potentials of about 3.46 V and 3.35 V vs $Li/Li^+$, respectively. At 2C, polarization differences become apparent, where the PVDF cell's average charge potential is 3.86 V, and its discharge potential is 2.84 V, while those of the CPC cells are 3.52, 3.68, and 3.71 V on charge and 3.24, 3.05, and 3.03 V on discharge (for P3HT-co-P3HT-$Im^+PSS^-$, P3HT-$Im^+PSS^-$, and P3HT-$TMA^+PSS^-$ respectively). Since the binder is the only variable between the cells, these results indicate that at high rates the resistivity of PVDF is a limitation to charge transfer through the cathode composite. Figures 5.18-5.19 provide the galvanostatic charge/discharge voltage profiles for all rates studied.

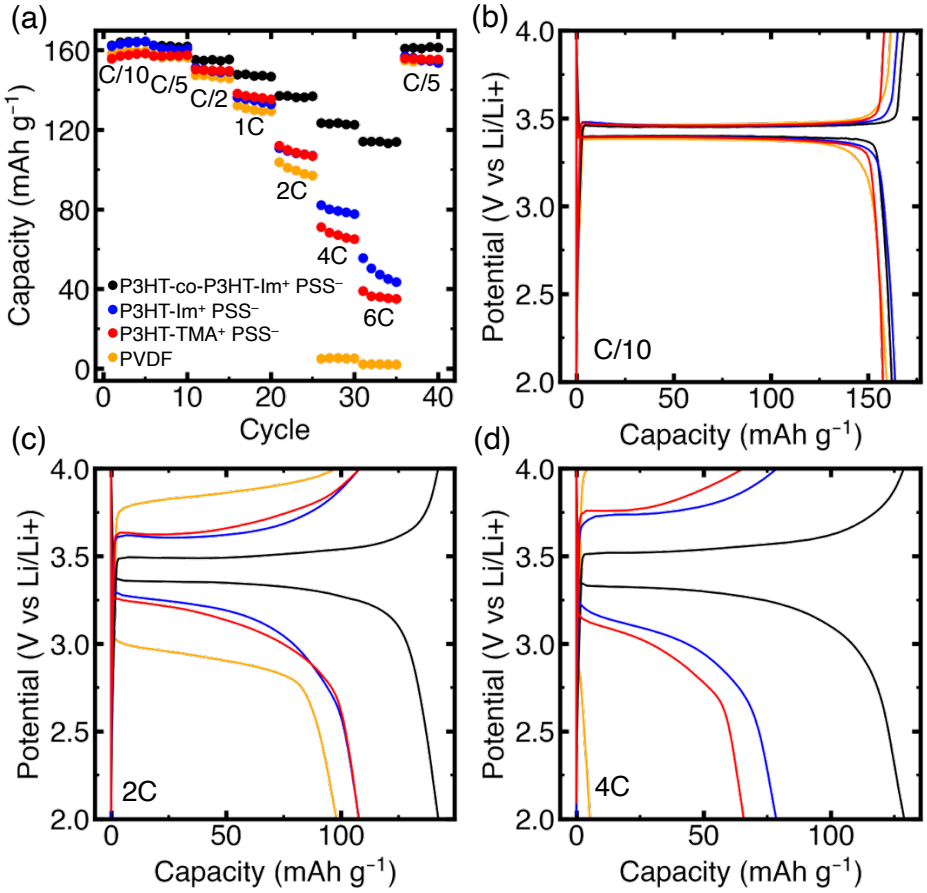


**Figure 5.8: Rate capability data for composite cathodes with varying binders**

Cells contain LFP:Carbon:Binder (85:6:9 wt.%) cathodes during symmetric galvanostatic charge/discharge. (a) Discharge capacity at the indicated rates. (b-f) Charge and discharge voltage profiles, reported for the 4$^{th}$ cycle at each indicated rate.

## 5.5 Conclusions

We demonstrate that electrostatically-stabilized complexation is a universal, effective design strategy to impart both ionic and electronic conduction, while also providing the stability necessary for battery binder applications. Several conjugated polymer chemistries were shown to have similar properties, displaying an ionic conductivity up to $10^{-5}$ S/cm, a lithium transference up to 0.26 at 80°C, and an electronic conductivity near 1 S/cm, notably higher than that of the conjugated polymers themselves. When applied as binders in $LiFePO_4$ composite cathodes, each complex displayed superior rate capability and a reduced polarization compared to a standard PVDF binder. In particular, the complex containing the 50% charge fraction copolymer (P3HT-co-P3HT-$Im^+PSS^-$) performed the best, delivering 114 mAh/g (70% of its C/10 capacity) at 6C, compared to the PVDF cell which delivered only 2.2 mAh/g (1.4% of the C/10 capacity). In summary, the applicability of conjugated polymer complexes as highly conductive battery binders is demonstrated with several polymer chemistries. This work demonstrates that coacervation is a promising and versatile strategy for binder material design to achieve appreciable performance improvements for high rate Li-ion battery applications.

**Acknowledgments**

We gratefully acknowledge support from the Department of Energy Office of Basic Energy Sciences (DE-SC0016390). The research reported here made use of shared facilities of the National Science Foundation Materials Research Science and Engineering Center (MRSEC) at UC Santa Barbara (NSF DMR 1720256), which is a member of the Materials Research Facilities Network (www.mrfn.org). G.T.P. and P.H.N. gratefully acknowledge support from

the National Science Foundation Graduate Research Fellowship Program under Grant No. 1650114 and 2139319, respectively.

## 5.6 Appendix

### Synthesis

Syntheses of P3HT-Im$^+$Br$^-$, P3HT-TMA$^+$Br$^-$, and P3HT-co-P3HT-Im$^+$Br$^-$ (50% charge fraction) were performed using modified literature procedures.[1–3] Poly(3-(6'-bromohexyl)thiophene) (P3BrHT) or P3HT-co-P3BrHT was first polymerized, and then post-polymerization functionalizations were performed to obtain the desired cationic thiophene derivatives. All reagents were sourced from Sigma-Aldrich unless otherwise stated. ACS grade solvents were sourced from Fisher Scientific. Isopropylmagnesium chloride was purchased as a 1.3M solution in THF. 2,5-dibromo-3-(6-bromohexyl)thiophene was purchased from eNovation Chemicals. Poly(sodium 4-styrenesulfonate) (Na$^+$PSS$^-$) 70 kDa was purchased from Sigma-Aldrich and further purified via dialysis, using ultrapure Milli-Q water.

***Polymerization***

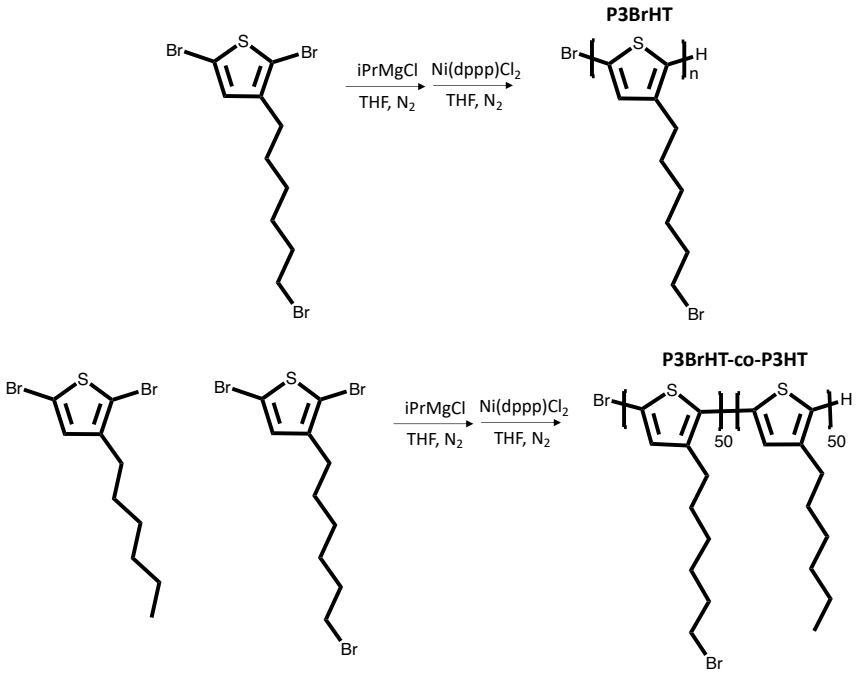


**Figure 5.9: Synthesis of P3BrHT and P3BrHT-co-P3HT (50:50).**

**Poly(3-(6'-bromohexyl)thiophene) (P3BrHT) and *P3BrHT-co-P3HT (50:50) random copolymer synthesis***

1 eq of 2,5 dibromo-3-(6-bromohexyl)thiophene or 0.5 eq. of 2,5 dibromo-3-(6-bromohexyl)thiophene and 0.5 eq of 2,5-dibromo-3-hexylthiophene were added to an oven-dried Schlenk flask, which was placed under vacuum for 2 hours. Dry, degassed THF was added via syringe and the mixture was sparged with Nitrogen. Isopropylmagnesium chloride (1.01 eq) was added dropwise and the mixture was stirred for 1.5 hr at ambient temperature under Nitrogen. 0.01 eq. of $Ni(dppp)Cl_2$ was added via syringe. The polymerization was stirred for 12 hr then quenched by rapid addition of 1M HCl and precipitated into methanol. The polymer was purified by washing in a Soxhlet apparatus with methanol and acetone before extraction with THF. The product was concentrated under vacuum.

P3BrHT 1H NMR (600 MHz, CDCl3) δ 7.18 − 6.92 (s, 1H), 3.53 − 3.37 (m, 2H), 2.93 − 2.55 (m,

2H), 2.04 − 1.81 (m, 2H), 1.80 − 1.58 (m, 2H), 1.57 − 1.30 (m, 4H)

P3BrHT-co-P3HT 1H NMR (600 MHz, CDCl3) δ 7.19-6.73 (s, 1H), 3.53 − 3.37 (m, 2H), 2.91-2.55 (m, 2H), 1.93 (m, 2H), 1.61 (m, 2H), 1.48 (m, 2H), 1.39 (m, 2H), 0.81 (t, 3H)

Gel permeation chromatography was performed on a Waters e2695 equipped with THF as the mobile phase. Results are quantified using a polystyrene standard calibrant.*:* ***P3BrHT*–:** Mn =16 kDa , Mw= 22 kDa, Đ =1.4 , ***P3BrHT-co-P3HT*** **:** Mn = 13 kDa , Mw= 17 kDa, Đ = 1.3.

***Post Polymerization Functionalizations***

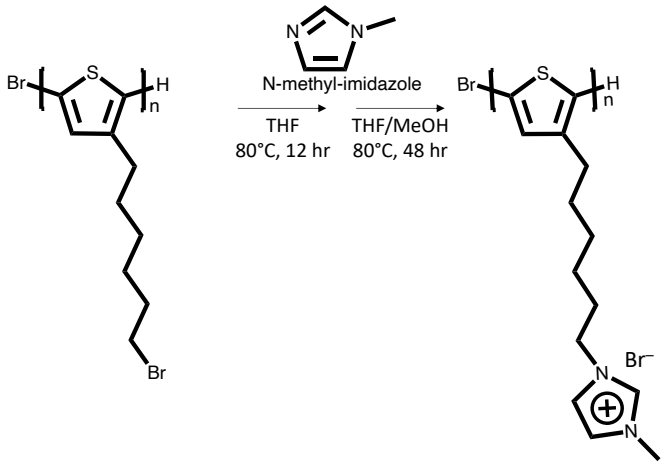

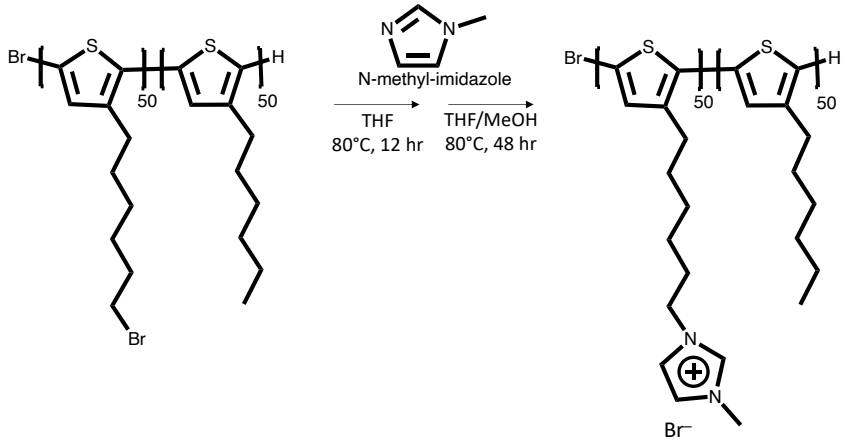


**Figure 5.10: Post-polymerization functionalization to form P3HT-Im$^+$Br$^-$ and P3HT-Im$^+$Br$^-$-co-P3HT**

**Poly(3-(6'-(N-methylimidazolium)hexyl)thiophene)**

The P3BrHT or P3BrHT-co-P3HT polymer was post-functionalized through an amine quaternization reaction. The polymer was first dissolved in THF. 1-methylimidazole (10 eq.) was added to the solution in ambient conditions. The solution was then stirred for 12 h under reflux. After 12 h, some polymer precipitate was observed in the flask. A small amount of methanol was added to fully dissolve the resulting polymer and the solution was stirred for an additional 24 hours to help achieve quantitative conversion. The polymer was then dialyzed using a 10 kDa cutoff dialysis membrane against a mixture of methanol and THF, with the dialysate replaced every 12 h.

P3HT-Im$^+$Br$^-$ $^1$H NMR (600 MHz, CD3OD) δ 8.50 (s, 1H), 7.39-7.34 (m, 2H), 7.18 (s, 1H), 4.14 (m, 2H), 3.83 (s, 3H), 2.85 (m, 2H), 1.87 (m, 2H), 1.71 (m, 2H), 1.48 (m, 2H), 1.39 (m, 2H)

P3HT-Im$^{+}$Br$^{-}$-co-P3HT 1H NMR (600 MHz, CD3OD) δ 8.90 (s, 1H), 7.51-7.34 (m, 2H), 7.18-6.62 (s, 1H), 4.14 (m, 2H), 3.83 (s, 3H), 2.85-2.25 (m, 2H), 1.73 (m, 2H), 1.61 (m, 2H), 1.48 (m, 2H), 1.39 (m, 2H), 0.81 (t, 3H)

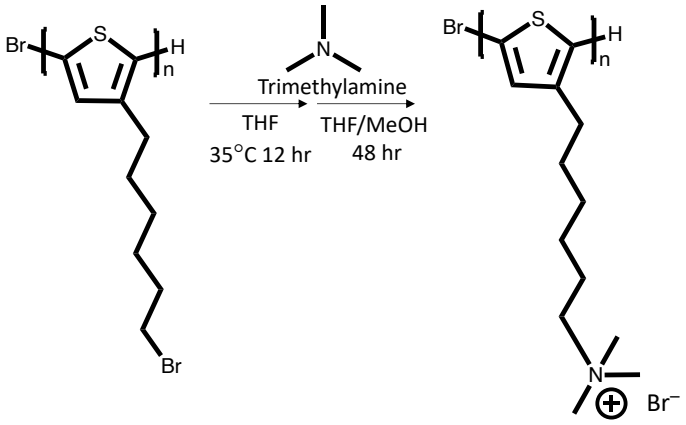


**Figure 5.11: Post-polymerization functionalization to form P3HT-TMA$^{+}$Br$^{-}$**

**Poly(3-(6'-trimethylammonium)hexyl)thiophene)**

The P3BrHT polymer was post-functionalized through an amine quaternization reaction. The polymer was first dissolved in THF. Trimethylamine (10 eq.) was added to the solution in ambient conditions. The solution was then stirred for 12 h at 35°C. After 12 h, some polymer precipitate was observed in the flask. Methanol was added to fully dissolve the resulting polymer, and an additional 2 eq of trimethylamine was added. The solution was stirred for an additional 24 hours, then the temperature was increased to 80°C and the system was refluxed for an additional 24 hours. The polymer was then dialyzed using a 10 kDa cutoff dialysis membrane against a mixture of methanol and THF, with the dialysate replaced every 12 h.

$^{1}$H NMR (600 MHz, $CD_3OD$) δ 7.18 (s, 1H), 3.35 (m, 2H), 3.12 (s, 9H), 2.85 (m, 2H), 1.87 (m, 2H), 1.71 (m, 2H), 1.48 (m, 2H), 1.39 (m, 2H)

**Additional Data**

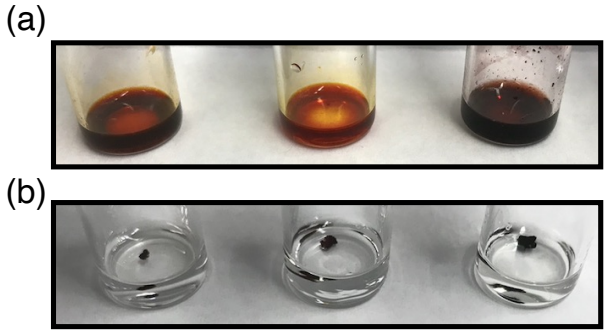


**Figure 5.12: Solubility change upon complexation**

Demonstration of solubility differences in the battery electrolyte (1M $LiPF_6$ in 1:1v EC:DMC) between the CPEs and CPCs after complexation (a) shows each CPE dissolved in the electrolyte. Shown from left to right is P3HT-TMA$^+$Br$^-$, P3HT-Im$^+$Br$^-$, and P3HT-co-P3HT-Im$^+$Br$^-$. (b) shows small pieces of each CPC after complexation and drying, where the ionic crosslinks prevent dissolution in the electrolyte. Shown from left to right is P3HT-TMA$^+$PSS$^-$, P3HT-Im$^+$PSS$^-$, and P3HT-co-P3HT-Im$^+$PSS$^-$.

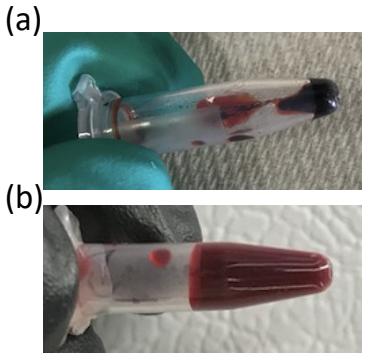


**Figure 5.13: Optical images of coacervate and supernatant phases**

(a) the coacervate and supernatant phases after separation via centrifuge. The dark, viscous, polymer rich phase at the bottom right of the tube is the isolated coacervate phase, while the lighter, free flowing fluid in the tube is the supernatant. (b) after removal of the supernatant and rinsing, a “complex gel” is made from the isolated and rinsed coacervate phase, swollen with additional solvent as desired to tune the processability.

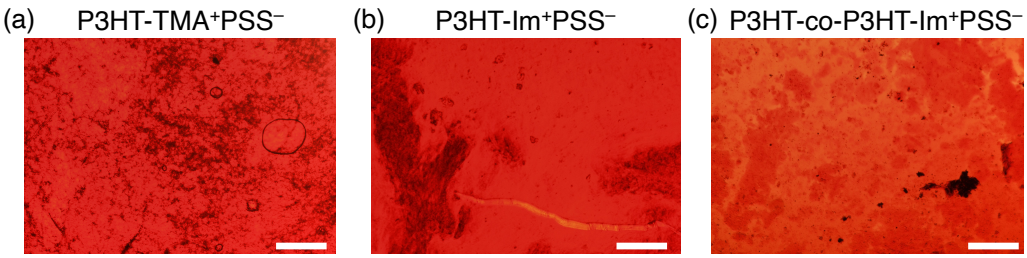


**Figure 5.14: Optical microscope images**

This images show precipitate formation, rather than coacervation as shown in Figure 5.2. Dark, irregular solid precipitates are undesirable for homogenously coating cathode materials with the polymer binder. Selecting the polymer concentrations and solvents described in the Methods section enabled coacervation. Scale bars represent 200 μm.

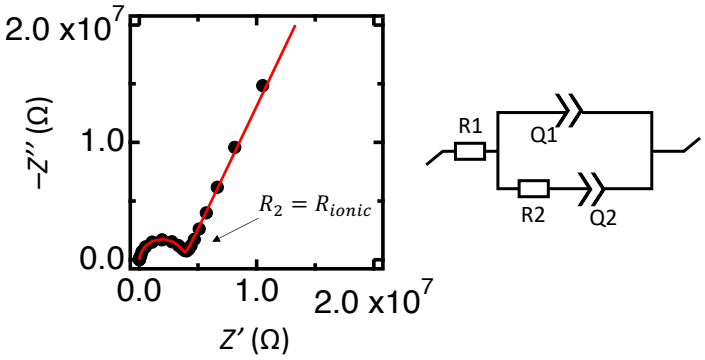


**Figure 5.15: Representative Nyquist plot for the ion conducting complexes between two, symmetric blocking electrodes.**

Data is from P3HT-co-P3HT-Im$^+$PSS$^-$ with r=0.5 (r= LiTFSI/$SO_3^-$ group). Black dots represent data and the red line represents the fit obtained using the equivalent circuit shown on the right.

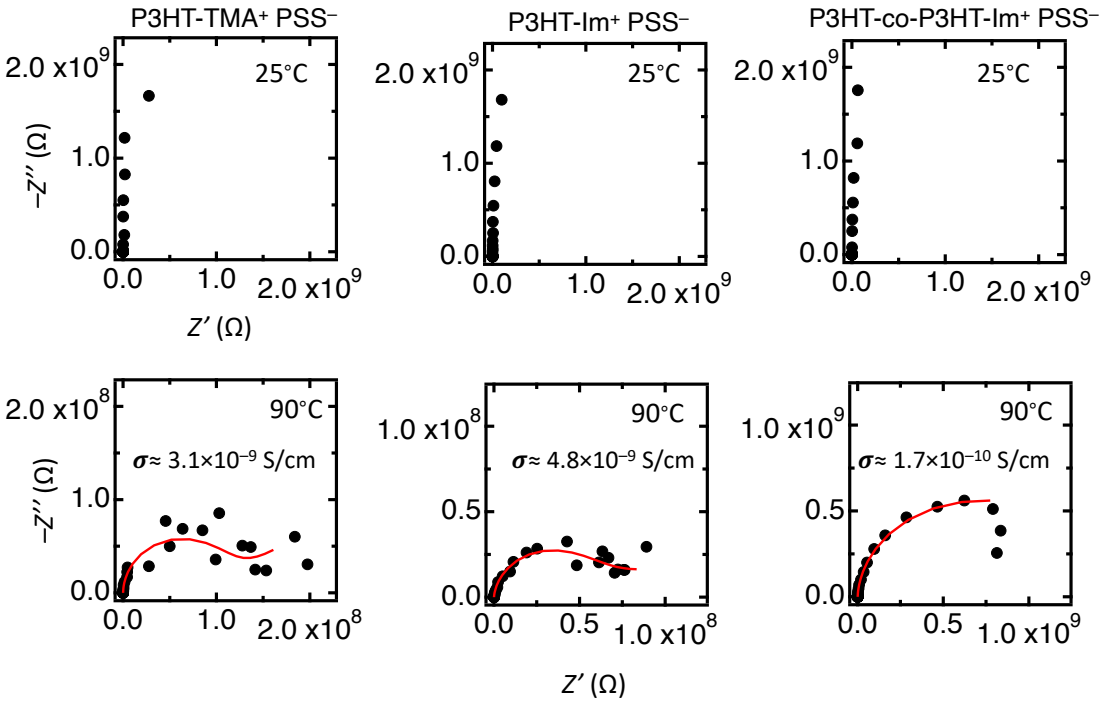


**Figure 5.16: Ionic conductivity of the neat complexes**

These results indicate that the complexation/washing process sufficiently removes charge compensating counterions. Columns are for the indicated complex, where the top row is the data collected at 25°C and the bottom row is the data at 90°C. At 25°C, no measurable signal appears, and the Nyquist plot is indicative of an open circuit, in line with a lack of ionic charge carriers. At 90°C, a small resemblance of a Nyquist plot indicative of ionic conductivity appears, but the result is noisy, and when fits are attempted (red lines) the resulting values are extremely low, again indicating negligible ionic conduction in the neat complexes.

*Lithium transference*

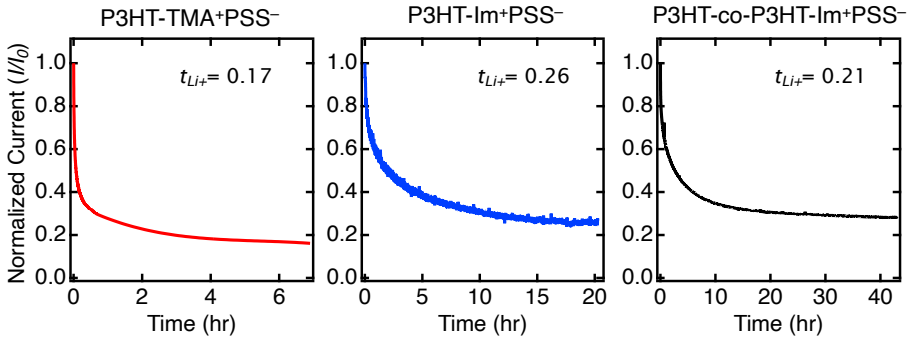


**Figure 5.17: Current decay for DC polarization study**

Each complex is sandwiched between lithium metal electrodes and a DC potential is applied as described in the methods section of the main text.

Li-ion battery performance relies on lithium transport within the electrode, and thus special attention must be given to the lithium transference ($t_{Li+}$), in addition to the overall ionic conductivity. Each complex displays an appreciable $t_{Li+}$ value (Figure 5.17), as measured by the DC polarization method developed by Bruce and Vincent.[4] The ability to transport, rather than trap, $Li^+$ is a critical property for conducting battery binders, but a non-trivial design goal for mixed conducting polymers. For instance, a widely used design strategy for mixed conductors is to apply ether functional groups to thiophene backbones.[5–7] While these systems effectively solvate lithium salts, they do so via strong polymer-lithium interactions. This effectively traps $Li^+$, resulting in most of the ionic current being carried by the anion.[1,8,9] Such trapping is not evident here. Additionally, P3HT-$TMA^+PSS^-$displays a higher $t_{Li+}$ of 0.17 than that reported for the CPE ($t_{Li+} \approx 0.04$).[10] This suggests that complexation can have a positive effect on lithium transport, likely due to the presence of both anionic and cationic polymer functional groups that may reduce the degree to which $Li^+$ migrates in anionic clusters, a key limiter to lithium mobility in the P3HT-$TMA^+$ CPE system.

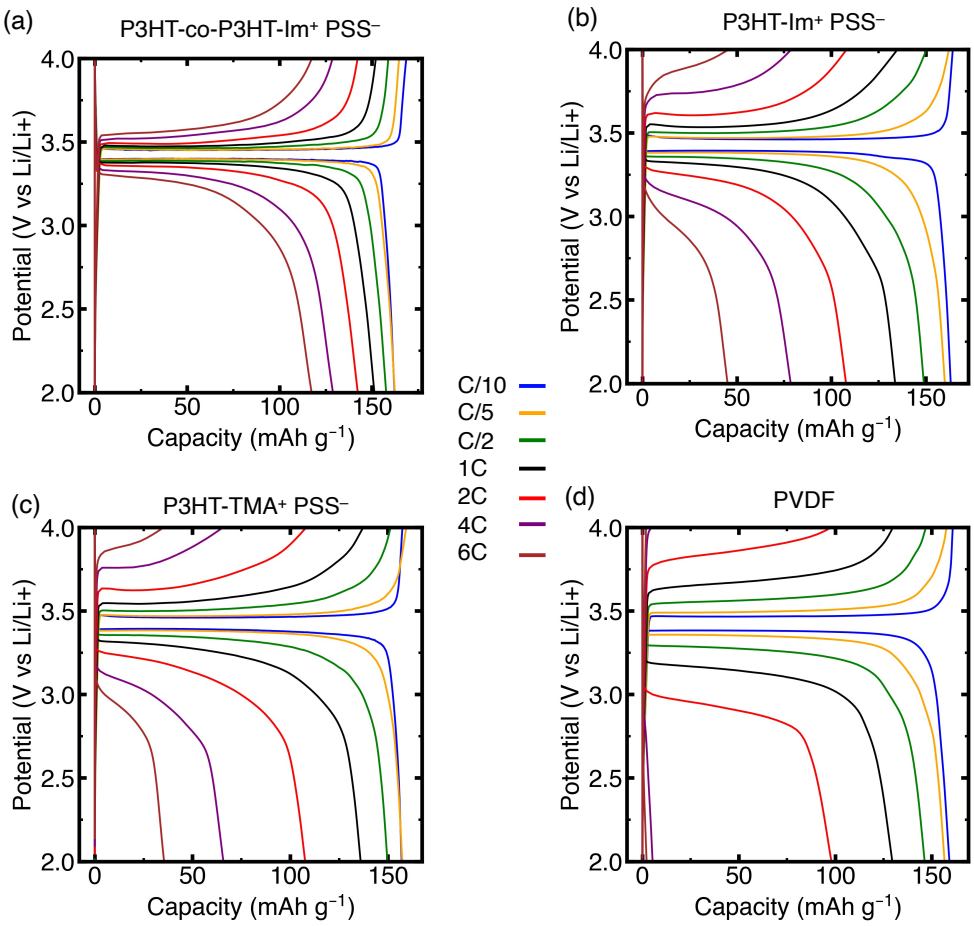


**Figure 5.18: Potential vs capacity curves plotted by binder chemistry**

Charge/discharge potential profiles for LFP:Carbon:Binder (85:6:9 wt.%) cathodes during symmetric galvanostatic charge/discharge.

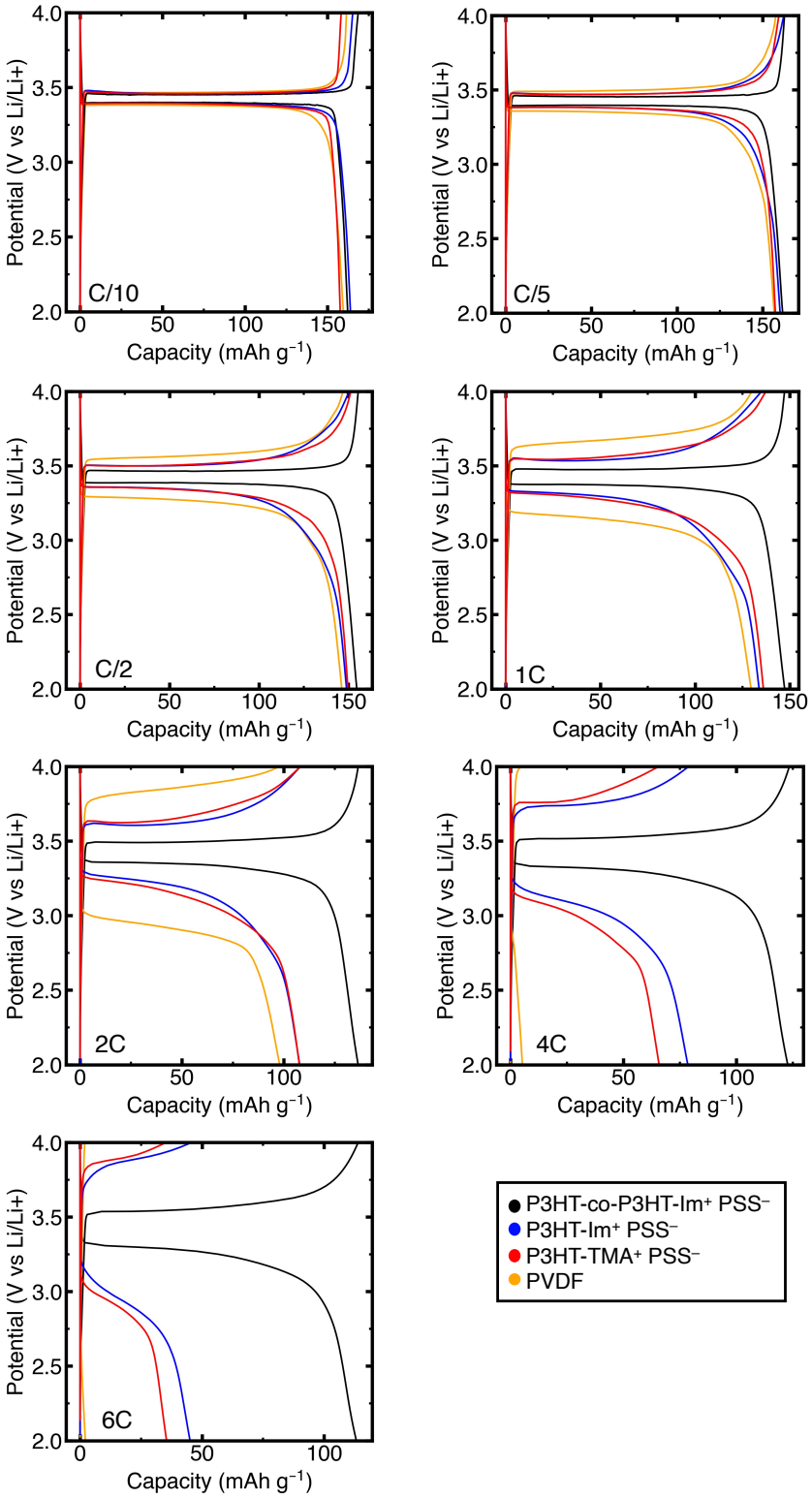


**Figure 5.19: Potential vs capacity curves plotted by rate**

A different depiction of the data in Figure 5.18, now showing charge/discharge potential profiles of cells containing each binder, with each panel displaying a given rate.

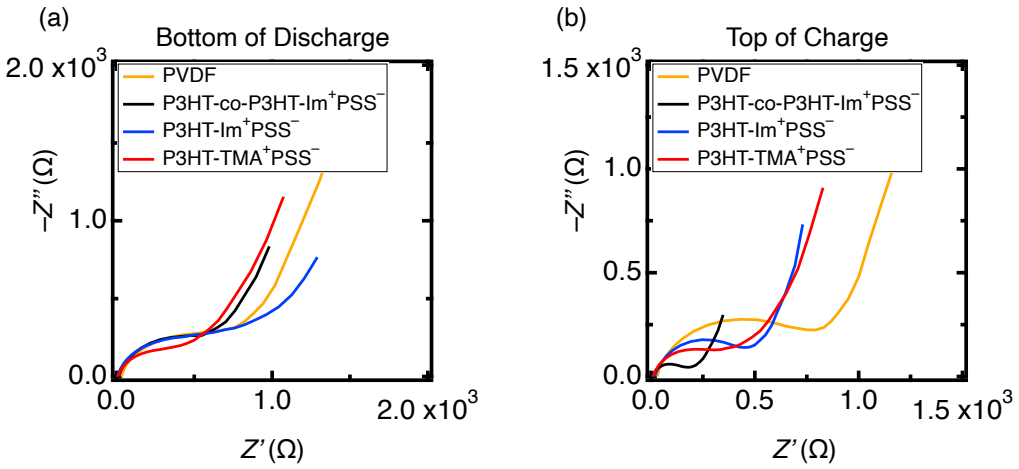


**Figure 5.20: Nyquist plots showing impedance of cells containing the indicated binders**

Data presented at (a) bottom of discharge and (b) top of charge, recorded during the final C/10 cycle. The conducting CPC binders are doped around 3.2 V vs $Li/Li^+$, and thus their conductivity is enhanced over the entire charge/discharge process.

# Chapter 6

# Conclusion and Outlook

Mixed conducting polymers are a powerful materials class with tunable properties amendable to a breadth of applications. This dissertation explores tailoring these materials specifically for battery binders. As was shown, this is not a straightforward engineering effort, requiring development and understanding of fundamental structure property relationships governing both lithium and electron transport. In the first chapter, insights were presented from the ion and electron conducting polymer communities, were transport of each charge carrier has been studied extensively in these independent materials classes. However, ions and electrons follow very different design rules in their respective materials systems, and integrating each property together required novel structures and approaches. It follows that previous work exploring conducting binders in Li-ion batteries did not quantify and control $Li^+$ transport in semiconducting polymers, but rather used established chemistries which optimize one property or the other.

The prior chapters discussed the work performed to develop polymers tailor-made for mixed conducting binder applications. Chapter 2 juxtaposed the most common mixed conducting design strategy (functionalizing a thiophene backbone with an ether side chain) to an ionic liquid like thiophene derivative. Here it was shown the side chain chemistry has critical impact on $Li^+$ transport, where the commonly implemented ether variant was shown to actually trap lithium ions. The cationic imidazolium group provided good lithium transference, emphasizing the importance of polymer-ion interaction strength to balance ion solvation and

mobility. This concept was explored further in Chapter 3, where it was shown that simply functionalizing a polythiophene with any cationic group is not sufficient for $Li^+$ mobility. Based on the results of the imidazolium derivative from Chapter 2, an intuitive hypothesis might be that any cationic sidechain will preferentially interact with the anion, promoting mobility of the $Li^+$ cation. Here it was shown this is not the case, as charge localization of the cationic group is critical. Localized charges promote strong polymer-ion interactions such that $Li^+$ is not fully dissociate and is strongly correlated in a local environment consisting of charged clusters and ion pairs. Through this, it was shown that the diffuse cationic charge on the imidazolium group is critical for $Li^+$ mobility. Additionally, the planar nature of this pendant afforded superior electronic conduction due to the ability to accommodate dopant counterions in a relatively ordered manner.

With these insights about intrinsic structure property relationships for $Li^+$ and electron transport, the model systems were adopted into real battery binders. However, the ideal candidate based on the work from Chapters 2 and 3 (an imidazolium functionalized polythiophene, P3HT-Im+) dissolved in all common battery electrolytes. This presented a fundamental hurdle- how to incorporate lithium conduction to the binder without dissolving in a liquid electrolyte. Additionally, the ability to practically process the binder in electrode slurries had to be maintained. Chapter 4 ultimately addressed this hurdle, where it was shown that electrostatically stabilized coacervation affords a processable system which is ultimately insoluble in the battery electrolyte and stable in the relevant electrochemical potential window for battery cathodes. Furthermore, complex coacervation proved to enhance the electronic conductivity of the system, while still maintaining good lithium mobility. These properties ultimately led to a polymer binder that afforded high rate capability and good cycle stability in

$LiFePO_4$ cathodes. Finally, Chapter 5 developed complex coacervation as broad platform strategy, where several polymer chemistries were shown to afford processability, stability, and good mixed conduction. Ultimately, these properties combined to enable dramatic performance improvements over the traditionally used, insulating binder (PVDF), where up to 70% of the cathode's capacity could be utilized at 6C, compared to only 1.4% when PVDF was the binder.

In sum, this dissertation developed complex coacervation as a promising material platform for mixed $Li^+$-electron conducting polymers, which can serve as promising "pick and place" battery binders- directly integrating into current cell formats to afford enhanced power, energy, and stability. In route to this development, valuable fundamental structure property relationships were developed. Additionally, design and characterization techniques were bridged between ion and electron conducting polymer communities, where the value of "bulk ionic transport measurements" such as the Bruce-Vincent method, PFG NMR, NMR Relaxometry, and EIS were demonstrated on semiconducting polymer systems, a material class which has largely been studied in thin film formats.

The hope and forward looking outlook is that the field will continue to study mixed conduction in the context of bulk ion solvation and transport in addition to dopant counterion dynamics. In particular, a better understanding of charge transport when both ionic and electronic charge carriers are present is critical, although experimentally difficult to access. As mentioned in Chapter 1, Lithium transference in electronically doped samples is difficult to measure via ion specific techniques such as PFG NMR due to thermal de-doping. DC polarization cannot be used as the lithium symmetric cell would be shorted when the conjugated polymer is electronically doped. The development of experimental techniques to

quantify lithium transport in “co-doped” systems would provide structure property relationships more directly relatable to the desired use case of the material.

Additionally, the versatility of multicomponent, electrostatically stabilized systems is large. While the systems presented here focused on lithium and electron transport, the overall design strategy shows that electrostatics can be leveraged to compatibilize two immiscible polymers and incorporate advantageous functional groups into a binder, without sacrificing stability or processability. One can imagine a variety of next generation versions were this concept is used to incorporate advanced functional groups into the binder that may aid in water scavenging, self-healing, SEI/CEI formation, or a slew of other properties. In particular, modifying the non-conjugated polyelectrolyte to add additional functionality is of interest. In this work, this polyelectrolyte was selected to have an opposite charge compared to that of the conjugated polyelectrolyte in order to facilitate electrostatic complexation. However, this task can be accomplished in systems with additional functionality as well. For instance, selecting a polyelectrolyte with elastomeric properties (ex. bottlebrush polymers) could enable optimization of both conductivity and mechanical properties, further improving performance as a binder. It is the hope that the structure property relationships and design strategies developed in this work will serve as a platform for future advanced mixed conducting polymers- both tailor-made systems engineered for advanced binder applications and model systems used to further elucidate fundamental insight into charge transport and mixed conduction design strategies.

# References


(1) Noriega, R.; Rivnay, J.; Vandewal, K.; Koch, F. P. V.; Stingelin, N.; Smith, P.; Toney, M. F.; Salleo, A. A General Relationship between Disorder, Aggregation and Charge Transport in Conjugated Polymers. *Nat Mater* **2013**, *12* (11), 1038–1044. https://doi.org/10.1038/nmat3722.

(2) Bässler, H.; Köhler, A. Charge Transport in Organic Semiconductors. *Top Curr Chem* **2012**, *312*, 1–65. https://doi.org/10.1007/128_2011_218.

(3) Mollinger, S. A.; Krajina, B. A.; Noriega, R.; Salleo, A.; Spakowitz, A. J. Percolation, Tie-Molecules, and the Microstructural Determinants of Charge Transport in Semicrystalline Conjugated Polymers. *ACS Macro Lett* **2015**, *4* (7), 708–712. https://doi.org/10.1021/acsmacrolett.5b00314.

(4) Schauser, N. S.; Seshadri, R.; Segalman, R. A. Multivalent Ion Conduction in Solid Polymer Systems. *Mol Syst Des Eng* **2019**, *4* (2), 263–279. https://doi.org/10.1039/c8me00096d.

(5) Armand, M. Polymers with Ionic Conductivity. *Advanced Materials* **1990**, *2* (6–7), 278–286. https://doi.org/10.1002/adma.19900020603.

(6) Vincent, C. A. Polymer Electrolytes. *Chem Br* **1989**, *25* (4). https://doi.org/10.1146/annurev-matsci-071312-121705.

(7) Ganesan, V. Ion Transport in Polymeric Ionic Liquids: Recent Developments and Open Questions. *Mol Syst Des Eng* **2019**, *4* (2), 280–293. https://doi.org/10.1039/c8me00114f.

(8) Bredas, J. L.; Street, G. B. *Polarons, Bipolarons, and Solitons in Conducting Polymers*; 1985; Vol. 18.

(9) Peterson, K. A.; Thomas, E. M.; Chabinyc, M. L. Thermoelectric Properties of Semiconducting Polymers. *Annu Rev Mater Res* **2020**, *50*, 551–574. https://doi.org/10.1146/annurev-matsci-082219-024716.

(10) Bredas, J.-L. Mind the Gap! *Mater. Horiz.* **2014**, *1* (1), 17–19. https://doi.org/10.1039/C3MH00098B.

(11) Chiang, C. K.; Fincher Jr, C. R.; Park, Y. W.; Heeger, A. J.; Shirakawa, H.; Louis, E. J.; Gau, S. C.; MacDiarmid, A. G. Electrical Conductivity in Doped Polyacetylene. *Phys Rev Lett* **1977**, *39* (17), 1098–1101. https://doi.org/10.1103/PhysRevB.24.7380.

(12) Köhler, A.; Bässler, H. Electronic Processes in Organic Semiconductors. *Electronic Processes in Organic Semiconductors* **2015**, No. April, 389–397. https://doi.org/10.1002/9783527685172.

(13) Russ, B.; Glaudell, A.; Urban, J. J.; Chabinyc, M. L.; Segalman, R. A. Organic Thermoelectric Materials for Energy Harvesting and Temperature Control. *Nat Rev Mater* **2016**, *1* (10). https://doi.org/10.1038/natrevmats.2016.50.

(14) Pace, G.; Nordness, O.; Asham, K.; Clément, R. J.; Segalman, R. A. Impact of Side Chain Chemistry on Lithium Transport in Mixed Ion-Electron-Conducting Polymers. *Chemistry of Materials* **2022**, *34* (10), 4672–4681. https://doi.org/10.1021/acs.chemmater.2c00592.

(15) Rawlings, D.; Lee, D.; Magdău, I. B.; Kim, J.; Pace, G.; Richardson, P. M.; Thomas, E. M.; Danielsen, S. P. O.; Tolbert, S.; Miller, T. F.; Seshadri, R.; Segalman, R. A. Li+ and Oxidant Addition to Control Ionic and Electronic Conduction in Ionic Liquid

Functionalized Conjugated Polymers. *Chemistry of Materials* **2021**, *33* (16), 6464–6474. https://doi.org/https://doi.org/10.1021/acs.chemmater.1c01811.
(16) Das, P.; Zayat, B.; Wei, Q.; Salamat, C. Z.; Magdău, I. B.; Elizalde-Segovia, R.; Rawlings, D.; Lee, D.; Pace, G.; Irshad, A.; Ye, L.; Schmitt, A.; Segalman, R. A.; Miller, T. F.; Tolbert, S. H.; Dunn, B. S.; Narayan, S. R.; Thompson, B. C. Dihexyl-Substituted Poly(3,4-Propylenedioxythiophene) as a Dual Ionic and Electronic Conductive Cathode Binder for Lithium-Ion Batteries. *Chemistry of Materials* **2020**, *32* (21), 9176–9189. https://doi.org/10.1021/acs.chemmater.0c02601.
(17) Mazaheripour, A.; Thomas, E. M.; Segalman, R. A.; Chabinyc, M. L. Nonaggregating Doped Polymers Based on Poly(3,4-Propylenedioxythiophene). *Macromolecules* **2019**, *52* (5), 2203–2213. https://doi.org/10.1021/acs.macromol.8b02389.
(18) Yee, P. Y.; Scholes, D. T.; Schwartz, B. J.; Tolbert, S. H. Dopant-Induced Ordering of Amorphous Regions in Regiorandom P3HT. *Journal of Physical Chemistry Letters* **2019**, *10* (17), 4929–4934. https://doi.org/10.1021/acs.jpclett.9b02070.
(19) Choudhary, K.; Chen, A. X.; Pitch, G. M.; Runser, R.; Urbina, A.; Dunn, T. J.; Kodur, M.; Kleinschmidt, A. T.; Wang, B. G.; Bunch, J. A.; Fenning, D. P.; Ayzner, A. L.; Lipomi, D. J. Comparison of the Mechanical Properties of a Conjugated Polymer Deposited Using Spin Coating, Interfacial Spreading, Solution Shearing, and Spray Coating. *ACS Appl Mater Interfaces* **2021**, *13* (43), 51436–51446. https://doi.org/10.1021/acsami.1c13043.
(20) Salleo, A.; Kline, R. J.; DeLongchamp, D. M.; Chabinyc, M. L. Microstructural Characterization and Charge Transport in Thin Films of Conjugated Polymers. *Advanced Materials* **2010**, *22* (34), 3812–3838. https://doi.org/https://doi.org/10.1002/adma.200903712.
(21) Thomas, E. M.; Davidson, E. C.; Katsumata, R.; Segalman, R. A.; Chabinyc, M. L. Branched Side Chains Govern Counterion Position and Doping Mechanism in Conjugated Polythiophenes. *ACS Macro Lett* **2018**, *7* (12), 1492–1497. https://doi.org/10.1021/acsmacrolett.8b00778.
(22) Han, C. C.; Elsenbaumer, R. L. Protonic Acids: Generally Applicable Dopants for Conducting Polymers. *Synth Met* **1989**, *30* (1), 123–131. https://doi.org/https://doi.org/10.1016/0379-6779(89)90648-6.
(23) Zaumseil, J.; Sirringhaus, H. Electron and Ambipolar Transport in Organic Field-Effect Transistors. *Chem Rev* **2007**, *107* (4), 1296–1323. https://doi.org/10.1021/cr0501543.
(24) Sui, Y.; Deng, Y.; Du, T.; Shi, Y.; Geng, Y. Design Strategies of N-Type Conjugated Polymers for Organic Thin-Film Transistors. *Mater Chem Front* **2019**, *3* (10), 1932–1951. https://doi.org/10.1039/c9qm00382g.
(25) Noriega, R.; Rivnay, J.; Vandewal, K.; Koch, F. P. V.; Stingelin, N.; Smith, P.; Toney, M. F.; Salleo, A. A General Relationship between Disorder, Aggregation and Charge Transport in Conjugated Polymers. *Nat Mater* **2013**, *12* (11), 1038–1044. https://doi.org/10.1038/nmat3722.
(26) Danielsen, S. P. O.; Nguyen, T. Q.; Fredrickson, G. H.; Segalman, R. A. Complexation of a Conjugated Polyelectrolyte and Impact on Optoelectronic Properties. *ACS Macro Lett* **2019**, *8* (1), 88–94. https://doi.org/10.1021/acsmacrolett.8b00924.

(27) Le, M. L.; Warner, C.; Segalman, R. A.; Chabinyc, M. L. Role of Complexation Strength on the Photophysical and Transport Properties of Semiconducting Charged Polymer Complexes. *Chemistry of Materials* **2023**. https://doi.org/10.1021/acs.chemmater.3c00627.
(28) Schauser, N. S.; Sanoja, G. E.; Bartels, J. M.; Jain, S. K.; Hu, J. G.; Han, S.; Walker, L. M.; Helgeson, M. E.; Seshadri, R.; Segalman, R. A. Decoupling Bulk Mechanics and Mono- and Multivalent Ion Transport in Polymers Based on Metal–Ligand Coordination. *Chemistry of Materials* **2018**, *30* (16), 5759–5769. https://doi.org/10.1021/acs.chemmater.8b02633.
(29) Xie, S.; Nikolaev, A.; Nordness, O. A.; C. Llanes, L.; Jones, S. D.; Richardson, P. M.; Wang, H.; Clément, R. J.; Read De Alaniz, J.; Segalman, R. A. Polymer Electrolyte Based on Cyano-Functionalized Polysiloxane with Enhanced Salt Dissolution and High Ionic Conductivity. *Macromolecules* **2022**, *55* (13), 5723–5732. https://doi.org/10.1021/acs.macromol.2c00329.
(30) Bresser, D.; Lyonnard, S.; Iojoiu, C.; Picard, L.; Passerini, S. Decoupling Segmental Relaxation and Ionic Conductivity for Lithium-Ion Polymer Electrolytes. *Molecular Systems Design and Engineering*. Royal Society of Chemistry August 1, 2019, pp 779–792. https://doi.org/10.1039/c9me00038k.
(31) Stacy, E. W.; Gainaru, C. P.; Gobet, M.; Wojnarowska, Z.; Bocharova, V.; Greenbaum, S. G.; Sokolov, A. P. Fundamental Limitations of Ionic Conductivity in Polymerized Ionic Liquids. *Macromolecules* **2018**, *51* (21), 8637–8645. https://doi.org/10.1021/acs.macromol.8b01221.
(32) Zhang, H.; Li, C.; Piszcz, M.; Coya, E.; Rojo, T.; Rodriguez-Martinez, L. M.; Armand, M.; Zhou, Z. Single Lithium-Ion Conducting Solid Polymer Electrolytes: Advances and Perspectives. *Chem Soc Rev* **2017**, *46* (3), 797–815. https://doi.org/10.1039/C6CS00491A.
(33) Yin, K.; Zhang, Z.; Yang, L.; Hirano, S.-I. An Imidazolium-Based Polymerized Ionic Liquid via Novel Synthetic Strategy as Polymer Electrolytes for Lithium Ion Batteries. *J Power Sources* **2014**, *258*, 150–154. https://doi.org/https://doi.org/10.1016/j.jpowsour.2014.02.057.
(34) Ohno, H. Molten Salt Type Polymer Electrolytes. *Electrochim Acta* **2001**, *46* (10), 1407–1411. https://doi.org/https://doi.org/10.1016/S0013-4686(00)00733-7.
(35) Jones, S. D.; Nguyen, H.; Richardson, P. M.; Chen, Y.-Q.; Wyckoff, K. E.; Hawker, C. J.; Clément, R. J.; Fredrickson, G. H.; Segalman, R. A. Design of Polymeric Zwitterionic Solid Electrolytes with Superionic Lithium Transport. *ACS Cent Sci* **2022**, *8* (2), 169–175. https://doi.org/https://doi.org/10.1021/acscentsci.1c01260.
(36) Patel, S. N.; Javier, A. E.; Stone, G. M.; Mullin, S. A.; Balsara, N. P. Simultaneous Conduction of Electronic Charge and Lithium Ions in Block Copolymers. *ACS Nano* **2012**, *6* (2), 1589–1600. https://doi.org/10.1021/nn2045664.
(37) Paulsen, B. D.; Tybrandt, K.; Stavrinidou, E.; Rivnay, J. Organic Mixed Ionic–Electronic Conductors. *Nat Mater* **2020**, *19* (1), 13–26. https://doi.org/10.1038/s41563-019-0435-z.
(38) Thomas, E. M.; Nguyen, P. H.; Jones, S. D.; Chabinyc, M. L.; Segalman, R. A. Electronic, Ionic, and Mixed Conduction in Polymeric Systems. *Annu Rev Mater Res* **2021**, *51* (1), 1–20. https://doi.org/10.1146/annurev-matsci-080619-110405.

(39) Dong, B. X.; Nowak, C.; Onorato, J. W.; Strzalka, J.; Escobedo, F. A.; Luscombe, C. K.; Nealey, P. F.; Patel, S. N. Influence of Side-Chain Chemistry on Structure and Ionic Conduction Characteristics of Polythiophene Derivatives: A Computational and Experimental Study. *Chemistry of Materials* **2019**, *31* (4), 1418–1429. https://doi.org/10.1021/acs.chemmater.8b05257.
(40) Das, P.; Elizalde-Segovia, R.; Zayat, B.; Salamat, C. Z.; Pace, G.; Zhai, K.; Vincent, R. C.; Dunn, B. S.; Segalman, R. A.; Tolbert, S. H.; Narayan, S. R.; Thompson, B. C. Enhancing the Ionic Conductivity of Poly(3,4-Propylenedioxythiophenes) with Oligoether Side Chains for Use as Conductive Cathode Binders in Lithium-Ion Batteries. *Chemistry of Materials* **2022**, *34* (6), 2672–2686. https://doi.org/10.1021/acs.chemmater.1c03971.
(41) Paulsen, B. D.; Fabiano, S.; Rivnay, J. Mixed Ionic-Electronic Transport in Polymers. *Annu Rev Mater Res* **2021**, *51* (1), 73–99. https://doi.org/10.1146/annurev-matsci-080619-101319.
(42) Fredrickson, G. H.; Xie, S.; Edmund, J.; Le, M. L.; Sun, D.; Grzetic, D. J.; Vigil, D. L.; Delaney, K. T.; Chabinyc, M. L.; Segalman, R. A. Ionic Compatibilization of Polymers. *ACS Polymers Au* **2022**, *2* (5), 299–312. https://doi.org/10.1021/acspolymersau.2c00026.
(43) Das, P. R.; Komsiyska, L.; Osters, O.; Wittstock, G. PEDOT: PSS as a Functional Binder for Cathodes in Lithium Ion Batteries. *J Electrochem Soc* **2015**, *162* (4), A674. https://doi.org/10.1149/2.0581504jes.
(44) Le, M. L.; Rawlings, D.; Danielsen, S. P. O.; Kennard, R. M.; Chabinyc, M. L.; Segalman, R. A. Aqueous Formulation of Concentrated Semiconductive Fluid Using Polyelectrolyte Coacervation. *ACS Macro Lett* **2021**, *10* (8), 1008–1014. https://doi.org/10.1021/acsmacrolett.1c00354.
(45) Danielsen, S. P. O.; Sanoja, G. E.; McCuskey, S. R.; Hammouda, B.; Bazan, G. C.; Fredrickson, G. H.; Segalman, R. A. Mixed Conductive Soft Solids by Electrostatically Driven Network Formation of a Conjugated Polyelectrolyte. *Chemistry of Materials* **2018**, *30* (4), 1417–1426. https://doi.org/10.1021/acs.chemmater.7b05303.
(46) Hollingsworth, W. R.; Segura, C.; Balderrama, J.; Lopez, N.; Schleissner, P.; Ayzner, A. L. Exciton Transfer and Emergent Excitonic States in Oppositely-Charged Conjugated Polyelectrolyte Complexes. *Journal of Physical Chemistry B* **2016**, *120* (31), 7767–7774. https://doi.org/10.1021/acs.jpcb.6b06533.
(47) Danielsen, S. P. O.; Thompson, B. J.; Fredrickson, G. H.; Nguyen, T.-Q.; Bazan, G. C.; Segalman, R. A. Ionic Tunability of Conjugated Polyelectrolyte Solutions. *Macromolecules* **2022**, *55* (9), 3437–3448. https://doi.org/10.1021/acs.macromol.2c00178.
(48) Segura, C. J.; Lucero, M.; Ayzner, A. L. Disassembly of an Interconjugated Polyelectrolyte Complex Using Ionic Surfactants. *ACS Appl Polym Mater* **2019**, *1* (5), 1034–1044. https://doi.org/10.1021/acsapm.9b00023.
(49) Peterhans, L.; Nicolaidou, E.; Diamantis, P.; Alloa, E.; Leclerc, M.; Surin, M.; Clément, S.; Rothlisberger, U.; Banerji, N.; Hayes, S. C. Structural and Photophysical Templating of Conjugated Polyelectrolytes with Single-Stranded DNA. *Chemistry of Materials* **2020**, *32* (17), 7347–7362. https://doi.org/10.1021/acs.chemmater.0c02251.

(50) Sing, C. E.; Perry, S. L. Recent Progress in the Science of Complex Coacervation. *Soft Matter* **2020**, *16* (12), 2885–2914. https://doi.org/10.1039/d0sm00001a.
(51) Gucht, J. van der; Spruijt, E.; Lemmers, M.; Cohen Stuart, M. A. Polyelectrolyte Complexes: Bulk Phases and Colloidal Systems. *J Colloid Interface Sci* **2011**, *361* (2), 407–422. https://doi.org/https://doi.org/10.1016/j.jcis.2011.05.080.
(52) Overbeek, J. T. G.; Voorn, M. J. Phase Separation in Polyelectrolyte Solutions. Theory of Complex Coacervation. *J Cell Comp Physiol* **1957**, *49* (S1), 7–26. https://doi.org/https://doi.org/10.1002/jcp.1030490404.
(53) Hamad, F. G.; Chen, Q.; Colby, R. H. Linear Viscoelasticity and Swelling of Polyelectrolyte Complex Coacervates. *Macromolecules* **2018**, *51* (15), 5547–5555. https://doi.org/10.1021/acs.macromol.8b00401.
(54) Fares, H. M.; Wang, Q.; Yang, M.; Schlenoff, J. B. Swelling and Inflation in Polyelectrolyte Complexes. *Macromolecules* **2019**, *52* (2), 610–619. https://doi.org/10.1021/acs.macromol.8b01838.
(55) Priftis, D.; Laugel, N.; Tirrell, M. Thermodynamic Characterization of Polypeptide Complex Coacervation. *Langmuir* **2012**, *28* (45), 15947–15957. https://doi.org/10.1021/la302729r.
(56) Ou, Z.; Muthukumar, M. Entropy and Enthalpy of Polyelectrolyte Complexation: Langevin Dynamics Simulations. *J Chem Phys* **2006**, *124* (15), 154902. https://doi.org/10.1063/1.2178803.
(57) Moon, H. C.; Kim, J. K. Phase Segregation of Poly(3-Dodecylthiophene)-Block-Poly(Methyl Methacrylate) Copolymers. *Polymer (Guildf)* **2013**, *54* (20), 5437–5442. https://doi.org/https://doi.org/10.1016/j.polymer.2013.07.063.
(58) Patel, S. N.; Javier, A. E.; Beers, K. M.; Pople, J. A.; Ho, V.; Segalman, R. A.; Balsara, N. P. Morphology and Thermodynamic Properties of a Copolymer with an Electronically Conducting Block: Poly(3-Ethylhexylthiophene)-Block-Poly(Ethylene Oxide). *Nano Lett* **2012**, *12* (9), 4901–4906. https://doi.org/10.1021/nl302454c.
(59) Xue, Z.; He, D.; Xie, X. Poly(Ethylene Oxide)-Based Electrolytes for Lithium-Ion Batteries. *J Mater Chem A Mater* **2015**, *3* (38), 19218–19253. https://doi.org/10.1039/C5TA03471J.
(60) Hallinan, D. T.; Balsara, N. P. Polymer Electrolytes. *Annu Rev Mater Res* **2013**, *43* (1), 503–525. https://doi.org/10.1146/annurev-matsci-071312-121705.
(61) Galluzzo, M. D.; Maslyn, J. A.; Shah, D. B.; Balsara, N. P. Ohm's Law for Ion Conduction in Lithium and beyond-Lithium Battery Electrolytes. *J Chem Phys* **2019**, *151* (2), 020901. https://doi.org/10.1063/1.5109684.
(62) Dong, B. X.; Nowak, C.; Onorato, J. W.; Ma, T.; Niklas, J.; Poluektov, O. G.; Grocke, G.; DiTusa, M. F.; Escobedo, F. A.; Luscombe, C. K.; Nealey, P. F.; Patel, S. N. Complex Relationship between Side-Chain Polarity, Conductivity, and Thermal Stability in Molecularly Doped Conjugated Polymers. *Chemistry of Materials* **2021**, *33* (2), 741–753. https://doi.org/10.1021/acs.chemmater.0c04153.
(63) Patel, S. N.; Javier, A. E.; Stone, G. M.; Mullin, S. A.; Balsara, N. P. Simultaneous Conduction of Electronic Charge and Lithium Ions in Block Copolymers. *ACS Nano* **2012**, *6* (2), 1589–1600. https://doi.org/10.1021/nn2045664.
(64) Patel, S. N.; Javier, A. E.; Balsara, N. P. Electrochemically Oxidized Electronic and Ionic Conducting Nanostructured Block Copolymers for Lithium Battery Electrodes. *ACS Nano* **2013**, *7* (7), 6056–6068. https://doi.org/10.1021/nn4018685.

(65) Huggins, R. A. Simple Method to Determine Electronic Conductivity and Ionic Components of the Conductors in Mixed a Review. *Ionics (Kiel)* **2002**, *8* (3–4), 300–313. https://doi.org/10.1007/BF02376083.
(66) Zayat, B.; Das, P.; Thompson, B. C.; Narayan, S. R. In Situ Measurement of Ionic and Electronic Conductivities of Conductive Polymers as a Function of Electrochemical Doping in Battery Electrolytes. *The Journal of Physical Chemistry C* **2021**, *125* (14), 7533–7541. https://doi.org/10.1021/acs.jpcc.0c08934.
(67) Shah, D. B.; Nguyen, H. Q.; Grundy, L. S.; Olson, K. R.; Mecham, S. J.; Desimone, J. M.; Balsara, N. P. Difference between Approximate and Rigorously Measured Transference Numbers in Fluorinated Electrolytes. *Physical Chemistry Chemical Physics* **2019**, *21* (15), 7857–7866. https://doi.org/10.1039/c9cp00216b.
(68) Evans, J.; Vincent, C. A.; Bruce, P. G. Electrochemical Measurement of Transference Numbers in Polymer Electrolytes. *Polymer (Guildf)* **1987**, *28* (13), 2324–2328. https://doi.org/https://doi.org/10.1016/0032-3861(87)90394-6.
(69) Timachova, K.; Chintapalli, M.; Olson, K. R.; Mecham, S. J.; DeSimone, J. M.; Balsara, N. P. Mechanism of Ion Transport in Perfluoropolyether Electrolytes with a Lithium Salt. *Soft Matter* **2017**, *13* (32), 5389–5396. https://doi.org/10.1039/c7sm00794a.
(70) Richardson, P. M.; Voice, A. M.; Ward, I. M. NMR Self Diffusion and Relaxation Time Measurements for Poly (Vinylidene Fluoride) (PVDF) Based Polymer Gel Electrolytes Containing LiBF4 and Propylene Carbonate. *Polymer (Guildf)* **2016**, *97*, 69–79. https://doi.org/10.1016/j.polymer.2016.03.074.
(71) Richardson, P. M.; Voice, A. M.; Ward, I. M. Two Distinct Lithium Diffusive Species for Polymer Gel Electrolytes Containing LiBF4, Propylene Carbonate (PC) and PVDF. *Int J Hydrogen Energy* **2014**, *39* (6), 2904–2908. https://doi.org/10.1016/j.ijhydene.2013.04.102.
(72) Lai, C. H.; Ashby, D. S.; Lin, T. C.; Lau, J.; Dawson, A.; Tolbert, S. H.; Dunn, B. S. Application of Poly(3-Hexylthiophene-2,5-Diyl) as a Protective Coating for High Rate Cathode Materials. *Chemistry of Materials* **2018**, *30* (8), 2589–2599. https://doi.org/10.1021/acs.chemmater.7b05116.
(73) Zhong, H.; He, A.; Lu, J.; Sun, M.; He, J.; Zhang, L. Carboxymethyl Chitosan/Conducting Polymer as Water-Soluble Composite Binder for LiFePO4 Cathode in Lithium Ion Batteries. *J Power Sources* **2016**, *336*, 107–114. https://doi.org/https://doi.org/10.1016/j.jpowsour.2016.10.041.
(74) Eliseeva, S. N.; Levin, O. V; Tolstopjatova, E. G.; Alekseeva, E. V; Apraksin, R. V; Kondratiev, V. V. New Functional Conducting Poly-3,4-Ethylenedioxythiopene:Polystyrene Sulfonate/Carboxymethylcellulose Binder for Improvement of Capacity of LiFePO4-Based Cathode Materials. *Mater Lett* **2015**, *161*, 117–119. https://doi.org/https://doi.org/10.1016/j.matlet.2015.08.078.
(75) Pan, J.; Xu, G.; Ding, B.; Chang, Z.; Wang, A.; Dou, H.; Zhang, X. PAA/PEDOT:PSS as a Multifunctional, Water-Soluble Binder to Improve the Capacity and Stability of Lithium–Sulfur Batteries. *RSC Adv* **2016**, *6* (47), 40650–40655. https://doi.org/10.1039/C6RA04230A.
(76) Wu, S.-L.; Javier, A. E.; Devaux, D.; Balsara, N. P.; Srinivasan, V. Discharge Characteristics of Lithium Battery Electrodes with a Semiconducting Polymer Studied

by Continuum Modeling and Experiment. *J Electrochem Soc* **2014**, *161* (12), A1836–A1843. https://doi.org/10.1149/2.0261412jes.
(77) Javier, A. E.; Patel, S. N.; Hallinan, D. T.; Srinivasan, V.; Balsara, N. P. Simultaneous Electronic and Ionic Conduction in a Block Copolymer: Application in Lithium Battery Electrodes. *Angewandte Chemie - International Edition* **2011**, *50* (42), 9848–9851. https://doi.org/10.1002/anie.201102953.
(78) Malti, A.; Edberg, J.; Granberg, H.; Khan, Z. U.; Andreasen, J. W.; Liu, X.; Zhao, D.; Zhang, H.; Yao, Y.; Brill, J. W.; Engquist, I.; Fahlman, M.; Wågberg, L.; Crispin, X.; Berggren, M. An Organic Mixed Ion–Electron Conductor for Power Electronics. *Advanced Science* **2016**, *3* (2), 1500305. https://doi.org/https://doi.org/10.1002/advs.201500305.
(79) Inal, S.; Rivnay, J.; Suiu, A.-O.; Malliaras, G. G.; McCulloch, I. Conjugated Polymers in Bioelectronics. *Acc Chem Res* **2018**, *51* (6), 1368–1376. https://doi.org/10.1021/acs.accounts.7b00624.
(80) Rawlings, D.; Thomas, E. M.; Segalman, R. A.; Chabinyc, M. L. Controlling the Doping Mechanism in Poly(3-Hexylthiophene) Thin-Film Transistors with Polymeric Ionic Liquid Dielectrics. *Chemistry of Materials* **2019**, *31*, 8820–8829. https://doi.org/10.1021/acs.chemmater.9b02803.
(81) Malti, A.; Edberg, J.; Granberg, H.; Khan, Z. U.; Andreasen, J. W.; Liu, X.; Zhao, D.; Zhang, H.; Yao, Y.; Brill, J. W.; Engquist, I.; Fahlman, M.; Wågberg, L.; Crispin, X.; Berggren, M. An Organic Mixed Ion–Electron Conductor for Power Electronics. *Advanced Science* **2016**, *3* (2), 1500305. https://doi.org/https://doi.org/10.1002/advs.201500305.
(82) Muench, S.; Wild, A.; Friebe, C.; Häupler, B.; Janoschka, T.; Schubert, U. S. Polymer-Based Organic Batteries. *Chem Rev* **2016**, *116* (16), 9438–9484. https://doi.org/10.1021/acs.chemrev.6b00070.
(83) Nowak, M. J.; Spiege, D.; Hotta, S.; Heeger, A. J.; Pincus, P. A. Charge Storage on a Conducting Polymer in Solution. *Macromolecules* **1989**, *22* (7), 2917–2926. https://doi.org/10.1021/ma00197a007.
(84) Sekitani, T.; Zschieschang, U.; Klauk, H.; Someya, T. Flexible Organic Transistors and Circuits with Extreme Bending Stability. *Nat Mater* **2010**, *9* (12), 1015–1022. https://doi.org/10.1038/nmat2896.
(85) Dong, H.; Fu, X.; Liu, J.; Wang, Z.; Hu, W. 25th Anniversary Article: Key Points for High-Mobility Organic Field-Effect Transistors. *Advanced Materials* **2013**, *25* (43), 6158–6183. https://doi.org/https://doi.org/10.1002/adma.201302514.
(86) Sirringhaus, H. 25th Anniversary Article: Organic Field-Effect Transistors: The Path Beyond Amorphous Silicon. *Advanced Materials* **2014**, *26* (9), 1319–1335. https://doi.org/https://doi.org/10.1002/adma.201304346.
(87) Rivnay, J.; Inal, S.; Salleo, A.; Owens, R. M.; Berggren, M.; Malliaras, G. G. Organic Electrochemical Transistors. *Nat Rev Mater* **2018**, *3*. https://doi.org/10.1038/natrevmats.2017.86.
(88) Enengl, C.; Enengl, S.; Pluczyk, S.; Havlicek, M.; Lapkowski, M.; Neugebauer, H.; Ehrenfreund, E. Doping-Induced Absorption Bands in P3HT: Polarons and Bipolarons. *ChemPhysChem* **2016**, *17* (23), 3836–3844. https://doi.org/10.1002/cphc.201600961.

(89) Schmode, P.; Savva, A.; Kahl, R.; Ohayon, D.; Meichsner, F.; Dolynchuk, O.; Thurn-Albrecht, T.; Inal, S.; Thelakkat, M. The Key Role of Side Chain Linkage in Structure Formation and Mixed Conduction of Ethylene Glycol Substituted Polythiophenes. *ACS Appl Mater Interfaces* **2020**, *12* (11), 13029–13039. https://doi.org/10.1021/acsami.9b21604.
(90) Noriega, R.; Rivnay, J.; Vandewal, K.; Koch, F. P. V; Stingelin, N.; Smith, P.; Toney, M. F.; Salleo, A. A General Relationship between Disorder, Aggregation and Charge Transport in Conjugated Polymers. *Nat Mater* **2013**, *12* (11), 1038–1044. https://doi.org/10.1038/nmat3722.
(91) Cendra, C.; Giovannitti, A.; Savva, A.; Venkatraman, V.; McCulloch, I.; Salleo, A.; Inal, S.; Rivnay, J. Role of the Anion on the Transport and Structure of Organic Mixed Conductors. *Adv Funct Mater* **2019**, *29* (5). https://doi.org/10.1002/adfm.201807034.
(92) Giovannitti, A.; Sbircea, D.-T.; Inal, S.; Nielsen, C. B.; Bandiello, E.; Hanifi, D. A.; Sessolo, M.; Malliaras, G. G.; McCulloch, I.; Rivnay, J. Controlling the Mode of Operation of Organic Transistors through Side-Chain Engineering. *Proceedings of the National Academy of Sciences* **2016**, *113* (43), 12017–12022. https://doi.org/10.1073/pnas.1608780113.
(93) Flagg, L. Q.; Bischak, C. G.; Onorato, J. W.; Rashid, R. B.; Luscombe, C. K.; Ginger, D. S. Polymer Crystallinity Controls Water Uptake in Glycol Side-Chain Polymer Organic Electrochemical Transistors. *J Am Chem Soc* **2019**, *141* (10), 4345–4354. https://doi.org/10.1021/jacs.8b12640.
(94) Fenton, D. E.; Parker, J. M.; Wright, P. V. Complexes of Alkali Metal Ions with Poly(Ethylene Oxide). *Polymer (Guildf)* **1973**, *14* (11), 589. https://doi.org/https://doi.org/10.1016/0032-3861(73)90146-8.
(95) Meyer, W. H. Polymer Electrolytes for Lithium-Ion Batteries. *Advanced Materials* **1998**, *10* (6), 439–448. https://doi.org/https://doi.org/10.1002/(SICI)1521-4095(199804)10:6<439::AID-ADMA439>3.0.CO;2-I.
(96) Webb, M. A.; Jung, Y.; Pesko, D. M.; Savoie, B. M.; Yamamoto, U.; Coates, G. W.; Balsara, N. P.; Wang, Z.-G.; Miller, T. F. I. I. I. Systematic Computational and Experimental Investigation of Lithium-Ion Transport Mechanisms in Polyester-Based Polymer Electrolytes. *ACS Cent Sci* **2015**, *1* (4), 198–205. https://doi.org/10.1021/acscentsci.5b00195.
(97) Chen, H.; Ling, M.; Hencz, L.; Ling, H. Y.; Li, G.; Lin, Z.; Liu, G.; Zhang, S. Exploring Chemical, Mechanical, and Electrical Functionalities of Binders for Advanced Energy-Storage Devices. *Chem Rev* **2018**, *118* (18), 8936–8982. https://doi.org/10.1021/acs.chemrev.8b00241.
(98) Lopez, J.; Mackanic, D. G.; Cui, Y.; Bao, Z. Designing Polymers for Advanced Battery Chemistries. *Nat Rev Mater* **2019**, *4* (5), 312–330. https://doi.org/10.1038/s41578-019-0103-6.
(99) Pace, G. T.; Wang, H.; Whitacre, J. F.; Wu, W. Comparative Study of Water-Processable Polymeric Binders in LiMn2O4 Cathode for Aqueous Electrolyte Batteries. *Nano Select* **2021**, *2* (5), 939–947. https://doi.org/https://doi.org/10.1002/nano.202000167.
(100) Bao, Z.; Dodabalapur, A.; Lovinger, A. J. Soluble and Processable Regioregular Poly(3-Hexylthiophene) for Thin Film Field-Effect Transistor Applications with High Mobility. *Appl Phys Lett* **1996**, *69* (26), 4108–4110. https://doi.org/10.1063/1.117834.

(101) Salem, N.; Lavrisa, M.; Abu-Lebdeh, Y. Ionically-Functionalized Poly(Thiophene) Conductive Polymers as Binders for Silicon and Graphite Anodes for Li-Ion Batteries. *Energy Technology* **2016**, *4* (2), 331–340. https://doi.org/10.1002/ente.201500250.
(102) Son, C. Y.; Wang, Z. G. Ion Transport in Small-Molecule and Polymer Electrolytes. *Journal of Chemical Physics* **2020**, *153* (10). https://doi.org/10.1063/5.0016163.
(103) Zhang, H.; Feng, W.; Zhou, Z.; Nie, J. Composite Electrolytes of Lithium Salt/Polymeric Ionic Liquid with Bis(Fluorosulfonyl)Imide. *Solid State Ion* **2014**, *256*, 61–67. https://doi.org/https://doi.org/10.1016/j.ssi.2014.01.003.
(104) Danielsen, S. P. O.; Davidson, E. C.; Fredrickson, G. H.; Segalman, R. A. Absence of Electrostatic Rigidity in Conjugated Polyelectrolytes with Pendant Charges. *ACS Macro Lett* **2019**, *8* (9), 1147–1152. https://doi.org/10.1021/acsmacrolett.9b00551.
(105) Richardson, P. M.; Voice, A. M.; Ward, I. M. Two Distinct Lithium Diffusive Species for Polymer Gel Electrolytes Containing LiBF4, Propylene Carbonate (PC) and PVDF. *Int J Hydrogen Energy* **2014**, *39* (6), 2904–2908. https://doi.org/https://doi.org/10.1016/j.ijhydene.2013.04.102.
(106) Richardson, P. M.; Voice, A. M.; Ward, I. M. NMR T1 Relaxation Time Measurements and Calculations with Translational and Rotational Components for Liquid Electrolytes Containing LiBF4 and Propylene Carbonate. *J Chem Phys* **2013**, *139* (21), 214501. https://doi.org/10.1063/1.4832038.
(107) Carr, H. Y.; Purcell, E. M. Effects of Diffusion on Free Precession in Nuclear Magnetic Resonance Experiments. *Physical Review* **1954**, *94* (3), 630–638. https://doi.org/10.1103/PhysRev.94.630.
(108) Meiboom, S.; Gill, D. Modified Spin-Echo Method for Measuring Nuclear Relaxation Times. *Review of Scientific Instruments* **1958**, *29* (8), 688–691. https://doi.org/10.1063/1.1716296.
(109) Pipertzis, A.; Mühlinghaus, M.; Mezger, M.; Scherf, U.; Floudas, G. Polymerized Ionic Liquids with Polythiophene Backbones: Self-Assembly, Thermal Properties, and Ion Conduction. *Macromolecules* **2018**, *51* (16), 6440–6450. https://doi.org/10.1021/acs.macromol.8b01201.
(110) Coropceanu, V.; Cornil, J.; da Silva Filho, D. A.; Olivier, Y.; Silbey, R.; Brédas, J.-L. Charge Transport in Organic Semiconductors. *Chem Rev* **2007**, *107* (4), 926–952. https://doi.org/10.1021/cr050140x.
(111) Paulsen, B. D.; Frisbie, C. D. Dependence of Conductivity on Charge Density and Electrochemical Potential in Polymer Semiconductors Gated with Ionic Liquids. *Journal of Physical Chemistry C* **2012**, *116* (4), 3132–3141. https://doi.org/10.1021/jp2093934.
(112) Bridges, C. R.; Ford, M. J.; Thomas, E. M.; Gomez, C.; Bazan, G. C.; Segalman, R. A. Effects of Side Chain Branch Point on Self Assembly, Structure, and Electronic Properties of High Mobility Semiconducting Polymers. *Macromolecules* **2018**, *51* (21), 8597–8604. https://doi.org/10.1021/acs.macromol.8b01906.
(113) Ali, F.; Forsyth, M.; Garcia, M. C.; Smith, M. E.; Strange, J. H. A 7Li and 19F NMR Relaxation Study of LiCF3SO3 in Plasticised Solid Polyether Electrolytes. *Solid State Nucl Magn Reson* **1995**, *5* (3), 217–225. https://doi.org/https://doi.org/10.1016/0926-2040(95)01192-1.
(114) Wilkening, M.; Heitjans, P. From Micro to Macro: Access to Long-Range Li+ Diffusion Parameters in Solids via Microscopic 6, 7Li Spin-Alignment Echo NMR

Spectroscopy. *ChemPhysChem* **2012**, *13* (1), 53–65. https://doi.org/https://doi.org/10.1002/cphc.201100580.
(115) Kuhn, A.; Kunze, M.; Sreeraj, P.; Wiemhöfer, H.-D.; Thangadurai, V.; Wilkening, M.; Heitjans, P. NMR Relaxometry as a Versatile Tool to Study Li Ion Dynamics in Potential Battery Materials. *Solid State Nucl Magn Reson* **2012**, *42*, 2–8. https://doi.org/https://doi.org/10.1016/j.ssnmr.2012.02.001.
(116) Williamson, M. J.; Southall, J. P.; Ward, I. M. Nuclear Magnetic Resonance Relaxation Measurements in Electrolyte Solutions Containing LiCF3SO3. *J Chem Phys* **1998**, *109* (18), 7893–7900. https://doi.org/10.1063/1.477436.
(117) Kunze, M.; Karatas, Y.; Wiemhöfer, H.-D.; Eckert, H.; Schönhoff, M. Activation of Transport and Local Dynamics in Polysiloxane-Based Salt-in-Polymer Electrolytes: A Multinuclear NMR Study. *Physical Chemistry Chemical Physics* **2010**, *12* (25), 6844–6851. https://doi.org/10.1039/B925840J.
(118) Chung, S. H.; Jeffrey, K. R.; Stevens, J. R. A 7Li Nuclear Magnetic Resonance Study of LiCF3SO3 Complexed in Poly(Propylene-glycol). *J Chem Phys* **1991**, *94* (3), 1803–1811. https://doi.org/10.1063/1.459954.
(119) Bloembergen, N.; Purcell, E. M.; Pound, R. V. Relaxation Effects in Nuclear Magnetic Resonance Absorption. *Physical Review* **1948**, *73* (7), 679–712. https://doi.org/10.1103/PhysRev.73.679.
(120) Diederichsen, K. M.; Buss, H. G.; McCloskey, B. D. The Compensation Effect in the Vogel-Tammann-Fulcher (VTF) Equation for Polymer-Based Electrolytes. *Macromolecules* **2017**, *50* (10), 3831–3840. https://doi.org/10.1021/acs.macromol.7b00423.
(121) Aziz, S. B.; Woo, T. J.; Kadir, M. F. Z.; Ahmed, H. M. A Conceptual Review on Polymer Electrolytes and Ion Transport Models. *Journal of Science: Advanced Materials and Devices* **2018**, *3* (1), 1–17. https://doi.org/https://doi.org/10.1016/j.jsamd.2018.01.002.
(122) Schauser, N. S.; Nikolaev, A.; Richardson, P. M.; Xie, S.; Johnson, K.; Susca, E. M.; Wang, H.; Seshadri, R.; Clément, R. J.; Read De Alaniz, J.; Segalman, R. A. Glass Transition Temperature and Ion Binding Determine Conductivity and Lithium-Ion Transport in Polymer Electrolytes. *ACS Macro Lett* **2021**, *10* (1), 104–109. https://doi.org/10.1021/acsmacrolett.0c00788.
(123) Paulsen, B. D.; Tybrandt, K.; Stavrinidou, E.; Rivnay, J. Organic Mixed Ionic–Electronic Conductors. *Nat Mater* **2020**, *19* (1), 13–26. https://doi.org/10.1038/s41563-019-0435-z.
(124) Brendel, J. C.; Schmidt, M. M.; Hagen, G.; Moos, R.; Thelakkat, M. Controlled Synthesis of Water-Soluble Conjugated Polyelectrolytes Leading to Excellent Hole Transport Mobility. *Chemistry of Materials* **2014**, *26* (6), 1992–1998. https://doi.org/10.1021/cm500500t.
(125) Nguyen, P. H.; Schmithorst, M. B.; Mates, T. E.; Segalman, R. A.; Chabinyc, M. L. Diffusion of Brønsted Acidic Dopants in Conjugated Polymers. *J Mater Chem C Mater* **2023**, *11* (22), 7462–7470. https://doi.org/10.1039/D3TC00415E.
(126) Nguyen, V. A.; Kuss, C. Review—Conducting Polymer-Based Binders for Lithium-Ion Batteries and Beyond. *J Electrochem Soc* **2020**, *167* (6), 065501. https://doi.org/10.1149/1945-7111/ab856b.

(127) Fan, F.; Wang, Y.; Hong, T.; Heres, M. F.; Saito, T.; Sokolov, A. P. Ion Conduction in Polymerized Ionic Liquids with Different Pendant Groups. *Macromolecules* **2015**, *48* (13), 4461–4470. https://doi.org/10.1021/acs.macromol.5b00257.
(128) Geng, Z.; Schauser, N. S.; Schauser, N. S.; Lee, J.; Lee, J.; Schmeller, R. P.; Barbon, S. M.; Segalman, R. A.; Segalman, R. A.; Segalman, R. A.; Lynd, N. A.; Hawker, C. J.; Hawker, C. J. Role of Side-Chain Architecture in Poly(Ethylene Oxide)-Based Copolymers(1) Geng, Z.; Schauser, N. S.; Schauser, N. S.; Lee, J.; Lee, J.; Schmeller, R. P.; Barbon, S. M.; Segalman, R. A.; Segalman, R. A.; Segalman, R. A.; Lynd, N. A.; Hawker, C. J.; Hawke. *Macromolecules* **2020**, *53* (12), 4960–4967. https://doi.org/10.1021/acs.macromol.0c01116.
(129) Schauser, N. S.; Grzetic, D. J.; Tabassum, T.; Kliegle, G. A.; Le, M. L.; Susca, E. M.; Antoine, S.; Keller, T. J.; Delaney, K. T.; Han, S.; Seshadri, R.; Fredrickson, G. H.; Segalman, R. A. The Role of Backbone Polarity on Aggregation and Conduction of Ions in Polymer Electrolytes. *J Am Chem Soc* **2020**, *142* (15), 7055–7065. https://doi.org/10.1021/jacs.0c00587.
(130) Ma, T.; Dong, B. X.; Onorato, J. W.; Niklas, J.; Poluektov, O.; Luscombe, C. K.; Patel, S. N. Correlating Conductivity and Seebeck Coefficient to Doping within Crystalline and Amorphous Domains in Poly(3-(Methoxyethoxyethoxy)Thiophene). *Journal of Polymer Science* **2021**, *59* (22), 2797–2808. https://doi.org/https://doi.org/10.1002/pol.20210608.
(131) Bhatt, M. P.; Thelen, J. L.; Balsara, N. P. Effect of Copolymer Composition on Electronic Conductivity of Electrochemically Oxidized Poly(3-Hexylthiophene)-b-Poly(Ethylene Oxide) Block Copolymers. *Chemistry of Materials* **2015**, *27* (14), 5141–5148. https://doi.org/10.1021/acs.chemmater.5b02085.
(132) Quill, T. J.; LeCroy, G.; Melianas, A.; Rawlings, D.; Thiburce, Q.; Sheelamanthula, R.; Cheng, C.; Tuchman, Y.; Keene, S. T.; McCulloch, I.; Segalman, R. A.; Chabinyc, M. L.; Salleo, A. Ion Pair Uptake in Ion Gel Devices Based on Organic Mixed Ionic–Electronic Conductors. *Adv Funct Mater* **2021**, *31* (47). https://doi.org/10.1002/adfm.202104301.
(133) Zhai, L.; Pilston, R. L.; Zaiger, K. L.; Stokes, K. K.; McCullough, R. D. A Simple Method to Generate Side-Chain Derivatives of Regioregular Polythiophene via the GRIM Metathesis and Post-Polymerization Functionalization. *Macromolecules* **2003**, *36* (1), 61–64. https://doi.org/10.1021/ma0255884.
(134) Zhang, C.; Du, K.; Zhang, X.; Zheng, X.; Cao, G.; Zhang, F.; Feng, F. Optical Properties of Phosphonium-, Quaternary Ammonium- and Imidazolium- Substituted Regioregular Polythiophenes and Application for Imaging Live Cells. *Dyes and Pigments* **2019**, *170*. https://doi.org/10.1016/j.dyepig.2019.107581.
(135) Jain, S. K.; Rawlings, D.; Antoine, S.; Segalman, R. A.; Han, S. Confinement Promotes Hydrogen Bond Network Formation and Grotthuss Proton Hopping in Ion-Conducting Block Copolymers. *Macromolecules* **2022**, *55* (2), 615–622. https://doi.org/10.1021/acs.macromol.1c01808.
(136) Bloembergen, N.; Purcell, E. M.; Pound, R. v. Relaxation Effects in Nuclear Magnetic Resonance Absorption. *Physical Review* **1948**, *73* (7), 679–712. https://doi.org/10.1103/PhysRev.73.679.

(137) Clark, J.; Chang, J. F.; Spano, F. C.; Friend, R. H.; Silva, C. Determining Exciton Bandwidth and Film Microstructure in Polythiophene Films Using Linear Absorption Spectroscopy. *Appl Phys Lett* **2009**, *94* (16). https://doi.org/10.1063/1.3110904.
(138) Bredas, J. L.; Street, G. B. Polarons, Bipolarons, and Solitons in Conducting Polymers. *Acc Chem Res* **1985**, *18* (10), 309–315. https://doi.org/10.1021/ar00118a005.
(139) Hamidi-Sakr, A.; Biniek, L.; Bantignies, J.-L.; Maurin, D.; Herrmann, L.; Leclerc, N.; Lévêque, P.; Vijayakumar, V.; Zimmermann, N.; Brinkmann, M. A Versatile Method to Fabricate Highly In-Plane Aligned Conducting Polymer Films with Anisotropic Charge Transport and Thermoelectric Properties: The Key Role of Alkyl Side Chain Layers on the Doping Mechanism. *Adv Funct Mater* **2017**, *27* (25), 1700173. https://doi.org/https://doi.org/10.1002/adfm.201700173.
(140) Scholes, D. T.; Yee, P. Y.; Lindemuth, J. R.; Kang, H.; Onorato, J.; Ghosh, R.; Luscombe, C. K.; Spano, F. C.; Tolbert, S. H.; Schwartz, B. J. The Effects of Crystallinity on Charge Transport and the Structure of Sequentially Processed F4TCNQ-Doped Conjugated Polymer Films. *Adv Funct Mater* **2017**, *27* (44), 1702654. https://doi.org/https://doi.org/10.1002/adfm.201702654.
(141) Matthews, R. P.; Welton, T.; Hunt, P. A. Hydrogen Bonding and π–π Interactions in Imidazolium-Chloride Ionic Liquid Clusters. *Physical Chemistry Chemical Physics* **2015**, *17* (22), 14437–14453. https://doi.org/10.1039/C5CP00459D.
(142) Gao, W.; Tian, Y.; Xuan, X. How the Cation–Cation π–π Stacking Occurs: A Theoretical Investigation into Ionic Clusters of Imidazolium. *J Mol Graph Model* **2015**, *60*, 118–123. https://doi.org/https://doi.org/10.1016/j.jmgm.2015.04.002.
(143) Tang, F.; Ohto, T.; Hasegawa, T.; Bonn, M.; Nagata, Y. Π+–Π+ Stacking of Imidazolium Cations Enhances Molecular Layering of Room Temperature Ionic Liquids at Their Interfaces. *Physical Chemistry Chemical Physics* **2017**, *19* (4), 2850–2856. https://doi.org/10.1039/C6CP07034E.
(144) Ilavsky, J. Nika: Software for Two-Dimensional Data Reduction. *J Appl Crystallogr* **2012**, *45* (2), 324–328. https://doi.org/10.1107/S0021889812004037.
(145) Beard, K. *Linden's Handbook of Batteries*, 5th ed.; McGraw Hill, 2019.
(146) Lee, S.; Manthiram, A. Can Cobalt Be Eliminated from Lithium-Ion Batteries? *ACS Energy Lett* **2022**, *7* (9), 3058–3063. https://doi.org/10.1021/acsenergylett.2c01553.
(147) Aiken, C. P.; Logan, E. R.; Eldesoky, A.; Hebecker, H.; Oxner, J. M.; Harlow, J. E.; Metzger, M.; Dahn, J. R. Li[Ni 0.5 Mn 0.3 Co 0.2 ]O 2 as a Superior Alternative to LiFePO4 for Long-Lived Low Voltage Li-Ion Cells. *J Electrochem Soc* **2022**, *169* (5), 050512. https://doi.org/10.1149/1945-7111/ac67b5.
(148) Padhi, A. K.; Nanjundaswamy, K. 5; Goodenough, J. B. Phospho-Olivines as Positive-Electrode Materials for Rechargeable Lithium Batteries. *J Electrochem Soc* **1997**, *144* (4), 1188–1194.
(149) Mizushima, K.; Jones, P. C.; Wiseman, P. J.; Goodenough, J. B. *LixCoO 2 (0<x~l): A NEW CATHODE MATERIAL FOR BATTERIES OF HIGH ENERGY DENSITY*; 1980; Vol. 15.
(150) Logan, E. R.; Hebecker, H.; Eldesoky, A.; Luscombe, A.; Johnson, M. B.; Dahn, J. R. Performance and Degradation of LiFePO 4 /Graphite Cells: The Impact of Water Contamination and an Evaluation of Common Electrolyte Additives . *J Electrochem Soc* **2020**, *167* (13), 130543. https://doi.org/10.1149/1945-7111/abbbbe.

(151) Chen, Z.; Dahn, J. R. Reducing Carbon in LiFePO[Sub 4]/C Composite Electrodes to Maximize Specific Energy, Volumetric Energy, and Tap Density. *J Electrochem Soc* **2002**, *149* (9), A1184. https://doi.org/10.1149/1.1498255.
(152) Prosini, P. P.; Carewska, M.; Scaccia, S.; Wisniewski, P.; Passerini, S.; Pasquali, M. A New Synthetic Route for Preparing LiFePO4 with Enhanced Electrochemical Performance. *J Electrochem Soc* **2002**, *149* (7), A886. https://doi.org/10.1149/1.1481716.
(153) Lee, J.; Teja, A. S. Synthesis of LiFePO4 Micro and Nanoparticles in Supercritical Water. *Mater Lett* **2006**, *60* (17), 2105–2109. https://doi.org/https://doi.org/10.1016/j.matlet.2005.12.083.
(154) Ferrari, S.; Lavall, R. L.; Capsoni, D.; Quartarone, E.; Magistris, A.; Mustarelli, P.; Canton, P. Influence of Particle Size and Crystal Orientation on the Electrochemical Behavior of Carbon-Coated LiFePO4. *The Journal of Physical Chemistry C* **2010**, *114* (29), 12598–12603. https://doi.org/10.1021/jp1025834.
(155) Ravet, N.; Chouinard, Y.; Magnan, J. F.; Besner, S.; Gauthier, M.; Armand, M. Electroactivity of Natural and Synthetic Triphylite. *J Power Sources* **2001**, *97–98*, 503–507. https://doi.org/https://doi.org/10.1016/S0378-7753(01)00727-3.
(156) Doeff, M. M.; Hu, Y.; McLarnon, F.; Kostecki, R. Effect of Surface Carbon Structure on the Electrochemical Performance of LiFePO4. *Electrochemical and Solid-State Letters* **2003**, *6* (10), A207. https://doi.org/10.1149/1.1601372.
(157) Belharouak, I.; Johnson, C.; Amine, K. Synthesis and Electrochemical Analysis of Vapor-Deposited Carbon-Coated LiFePO4. *Electrochem commun* **2005**, *7* (10), 983–988. https://doi.org/https://doi.org/10.1016/j.elecom.2005.06.019.
(158) Ait Salah, A.; Mauger, A.; Zaghib, K.; Goodenough, J. B.; Ravet, N.; Gauthier, M.; Gendron, F.; Julien, C. M. Reduction Fe3+ of Impurities in LiFePO4 from Pyrolysis of Organic Precursor Used for Carbon Deposition. *J Electrochem Soc* **2006**, *153* (9), A1692. https://doi.org/10.1149/1.2213527.
(159) Yu, D. Y. W.; Fietzek, C.; Weydanz, W.; Donoue, K.; Inoue, T.; Kurokawa, H.; Fujitani, S. Study of LiFePO4 by Cyclic Voltammetry. *J Electrochem Soc* **2007**, *154* (4), A253. https://doi.org/10.1149/1.2434687.
(160) Evans, C. M.; Sanoja, G. E.; Popere, B. C.; Segalman, R. A. Anhydrous Proton Transport in Polymerized Ionic Liquid Block Copolymers: Roles of Block Length, Ionic Content, and Confinement. *Macromolecules* **2016**, *49* (1), 395–404. https://doi.org/10.1021/acs.macromol.5b02202.
(161) Le, M. L.; Grzetic, D. J.; Delaney, K. T.; Yang, K. C.; Xie, S.; Fredrickson, G. H.; Chabinyc, M. L.; Segalman, R. A. Electrostatic Interactions Control the Nanostructure of Conjugated Polyelectrolyte-Polymeric Ionic Liquid Blends. *Macromolecules* **2022**, *55* (18), 8321–8331. https://doi.org/10.1021/acs.macromol.2c01142.
(162) Orikasa, Y.; Gogyo, Y.; Yamashige, H.; Katayama, M.; Chen, K.; Mori, T.; Yamamoto, K.; Masese, T.; Inada, Y.; Ohta, T.; Siroma, Z.; Kato, S.; Kinoshita, H.; Arai, H.; Ogumi, Z.; Uchimoto, Y. Ionic Conduction in Lithium Ion Battery Composite Electrode Governs Cross-Sectional Reaction Distribution. *Sci Rep* **2016**, *6* (1), 26382. https://doi.org/10.1038/srep26382.
(163) Shi, Y.; Zhou, X.; Zhang, J.; Bruck, A. M.; Bond, A. C.; Marschilok, A. C.; Takeuchi, K. J.; Takeuchi, E. S.; Yu, G. Nanostructured Conductive Polymer Gels as a General Framework Material To Improve Electrochemical Performance of Cathode Materials

in Li-Ion Batteries. *Nano Lett* **2017**, *17* (3), 1906–1914. https://doi.org/10.1021/acs.nanolett.6b05227.
(164) Kazemiabnavi, S.; Zhang, Z.; Thornton, K.; Banerjee, S. Electrochemical Stability Window of Imidazolium-Based Ionic Liquids as Electrolytes for Lithium Batteries. *Journal of Physical Chemistry B* **2016**, *120* (25), 5691–5702. https://doi.org/10.1021/acs.jpcb.6b03433.
(165) Chen, Z.; Dahn, J. R. Reducing Carbon in LiFePO[Sub 4]/C Composite Electrodes to Maximize Specific Energy, Volumetric Energy, and Tap Density. *J Electrochem Soc* **2002**, *149* (9), A1184. https://doi.org/10.1149/1.1498255.
(166) van der Ven, A.; See, K. A.; Pilon, L. Hysteresis in Electrochemical Systems. *Battery Energy* **2022**, *1* (2), 20210017. https://doi.org/https://doi.org/10.1002/bte2.20210017.
(167) Tang, K.; Yu, X.; Sun, J.; Li, H.; Huang, X. Kinetic Analysis on LiFePO4 Thin Films by CV, GITT, and EIS. *Electrochim Acta* **2011**, *56* (13), 4869–4875. https://doi.org/10.1016/j.electacta.2011.02.119.
(168) Weppner, W.; Huggins, R. A. Determination of the Kinetic Parameters of Mixed-Conducting Electrodes and Application to the System Li3Sb. *J Electrochem Soc* **1977**, *124* (10), 1569–1578. https://doi.org/10.1149/1.2133112.
(169) Park, K. Y.; Park, I.; Kim, H.; Yoon, G.; Gwon, H.; Cho, Y.; Yun, Y. S.; Kim, J. J.; Lee, S.; Ahn, D.; Kim, Y.; Kim, H.; Hwang, I.; Yoon, W. S.; Kang, K. Lithium-Excess Olivine Electrode for Lithium Rechargeable Batteries. *Energy Environ Sci* **2016**, *9* (9), 2902–2915. https://doi.org/10.1039/c6ee01266c.
(170) Li, W.; Garg, A.; Le, M. L. P.; Ruhatiya, C.; Gao, L.; Tran, V. M. Electrochemical Performance Investigation of LiFePO4/C0.15-x (X=0.05, 0.1, 0.15 CNTs) Electrodes at Various Calcination Temperatures: Experimental and Intelligent Modelling Approach. *Electrochim Acta* **2020**, *330*, 135314. https://doi.org/10.1016/j.electacta.2019.135314.
(171) Torai, S.; Nakagomi, M.; Yoshitake, S.; Yamaguchi, S.; Oyama, N. State-of-Health Estimation of LiFePO4/Graphite Batteries Based on a Model Using Differential Capacity. *J Power Sources* **2016**, *306*, 62–69. https://doi.org/10.1016/j.jpowsour.2015.11.070.
(172) Ovejas, V. J.; Cuadras, A. Effects of Cycling on Lithium-Ion Battery Hysteresis and Overvoltage. *Sci Rep* **2019**, *9* (1), 14875. https://doi.org/10.1038/s41598-019-51474-5.
(173) Wotango, A. S.; Su, W.-N.; Leggesse, E. G.; Haregewoin, A. M.; Lin, M.-H.; Zegeye, T. A.; Cheng, J.-H.; Hwang, B.-J. Improved Interfacial Properties of MCMB Electrode by 1-(Trimethylsilyl)Imidazole as New Electrolyte Additive To Suppress LiPF6 Decomposition. *ACS Appl Mater Interfaces* **2017**, *9* (3), 2410–2420. https://doi.org/10.1021/acsami.6b13105.
(174) Lux, S. F.; Lucas, I. T.; Pollak, E.; Passerini, S.; Winter, M.; Kostecki, R. The Mechanism of HF Formation in LiPF6 Based Organic Carbonate Electrolytes. *Electrochem commun* **2012**, *14* (1), 47–50. https://doi.org/https://doi.org/10.1016/j.elecom.2011.10.026.
(175) Chen, X.; Xu, W.; Engelhard, M. H.; Zheng, J.; Zhang, Y.; Ding, F.; Qian, J.; Zhang, J.-G. Mixed Salts of LiTFSI and LiBOB for Stable LiFePO4-Based Batteries at Elevated Temperatures. *J Mater Chem A Mater* **2014**, *2* (7), 2346–2352. https://doi.org/10.1039/C3TA13043F.

(176) Wu, M.; Song, X.; Liu, X.; Battaglia, V.; Yang, W.; Liu, G. Manipulating the Polarity of Conductive Polymer Binders for Si-Based Anodes in Lithium-Ion Batteries. *J Mater Chem A Mater* **2015**, *3* (7), 3651–3658. https://doi.org/10.1039/C4TA06594H.
(177) Qian, J.; Wiener, C. G.; Zhu, Y.; Vogt, B. D. Swelling and Plasticization of Polymeric Binders by Li-Containing Carbonate Electrolytes Using Quartz Crystal Microbalance with Dissipation. *Polymer (Guildf)* **2018**, *143*, 237–244. https://doi.org/https://doi.org/10.1016/j.polymer.2018.04.021.
(178) Shi, Y.; Zhou, X.; Yu, G. Material and Structural Design of Novel Binder Systems for High-Energy, High-Power Lithium-Ion Batteries. *Acc Chem Res* **2017**, *50* (11), 2642–2652. https://doi.org/10.1021/acs.accounts.7b00402.
(179) Wu, S.-L.; Javier, A. E.; Devaux, D.; Balsara, N. P.; Srinivasan, V. Discharge Characteristics of Lithium Battery Electrodes with a Semiconducting Polymer Studied by Continuum Modeling and Experiment. *J Electrochem Soc* **2014**, *161* (12), A1836–A1843. https://doi.org/10.1149/2.0261412jes.
(180) Kim, J.-M.; Park, H.-S.; Park, J.-H.; Kim, T.-H.; Song, H.-K.; Lee, S.-Y. Conducting Polymer-Skinned Electroactive Materials of Lithium-Ion Batteries: Ready for Monocomponent Electrodes without Additional Binders and Conductive Agents. *ACS Appl Mater Interfaces* **2014**, *6* (15), 12789–12797. https://doi.org/10.1021/am502736m.
(181) Park, K.-S.; Schougaard, S. B.; Goodenough, J. B. Conducting-Polymer/Iron-Redox-Couple Composite Cathodes for Lithium Secondary Batteries. *Advanced Materials* **2007**, *19* (6), 848–851. https://doi.org/https://doi.org/10.1002/adma.200600369.
(182) Ju, S. H.; Kang, I.-S.; Lee, Y.-S.; Shin, W.-K.; Kim, S.; Shin, K.; Kim, D.-W. Improvement of the Cycling Performance of LiNi0.6Co0.2Mn0.2O2 Cathode Active Materials by a Dual-Conductive Polymer Coating. *ACS Appl Mater Interfaces* **2014**, *6* (4), 2546–2552. https://doi.org/10.1021/am404965p.
(183) Lee, J.; Choi, W. Surface Modification of Over-Lithiated Layered Oxides with PEDOT:PSS Conducting Polymer in Lithium-Ion Batteries. *J Electrochem Soc* **2015**, *162* (4), A743. https://doi.org/10.1149/2.0801504jes.
(184) Groenendaal, L.; Jonas, F.; Freitag, D.; Pielartzik, H.; Reynolds, J. R. Poly(3,4-Ethylenedioxythiophene) and Its Derivatives: Past, Present, and Future. *Advanced Materials* **2000**, *12* (7), 481–494. https://doi.org/10.1002/(SICI)1521-4095(200004)12:7<481::AID-ADMA481>3.0.CO;2-C.
(185) Groenendaal, L.; Zotti, G.; Aubert, P.-H.; Waybright, S. M.; Reynolds, J. R. Electrochemistry of Poly(3,4-Alkylenedioxythiophene) Derivatives. *Advanced Materials* **2003**, *15* (11), 855–879. https://doi.org/https://doi.org/10.1002/adma.200300376.
(186) Ling, M.; Qiu, J.; Li, S.; Yan, C.; Kiefel, M. J.; Liu, G.; Zhang, S. Multifunctional SA-PProDOT Binder for Lithium Ion Batteries. *Nano Lett* **2015**, *15* (7), 4440–4447. https://doi.org/10.1021/acs.nanolett.5b00795.
(187) Pace, G. T.; Le, M. L.; Clément, R. J.; Segalman, R. A. A Coacervate-Based Mixed-Conducting Binder for High-Power, High-Energy Batteries. *ACS Energy Lett* **2023**, 2781–2788. https://doi.org/10.1021/acsenergylett.3c00829.
(188) Banani, S. F.; Lee, H. O.; Hyman, A. A.; Rosen, M. K. Biomolecular Condensates: Organizers of Cellular Biochemistry. *Nat Rev Mol Cell Biol* **2017**, *18* (5), 285–298. https://doi.org/10.1038/nrm.2017.7.

(189) Martin, E. W.; Mittag, T. Relationship of Sequence and Phase Separation in Protein Low-Complexity Regions. *Biochemistry* **2018**, *57* (17), 2478–2487. https://doi.org/10.1021/acs.biochem.8b00008.
(190) Johnston, A. R.; Perry, S. L.; Ayzner, A. L. Associative Phase Separation of Aqueous π-Conjugated Polyelectrolytes Couples Photophysical and Mechanical Properties. *Chemistry of Materials* **2021**, *33* (4), 1116–1129. https://doi.org/10.1021/acs.chemmater.0c02424.
(191) Radhakrishna, M.; Basu, K.; Liu, Y.; Shamsi, R.; Perry, S. L.; Sing, C. E. Molecular Connectivity and Correlation Effects on Polymer Coacervation. *Macromolecules* **2017**, *50* (7), 3030–3037. https://doi.org/10.1021/acs.macromol.6b02582.
(192) Li, L.; Srivastava, S.; Andreev, M.; Marciel, A. B.; de Pablo, J. J.; Tirrell, M. v. Phase Behavior and Salt Partitioning in Polyelectrolyte Complex Coacervates. *Macromolecules* **2018**, *51* (8), 2988–2995. https://doi.org/10.1021/acs.macromol.8b00238.
(193) Liu, Y.; Momani, B.; Winter, H. H.; Perry, S. L. Rheological Characterization of Liquid-to-Solid Transitions in Bulk Polyelectrolyte Complexes. *Soft Matter* **2017**, *13* (40), 7332–7340. https://doi.org/10.1039/C7SM01285C.
(194) Fu, J.; Schlenoff, J. B. Driving Forces for Oppositely Charged Polyion Association in Aqueous Solutions: Enthalpic, Entropic, but Not Electrostatic. *J Am Chem Soc* **2016**, *138* (3), 980–990. https://doi.org/10.1021/jacs.5b11878.
(195) Priftis, D.; Megley, K.; Laugel, N.; Tirrell, M. Complex Coacervation of Poly(Ethylene-Imine)/Polypeptide Aqueous Solutions: Thermodynamic and Rheological Characterization. *J Colloid Interface Sci* **2013**, *398*, 39–50. https://doi.org/https://doi.org/10.1016/j.jcis.2013.01.055.
(196) Chang, L.-W.; Lytle, T. K.; Radhakrishna, M.; Madinya, J. J.; Vélez, J.; Sing, C. E.; Perry, S. L. Sequence and Entropy-Based Control of Complex Coacervates. *Nat Commun* **2017**, *8* (1), 1273. https://doi.org/10.1038/s41467-017-01249-1.
(197) Nikolaev, A.; Richardson, P. M.; Xie, S.; Canzian Llanes, L.; Jones, S. D.; Nordness, O.; Wang, H.; Bazan, G. C.; Segalman, R. A.; Clément, R. J.; Read de Alaniz, J. Role of Electron-Deficient Imidazoles in Ion Transport and Conductivity in Solid-State Polymer Electrolytes. *Macromolecules* **2022**, *55* (3), 971–977. https://doi.org/10.1021/acs.macromol.1c01979.
(198) Pace, G.; Nordness, O.; Nguyen, P.; Choi, Y.-J.; Tran, C.; Clément, R.; Segalman, R. Tuning Transport via Interaction Strength in Cationic Conjugated Polyelectrolytes. *Macromolecules* No. Submitted.
(199) Zhang, H.; Liu, C.; Zheng, L.; Feng, W.; Zhou, Z.; Nie, J. Solid Polymer Electrolyte Comprised of Lithium Salt/Ether Functionalized Ammonium-Based Polymeric Ionic Liquid with Bis(Fluorosulfonyl)Imide. *Electrochim Acta* **2015**, *159*, 93–101. https://doi.org/https://doi.org/10.1016/j.electacta.2015.01.213.